The Synthesis of Precursors for the Deposition of Photovoltaic Thin Films

Sudlow, Anna

Award date:
2012

Awarding institution:
University of Bath

The Synthesis of Precursors for the Deposition of Photovoltaic Thin Films

Anna Louise Sudlow

A thesis submitted for the degree of Doctor of Philosophy

University of Bath

Department of Chemistry

May 2012

Copyright

University of Bath, May 2012

Abstract

The work in the thesis describes attempts to synthesise precursors for the deposition of thin films for use in thin-film photovoltaic cells.

Chapter One – Introduction provides a brief background to photovoltaic cells with specific detail given to thin-film photovoltaic cells. The concepts of chemical vapour deposition (CVD) and precursor design are discussed with relevant precursors are highlighted.

Chapter Two – Xanthates provides details of the synthesis and characterisation of a series of metal xanthates. The materials chemistry of the xanthates is then discussed.

Chapter Three – Dithiocarbamates provides details of the synthesis and characterisation of a series of metal dithiocarbamates. The materials chemistry of the dithiocarbamates is then discussed.

Chapter Four – Materials Work on Cu_2ZnSnS_2 and $CuSbS_2$ provides a discussion of attempts to deposit thin films of Cu_2ZnSnS_4 and $CuSbS_2$ from the precursors discussed in chapters two and three.

Chapter Five – Heterobimetallic precursors provides details of the synthesis and characterisation of a series of heterobimetallic precursors liked by chlorine bridges and subsequent attempts to replace the chlorine atoms with thiolate ligands.

Chapter Six – Precursors for ZnO:F provides details of the synthesis and characterisation of a series of single source precursors designed for the deposition of ZnO:F thin films. The materials chemistry and subsequent CVD trials are then discussed.

Acknowledgements

Firstly, I would like to thank my supervisor Kieran Molloy for his help and guidance throughout my PhD, I would also like to thank him for his patience with my ability to recrystallise $(Ph_3P)_2CuCl$ many, many times! I would also like to thank Dr. Steve Richards for putting up with my many questions and for all of his help with the new CVD kit and the TGA.

I would like to thank members of my group past and present, Nathan, Dave, Jeff, Steve and Ioana for being great company throughout my PhD. I also would like to thank everyone in Bath for all of the many lunches, dinners and nights out that have made my time here really enjoyable.

I would also like to thank all of my wonderful friends in Bristol who have made the final few months of writing up so enjoyable.

There are various people who have been invaluable in providing guidance with analytical measurements. These include John Lowe for all of his help with NMR, Gabriele Kociok-Köhn and Mary Mahon for solving XRD structures, Gabriele Kociok-Köhn (again) and Sophie Beckett for providing assistance with PXRD measurements, and also Tom Wildsmith for ensuring that those last few samples got run! My thanks go to John Mitchells and Ursula Potter who have been a great help in explaining the principles of SEM and TEM and for all of the training given in the use of these instruments. Thanks also to Daniel Wolverston for providing Raman spectroscopy measurements.

Many thanks to my parents, Kevin and Sue, who, amongst other things, have given me food and a place to live for the last few months. Also my brother Tim who kindly provided a distraction from writing whilst I was there!

Finally I would like to thank Tom for his love and support throughout my PhD. He has been incredibly helpful and understanding.

Abbreviations

α: alpha

Å: Angstrom

AACVD: Aerosol Assisted Chemical Vapour Deposition

ALD: Atomic Layer Deposition

APCVD: Atmospheric Pressure Chemical Vapour Deposition

ASU: Asymmetric Unit

^{t}Amyl: tertiary amyl, $C(CH_3)_2(CH_2CH_3)$

β: beta

Bn: benzyl, $CH_2C_6H_5$

^{i}Bu: *iso*-butyl, $CH(CH_3)_2CH_3$

^{n}Bu: *n*-butyl, $CH_2CH_2CH_2CH_3$

^{t}Bu: *tertiary*-butyl, $C(CH_3)_3$

CVD: Chemical Vapour Deposition

Cy: Cyclohexyl

°: Degree

δ: delta, Chemical Shift

d: Doublet

EDX: Electron-Dispersive X-Ray Specrtoscopy

Et: ethyl, CH_2CH_3

LED: Light Emitting Diode

LPCVD: Low Pressure Chemical Vapour Deposition

μ: mu

m: Multiplet

Me: methyl, CH_3

m.p.: melting point

MOCVD: Metal Organic Chemical Vapour Deposition

nm: Nanometers
NMR: Nuclear Magnetic Resonance

%: Percentage
^{i}Pr: *iso*-propyl, $CH(CH_3)_2$
Ph: Phenyl, C_6H_5
ppm: Parts Per Million
PVD: Physical Vapour Deposition
PXRD: Powder X-Ray Diffraction

q: Quartet
quin: Quintet

R_f: fluorinated alkyl group

s: Singlet
SEM: Scanning Electron Microscopy
sept: Septet
sxt: Sextet

τ: tau
t: Triplet
TGA: Thermogravimetric Analysis
TMS: Trimethylsilyl

XRD: X-Ray Diffraction

Declaration

The work described in this thesis was conducted by the author at the University of Bath between September 2008 and March 2012. It represents the author's original and independent work, except where specific reference is made to the contrary. Neither the whole nor and part of this thesis has been submitted previously in support of a degree at this or any other university. It does not exceed the prescribed limit, including tables, references and appendices.

Guide to Compound Numbering

(1) $Zn(S_2COEt)_2$

(2) $Zn(S_2CO^iPr)_2$

(3) $Zn(S_2CO^nPr)_2$

(4) $Zn(S_2CO^nBu)_2$

(5) $Zn(S_2CO^nHex)_2$

(6) $Zn(S_2COEt)_2TMEDA$

(7) $Sn(S_2COEt)_2$

(8) $Sn(S_2COEt)_4$

(9) $Sb(S_2COEt)_3$

(10) $(Ph_3P)_2CuS_2COEt$

(11) $(Ph_3P)_2CuS_2CO^iPr$

(12) $(Ph_3P)_2CuS_2CO^tBu$

(13) $(Ph_3P)_2CuS_2CO^tAmyl$

(14) $[(OPh)_3P]_2CuS_2COEt$

(15) $(^nBu_3P)_2CuS_2COEt$

(16) $(^nBu_3P)_2CuS_2CO^nBu$

(17) $Zn[S_2CN(Me)^nBu]_2$

(18) $Zn[S_2CN(Me)Bn]_2$

(19) $Sn[S_2CN(Me)^nBu]_2$

(20) $Sn[S_2CN(Me)Bn]_2$

(21) $\{Sn[S_2CN(Me)Bn]_2S\}_2$

(22) $Sb[S_2CN(Me)^nBu]_3$

(23) $Sb[S_2CN(Me)Bn]_3$

(24) $(Ph_3P)_2CuS_2CN(Me)^nBu$

(25) $(Ph_3P)_2CuS_2CN(Me)Bn$

(26) $(Ph_3P)_4Cu_2ZnCl_4$

(27) $[(Me_3P)_2Cu_2Cl_4Zn]_n$

(28) $[(Me_3P)_4Cu]^+[ZnCl_4Cu(PMe_3)_2]^-$

(29) $(Ph_3P)_2CuCl_2SnCl$

(30) $(Me_3P)_3CuSnCl_3$

(31) $(Ph_3P)_2CuCl_2SbCl_2$

(32) $(Ph_3P)_3CuCl_2SbCl_2$

(33) $[Sb_2Cl_9]^{3-}[(Me_3P)_2Cu]^+[HPMe_3]_2^+$

(34) $[Sb_2Cl_7(Me_3P)_2]^-[Cu(Me_3P)_4]^+$

(35) $[MeZn(O_2CC_2F_5)]_n$

(36) $[Zn_5Me_2(OMe)_2(O_2CC_2F_5)_6]_2$

(37) $[MeZn(O_2CC_3F_7)]_n$

(38) $[Zn_5Me_2(OMe)_2(O_2CC_3F_7)_6]_2$

(39) $[EtZn(O_2CC_2F_5)]_n$

(40) $Zn_9(OEt)_2O(O_2CC_2F_5)_{12}(O)_2$

(41) $[EtZn(O_2CC_3F_7)]_n$

(42) $Zn_8Et_4(OEt)_4(O_2CC_3F_7)_6(O)$

(43) $MeZn(O_2CC_2F_5)TMEDA$

(44) $MeZn(O_2CC_3F_7)TMEDA$

(45) $EtZn(O_2CC_2F_5)TMEDA$

(46) $EtZn(O_2CC_3F_7)TMEDA$

(47) $[Zn(O_2CC_2F_5)_2TMEDA]_2$

(48) $[Zn(O_2CC_3F_7)_2TMEDA]_2$

(49) $[Zn(O_2CC_3F_7)_2TMEDA]_2.H_2O$

Contents

Abstract ii

Acknowledgments iii

Abbreviations iv

Declaration vi

Guide to Compound Numbering vii

Contents viii

Figures and Tables list xiii

Chapter One: Introduction

1.1 Introduction 2

1.2 Photovoltaic Cells 2

1.3 Silion Cells 3

1.4 Thin Film Cells 3

1.4.1 $CuSbS_2$ 4

1.4.2 Cu_2ZnSnS_4 5

1.5Transparent Conducting Oxides 6

1.6 Chemical Vapour Deposition 7

1.6.1 APCVD and LPCVD 9

1.6.2 AACVD 10

1.6.3 Decomposition Pathways 10

1.6.4 Film Growth Mechanisms 11

1.7 Precursors 12

1.8 Precursors for Metal Sulphide Films 14

1.8.1 Dual-Source Precursors 14

1.8.2 Thiolates 15

1.8.3 Dithiocarbamates 18

1.8.4 Xanthates 20

1.9 Aims of Project 21

1.10 References 23

Chapter Two: Xanthates 29

2.1 Introduction 30

2.1.1 Zinc Xanthates 31

2.1.2 Tin Xanthates 31

2.1.3 Antimony (III) Xanthates 32

2.1.4 Copper Xanthates 33

2.2 Results and Discussion 34

2.2.1 Zinc Xanthates 34

2.2.2 Tin Xanthates 37

2.2.3 Antimony Ethyl Xanthate 45

2.2.4 Copper Xanthates 46

2.1.5 Conclusions 54

2.3 Experimental 56

2.4 References 61

Chapter Three: Dithiocarbamates 63

3.1 Introduction 64

3.1.1 Zinc Dithiocarbamates 64

3.1.2 Tin Dithiocarbamates 65

3.1.3 Antimony Dithiocarbamates 67

3.1.4 Copper Dithiocarbamates 68

3.2 Results and Discussion 69

3.2.1 Zinc Dithiocarbamates 69

3.2.2 Tin Dithiocarbamates 70

3.2.3 Antimony Dithiocarbamates 73

3.2.4 Copper Dithiocarbamates 74

3.2.5 Conclusions 76

3.3 Experimental 79

3.4 References 82

Chapter Four: Materials Work on Cu_2ZnSnS_4 and $CuSbS_2$ 84

4.1 Introduction 85

4.1.1 Cu_2ZnSnS_2 85

4.1.2 $CuSbS_2$ 86

4.2 Results and Discussion 86

4.2.1 AACVD Trials Using Xanthates 86

4.2.2 AACVD Trials Using a Mixture of Xanthates and Dithiocarbamates 95

4.2.3 AACVD Trials Using Dithiocarbamates 100

4.2.4 AACVD of $CuSbS_2$ Using Salts and Thiurea 108

4.2.5 Doctor Blading of Cu_2ZnSnS_2 109

4.2.6 Synthesis of Cu_2ZnSnS_2 Nanoparticles 112

4.2.7 Conclusions 114

4.3 Experimental 115

4.4 References 116

Chapter Five: Heterobimetallic Precusors 118

5.1 Introduction 119

5.1.1 Cu-S-Zn Compounds 120

5.1.2 Cu-S-Sn Compounds 120

5.1.3 Cu-S-Sb Compounds 121

5.2 Results and Discussion 122

5.2.1 Zn/Cu Heterobimetallic Species 122

5.2.2 Sn/Cu Heterobimetallic Species 127

5.2.3 Sb/Cu Heterobimetallic Species 130

5.2.4 Reactions with NaSEt and $(TMS)_2S$ 139

5.2.5 Conclusions 140

5.3 Experimental 141

5.4 References 144

Chapter Six: Precursors for ZnO:F 146

6.1 Introduction 147

6.1.1 Fluorine-Doped Zinc Oxide 148

6.2.2 Precursors for ZnO Films 148

6.2 Results and Discussion 151

6.2.1 Organozinc Fluorocarboxylates 151

6.2.2 Related Organozinc Fluorocarboxylates 158

6.2.3 TMEDA Adducts of Organozinc Fluorocarboxylates 168

6.2.4 TMEDA Adducts of Zinc Fluorocarboxylates 174

6.2.5 Conclusions 181

6.3 Experimental 182

6.4 References 186

Chapter Seven: Conclusions and Future Work 190

7.1 Deposition of Cu_2ZnSnS_4 191

7.2 Deposition of $CuSbS_2$ 191

7.3 Heterobimetallic Precusors 192

7.4 Deposition of ZnO:F 192

Appendix One: General Procedures 194

A1.1 Laboratory Techniques 194

A1.2 Instrumentation 194

A1.3 CVD Reactors 195

A1.4 Flashing LED Experiment 197

Appendix Two: X-Ray Crystallographic Information 198

Figures and Tables

Chapter One: Introduction

Figure 1.1 $CuInS_2$ cell 3

Figure 1.2 Chalcopyrite structure of $CuInS_2$ 5

Figure 1.3 Unit cell of Cu_2ZnSnS_4 6

Figure 1.4 Fundamental steps involved in CVD process 9

Scheme 1.1 Mechanism of β-hydride elimination 11

Scheme 1.2 Mechanism of α–hydride elimination 11

Figure 1.5 Film growth mechanisms 12

Figure 1.6 Structure of $Sn(OC_6H_2\text{-}4\text{-}Me\text{-}2,6\text{-}^tBu)_2$ 14

Figure 1.7 Structure of $Zn_4(SPh)_8(ROH)$ 16

Figure 1.8 Structure of $[Cd(SC_6H_2{}^tBu\text{-}2,4,6)_2]_2$ 17

Figure 1.9 Structure of $[(^tBu)_2InS^tBu]_2$ 17

Figure 1.10 Structure of $Sn(SCH_2CH_2(CF_2)_5CF_3)_4$ 18

Figure 1.11 Structure of $Zn(S_2CNEt_2)_2$ 19

Figure 1.12 Structure of $Sn(SCy)_2(S_2CNEt_2)_2$ 19

Scheme 1.3 Chugaev elimination reaction 20

Scheme 1.4 Alternative Decomposition Mechanisms 21

Figure 1.16 $Ni(S_2CO^nBu)_2(NC_5H_5)$ 21

Chapter Two: Xanthates

Scheme 2.1 Chugaev elimination reaction 30

Figure 2.1 Structure of $Zn(S_2COEt)_2$ 31

Figure 2.2 Structure of $Sn(S_2COMe)_2$ 32

Figure 2.3 Structure of $Sb(S_2COMe)_3$ 32

Figure 2.4 Structure of $CuS_2CO\ C_6H_2$-2,6-$^tBu_2$-4-Me 33

Figure 2.5 TGA of **(1)** - **(6)** 35

Table 2.1 Comparison of decomposition profiles of **(1)** – **(6)** 37

Figure 2.6 $Sn(S_2COEt)_2$ **(7)** 38

Figure 2.7 Isobidentate and anisobidentate bonding 38

Figure 2.8 Packing of **(7)** 39

Table 1.2 Selected bond distances of **(7)** and $Sn(S_2COMe)_2$ 40

Figure 2.9 TGAs of **(7)** and **(8)** 40

Figure 2.10 Raman of $Sn(S_2COEt)_2$ decomposition product 41

Table 2.3 Raman shifts for tin sulphides 41

Figure 2.11 SEM Image of SnS_2 on glass 42

Figure 2.12 EDX Analysis of SnS_2 film 43

Figure 2.13 SEM Image of SnS_2 on Mo coated glass 44

Figure 2.14 SEM Image of an SnS nanoparticle 44

Figure 2.15 TGA of $Sb(S_2COEt)_3$ **(9)** 45

Figure 2.16 Crystal structure of $(Ph_3P)_2CuS_2CO^tBu$ **(12)** 46

Table 2.4. Selected bond distances and angles of **(10)** – **(13)** 47

Figure 2.17 TGA of **(10) - (13)** 48

Table 2.5 Comparison of decomposition profiles of **(10)** – **(13)** 50

Figure 2.18 Structure of $[(PhO)_3P]_2CuS_2COEt$ **(14)** 51

Table 2.5 Selected bond distances and angles of **(14)** 51

Figure 2.19 TGA of **(14) - (16)** 52

Table 2.7 Comparison of decomposition profiles of **(14)** – **(16)** 53

Figure 2.20 SEM Image of Cu_2S on glass 53

Figure 2.21 PXRD Pattern of Cu_2S on glass 54

Table 2.8 Comparison of decomposition temperatures and products of **(1)** – **(16)** 56

Chapter Three: Dithiocarbamates

Figure 3.1 Bidentate and monodentate coordination of dithiocarbamate ligands 64

Figure 3.2 General structure of $Zn(S_2CNMeR)_2$, R=Et, ^nPr, ^iPr, ^nBu 65

Figure 3.3 Structure of $Sn(S_2CN(CH_2)_4)_4$ 66

Figure 3.4 Structure of $Sb[S_2CN(Me)^nBu]_3$ 67

Figure 3.5 Structure of $(Ph_3P)_2CuS_2CNMeBn$ 68

Figure 3.6 TGAs of **(17)** and **(18)** 69

Figure 3.7 Structure of $\{Sn[S_2CN(Me)Bn]_2S\}_2$ **(21)** 70

Table 3.1 Selected bond distances of **(21)** and $[Sn(S_2CNEt_2)S]_2$ 71

Figure 3.8 TGAs of **(19)** and **(20)** 72

Figure 3.9 TGAs of **(22)** and **(23)** 73

Figure 3.10 Structure of $(Ph_3P)_2CuS_2CN(Me)Bu$ **(24)** 74

Table 3.2 Selected bond distances and angles of **(24)** and **(25)** 75

Table 3.3 Comparison of decomposition temperatures and products of **(1)** – **(25)** 78

Chapter Four: Materials Work on Cu_2ZnSnS_4 and $CuSbS_2$

Figure 4.1 Powder diffraction pattern of thermal decomposition product 87

Figure 4.2 TGA of **(4)**, **(7)** and **(16)** 88

Figure 4.3 SEM image of film grown from **(4)**, **(7)** and **(16)** 88

Figure 4.4 PXRD of film grown from **(4)**, **(7)** and **(16)** 89

Figure 4.5 TGA of **(5)**, **(7)** and **(16)** 90

Figure 4.6 SEM image of film grown from **(5)**, **(7)** and **(16)** at 250°C 90

Figure 4.7 PXRD of film grown from **(5)**, **(7)** and **(16)** at 250°C 91

Figure 4.8 SEM image of film grown from **(5)**, **(7)** and **(16)** at 400°C 92

Figure 4.9 Powder diffraction pattern of $CuSbS_2$ 93

Figure 4.10 TGA of (9) and (16) 93

Figure 4.11 SEM image of film grown from **(9)** and **(16)** 94

Figure 4.12 TGA of **(16)**, **(17)** and **(19)** 95

Figure 4.13 SEM image of film grown from **(16)**, **(17)** and **(19)** 96

Figure 4.14 TGA of **(16)**, **(18)** and **(20)** 97

Figure 4.15 SEM image of film grown from **(16)**, **(18)** and **(20)** 97

Figure 4.16 TGA of **(16)**, **(22)** and **(23)** 98

Figure 4.17 SEM image of film grown from **(16)** and **(22)** 99

Figure 4.18 SEM image of film grown from **(16)** and **(23)** 100

Figure 4.19 TGA of **(17)**, **(19)** and **(24)** 101

Figure 4.20 SEM image of film grown from **(17)**, **(19)** and **(24)** 101

Figure 4.21 TGA of **(18)**, **(20)** and **(25)** 102

Figure 4.22 SEM image of film grown from **(18)**, **(20)** and **(25)** 103

Figure 4.23 TGA of **(22)** and **(24)** 104

Figure 4.24 SEM image of film grown from **(22)** and **(24)** 104

Figure 4.25 PXRD of film grown from **(22)** and **(24)** 105

Table 4.1 PXRD peaks and information 105

Figure 4.26 TGA of **(23)** and **(25)** 106

Figure 4.27 SEM Image of film grown from **(23)** and **(25)** 106

Figure 4.28 PXRD of film grown from **(23)** and **(25)** 107

Table 4.2 PXRD peaks and information 107

Figure 4.29 SEM image of film grown from CuI, $SbCl_3$ and thiurea 108

Figure 4.30 PXRD of film grown from CuI, $SbCl_3$ and thiurea 109

Figure 4.31 SEM image of doctor bladed film 110

Figure 4.32 SEM image of doctor bladed film 111

Figure 4.33 PXRD of film obtained from doctor bladeding 111

Table 4.3 PXRD peaks and information 112

Figure 4.34 TEM image of nanoparticles 113

Chapter Five: Heterobimetallic Precursors

Figure 5.1 Structure of $(Ph_3P)_2CuIn(SEt)_4$ 119

Figure 5.2 Coordination in (a) $[Sb_2(edt)_2(\mu_3\text{-}S)CuCl(CuSCN)]_n$, (b) $\{[Sb(edt)(pymt)]_2(CuSCN)_3\}_n$ and (c) $[Sb(edt)(pymt)(CuCSN)_2]_n$ 121

Scheme 5.1 Synthesis of **(26)** – **(28)** 122

Figure 5.3 Structure of **(26)** 123

Table 5.1 Selected bond distances in **(26)** 124

Figure 5.4 Structure of **(27)** 124

Table 5.2 Selected bond distances in **(27)** 125

Figure 5.5 Structure of **(28)** 125

Table 5.5 Selected bond distances in **(28)** 126

Scheme 5.2 Synthesis of **(29)** and **(30)** 127

Figure 5.6 Structure of **(29)** 127

Table 5.4 Selected bond distance in **(29)** 128

Figure 5.7 Structure of **(30)** 129

Table 5.5 Selected bond distances in **(30)** 130

Scheme 5.3 Synthesis of **(31)** and **(32)** 131

Figure 5.8 Structure of **(31)** 131

Table 5.6 Selected bond distances in **(31)** and **(32)** 132

Figure 5.9 Structure of **(32)** 133

Figure 5.10 Structure of **(32)**, showing Ph-Sb interaction 134

Figure 5.11 Structure of **(33)** 135

Table 5.7 Selected bond distances in **(33)** 136

Figure 5.12 Structure of **(34)** 137

Table 5.8 Selected bond distances in **(34)** 137

Scheme 5.4 Reactions with NaSEt 139

Scheme 5.5 Further Reactions with NaSEt 139

Scheme 5.6 Reactions with $(TMS)_2S$ 140

Chapter Six: Precursors for ZnO:F

Figure 6.1 Simplified diagram of a thin-film solar cell 147

Figure 6.2 Structure of $[MeZntdmap]_2$ 149

Figure 6.3 keto – enol tautomerism 149

Figure 6.4 Monodentate and bidentate coordination of metal carboxylates 150

Scheme 6.1 Synthesis of **(35)**, **(37)**, **(39)** and **(41)** 151

Figure 6.5 Structure of **(39)** 152

Figure 6.6 Structure of **(41)** 153

Table 6.1 Selected bond distances and angles in **(39)** and **(41)** 154

Figure 6.7 TGA of **(35)**, **(37)**, **(39)** and **(41)** 155

Figure 6.8 SEM image of film grown from **(35)** 157

Figure 6.9 PXRD of film grown from **(35)** 157

Figure 6.10 Structure of **(36)** 159

Table 6.2 Selected bond distances in **(36)** 160

Figure 6.11 Structure of **(36)** with C_2F_5 groups omitted 161

Figure 6.12 Structure of **(40)** 161

Figure 6.13 Structure of **(40)** with C_2F_5 groups omitted 163

Table 6.3 Selected bond distances in (**40)** 163

Scheme 6.2 Mechanism of O_2 attack on $[EtZn(O_2CPh)]_n$ 164

Scheme 6.3 Possible Schlenk Equilibria in **(39)** 165

Figure 6.14 Structure of **(42)** 165

Figure 6.15 Structure of **(42)** with C_2F_5 groups omitted 167

Table 6.4 Selected bond distances in (**42)** 167

Scheme 6.4 Synthesis of **(43)** – **(46)** 168

Figure 6.16 Structure of (**45)** 168

Figure 6.17 Structure of **(45)** showing hydrogen bond 169

Table 6.5 Selected bond distances and angles of **(45)** 170

Figure 6.18 TGA of **(43)** – **(46)** 170

Table 6.6 Steps seen in the TGAs of **(43)** – **(46)** 172

Figure 6.19 SEM image of film grown from **(44)** 173

Figure 6.20 PXRD of film grown from **(44)** 173

Scheme 6.5 Synthesis of **(47)** and **(48)** 174

Figure 6.21 Structure of **(47)** 174

Table 6.7 Selected bond distances of **(47)** 175

Figure 6.22 Structure of **(49)** 176

Figure 6.23 Structure of **(49)**, with C_3F_7 groups omitted 177

Table 6.8 Selected bond distances of **(49)** 178

Figure 6.24 TGA of **(47)** and **(48)** 179

Figure 6.25 SEM image of film grown from **(47)** and **(48)** 180

Figure 6.26 PXRD of film grown from **(47)** and **(48)** 180

Chapter Seven: Conclusions and Future Work

Figure A1.1 AACVD apparatus 196

Figure A1.1 LPCVD apparatus 196

Figure A1.3 Flashing LED experiment apparatus 197

Chapter One
Introduction

1.1 Introduction

This thesis describes attempts to synthesise precursors for the deposition of layers used in thin film photovoltaic cells, namely Cu_2ZnSnS_4 and $CuSbS_2$ as absorber layers and ZnO:F as the front contact. The literature survey describes the global importance of solar cells and the progress made with research on them. It also describes the process of Chemical Vapour Deposition and the precursors that could be used in the production of the various layers.

1.2 Photovoltaic Cells

In view of the world's ever-increasing demand for energy, limitation of usable fossil fuels and the impact of large exhaust pollutant on the environment during their use, there is an urgent need to exploit new energy sources that are plentiful, renewable and clean. In March 2007 The Council of the European Union announced that it aims to reduce green house gas emissions by 60-80% by 2050. It also aims to increase the share of renewable energies in overall EU energy consumption to 20% by 2020.[1] If these targets are addressed by the Government the development of solar technologies will increase exponentially in the coming years.

Historically, solar-electric technology has been investigated for many years. Interest began to grow when Daryl Chapin, Gerald Pearson and Calvin Fuller produced a crystalline silicon device that had an efficiency of 6% in 1954, while previous devices had only managed to produce efficiencies of around 1%.[2] Over the past 30 years research progress has been significant, with the highest reported efficiencies of single-junction cells reaching 28.1% in a GaAs cell.[3] Multi-junction cells achieve much higher efficiencies with the highest to date reaching 43.5%[3]

The photovoltaics market is split into many different types of solar cell, silicon cells, thin film cells, multijunction cells, dye sensitised cells and organic cells being the five main types.[4]

1.3 Silicon cells

Currently silicon based cells dominate the photovoltaics market 94% of the photovoltaics commercial shipments in 2004 consisted of single crystal, multicrystalline, ribbon and sheet silicon.[5] With the increasing demand for solar cells there are concerns over the manufacturing capacities and supplies of silicon.[4]

Silicon cells have been thoroughly investigated since 1954 and efficiencies now reach around 92% of the theoretical limit of 29%.[6] The developments of these designs has included metal/insulator/n-type/p-type,[7] passivated-emitter solar cells,[8] single-sided and double-sided buried contacts,[9] point contact [10] and bifacial cells.[11]

As silicon has an indirect band gap, silicon cells require a thick absorber layer (>100μm) to absorb enough solar radiation to obtain high efficiencies.[12] The grain boundaries in silicon-based cells also act as recombination centres in the cell, meaning that single-crystalline silicon is required for high efficiencies.[13]

Thin film solar cells utilise direct band gap absorbers, meaning that much less material is required to absorb a sufficient portion of solar radiation.[13]

1.4 Thin Film Cells

Thin film cells consist of many different layers, each having an important role in the working of the cell. Typical layers seen in a thin film cell are a back contact, an n-type transparent layer, a p-type absorber layer and a front contact. A $CuInS_2$ cell is shown in Figure 1.1. This cell has all of the typical layers seen in a thin film cell.[14]

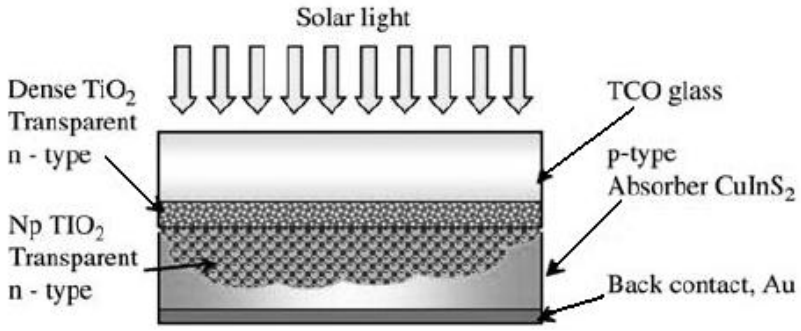

Figure 1.1 $CuInS_2$ cell[14]

The current cells with the highest efficiencies have CdTe and $Cu(In,Ga)Se_2$ (CIGS) absorber layers with highest reported efficiencies of 16.7% and 20.3% respectively.[3] These cells have problems with toxicity and price. Both contain rare and expensive elements (Te and In), and it has been estimated that due to the availability of tellurium and indium the generating capacity of these cells could be limited to 4% and 1% of the current global electricity demand for CdTe and CIGS respectively.[15] CdTe cells also contain Cd which is toxic and so an alternative absorber layer would be beneficial. A series of low cost alternatives are being investigated. For a semiconducting thin film to be suitable for the solar absorber layer a band gap between 0.9eV and 1.9eV is required.[16] Thin films of Cu_2ZnSnS_4 and $CuSbS_2$ have direct band gaps of 1.45-1.5eV and 1.5eV respectively and absorption coefficients of over $10^4 cm^{-1}$, as such these films fulfill the requirements for solar absorber layers in low cost thin film photovoltaic devices. [16-17]

1.4.1 $CuSbS_2$

$CuInS_2$ (CIS) is part of the I-III-VI_2 group of semiconductors with chalcopyrite structure (Figure 1.2) and has already been widely used as a solar absorber layer.[18] Unfortunately, due to the high price of indium CIS absorber layers are not commercially viable and so an alternative absorber layer is required. $CuSbS_2$ is also part of the I-III-VI_2 group of semiconductors with chalcopyrite structure. $CuSbS_2$ is a direct semiconductor with a band gap of 1.5eV and as such is an ideal candidate for use as a solar absorber layer in a thin film solar cell.[19] The price of antimony is also considerably lower than that of indium.[14] This absorber layer is not very widely investigated and currently no efficiencies for cells with $CuSbS_2$ absorber layers have been reported.

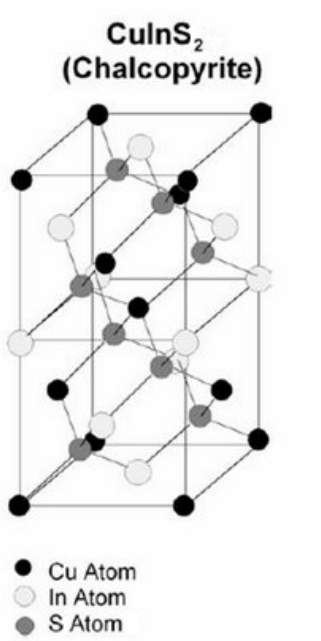

Figure 1.2 Chalcopyrite structure of $CuInS_2$[18]

1.4.2 Cu_2ZnSnS_4

To date the best solar cell using Cu_2ZnSnS_4 as an absorber layer was produced by Shin *et al.* using thermal evaporation of elemental Cu, Zn, Sn and S at 150°C under vacuum followed by annealing at 570°C; this cell reached an efficiency of 8.4%.[20] However this efficiency is much lower than the theoretical limit of 32.2% for Cu_2ZnSnS_4,[21] higher efficiencies have been achieved using a mixture of sulphur and selenium, $Cu_2ZnSn(S, Se)_4$. The addition of selenium lowers the band gap.[13] Currently the highest efficiency of a cell using sulphur and selenium is 10.1%, with a band gap of 1.15eV, deposited by spin coating a solution of Cu_2S, Zn, SnSe, Se and S in hydrazine and annealing at 540°C in a sulphur environment.[22]

The structure of Cu_2ZnSnS_4 is similar to chalcopyrites such as $CuInS_2$. To obtain the unit cell (Figure 1.3) of Cu_2ZnSnS_4 from $CuInS_2$, replace the In atoms with Sn and Zn.[17, 23] As tin and zinc are naturally abundant in the earth's crust and therefore much cheaper than indium this replacement is advantageous.[21]

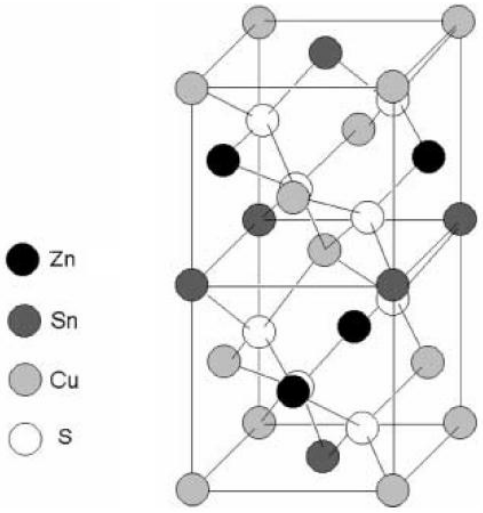

Figure 1.3 Unit cell of Cu_2ZnSnS_4[23]

1.5 Transparent Conducting Oxides

Transparent conducting oxide (TCO) thin films are films of metal oxides, which are normally wide band gap semiconductors, with an added dopant to increase conductivity. One of the first reports of a TCO was SnO_2:Cl deposited by spray pyrolysis in 1947.[24] From around 1995 research into TCOs has increased dramatically, with new materials being discovered frequently.[25] TCOs have a wide range of uses in devices such as flat screen displays,[26] electrochromic devices,[27] organic light emitting diodes,[28] thin film resistors[29] and energy efficient windows.[30] Historically, SnO_2:F, ZnO:Al and In_2O_3:Sn have been the most widely investigated TCOs.[31] In the past 5-10 years other types of TCO have been investigated, such as ZnO:F,[32] In-Zn-O,[31], Cd_2SnO_4 [33] and ZnO:B.[34]

Currently one of the fastest growing uses for TCOs is as a contact in photovoltaic cells.[25] The front contact in a photovoltaic cell is normally a metallic grid, a TCO or a combination of the two.[30] Silicon-based cells generally use a metallic grid, although thin film silicon technologies tend to use a TCO based on SnO_2.[25] Thin film cells have historically used SnO_2:F as the front contact.[35] Research into the stability of TCOs has shown that ZnO based layers are resistant to oxidizing and reducing agents to 800K.[36] As a result of this ZnO based layers are being progressively more used in thin film cells.[37]

1.6 Chemical Vapour Deposition

Chemical Vapour Deposition (CVD) is a technique used to deposit thin films onto a substrate. The process of CVD involves precursors in the vapour phase undergoing a series of chemical reactions, both in the gas phase and on the surface.[38]

CVD is a relatively old technique, the first example of a chemically deposited film is the production of carbon filaments for the incandescent lamp industry in 1880.[39] The deposition of tungsten metal is one of the earliest examples of the CVD of metals; Wöhler used WCl_6 and hydrogen carrier gas in 1855.[40] Later that century the Mond process was developed, this was used for the refinement of nickel ore and involved nickel metal being deposited from $Ni(CO)_4$.[41]

One of the earliest examples of a silicon thin film deposited using CVD is the hydrogen reduction of $SiCl_4$ in 1909.[42] Crystalline silicon based thin film photo-cells were being investigated as early as 1946.[43]

Pilkington developed an "on-line" method for coating glass with various thin films when on the float glass production line using atmospheric pressure CVD. This was an important development in the CVD industry as it enabled a much larger scale of coated glass to be made when compared to other "off-line" methods such as sputtering. Notable films include fluorine doped tin oxide, SnO_2:F and TiO_2.[38]

There was a rapid development of the microelectronics industry in the 1970s, which meant that very thin, high purity, and highly uniform films with a strict control over composition and doping were required. Thin n- or p-doped epitaxial silicon were required for all Si-integrated circuit technology. Closed tube transport of SiI_4 from heating solid Si in the presence of iodine is one of the first examples of Si epitaxy.[44] Later large scale production of Si epitaxial films started, these were made by pyrolysis of SiH_4 in the presence of H_2.[45]

In the 1960s interest in the use of metal organic precursors for CVD applications started. InP was the first III-V material to be prepared from a metal organic precursor. In 1960 Didchenko *et al.* reported the use of Me_3In and liquid PH_3 in a closed tube thermal decomposition at 275-300°C to produce InP.[46] Later, in 1962 InSb and GaAs were both produced using metal organic precursors. Me_3In and SbH_3 were heated to 160°C in a closed tube to produce InSb. Similarly Me_3Ga and AsH_3 were heated to 200°C in a closed tube to produce GaAs.[47] In 1968 Manasevit

reported the use of metal organic precursors for the chemical vapour deposition of III-V materials. GaAs was deposited by pyrolysis of gas phase Et_3Ga and AsH_3 in an open tube system using H_2 carrier gas.[48] Manasevit named the process metal-organic CVD (MOCVD) and filed a patent for a series of III-V materials and wide band gap semiconductors by MOCVD.[49]

High-T_c superconducting oxides were discovered in the mid 1980s. This led to a rapid development of MOCVD in the late 1980s in order to try and produce thin films of these materials. Metal precursors for films such as $YBa_2Cu_3O_7$ and other superconducting oxides proved to have low volatility and so classical MOCVD proved to be a problem.[50] To overcome this problem, liquid injection MOCVD was developed. This process involves dissolving the precursor in an inert solvent, which is kept outside the reactor and delivered at a controlled rate into a heated evaporator and carried into the reactor zone by a carrier gas.[38]

The process of CVD can be summarised in several steps (Figure 1.4):[38]

1. Evaporation and transport of precursors into the main gas flow and then into the reaction zone.
2. Chemical reactions of precursors in the gas phase to produce reactive intermediates and gaseous by-products.
3. Transport of reactants to substrate surface.
4. Adsorption of reactants onto substrate surface.
5. Diffusion over the surface of the substrate.
6. Nucleation and surface chemical reactions leading to solid film formation.
7. Desorption of remaining fragments of the decomposition.
8. Mass transport of remaining fragments away from the reaction zone.

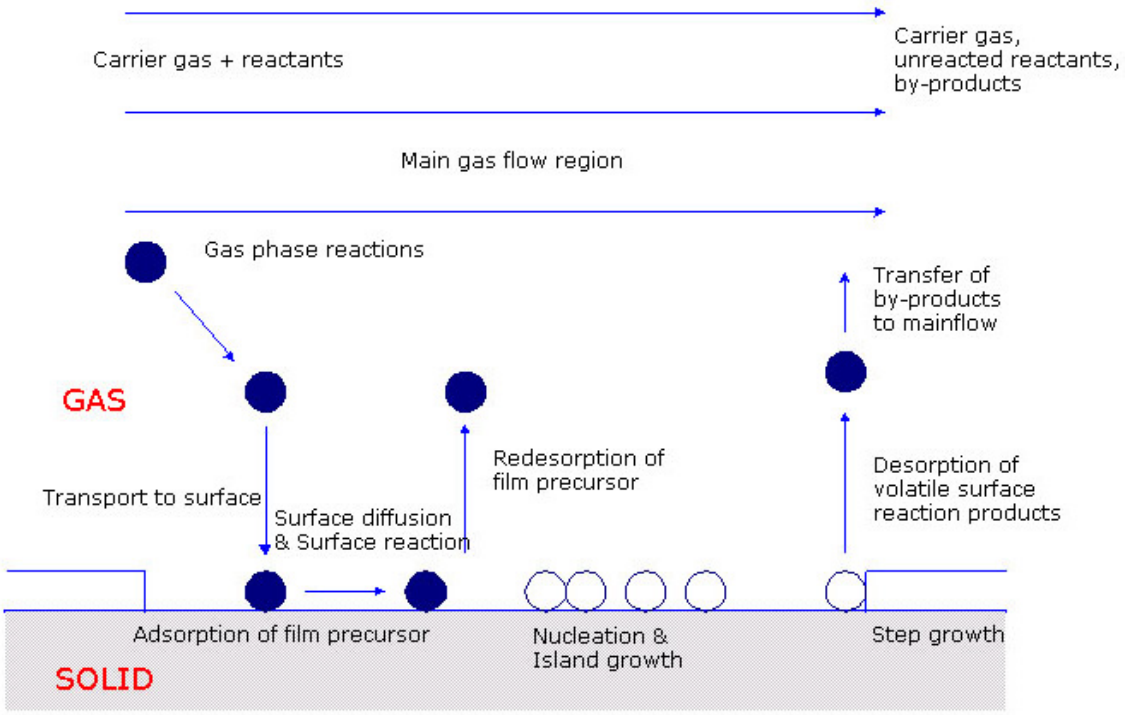

Figure 1.4 Fundamental steps involved in CVD process[38]

There are many different types of CVD, which type is used is dependent on the precursor. Factors such as decomposition temperature, volatility and solubility will determine which type of CVD is appropriate. This project concentrates on using Atmospheric Pressure CVD (APCVD), Low Pressure CVD (LPCVD) and Aerosol Assisted CVD (AACVD). APCVD can be used when the precursors are volatile at atmospheric pressure, LPCVD can be used when the precursors show some volatility but need a reduced pressure to get a reasonable amount of carry over onto the substrate. AACVD can be used when the precursors are not volatile but are soluble as the technique involvs the dissolution of the precursors in a solvent which is then nebulised.

1.6.1 APCVD and LPCVD

APCVD is the simpler of the two techniques as it is done at atmospheric pressure; LPCVD requires a more complex reactor design. LPCVD can produce films with precursors with lower volatility than those used in APCVD. APCVD was widely used in the 1970s to coat transparent conducting oxides (TCOs) onto glass

substrates. More recently LPCVD has been utilized by the microelectronics industry.[38]

LPCVD has been found to produce films with better thickness uniformity, fewer pinholes, finer surface texture and fewer particulate contaminants. This is thought to be due to the inhibition of the gas-phase reactions seen in APCVD that produce particulates that contaminate the films.[39]

1.6.2 AACVD

AACVD is a useful technique when precursors have low volatility or low thermal stability, although precursors must have some solubility. In the process of AACVD precursors are dissolved in an inert solvent, this solution is then nebulised into the carrier gas stream and the precursor is carried into the reactor to deposit the required film.

AACVD is advantageous as the precursors are dissolved in solvent which is then carried in the gas stream and so the precursor does not need to be volatile. Another advantage of AACVD is that the precursor solution is held outside of the reactor and so is not heated; this enables use of precursors with low thermal stability. One disadvantage is there is a possibility of solvent decomposition on the substrate and so greater contamination of the film may be observed.

1.6.3 Decomposition Pathways

Precursors can decompose in a variety of ways; the main two pathways are β-hydride elimination and α–hydride elimination. In β-hydride elimination a metal-alkyl complex is converted into a metal-hydride complex and an alkene, the intermediate in the reaction is thought to be a planar, four-coordinate metal-alkene hydride. From the intermediate the hydrogen atom on a β-carbon atom is transferred to the metal centre, forming a hydro metal-alkene complex. This complex can then lose the coordinated alkene by displacement or dissociation (Scheme 1.1). β-hydride elimination can only take place when there is an available β-hydrogen on the metal complex.[39]

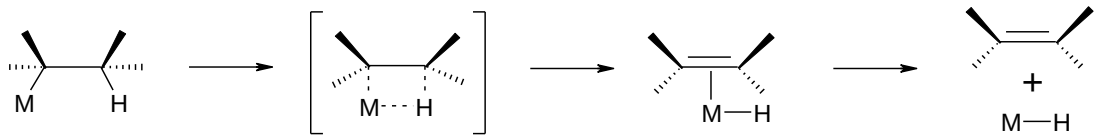

Scheme 1.1 Mechanism of β-hydride elimination

When there is no available β-hydrogen, α–hydride elimination may take place instead. This process is less common than β-hydride elimination but is still an important process to consider in the decomposition of metal-alkyl complexes. In α–hydride elimination a metal-alkyl complex is converted into a metal alkylidine complex and a free hydrocarbon. The mechanism starts with a hydrogen atom on a carbon atom α to the metal centre being transferred to another alkyl group on the metal. The process is thought to occur through a four-coordinate planar intermediate. From the intermediate the alkane formed is eliminated to generate a metal alkylidine complex and a free hydrocarbon (Scheme 1.2). α–hydride elimination often leaves large amounts of carbon contamination in the film due to the formation of surface bound alkylidine analogues.[39]

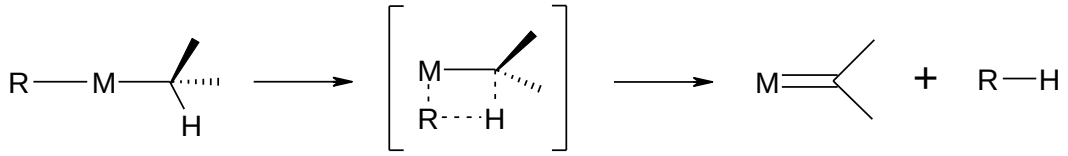

Scheme 1.2 Mechanism of α–hydride elimination

1.6.4 Film Growth Mechanisms

In the CVD process there are different proposed mechanisms for the growth of a film on a substrate. Figure 1.5 illustrates the three classical mechanisms for the growth of metal containing films.[51]

1. Layer or Franck-van der Merwe growth: in this model the first layer typically forms a complete monolayer of the desired film on the substrate before being covered by a second, more weakly bound layer. This is due to a stronger interaction between the deposited atoms and the substrate

than with each other. It is also possible for the second layer to begin to form before the substrate is completely covered; this is known as "simultaneous multilayer growth" and is dependent on the relative rates of nucleation and growth of the deposition.

2. Layer Plus Island or Stranski-Krastanov growth: in this model layers are formed initially. After several layers, continuous layer growth becomes unfavourable and island growth occurs on top of the already deposited layers. This is highly dependent on the decomposition temperature and the nature of the substrate.
3. Island or Volmer-Webber growth: in this model droplets or clusters initially nucleate on the substrate. These island sites are then built up with subsequent deposited atoms. This is due to the depositing atoms being more strongly bound to each other than to the substrate.

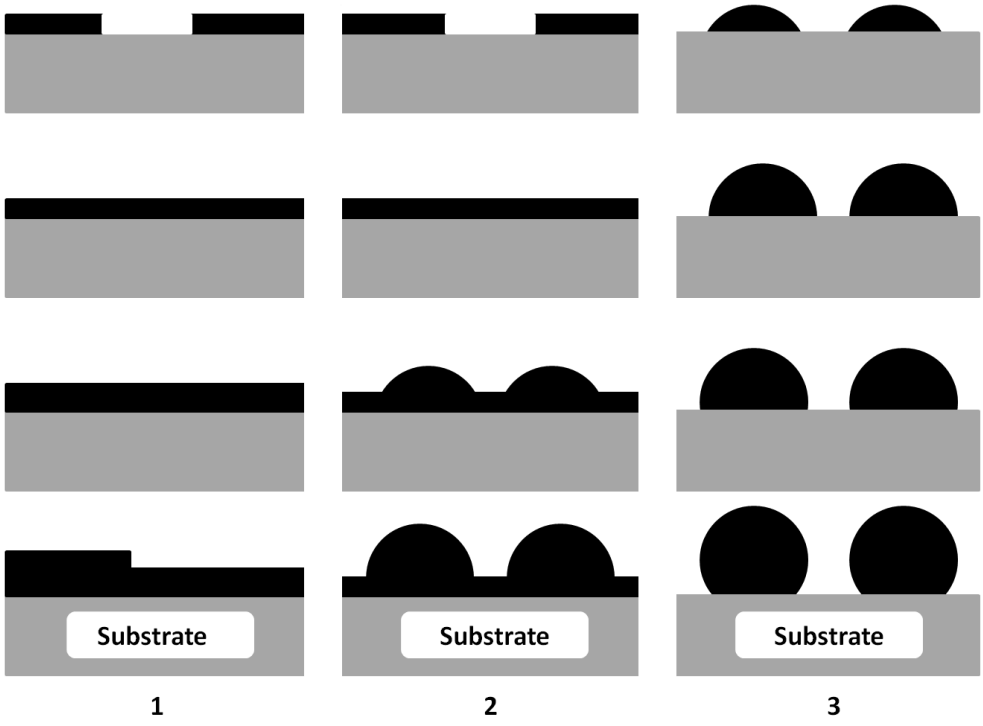

Figure 1.5 Film growth mechanisms

1.7 Precursors

For a precursor to be appropriate for use in CVD a number of requirements must be adhered to:

1. The precursor must have high volatility and a high vapour pressure (for use in APCVD and LPCVD)
2. The precursor must be soluble in an appropriate solvent (for use in AACVD).
3. The precursor needs good thermal stability during evaporation and transport into the gas phase, there must also be a sufficient gap between evaporation and decomposition temperatures.
4. The precursor must decompose cleanly, leaving no trace impurities in the desired film.
5. For bimetallic films using dual source precursors there must be good compatibility between the two precursors.

If a precursor does not have the required volatility there are ways that the volatility can be improved:

1. The use of bulky substituents can enhance the volatility of the precursor by reducing the aggregation of the complex. For example $Sn(OMe)_2$ exists as a polymer in the solid state[52] whereas $Sn(OC_6H_2\text{-}4\text{-}Me\text{-}2,6\text{-}^tBu)_2$ is a monomer in the solid state (Figure 1.6).[53]
2. Replacing the hydrogen atoms in the ligand with fluorine atoms reduces the amount of hydrogen bonds and increases the volatility of the precursor, the lone pair repulsion on peripheral fluorine atoms also increases the volatility. Replacing hydrogen atoms with fluorine atoms will also increase the basicity of ligands such as $M\text{-}ER_f$ by withdrawing the lone pair from E, this reduced the tendency to oligomerise, for example using $M(SCF_2CF_3)_2$ instead of $M(SCH_2CH_3)_2$. This can cause fluorine contamination in the film however as the M-F bond is very stable and close contacts between the metal atom and the fluorine atoms can be formed.
3. By saturating the coordination sphere of the metal the volatility is also increased. This is due to the reduction in aggregation. For example the use of donor functionalised alkoxides, containing an electronegative atom such as N in the organic substituent, can increase volatility over unfunctionalised alkoxides. This is because the electronegative atom can

interact with the metal centre through its lone pair. This stabilises the metal centre through increased coordination and reduces aggregation and increases volatility.

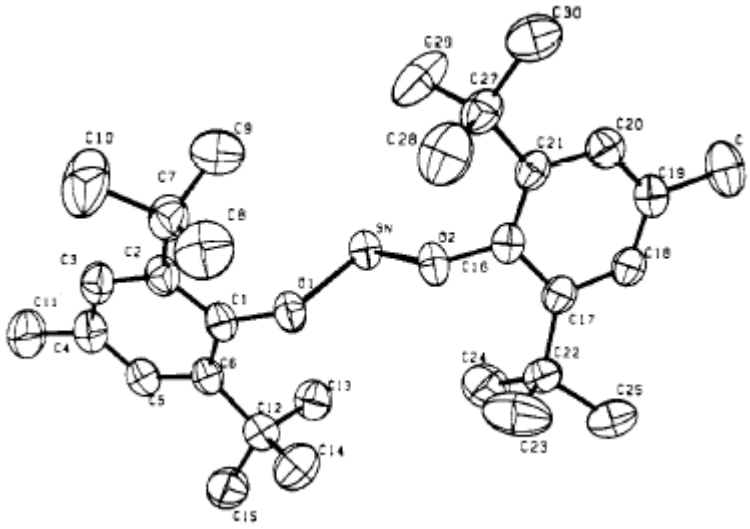

Figure 1.6 $Sn(OC_6H_2\text{-}4\text{-}Me\text{-}2,6\text{-}^tBu)_2$[53]

1.8 Precursors for Metal Sulphide Films

1.8.1 Dual-Source Precursors

One of the first examples of a metal sulphide film deposited using CVD was reported by Manasevit *et al.* in 1971. The reported deposition used dimethylcadmium (Me_2Cd) and diethylzinc (Et_2Zn) with H_2S on Al_2O_3, $MgAl_2O_4$ and BeO substrates.[54] Using simple metal alkyls and hydrogen sulphide caused many problems. As metal alkyls are generally highly pyrophoric, this meant that a considerable amount of engineering was required to be able to handle these substances safely. In addition to this, metal alkyls are also highly sensitive to air and moisture, which resulted in incorporation of oxygen contaminants in the films if even a trace amount of air or moisture was present in the deposition procedure. The high reactivity of the metal alkyls also caused problems with 'homogeneous pre-reaction' whereby the precursors reacted in the gas phase before they reached the reaction zone. This resulted in solid material being deposited onto the film which affected the film morphology and stoichiometry. As a high imbalance in mole ratios of the precursors is normally needed to control the stoichiometry of the films, an

excess of precursor is used, resulting in a considerable amount of precursor that is not incorporated into the films and hence wasted.[55]

To overcome the problem of 'homogeneous prereaction', adducts of the alkyls of zinc and cadmium were introduced as precursors. Adducts such as the dioxane ($C_4H_8O_2$),[56] thioxane (C_4H_8OS),[56c] triethylamine (NEt_3)[57] and triazine ($C_3H_3N_3$)[57a] adducts of alkyl zinc and cadmium have been utilised to grow ZnS and CdS films by MOCVD. The triethylamine adduct, $Me_2Zn(NEt_3)_2$, has been discovered to be the most useful with many groups reporting the deposition of chalcogenide materials from it. [57-58] The use of adducts has other advantages: the vapour pressure of the metal alkyl is reduced, eradicating the need to cool bubblers of dimethylzinc. During the preparation of the adduct the metal alkyl moiety is purified and so the deposited films have improved electrical properties.[55] Although some problems are overcome by the use of adducts, the use of a single-source precursor is still more desirable. A single-source precursor would eliminate the need to use highly toxic and pyrophoric metal alkyls and hydrogen sulphide.

Single-source precursors contain all of the desired elements in one molecule. For example a single-source precursor for a metal sulphide film would have to contain both the metal and sulphur. Single-source precursors also need to decompose to produce the desired film without any need for additional reactants. For example for a metal sulphide film the precursor would have to decompose to produce the desired metal sulphide without the use of toxic H_2S. The use of single-source precursors is advantageous as it eliminates problems with control of film stoichiometry and can eliminate the need to use toxic gases. One disadvantage with single-source precursors is that it can be difficult to make a precursor containing all of the desired elements, particularly when trying to produce a bimetallic film.

1.8.2 Thiolates

Extensive research has been performed to find single-source precursors for the deposition of metal sulphide films, particularly ZnS and CdS films due to their use in optical coatings,[59] blue-green laser diode devices,[60] thin film electroluminescent displays,[61] solid state solar cells,[62] photoconductors, transistors, sensors and transducers.[63]

Possible single-source precursors include metal thiolates, $M(SR)_n$, which are analogues to the metal alkoxides used to deposit metal oxide thin films. Thiolate complexes of zinc and cadmium with simple R groups are generally polymeric in structure, with a tetrahedral metal centre, and are as such practically involatile. For example $Zn(SPh)_2$ polymerises in alcohols to form $Zn_4(SPh)_8(ROH)$, R=Me, Et, Pr, Bu (Figure 1.7).[64] Polymer chains have been obtained with some structural modifications. For example $Cd(SR)_2$ (R = 1-pyridyl) has a polymer chain structure.[65] Although the degree of aggregation has been decreased with these polymer chains the precursors are still not volatile enough to be suitable for MOCVD.

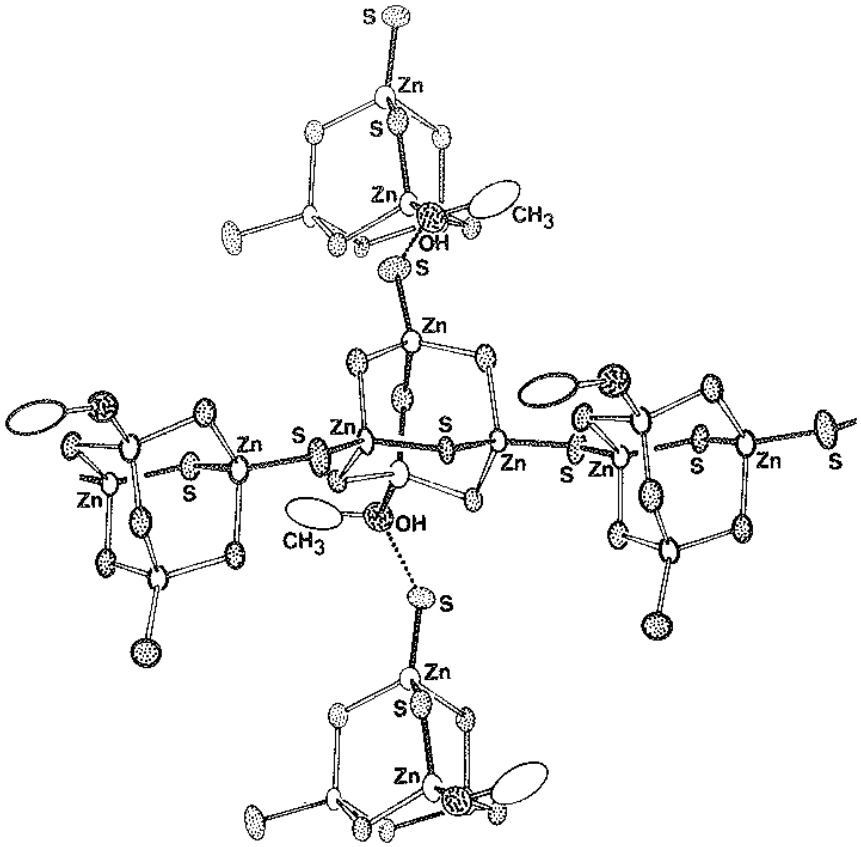

Figure 1.7 Structure of $Zn_4(SPh)_8(ROH)$[64]

Dimeric Zn and Cd thiolates were prepared using 2,4,6-tritert-butylphenyl ($C_6H_2{}^tBu_3$-2,4,6). The Cd thiolate (Figure 1.8) was used to deposit CdS films successfully.[66] However due to the use of bulky substituents, there is a considerable amount of carbon added to the ligand, meaning that it is a possibility of substantial carbon contamination in the prepared films.[55]

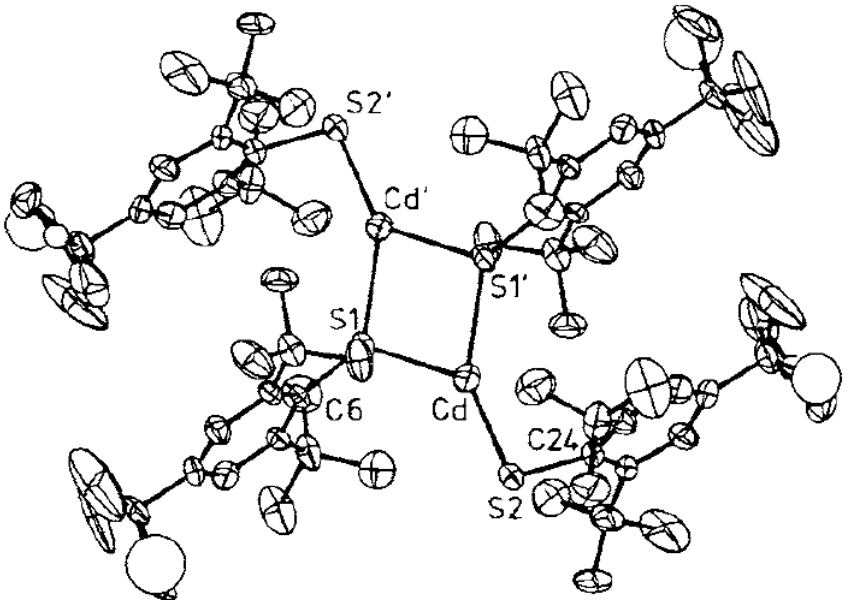

Figure 1.8 Structure of $[Cd(SC_6H_2{}^tBu\text{-}2,4,6)_2]_2$[67]

Indium and gallium thiolate complexes generally have a similar polymeric structure to zinc and cadmium thiolates. Using a similar approach dimeric thiolates can be obtained with the use of bulky substituents. For example $[{}^tBuIn(S{}^tBu)]_2$ is dimeric (Figure 1.9) and has been used to deposit In_2S_3.[68]

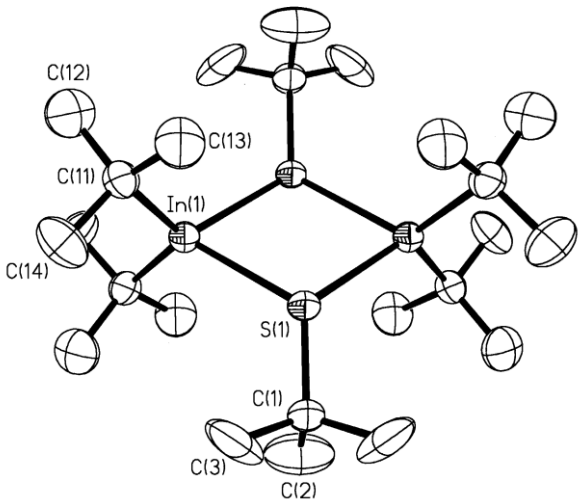

Figure 1.9 Structure of $[({}^tBu)_2InS{}^tBu]_2$[69]

Other Main Group thiolates used in the deposition of metal sulphides include a series of tin (IV) thiolates. In 2001 Molloy *et al.* reported the deposition of SnS_2, SnS and Sn_2S_3 from highly volatile fluorinated tin thiolates, such as $Sn(SCH_2CH_2(CF_2)_5CF_3)_4$ (Figure 1.10).[70]

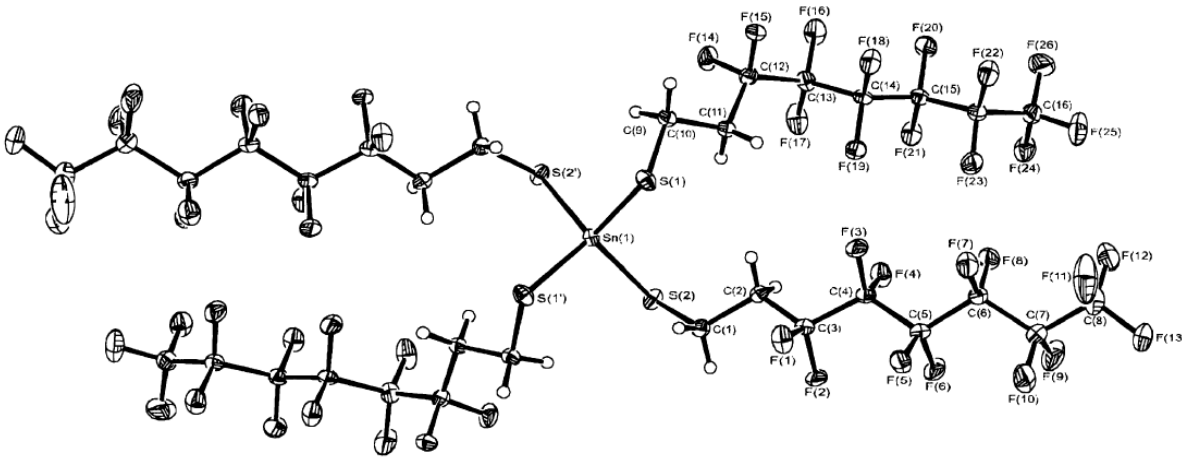

Figure 1.10 Structure of $Sn(SCH_2CH_2(CF_2)_5CF_3)_4$

More recently Vittal *et al.* reported the synthesis and subsequent thermal decomposition of $[(Ph_3P)CuIn(SCOPh)_4]$. The resulting product was $CuInS_2$. They speculated that it would be possible to use this precursor in CVD to deposit thin films of $CuInS_2$.[71]

1.8.3 Dithiocarbamates

Dithiocarbamates have the general chemical formula $M(S_2CNRR')_n$ and have been used as single source precursors to grow many metal sulphide films. Saunders *et al.* reported the growth of ZnS thin films from $Zn(S_2CNEt_2)_2$, one of the first examples of a dithiocarbamate being used to deposit a metal sulphide.[72]

Later work by O'Brien *et al*. concluded that films grown from asymmetrically susbstitued dithiocarbamates produced better quality films. O'Brien *et al.* compared films grown from $Cd(S_2CNEt_2)_2$ and $Zn(S_2CNEt_2)_2$ (Figure 1.11) with $Zn(S_2CNMe^nBu)_2$ and $Cd(S_2CNMe^nBu)_2$.[73] They found that the asymmetrically substituted precursors were more volatile and had lower melting points, making them more desirable precursors than their symmetrically substituted analogues.[74]

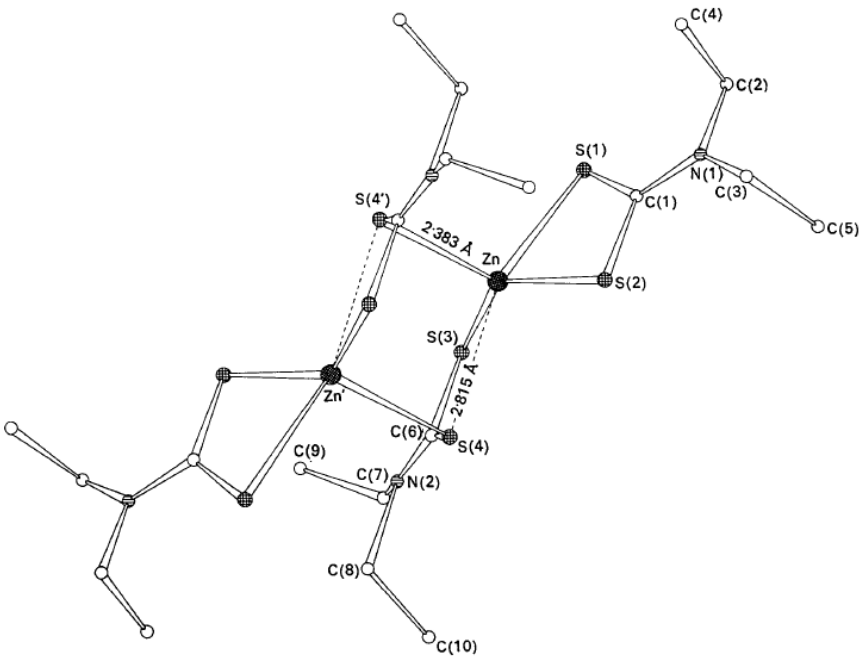

Figure 1.11 $Zn(S_2CNEt_2)_2$[73]

Other metal sulphide films grown from dithiocarbamates include CuS from $Cu(S_2CNMeHex)_2$[75] and In_2S_3 from $In(S_2CNMeEt)_3$.[76] In 2001 Molloy *et al.* reported the deposition of SnS from a series of asymmetric dithiocarbamates, however to produce the SnS films a flow of H_2S was required.[77] Later in 2002 Molloy *et al.* reported the deposition of SnS_2 and SnS from the single source precursors $Sn(S_2CNEt_2)_4$ and $Sn(SR)_2(S_2CNEt_2)_2$ (R = Cy (Figure 1.12), CH_2CF_3) respectively.[78]

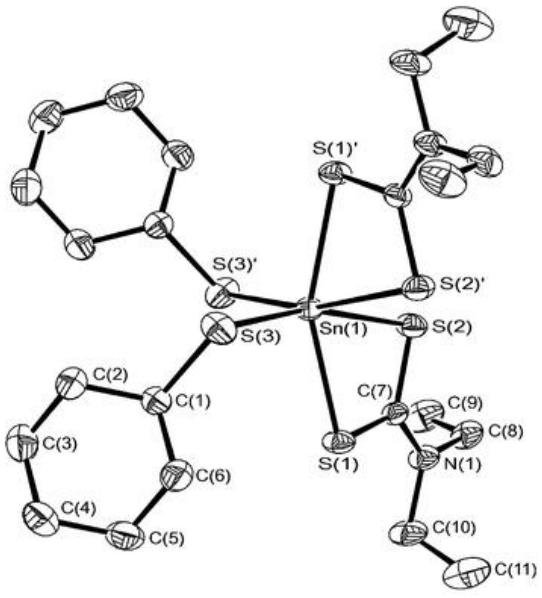

Figure 1.12 $Sn(SCy)_2(S_2CNEt_2)_2$

1.8.4 Xanthates

Xanthates are also known as dithiocarbonates and have the general chemical formula $M(S_2COR)_n$. They have also been used as single source precursors to deposit metal sulphide films by MOCVD.[79] Structurally they are very similar to dithiocarbamates with the NRR' group of the dithiocarbamate replaced with an OR group in the xanthate.

Xanthates are good candidates for the chemical vapour deposition of metal sulphide films as they have pre formed M-S bonds that enable their clean conversion to the corresponding metal sulphide.[80] Xanthates also tend to decompose at lower temperatures than their dithiocarbamate analogue.[81]

Xanthates are thought to decompose by the Chugaev elimination reaction (Scheme 1.3). The process forms an alkene by a syn-elimination from a six-membered cyclic transition state. A metal sulphide could then be formed by a subsequent carbonyl sulphide and hydrogen sulphide elimination process.[79c]

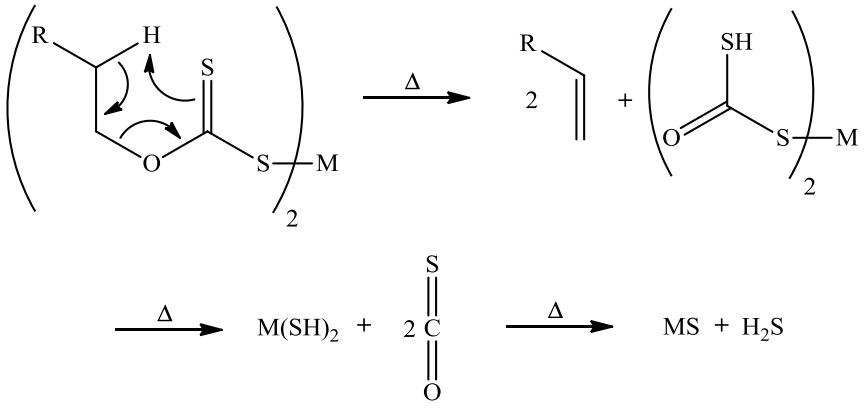

Scheme 1.3 Chugaev elimination reaction

Two alternative decomposition methods have been suggested for phopshine stabilised copper (I) xanthates; one of these proceeds with the initial loss of CS_2 from one xanthate and then the subsequent loss of EtOC(S)OEt and the phosphine from another xanthate and the remaining EtO-Cu(L) to form Cu_2S. The other mechanism involed initial loss of COS from one xanthate then the subsequent loss of EtOC(S)SEt and the phopshine from the remaining EtS-Cu(L) and another xanthate to form Cu_2S (Scheme 1.4)[82]

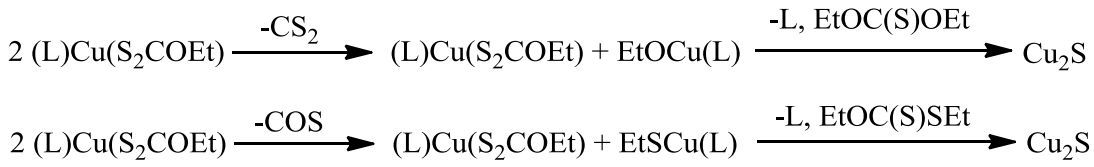

Scheme 1.4 Alternative Decomposition Mechanisms

Metal sulphide films that have been grown from xanthates include ZnS from $Zn(S_2CO^iPr)_2$, CdS from $Cd(S_2CO^iPr)_2$,[79a] NiS from $Ni(S_2CO^nBu)_2(NC_5H_5)_2$ (Figure 1.13) [79c] and In_2S_3 from $In(S_2CO^iPr)_3$.[79b]

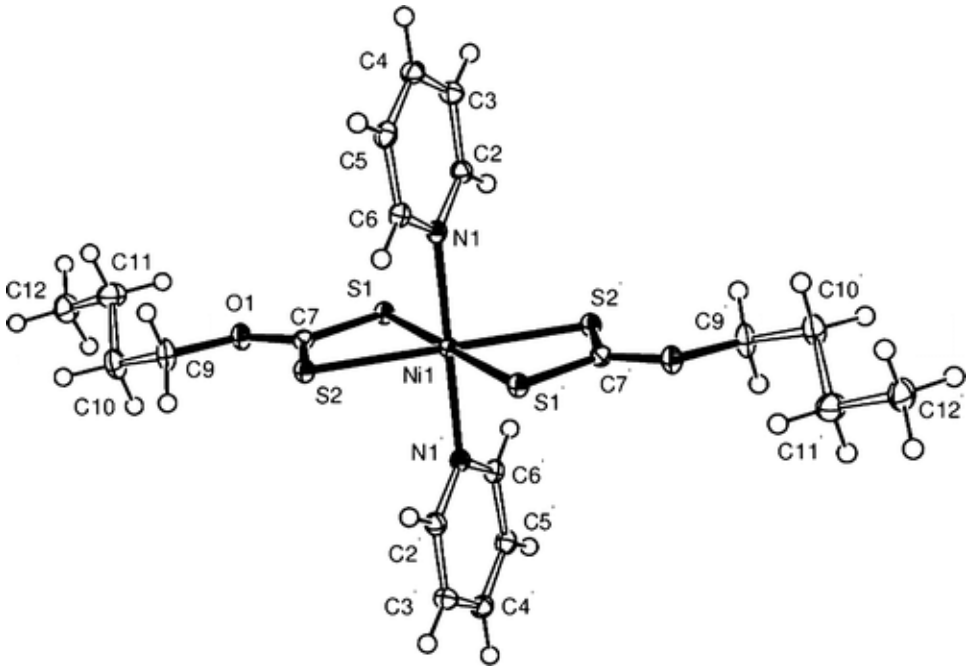

Figure 1.3 $Ni(S_2CO^nBu)_2(NC_5H_5)$

1.9 Aims of Project

The aims of this project are to investigate low cost deposition of layers that can be used in thin film photovoltaics, specifically Cu_2ZnSnS_4, $CuSbS_2$ as absorber layers and ZnO:F as a TCO.

$CuSbS_2$ thin films have been made using chemical bath deposition[83], thermal evaporation,[84] sputtering,[19] electrochemical deposition[85] and spray pyrolysis.[18] Currently there are no reported efficiencies of solar cells with $CuSbS_2$ absorber layers, although cells have been made.[83, 86]

Thin films of Cu_2ZnSnS_4 have been made using sputtering,[87] thermal evaporation,[88] non-vacuum electroplating,[17] co-evaporation,[89] multi-stage

evaporation,[90] spray pyrolysis[91] and sulphurisation of sol-gel deposited precursors.[92] The method chosen to try to deposit films of $CuSbS_2$ and Cu_2ZnSnS_4 is CVD. As both target films contain two or more metals as well as sulphur it is unlikely that a single-source precursor will be discovered. As such, multi-source precursors have been utilized, as discussed above, there are many problems with using multi-source precursors, namely the difficulty in obtaining a match in decomposition temperature and either volatility or solubility. This thesis describes the synthesis of precursors for copper, zinc, tin and antimony sulphide thin films, specifically xanthates and dithiocarbamates, and the subsequent materials analysis to obtain a match in decomposition temperature and volatility or solubility.

In the past few years there has been a lot of interest in the synthesis of Cu_2ZnSnS_4 nanoparticles for use in thin film photovoltaics, cells can be made by screen printing the nanoparticles.[93] Nanoparticles of Cu_2ZnSnS_4 have been synthesised using salts of Cu, Zn and Sn, normally chlorides and acetates, and a sulphur source, generally elemental sulphur.[94] Recently Khare *et. al* have reported the synthesis of Cu_2ZnSnS_4 nanoparticles from dithiocarbamate complexes of Cu, Zn and Sn.[95] A similar approach to make Cu_2ZnSnS_4 nanoparticles has been investigated with the above xanthate precursors found to be a most suitable match for CVD.

A second aspect of the project is to investigate alternative transparent semiconducting oxides. Currently In_2O_3:Sn and SnO_2:F are widely used, ZnO:F has been investigated more in the past 5-10 years and has been identified as a promising TCO.[35] Thin films of ZnO:F have been deposited using spray pyrolysis[96], sol-gel spin coating,[97] sputtering[98] and APCVD.[99] Currently the only films of ZnO:F reported which have been deposited by CVD have used dual-source precursors. The aim of this part of the project is to find a single-source precursor for the deposition of ZnO:F. Following on from work by Stanley *et. al* with the deposition of SnO:F films from organotin fluorocarboxylates,[100] the synthesis of organozinc fluorocarboxylates has been investigated and the resulting materials properties studied. Promising precursors were also subject to CVD trials.

1.10 References

1. Revised version of the Presidency Conclusion of the European Council. Council of the European Union, Brussels, 2007.
2. Chapin, D. M.; Pearson, G. L.; Fuller, C. S., *J. Appl. Phys.* **1954,** *25*, 676.
3. Green, M. A.; Emery, K.; Hishikawa, Y.; Warta, W.; Dunlop, E. D., *Prog. Photovolt.* **2011,** *19* (5), 565.
4. Kazmerski, L. L., *J. Electron Spec. Related Phenomena* **2006,** *150*, 105.
5. Maycock, P. D., *PV News* 2005.
6. Swanson, R. DOE Solar Program Review, Denver, NREL: Denver, 2005.
7. Green, M. A.; Blakers, A. W.; Wenham, S. R.; Narayanan, S.; Willison, M. R.; Tauouk, M.; Szpitalak, T. 18th IEEE Photovoltaic Specialists Conference, New York, IEEE: New York, 1986; p 39.
8. Zhao, I.; Wang, A.; Altmatt, P.; Green, M. A., *Appl. Phys. Lett.* **1987,** *62*, 243.
9. (a) Chong, C. M.; Zhang, F.; Sproul, A.; Wenham, S. R.; Green, M. A. 20th IEEE Photovoltaic Specialists Conference, New York, IEEE: New York, 1988; p 529; (b) Ebong, A. U.; Lee, S. H.; Honsberg, C. B.; Wenham, S. R. 25th IEEE Photovoltaic Specialists Conference, New York, IEEE: New York, 1996; p 513.
10. Swanson, R., *Solar Cells* **1986,** *17*, 85.
11. Eguren, H.; Alamo, J. d.; Cuevas, A.; Luque, A. 15th IEEE Photovoltaic Specialists Conference, New York, IEEE: New York, 1981; p 1343.
12. Goetzberger, A.; Luther, J.; Willeke, G., *Sol. Energy Mater. Sol. Cells* **2002,** *74* (1-4), 1.
13. Mitzi, D. B.; Gunawan, O.; Todorov, T. K.; Wang, K.; Guha, S., *Sol. Energy Mater. Sol. Cells* **2011,** *95* (6), 1421.
14. Manolache, S.; Dua, A.; Isac, L.; Nanu, M.; Goossens, A.; Schoonman, J., *Thin Solid Films* **2007,** *515*, 5957.
15. Anderson, B. A., *Prog. Photovolt.* **2000,** *8*, 61.
16. Gerein, N. J.; Haber, J. A., *Chem. Mater.* **2006,** *18* (26), 6297.
17. Ennaoui, A.; Lux-Steiner, M.; Weber, A.; Abou-Ras, D.; Kötschau, I.; Schock, H.-W.; R. Schurr; Hölzing, A.; Jost, S.; Hock, R.; Voß, T.; Schulze, J.; Kirbs, A., *Thin Solid Films* **2009,** *517* (7), 2511.
18. Rabhi, A.; Kanzari, M.; Rezig, B., *Thin Solid Films* **2009,** *517* (7), 2477.
19. Lazcano, Y. R.; Nair, M. T. S.; Nair, P. K., *J. Cryst. Growth* **2001,** *223*, 399.

20. Shin, B.; Gunawan, O.; Zhu, Y.; Bojarczuk, N. A.; Chey, S. J.; Guha, S., *Prog. Photovolt.* **2011**.
21. Guo, Q.; Hillhouse, H. W.; Agrawal, R., *J. Am. Chem. Soc.* **2009,** *131*, 11672.
22. Barkhouse, D. A. R.; Gunawan, O.; Gokmen, T.; Todorov, T. K.; Mitzi, D. B., *Prog. Photovolt.* **2012,** *20* (1), 6.
23. Bernardini, G. P.; Borrini, D.; Caneschi, A.; Benedetto, F. D.; Gatteschi, D.; Ristori, S.; Romanelli, M., *Phys. Chem. Minerals* **2000,** *27*, 453.
24. McMaster, H. A. Conductive coating for glass and method of application. US2429420, 1947.
25. Ginley, D. S., *Handbook of Transparent Conductors*. Springer: New York, 2010.
26. Minami, T., *Semicond. Sci. Technol.* **2005,** *20* (4), S35.
27. Granqvist, C. G.; Green, S.; Niklasson, G. A.; Mlyuka, N. R.; von Kræmer, S.; Georén, P., *Thin Solid Films* **2010,** *518* (11), 3046.
28. Cui, J.; Wang, A.; Edleman, N. L.; Ni, J.; Lee, P.; Armstrong, N. R.; Marks, T. J., *Adv. Mater.* **2001,** *13* (19), 1476.
29. Nomura, K.; Ohta, H.; Takagi, A.; Kamiya, T.; Hirano, M.; Hosono, H., *Nature* **2004,** *432* (7016), 488.
30. Granqvist, C. G., *Sol. Energy Mater. Sol. Cells* **2007,** *91* (17), 1529.
31. Taylor, M. P.; Readey, D. W.; van Hest, M.; Teplin, C. W.; Alleman, J. L.; Dabney, M. S.; Gedvilas, L. M.; Keyes, B. M.; To, B.; Perkins, J. D.; Ginley, D. S., *Adv. Funct. Mater.* **2008,** *18* (20), 3169.
32. Ku, D. Y.; Kim, Y. H.; Lee, K. S.; Lee, T. S.; Cheong, B.; Seong, T. Y.; Kim, W. M., *Journal of Electroceramics* **2009,** *23* (2-4), 415.
33. Krishnakumar, V.; Ramamurthi, K.; Kumaravel, R.; Santhakumar, K., *Curr. Appl. Phys.* **2009,** *9* (2), 467.
34. Chen, X. L.; Xu, B. H.; Xue, J. M.; Zhao, Y.; Wei, C. C.; Sun, J.; Wang, Y.; Zhang, X. D.; Geng, X. H., *Thin Solid Films* **2007,** *515* (7-8), 3753.
35. Gordon, R. G., *MRS Bull.* **2000,** *25* (8), 52.
36. Major, S.; Chopra, K. L., *Sol. Energy Mater. Sol. Cells* **1988,** *17* (5), 319.
37. Chopra, K. L.; Paulson, P. D.; Dutta, V., *Prog. Photovolt.* **2004,** *12* (2-3), 69.
38. Jones, A. C.; Hitchman, M. L., *Chemical Vapour Deposition - Precursors, Processes and Applications*. The Royal Society of Chemistry,: Cambridge, 2009.

39. Karlin, K. D., *Prog. Inorg. Chem.* **1994,** *41*.
40. Wohler, F.; Uslar, L., *Lieb. Ann.* **1855,** *94*, 255.
41. (a) Mond, L.; Langer, C.; Quincke, F., *J. Chem. Soc.* **1890,** *57*, 749; (b) Mond, R., *Chem. Ind.* **1930,** *49T*, 371.
42. Pring, J. N.; Fielding, W., *J. Chem. Soc.* **1909,** *95*, 1497.
43. Teal, G. K.; Fisher, J. R.; Treptow., A. W., *J. Appl. Phys.* **1946,** *17*, 879.
44. Glang, R.; Kippenham, B. W., *IBM J. Res. Devel.* **1960**, 299.
45. Meyerson, B. S., *Chemical Vapor Deposition*. Academic Press: New York, 1989.
46. Didchenko, R.; Alix, J. D.; Toeniskoettler, R. H., *J. Inorg. Chem.* **1960,** *4*, 35.
47. Harrison, B.; Tomkins., E. H., *Inorg. Chem.* **1962,** *1*, 951.
48. Manasevit, H. M., *Appl. Phys. Lett.* **1968,** *12*, 156.
49. Manasevit, H. M. *U.S. Patent*, 4,368,098C. 1983.
50. Berry, A. D.; Gaskill, D. K.; Holm, R. T.; Cukauskas, E. J.; Kaplan, R.; Henry, R. L., *Appl. Phys. Lett.* **1988,** *52*, 1743.
51. (a) Jensen, K. F., *Adv. Chem. Ser.* **1989**, 199; (b) Venables, J. A.; Spiller, G. D. T.; Hanbrucka, M., *Rep. Prog. Phys.* **1984,** *47*, 399; (c) Bauer, E., *Z. Kristallogr.* **1958,** *110*, 372.
52. Gsell, R.; Zeldin, M., *J. Inorg. Nucl. Chem.* **1975,** *37*, 1133.
53. Cetinkaya, B.; Gumruku, I.; Lappert, M. F.; Atwood, J. L.; Rogers, R. D.; Zaworotko, M. J., *J. Am. Chem. Soc* **1980,** *102*, 2088.
54. Manasevit, H. M.; Simpson, W. I., *J. Electrochem. Soc.* **1971,** *118*, 644.
55. O'Brien, P.; Nomura, R., *J. Mater. Chem.* **1995,** *5* (11), 1761.
56. (a) Wright, P. J.; Cockayne, B.; Williams, A. J.; Jones, A. C.; Orrell, E. D., *J. Cryst. Growth* **1987,** *84*, 552; (b) Wright, P. J.; Cockayne, B.; Jones, A. C., *Chemtronics* **1988,** *3*, 35; (c) Cockayne, B.; Wright, P. J.; Armstrong, A. J.; Jones, A. C.; Orrell, E. D., *J. Cryst. Growth* **1988,** *91*, 57.
57. (a) Wright, P. J.; Parbrook, P. J.; Cockayne, B.; Jones, A. C.; Orrell, E. D.; O'Donnell, K. P.; Henderson, B., *J. Cryst. Growth* **1989,** *94*, 441; (b) Wright, P. J.; Cockayne, B.; Parbrook, P. J.; Jones, A. C.; O'Brien, P.; Walsh, J. R., *J. Cryst. Growth* **1990,** *104*, 601.
58. (a) Yates, H. M.; Williams, J. O., *J. Cryst. Growth* **1991,** *107*, 387; (b) Jensen, K. F.; Annapragada, A.; K. L. Ho, J. S. H.; Patnaik, S.; Salim, S., *J. Physique, IZ* **1991,** *C2*, 243; (c) Foster, D. F.; Patterson, I. L. J.; James, L. D.; Cole-

Hamilton, D. J.; Armitage, D. N.; Yates, H. M.; Wright, A. C.; Williams, J. O., *Adv. Mater. Opt. Electron* **1994,** *3*, 163; (d) Huh, J.-S.; Patniak, S.; Jensen, K. F., *J. Electron. Mater* **1993,** *22*, 509.

59. Itoh, S.; Nakayama, N.; Ohata, T.; Ozawa, M.; Okuyama, H.; Nakano, K.; Ikeda, M.; Ishibashi, A.; Mori, Y., *Jpn. J. Appl. Phys. Lett.* **1994,** *59*, L639.
60. Hasse, M. A.; Qui, J.; DePuydt, J. M.; Cheng, H., *Appl. Phys. Lett.* **1991,** *59*, 1272.
61. Tornqvist, R. O.; Arston, J.; Karp, J.; Tannienen, V. P., *IEEE Trans. Electron. Devices* **1983,** *30ED*, 468.
62. Kim, H.-D.; Ahn, B.-T.; Im, H.-B., *Thin Solid Films* **1993,** *232*, 28.
63. Yoshikawa, A.; Yamaga, S.; Tanaka, K.; Kasai, H., *J. Cryst. Growth* **1985,** *72*, 13.
64. Dance, I. G., *Polyhedron* **1986,** *5* (5), 1037.
65. Hursthouse, M. B.; Khan, O. F. Z.; Mazid, M.; Motevalli, M.; O'Brien, P., *Polyhedron* **1990,** *9*, 541.
66. Bochmann, M.; Webb, K. J.; Hails, J. E.; Wolverson, D., *Eur. J. Solid State lnorg. Chem.* **1992,** *29*, 155.
67. Bochmann, M.; Webb, K.; Harman, M.; Hursthouse, M. B., *Angew. Chem., Int. Ed.* **1990,** *29* (6), 638.
68. MacInnes, A. N.; Power, M. B.; Barron, A. R., *Adv. Mater. Opt. Electron* **1992,** *1*, 229.
69. L. Stoll, S.; G. Bott, S.; R. Barron, A., *J. Chem. Soc., Dalton Trans.* **1997,** (8), 1315.
70. Hibbert, T. G.; Mahon, M. F.; Molloy, K. C.; Price, L. S.; Parkin, I. P., *J. Mater. Chem.* **2001,** *11*, 469.
71. Batabyal, S. K.; Tian, L.; Venkatram, N.; Ji, W.; Vittal, J. J., *J. Phys. Chem.* **2009,** *113* (33), 15037.
72. Saunders, A.; Vecht, A.; Tyrrell, G., The preparation of ternary thin films by novel MOCVD techniques. In *Ternary Multinary Compd., Proc. Int. Conf.*, Satyen, D. K.; Zunger, A., Eds. Mater. Res. Soc.: London, 1987; pp 213.
73. Bonamico, M.; Mazzone, G.; Vaciago, A.; Zambonelli, L., *Acta Crystallogr.* **1965,** *19* (6), 898.

74. (a) Motevalli, M.; O'Brien, P.; Walsh, J. R.; Watson, I. M., *Polyhedron* **1996,** *15* (16), 2801; (b) O'Brien, P.; Walsh, J. R.; Watson, I. M.; Hart, L.; Silva, S. R. P., *J. Cryst. Growth* **1996,** *167* (1-2), 133.
75. Kemmler, M.; Lazell, M.; O'Brien, P.; Otway, D. J.; Park, J. H.; Walsh, J. R., *J. Mater. Sci-Mater. El.* **2002,** *13*, 531.
76. Haggata, S. W.; Malik, M. A.; Motevalli, M.; O'Brien, P.; Knowles, J. C., *J. Chem. Mater.* **1995,** *7*, 716.
77. Kana, A. T.; Hibbert, T. G.; Mahon, M. F.; Molloy, K. C.; Parkin, I. P.; Price, L. S., *Polyhedron* **2001,** *20* (24-25), 2989.
78. Barone, G.; Chaplin, T.; Hibbert, T. G.; Kana, A. T.; Mahon, M. F.; Molloy, K. C.; Worsley, I. D.; Parkin, I. P.; Price, L. S., *J. Chem. Soc., Dalton Trans.* **2002**, 1085.
79. (a) Barreca, D.; Gasparotto, A.; Maragno, C.; Seraglia, R.; Tondello, E.; Venzo, A.; Krishnon, V.; Bertagnolli, H., *Appl.Organomet. Chem.* **2005,** *19* (1), 59; (b) Bessergenev, V. G.; Ivanova, E. N.; Kovalevskaya, Y. A.; Gromilov, S. A.; Kirichenko, V. N.; Larionov, S. V., *Inorg. Mater.* **1996,** *32*, 592; (c) Alam, N.; Hill, M. S.; Kociok-Kohn, G.; Zeller, M.; Mazhar, M.; Molloy, K. C., *Chem. Mater.* **2008,** *20* (19), 6157.
80. Armelao, L.; Barreca, D.; Bottaro, G.; Gasparotto, A.; Maragno, C.; Sada, C.; Spalding, T. R.; Tondello, E., *Electrochem. Soc. Proc.* **2003,** *8*, 1104.
81. Koh, Y. W.; Lai, C. S.; Du, A. Y.; Tiekink, E. R. T.; Loh, K. P., *Chem. Mater.* **2003,** *15*, 4544.
82. Afzaal, M.; Rosenberg, C. L.; Malik, M. A.; White, A. J. P.; O'Brien, P., *New Journal of Chemistry* **2011,** *35* (12), 2773.
83. Messina, S.; Nair, M. T. S.; Nair, P. K., *Thin Solid Films* **2007,** *515*, 5777.
84. Rabhi, A.; Kanzari, M.; Rezig, B., *Mater. Lett.* **2008,** *62*, 3576.
85. Colombara, D.; Peter, L. M.; Rogers, K. D.; Painter, J. D.; Roncallo, S., *Thin Solid Films* **2011,** *519* (21), 7438.
86. Rodriguez-Lazcano, Y.; Nair, M. T. S.; Nair, P. K., *J. Electrochem. Soc.* **2005,** *152* (8), G635.
87. Ito, K.; Nakazawa, T., *Jpn. J. Appl. Phys.* **1988,** *27* (11), 2094.
88. Friedlmeier, T.; Weiser, N.; Walter, T.; Dittrich, H.; Schock, H. W. 14th European Photovoltaic Solar Energy Conference and Exhibition, Belford, Belford, 1997; p 1242.

89. Tanaka, T.; Kawasaki, D.; Nishio, M.; Guo, Q.; Ogawa, H., *Phys. Status Solidi* **2006,** *3* (8), 2844.
90. Weber, A.; Krauth, H.; Perlt, S.; Schubert, B.; Kötschau, I.; Schorr, S.; Schock, H. W., *Thin Solid Films* **2009,** *517*, 2524.
91. Nakayama, N.; Ito, K., *Appl.Surf. Sci.* **1996,** *92*, 171.
92. Tanaka, K.; Moritake, N.; Uchiki, H., *Sol. Energy Mater. Sol. Cells* **2007,** *91* (13), 1199.
93. Guo, Q. J.; Hillhouse, H. W.; Agrawal, R., *J. Am. Chem. Soc.* **2009,** *131* (33), 11672.
94. (a) Riha, S. C.; Parkinson, B. A.; Prieto, A. L., *J. Am. Chem. Soc.* **2009,** *131* (34), 12054; (b) Shavel, A.; Arbiol, J.; Cabot, A., *J. Am. Chem. Soc.* **2010,** *132* (13), 4514; (c) Cao, M.; Shen, Y., *J. Cryst. Growth* **2011,** *318* (1), 1117.
95. Khare, A.; Wills, A. W.; Ammerman, L. M.; Norris, D. J.; Aydil, E. S., *Chem. Commun.* **2011,** *47* (42), 11721.
96. Olvera, M. D. L.; Maldonado, A.; Asomoza, R.; Solorza, O.; Acosta, D. R., *Thin Solid Films* **2001,** *394* (1-2), 242.
97. Nam, G. M.; Kwon, M. S., *Electron. Mater. Lett.* **2011,** *7* (2), 127.
98. Yoon, H. S.; Lee, K. S.; Lee, T. S.; Cheong, B.; Choi, D. K.; Kim, D. H.; Kim, W. M., *Sol. Energy Mater. Sol. Cells* **2008,** *92* (11), 1366.
99. (a) Liang, H. F.; Gordon, R. G., *J. Mater. Sci.* **2007,** *42* (15), 6388; (b) Hu, J. H.; Gordon, R. G., *Solar Cells* **1991,** *30* (1-4), 437.
100. (a) Mahon, M. F.; Molloy, K. C.; Stanley, J. E.; Rankin, D. W. H.; Robertson, H. E.; Johnston, B. F., *Appl. Organomet. Chem.* **2005,** *19* (5), 658; (b) Molloy, K. C.; Stanley, J. E., *Appl. Organomet. Chem.* **2009,** *23* (2), 62.

Chapter Two
Xanthates

2.1 Introduction

This chapter describes attempts to synthesise Zn, Sn, Sb and Cu xanthates and to determine their decomposition products. The target materials Cu_2ZnSnS_4 and $CuSbS_2$ are complex and as such attempts to make single-source precursors are very difficult. As a result precursors for Zn, Sn, Sb and Cu sulphides were chosen, with the intention to mix the most appropriate Zn, Sn and Cu or Sb and Cu precursors and to deposit films *via* CVD. As the precursors were to be mixed, the decomposition profiles have been studied in order to obtain the best match in decomposition temperature, the volatilities and solubilities have also been investigated in order to determine which type of CVD is most appropriate.

Xanthates have the general formula $M(S_2COR)_n$ and were first discovered in 1822.[1] They have been widely used as floatation agents,[2] reagents for the separation and determination of a wide number of cations,[3] additives in lubricants,[4] catalysts[5] and accelerants in rubber production.[6] More recently they have been used as precursors for metal sulphide thin films.[7] They are thought to decompose by the Chugaev elimination reaction whereby a syn-elimination from a six-membered cyclic transition state produces an alkene, further elimination of carbonyl sulphide and then hydrogen sulphide produces a metal sulphide (Scheme 2.1),[8] although alternative mechanisms have been suggested for the decomposition of Cu(I) xanthates.[9]

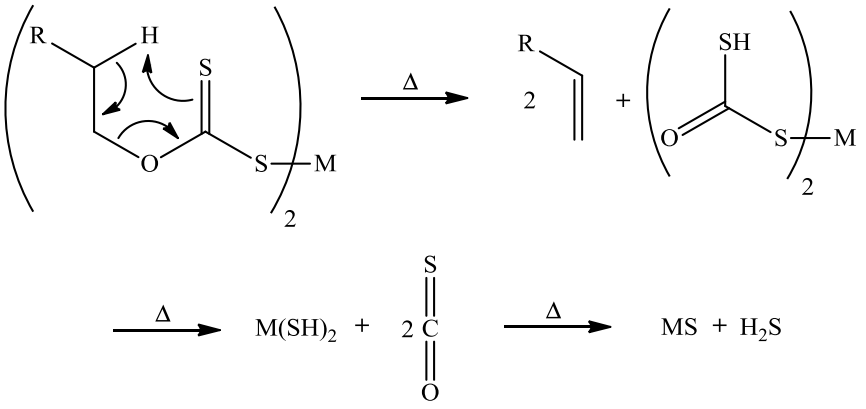

Scheme 2.1 Chugaev elimination reaction

2.1.1 Zinc Xanthates

Zinc xanthates tend to have polymeric structures when the R group is small; $Zn(S_2COR)_2$ (R=Me, Et) are both polymeric (Figure 2.1).[10] An increase in substituent size brings the degree of aggregation down to form a tetramer in $Zn(S_2CO^iPr)_2$.[11] The use of adducts brings the degree of aggregation down even further, the structures of $Zn(S_2COEt)_2$.L (L=py, 2,2-bipy, TMEDA) are all momomeric.[12]

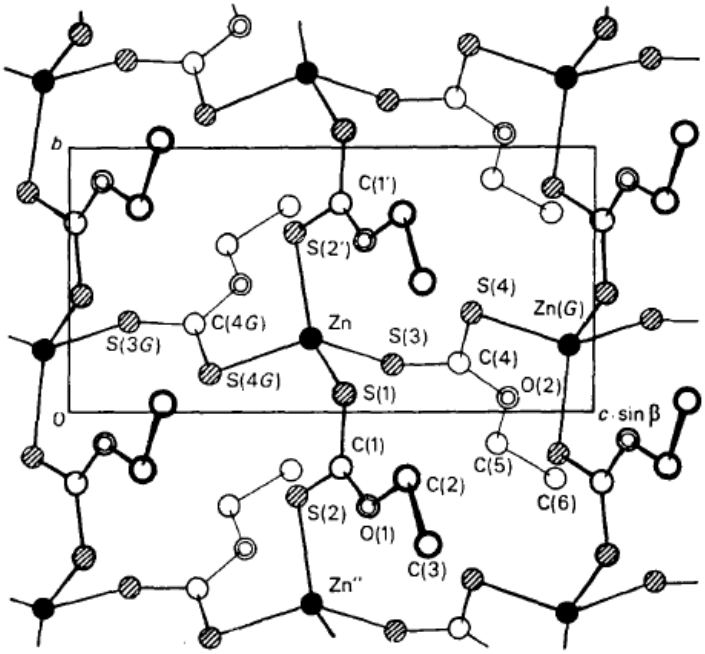

Figure 2.1 Structure of $Zn(S_2COEt)_2$[10]

Zinc xanthates, $Zn(S_2COR)_2$, have been shown to decompose to ZnS. Films of ZnS have been grown from $Zn(S_2COR)_2$ (R=Et, ^{i}Pr) by LPCVD.[13]

2.1.2 Tin Xanthates

Although many heteroleptic tin xanthates have been reported, much less is known about binary tin xanthates. The structures of $Sn(S_2COMe)_2$[14] (Figure 2.2) and $Sn(S_2COEt)_4$[15] are the only ones to have been reported. Both structures are monomeric, making them good candidates for the CVD of SnS or SnS_2, dependent on their respective decomposition pathways.[14-15] Currently no work has been done on the deposition of tin sulphide thin films from xanthates. Nanoparticles of SnS

have been synthesised using the reaction of $SnCl_2$ with KS_2COEt at 180°C, which presumable forms $Sn(S_2COEt)_2$ in situ.[16]

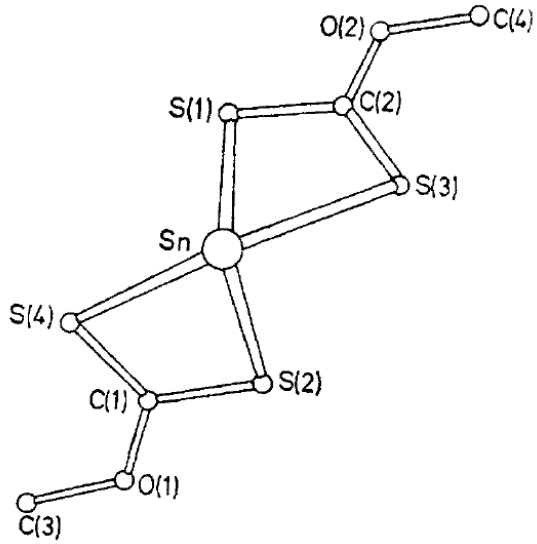

Figure 2.2 Structure of $Sn(S_2COMe)_2$[14]

2.1.3 Antimony (III) Xanthates

Structurally, antimony xanthates exhibit two distinct geometries. The first geometry is adopted by $Sb(S_2COMe)_3$ (Figure 2.3), where two xanthate ligands are approximately co-planar, with one xanthate ligand orthogonal to the plane.[17] One sulphur atom on the co-planar ligands interacts with another antimony atom, creating a dimer. The second geometry is adopted by $Sb(S_2COR)_3$ (R=Et, ^{i}Pr) where the structure is a distorted octahedran about the antimony and there are no other interactions with other molecules.[18]

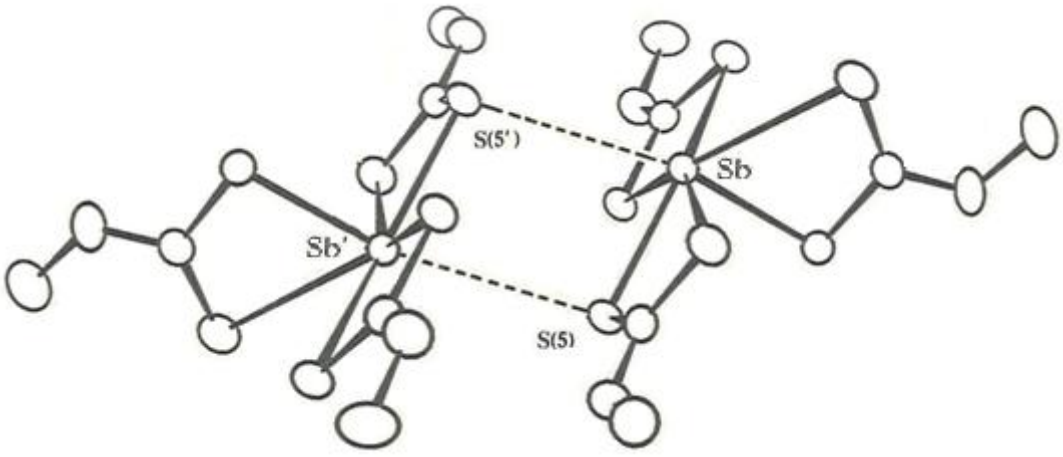

Figure 2.3 Structure of $Sb(S_2COMe)_3$[17a]

Antimony xanthates have been shown to decompose to Sb_2S_3.[19] Crystalline thin films of Sb_2S_3 have been deposited using AACVD from the precursors $Sb(S_2COR)_3$ (R=Et, Me).[20]

2.1.4 Copper Xanthates

A wide number of binary Cu(I) xanthates have been reported but only two have been structurally characterised, CuS_2COR (R=Me, C_6H_2-2,6-$^tBu_2$-4-Me). CuS_2COMe exhibits a polymeric structure, while substitution of Me for a bulky substituent as in $CuS_2COC_6H_2$-2,6-$^tBu_2$-4-Me leads to a tetrameric structure (Figure 2.4).[21] The addition of two triphenylphosphine donors further reduces the degree of oligomorisation, with a monomeric structure found in $(Ph_3P)_2CuS_2COEt$.[22]

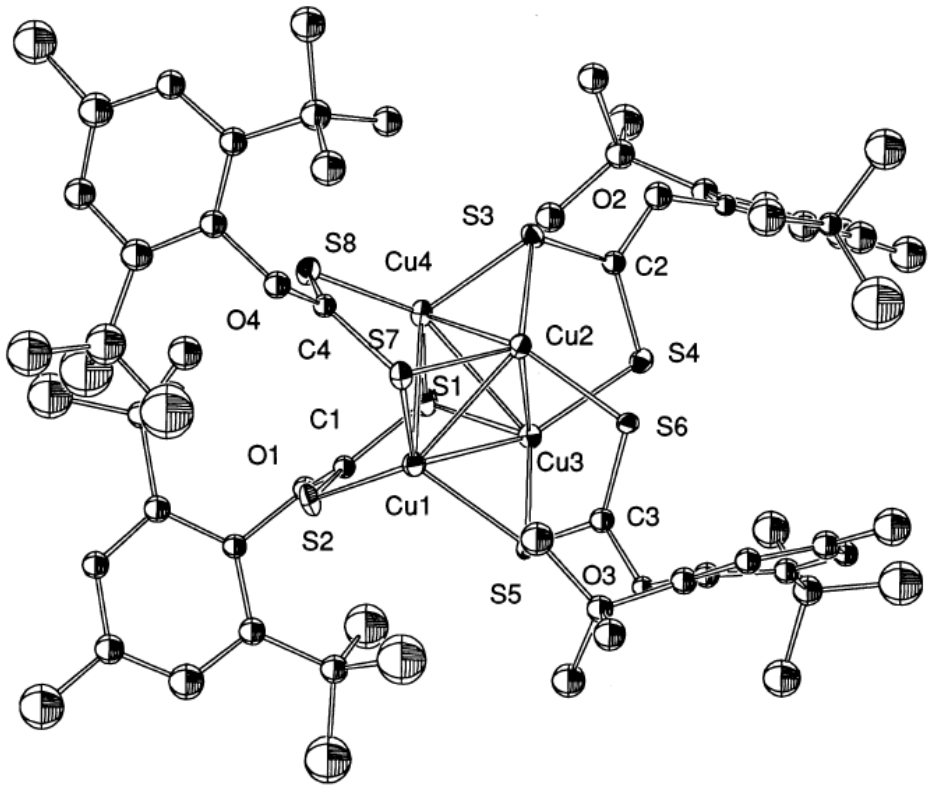

Figure 2.4 Structure of $CuS_2COC_6H_2$-2,6-$^tBu_2$-4-Me[21a]

Although many Cu(II) xanthates have been reported, such as $Cu(S_2COR)_2$ (R=Me, Et, ^{i}Pr, ^{i}Bu, ^{s}Bu, ^{n}Bu, Oct), there are currently no structures in the literature.[23] Cu(II) xanthates are known to be unstable and undergo a redox decomposition to give the corresponding Cu(I) xanthate and a dixanthogen (ROC(S)S-SC(S)OR).[9]

Currently, there have been no reports of copper sulphide thin films deposited from xanthate precursors, although CuS nanoplatelets have been formed from $Cu(S_2COEt)_2$.[24]

2.2 Results and Discussion

2.2.1 Zinc Xanthates

Sodium xanthates were prepared following a literature method. CS_2 was added to a mixture of NaH and the appropriate alcohol in Et_2O.[25] Zinc xanthates, $Zn(S_2COR)_2$ R=Et **(1)**, ^{i}Pr **(2)**, ^{n}Pr **(3)**, ^{n}Bu **(4)**, ^{n}Hex **(5)**, were then prepared following a literature method for the synthesis of $Zn(S_2COEt)_2$.[3] Zinc nitrate was added to the appropriate sodium xanthate in water, the precipitate was filtered and dried *in vacuo*, the products were characterised by microanalysis and NMR. Attempts to make $Zn(S_2CO^{t}Bu)_2$ and $Zn(S_2CO^{t}Amyl)_2$ were unsuccessful. An insoluble white product remained with a melting point that was >300°C, which was assumed to be ZnS. It is possible that in this case the precursors became so unstable that they decomposed as soon as they were made. $Zn(S_2COEt)_2$TMEDA **(6)** was prepared following a literature method,[12b] in which TMEDA was added to a solution of **(1)** in EtOH and the precipitate recrystalised from THF; the resulting product was characterised by microanalysis and NMR.

All xanthates are very easy to synthesise, although **(2)** will decompose in solution if stirring is continued for too long. **(1)** and **(2)** and **(3)** are fairly insoluble, they will dissolve in large amounts of MeOH, EtOH, THF, CH_2Cl_2 and $CHCl_3$. **(4)**, **(5)** and **(6)** are more soluble and will also dissolve fairly readily in MeOH, EtOH, THF, CH_2Cl_2 and $CHCl_3$.

Materials analysis

Thermogravimetric analysis (TGA) of **(1)** - **(6)** shows decomposition to ZnS (Figure 2.5). Sharp decomposition of **(1)** begins at 128°C and finishes at 173°C, resulting in a 38.4% weight remaining which is comparable with that expected if decomposition was to $Zn(SH)_2$ which would leave a residue of 42.5%. Then at 202°C much slower decomposition takes place until 370°C leaving 34.1% weight.

This is slightly higher than the 31.6 residual weight % expected for decomposition to ZnS, indicating incomplete decomposition or some contamination of the final product.

Similarly decomposition of **(2)** begins at 200°C, resulting in a 34.1% weight remaining, which is comparable to that expected for $Zn(SH)_2$ (38.9%), then at 248°C slower decomposition takes place until 325°C leaving a 29.5% weight. This is much closer to the 28.7% expected for ZnS.

(3) shows a gradual loss in weight from 50°C, possibly indicating some volatility, sharp decomposition takes place from 134°C to 170°C, leaving a residual weight % of 30.3% which is lower than that expected if initial decomposition was to $Zn(SH)_2$ (38.9%). Much slower decomposition then takes place to 341°C leaving a residual weight % of 21.7%, much lower than the expected value of 28.7% for ZnS, confirming some volatility in the precursor.

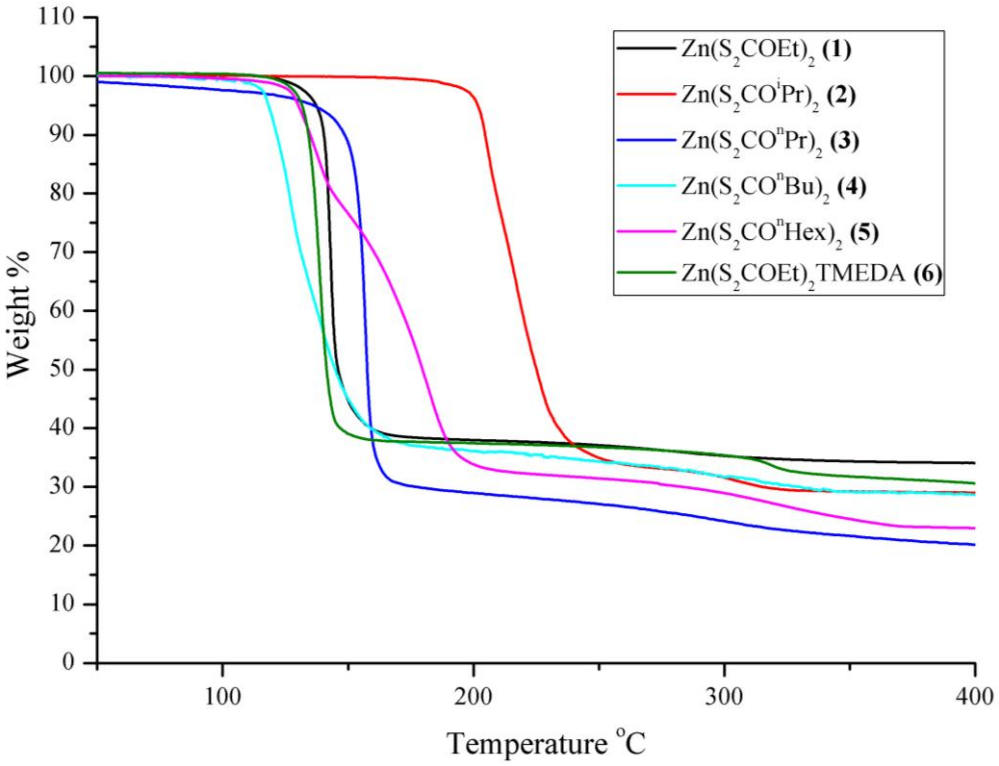

Figure 2.5 TGA of **(1)** - **(6)** at a heating rate of 5°C/min

Decomposition of **(4)** begins at 110°C, resulting in a 36.6% weight remaining, similar to the 35.9% expected for decomposition to $Zn(SH)_2$, then at 177°C slower decomposition takes place until 343°C leaving a 28.5% weight. This is only slightly

higher than the calculated weight % for ZnS at 26.6%. Decomposition of **(5)** is different to the previous xanthates, there are three distinct steps seen in the decomposition. **(5)** initially decomposes at 127°C, a second step starts at 146°C, corresponding to a weight % of 80.1%, with a similar decomposition rate, it would appear that one of the substituents has partially decomposed here, the theoretical value for $Zn(S_2COhex)(S_2COH)$ is 79.9%. The residual weight left after the second step is 31.8%, which is comparable to the value expected for $Zn(SH)_2$ of 31.1%. From 170-341°C a slower decomposition takes place with a final value of 22.8%, this is comparable to the predicted value for ZnS of 22.9%.

Sharp decomposition of **(6)** starts at 125°C and finishes at 153°C leaving a residue of 37.7%, higher than expected for $Zn(SH)_2$ which would leave a 30.8% residue. A much slower decomposition then takes place from 302°C to 328°C leaving a residue of 31.9%, this is significantly higher than the 22.7% expected for ZnS. This would suggest that **(6)** has not fully decomposed, considering that **(1)**, which also has an ethyl substituent, decomposes relatively cleanly, it is possible that the TMEDA has not fully dissociated from **(6)**, leaving a higher than expected residue.

Table 2.1 shows the final percentages of the decomposition and compares them with the expected values if decomposition was to ZnS and $Zn(SH)_2$. Also included are the values of initial decomposition to $Zn(S_2C{=}O)$ as this was a product that was seen in the decomposition of a series of nickel xanthates. These xanthates also has an initial sharp decomposition which was discovered to be to $Ni(S_2C{=}O)$, then a second slower step to NiS, observed by Alam *et. al.*.[8] From the values it looks more likely that in this case, with the exception of **(6)** the initial decomposition is to $Zn(SH)_2$ rather than $Zn(S_2C{=}O)$. The values of decomposition to $Zn(S_2C{=}O)$ are much higher than the values obtained from the TGAs. In the case of **(6)** the value of the second step is much closer to the value expected for decomposition to $Zn(S_2C{=}O)$, however the end product is also much higher than predicted for ZnS. It would seem strange that the decomposition mechanisms are different and it is more likely that incomplete decomposition has taken place in this case.

Table 2.1 Comparison of decomposition profiles of **(1)** – **(6)**

	(1)	**(2)**	**(3)**	**(4)**	**(5)**	**(4)**
% 1st step	38.4	34.1	29.4	36.6	80.1	37.7
% if $Zn(SH)_2$	42.5	38.9	38.9	35.9	31.1	30.8
% if $Zn(S_2C{=}O)$	51.1	46.7	46.7	43.1	37.3	36.9
% 2nd step	-	-	-	-	31.8	-
% final step	34.1	29.5	21.7	28.5	22.8	31.9
% if ZnS	31.6	28.7	28.7	26.6	22.9	22.7

Conclusions

A comparison of the decomposition temperatures of the zinc xanthates synthesised shows that **(1)**, **(3)** and **(6)** all have similar decomposition temperatures, with the onset of all being from 125°C-134°C and the end point of the sharp decomposition being from 153-173°C. **(4)** Decomposes much more readily with the onset of decomposition starting at 110°C, however the decomposition is not as sharp as seen in **(1)**, **(3)** and **(6)**, with the end point at 177°C. **(2)** decomposed much later than all of the other xanthates, with decomposition not starting until 200°C and ending at 248°C.

The decomposition profile of **(5)** is unique in the xanthates tested, with three distinct steps seen, decomposition starts at around the same temperature as **(1)**, **(3)**, **(4)** and **(6)** at 127°C and ends at a similar temperature of 170°C. However, a second step is seen at 146°C which is not seen in any of the other xanthates. All xanthates show a final, much slower decomposition step, all completing decomposition at around the same temperature, 370°C, 325°C, 341°C, 343°C, 341°C and 321°C respectively. With the exception of **(6)**, all xanthates decompose cleanly to ZnS; **(6)** shows some residual weight that could lead to contamination in films if used as a precursor. **(3)** is the only precursor to show some volatility, with a gradual weight loss from 50°C and a final weight % lower than that expected for ZnS.

2.2.2 Tin Xanthates

Tin xanthates were prepared following a literature method.[15] Sodium ethyl xanthate was added to $SnCl_2$ in water. $Sn(S_2COEt)_2$ **(7)** was characterised by microanalysis and NMR. Attempts to make $Sn(S_2CO^iPr)_2$ and $Sn(S_2CO^tBu)_2$ were

not successful. The reaction briefly turned yellow which would suggest the xanthates were made. The reaction then turned brown/black which suggests that the xanthates decomposed to a tin sulphide. The decomposition took place even when stirring was stopped immediately after addition of the sodium xanthates. Sodium ethyl xanthate was added to $SnCl_4$ in toluene, the resulting orange oil was precipitated with the addition of hexane, $Sn(S_2COEt)_4$ **(8)** was characterised by microanalysis and NMR.

Structural analysis

Crystals of **(7)** were obtained by recrystallisation from methanol and cooling to -20°C. The structure is shown in Figure 2.6 The only other example of a tin(II) structure that has been reported is that of $Sn(S_2COMe)_2$.[26]

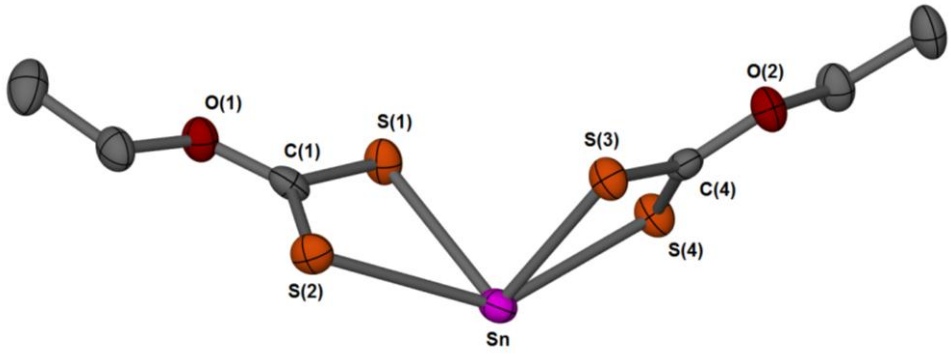

Figure 2.6 Structure of **(7)**, thermal ellipsoids drawn at 50%

Selected bond distances are compared with $Sn(S_2COMe)_2$ (Table 2.2). The structure of **(7)** shows that the xanthate groups are both bidentate in their coordination to the central tin atom. The Sn-S(1) and Sn-S(3) bond distances are significantly shorter than the Sn-S(2) and Sn-S(4) bond distances. i.e. anisobidentate chelation (Figure 2.7). The C-S bond lengths are much more similar to each other.

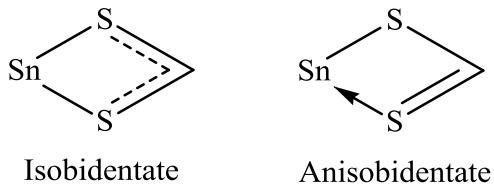

Figure 2.7 Isobidentate and anisobidentate bonding

The packing of the structure shows that the molecules of **(7)** sit on top of each other in the lattice (Figure 2.8). There are Sn-S secondary bonding interactions between the next tin centre and the S(1) and S(3) sulphur atoms, 3.513(14)Å and 3.476(13)Å respectively. This makes the coordination geometry of around the central tin atom distorted octahedral. This is also seen in the structure of $Sn(S_2COMe)_2$.[26]

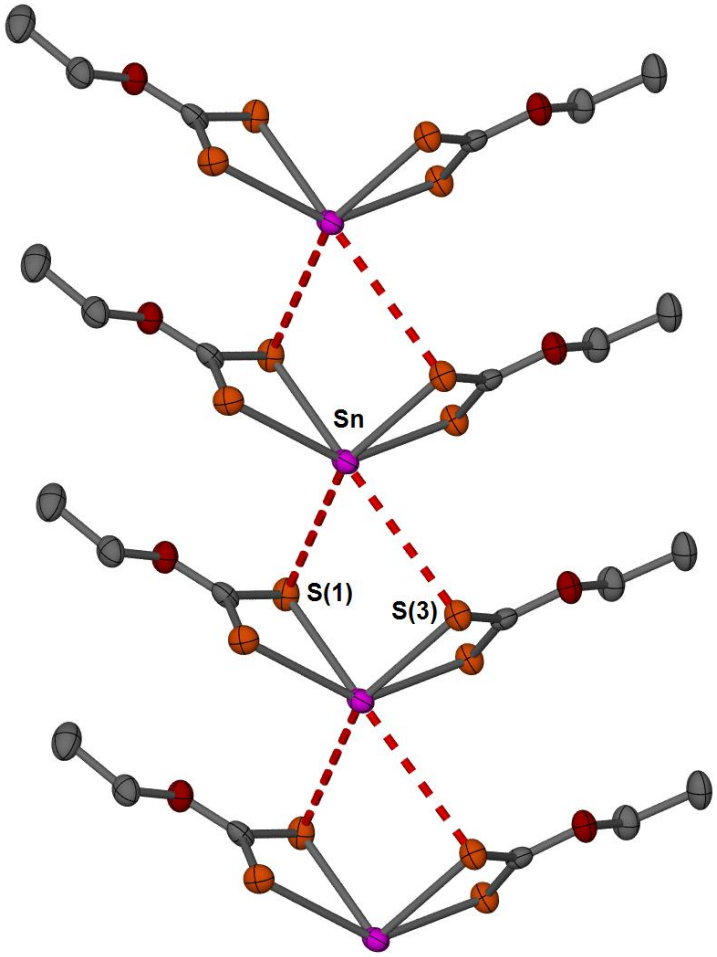

Figure 2.8 Packing of **(7)**, thermal ellipsoids drawn at 50%

Table 2.2 Selected bond distances (Å) of **(7)** and $Sn(S_2COMe)_2$

	$Sn(S_2COEt)_2$ (7)	**$Sn(S_2COMe)_2$[26]**
Sn-S(1)	2.6391(12)	2.643(3)
Sn-S(2)	2.8849(12)	2.838(3)
Sn-S(3)	2.6204(12)	2.604(4)
Sn-S(4)	2.7549(10)	2.802(3)
S(1)-C(1)	1.718(4)	1.695(10)
S(2)-C(1)	1.684(4)	1.672(10)
S(3)-C(4)	1.719(4)	1.707(10)
S(4)-C(4)	1.684(5)	1.662(9)

Materials analysis

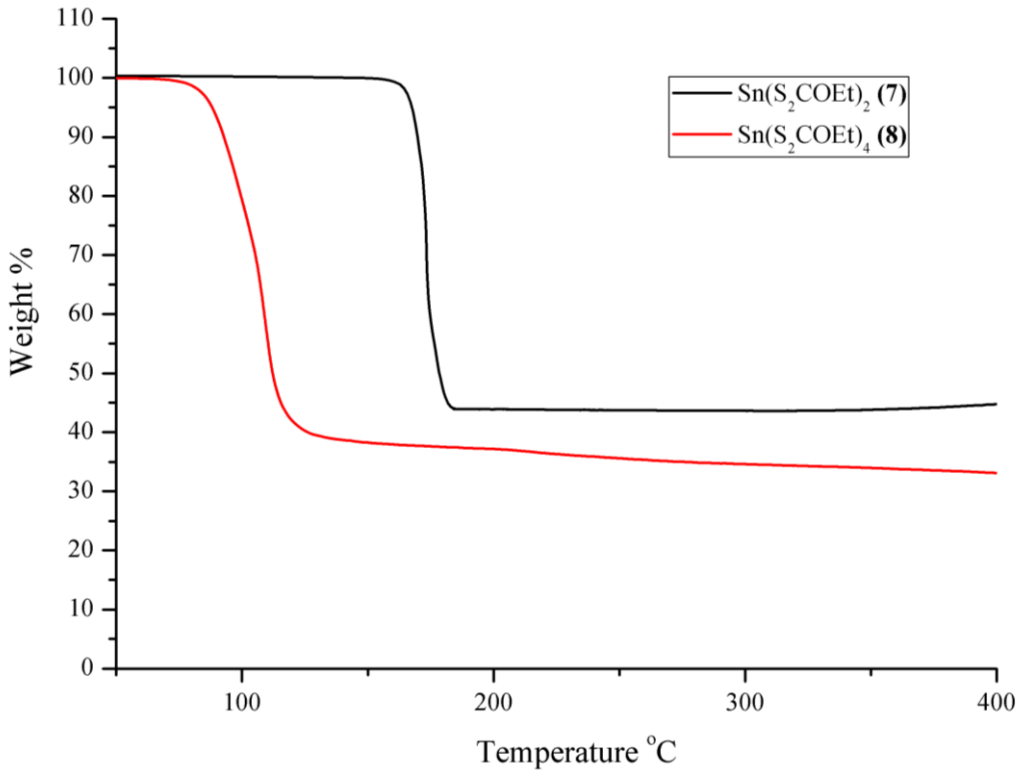

Figure 2.9 TGAs of **(7)** and **(8)** at a heating rate of 5°C/min

TGA analysis of **(7)** and **(8)** (Figure 2.9) shows decomposition to SnS_2. Decomposition of **(7)** starts at 158°C and finishes at 186°C leaving a residue of 43.9%, this is comparable to both the calculated weight % of SnS (42.0%) and SnS_2

(50.8%). If decomposition is to SnS the calculated weight % is 42.0%, in which case the decomposition product has some residual contamination. The calculated weight % of SnS_2 is 50.8%, if decomposition is to SnS_2 then there must be some volatility in the precursor. As the results were ambiguous, Raman was performed on the powder obtained from heating **(7)** to 400°C under N_2. Only one peak was seen in the Raman at 311cm^{-1} (Figure 2.10), which is consistent with the larger of the two expected peaks for SnS_2 at 312cm^{-1}, all Raman shifts for the different tin sulphides are shown in Table 2.3.[27] As the Raman confirms the decomposition product to be SnS_2, this indicates that there must be some volatility in the precursor as the final product was lower in weight than expected.

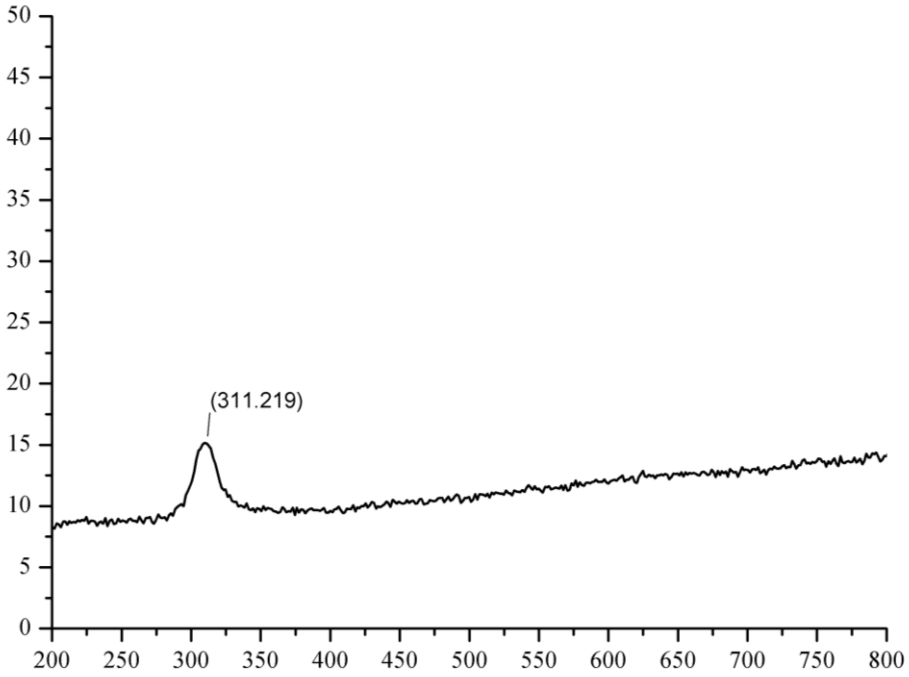

Figure 2.10 Raman of $Sn(S_2COEt)_2$ decomposition product

Table 2.3 Raman shifts for tin sulphides[27]

Material	Raman shift, cm^{-1}
SnS	288, 220, 189, 163, 96
Sn_2S_3	307, 251, 234, 183, 87, 71, 60, 52, 36
SnS_2	312, 215

(8) decomposed much more readily, starting at 73°C and finishing at 139°C, with the decomposition being slightly slower than that of **(7)**. The residue left after initial decomposition is 39.4% which is much higher than both the calculated values for SnS_2 and SnS at 30.4% and 25.1% respectively. A much more gradual decomposition takes place at 139°C going down to a residual mass of 33.1% at 400°C, becoming much closer to the expected value for SnS_2. From the Chugaev elimination reaction it is possible that **(8)** has partially decomposed to form $Sn(SH)_4$, which would have a calculated percentage of 41.7%, this is comparable to the initial weight loss seen, it is then possible that further slower decomposition leads to SnS_2, as seen in the zinc xanthates. It is unlikely that the initial decomposition is to $Sn(S_2C{=}O)$ as the expected value for this (35.1%) is much lower than the experimental value found.

CVD Trials

Due to the cleaner decomposition and the higher thermal stability of **(7)**, this was chosen as the precursor for CVD trials. Although some volatility was seen in the TGA it was not significant so AACVD was chosen as the method as **(7)** is readily soluble in most organic solvents, excluding MeOH, EtOH and hexane. AACVD was performed by dissolving **(7)** (0.41mmol) in THF (50ml) at 250°C for 4 hours on both glass and molybdenum coated glass.

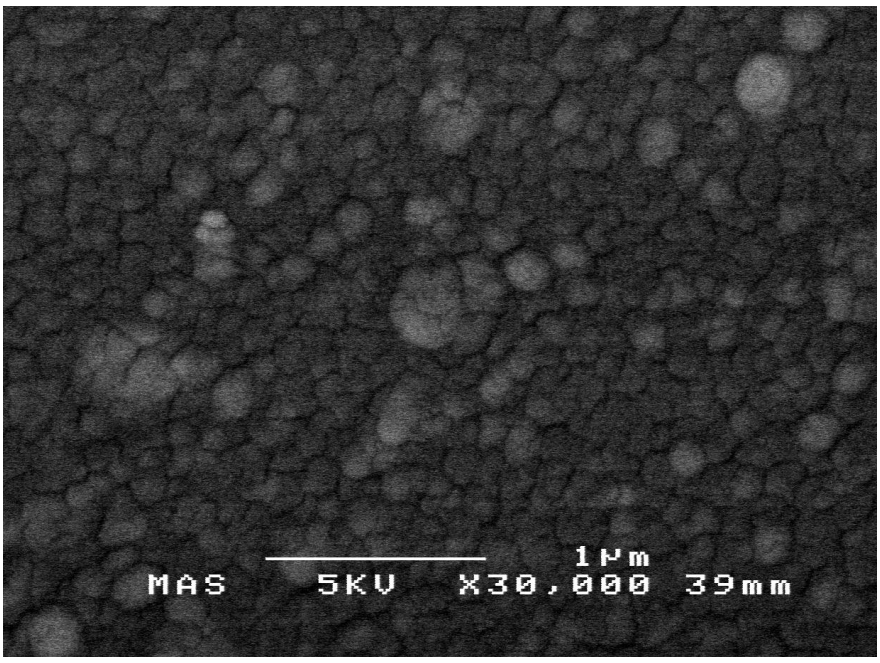

Figure 2.11 SEM image of SnS_2 on glass

Films deposited on glass are yellow and look fairly thin. SEM imaging (Figure 2.11) shows a textured film, which is cracked around blocks of diameter ca. 200nm. There are some lighter spots seen which have areas varying from 100nm to 500nm. EDX analysis (Figure 2.12) shows both Sn and S present in the film with a uniform distribution, accurate quantitative analysis was not possible as one of the Sn peaks overlaps with the Ca peaks from the glass. Films were amorphous so PXRD analysis was not possible although the yellow colour of the films suggests deposition of SnS_2.

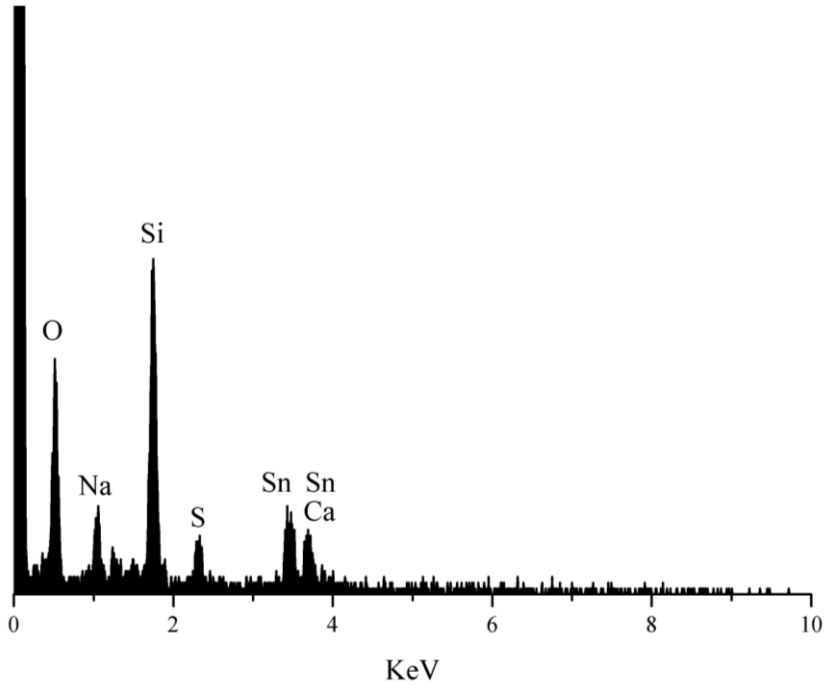

Figure 2.12 EDX Analysis of SnS_2 film

Films deposited on Mo coated glass are metallic in appearance. SEM imaging (Figure 2.13) shows a film with blocks that are much more defined than the film deposited on glass; blocks vary in size from 100nm to 950nm at the largest axis. EDX analysis confirms the presence of Sn and S in the film Quantitative EDX was not possible in this case as the S peaks overlap with the Mo peaks. Unfortunately PXRD was not possible as the films were either too thin or amorphous.

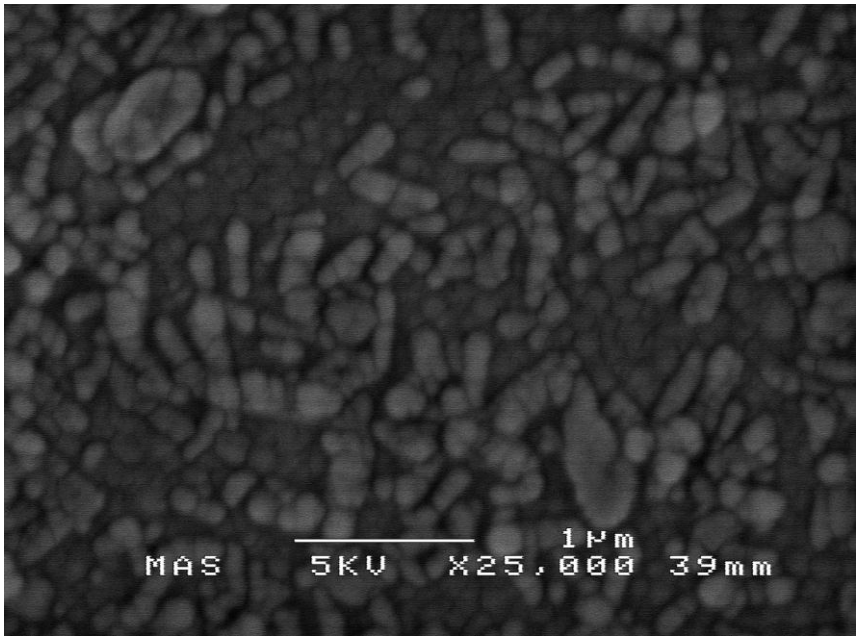

Figure 2.13 SEM image of SnS_2 on Mo coated glass

Nanoparticle synthesis

An attempt at nanoparticles synthesis was made by heating **(7)** in TOPO and oleylamine. TOPO (7.73g, 20mmol) was heated to 300°C, **(7)** (0.18g, 0.5mmol) was dissolved in oleylamine (10ml) and injected into the heated TOPO. The solution was left stirring for 60 minutes at 300°C, after which time the solution had turned from muddy brown to transparent dark brown. The solution was then cooled rapidly in a cold water bath. Nanoparticles were precipitated with MeOH and washed three times.

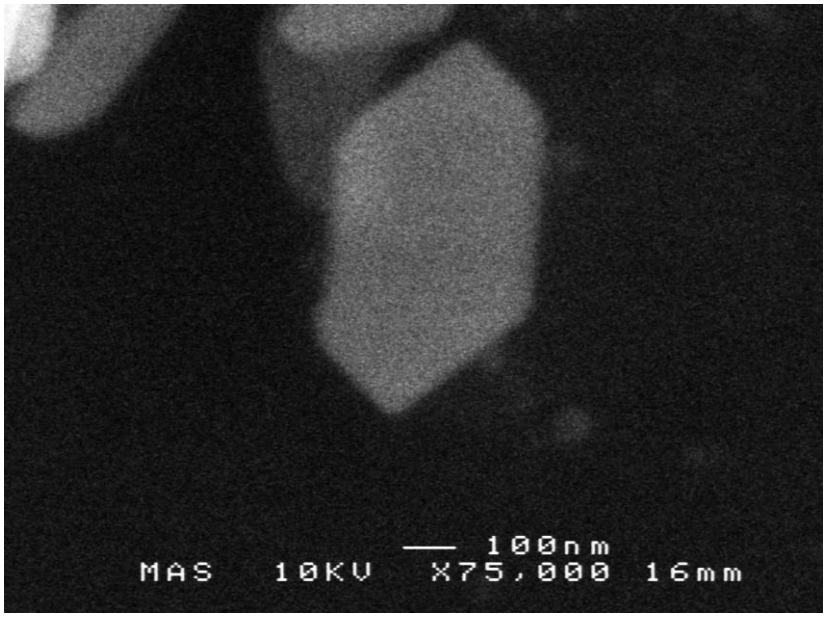

Figure 2.14 SEM image of an SnS nanoparticle

SEM imaging (Figure 2.14) shows hexagonal particles of 300nm in width and 600nm in height. EDX confirms the presence of Sn and S in a 1:1 ratio. It is interesting to note that the synthesis of nanoparticles produces a different form of tin sulphide than the CVD trials using the same precursor.

2.2.3 Antimony Ethyl Xanthate

Antimony ethyl xanthate **(9)** was prepared following literature method.[20] Potassium ethyl xanthate was added to antimony chloride in CH_2Cl_2, the product was filtered and crystalised by slow evaporation then characterised by NMR.

Materials analysis

TGA analysis of **(9)** shows decomposition to Sb_2S_3 (Figure 2.15). Decomposition starts at 93°C and ends at 144°C with 37.6% weight remaining, this is lower than that expected if initial decomposition is to either $Sb(SH)_3$ (45.4%) or $Sb(S_2C{=}O)$ (43.8%). The initial decomposition is much closer to the theoretical value for loss of one xanthate group and decomposition of the remaining two, leaving $Sb(SH)_2$ (38.6%), however an Sb(II) ion is not likely to have been formed. After that, slower decomposition takes place and ends at 262°C with a percentage weight of 34.7%; this is comparable to a predicted weight % of 35.0 for Sb_2S_3.

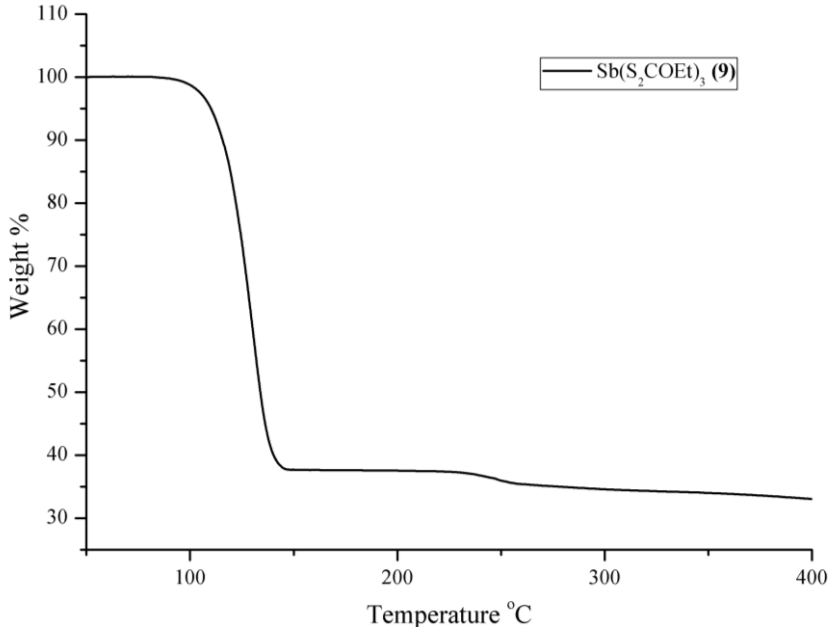

Figure 2.15 TGA of $Sb(S_2COEt)_3$ **(9)** at a heating rate of 5°C/min

2.2.4 Copper Xanthates

A series of copper xanthates were made to try to match the decomposition temperature of the zinc, tin and antimony xanthates. $(PPh_3)_3CuCl$ was first synthesised following a literature method,[28] by adding CuCl to a solution of PPh_3 in $CHCl_3$.[28] $(PPh_3)_3CuCl$ was then used in the synthesis of $(PPh_3)_2Cu(S_2COR)$ R = Et **(10)**, ^{i}Pr **(11)**, ^{t}Bu **(12)**, and ^{t}Amyl **(13)** following a literature method for the synthesis of $(PPh_3)_2Cu(S_2COEt)$.[29] The appropriate sodium xanthate was added to a solution of $(PPh_3)_3CuCl$ in $CHCl_3$.[29] The xanthates were characterised by microanalysis and NMR.

Structural analysis

Addition of Et_2O and cooling to -20°C gave crystals of **(10)**-**(13)** of which only the structure of **(10)** has already been reported.[22] **(11)**, **(12)** and **(13)** are structurally similar, and so only the structure of **(12)** is shown (Figure 2.16). However there are differences in the bond lengths and angles of all of the structures. Selected bond distances and angles are compared in Table 2.4.

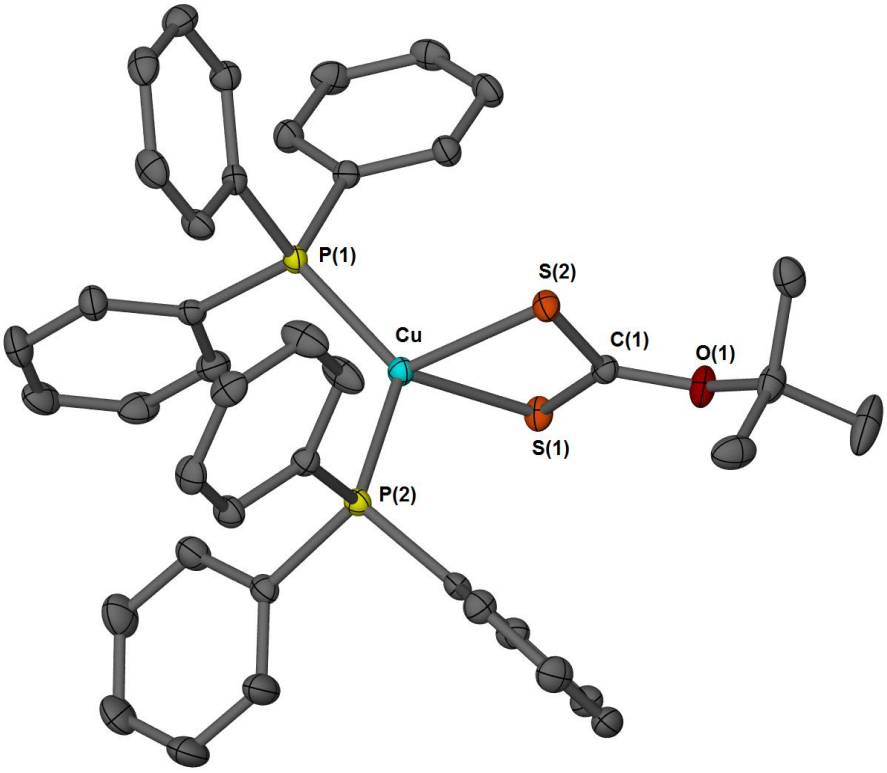

Figure 2.16 Structure of **(12)**, thermal ellipsoids drawn at 50%

The structures of **(11), (12)** and **(13)** all show two PPh_3 groups coordinated to the central copper atoms. The xanthate group is bidentate in all cases. **(11)** and **(12)** have much longer Cu-S(1) bond lengths than Cu-S(2) bond lengths, this shows that the chelation is anisobidentate. However although the bond lengths of Cu-S(1) and Cu-S(2) in **(10)** and **(13)** are also different, there is much less of a difference than in **(11)** and **(12)**, suggesting that bonding is much more isobidentate in **(10)** and **(13)**. All of the C-S bond lengths in each of the structures are either the same or very similar, and don't seem to be affected by the differences in Cu-S bond lengths, however it is interesting to note that where the Cu-S bond distances are most different [**(11)** and **(12)**], the C-S bond distances are the closest in value to one another and vice versa in the case of **(10)** and **(13)**.

Table 2.4 Selected bond distances (Å) and angles (°) of **(10)** – **(13)**

	^{i}Pr (11)	**^{t}Bu (12)**	**^{t}Amyl (13)**	**Et (10)[22]**
Cu-S(1)	2.4892(10)	2.4500(10)	2.4244(12)	2.451(2)
Cu-S(2)	2.3653(10)	2.3782(4)	2.4081(12)	2.404(2)
S(1)-C(1)	1.6918(18)	1.6935(16)	1.700(3)	1.702(12)
S(2)-C(1)	1.689(2)	1.6937(17)	1.691(3)	1.664(12)
Cu-P(1)	2.2434(10)	2.2477(10)	2.2548(11)	2.245(2)
Cu-P(2)	2.2597(10)	2.2710(10)	2.2585(12)	2.265(2)
P(1)-Cu-P(2)	126.103(19)	125.289(17)	124.74(2)	127.1(1)
S(1)-Cu-S(2)	74.389(17)	74.499(15)	74.49(2)	74.6(1)

Materials analysis

TGA analysis of **(10) - (13)** shows decomposition to Cu_2S (Figure 2.17).

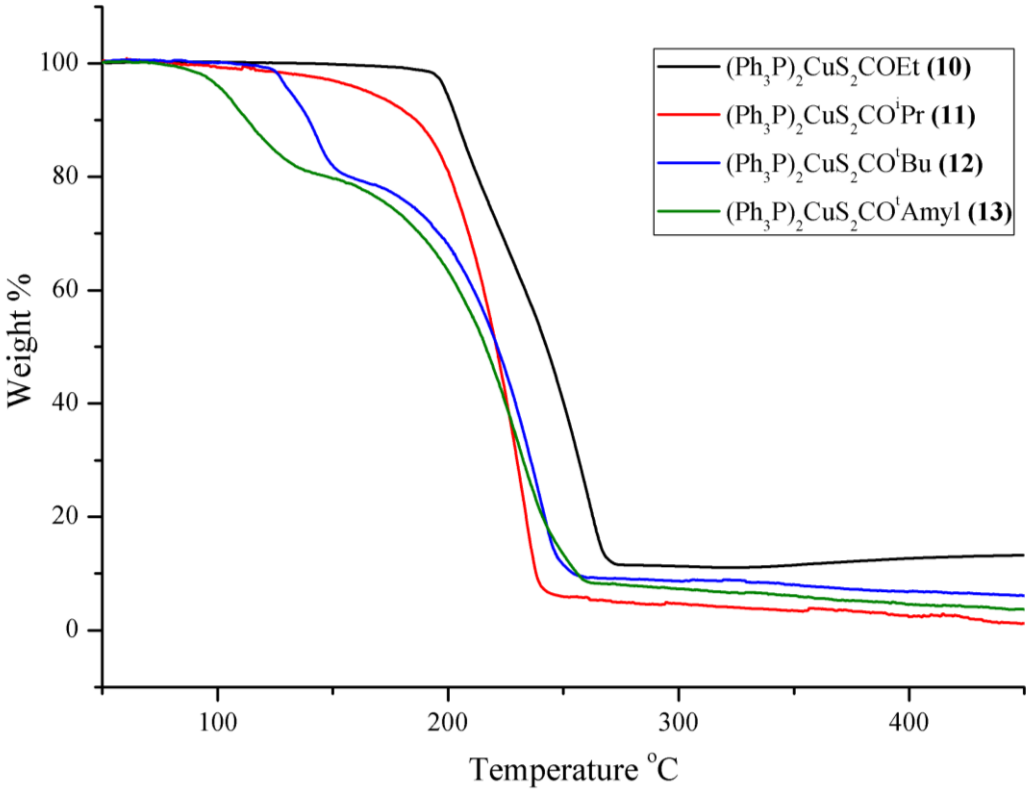

Figure 2.17 TGA of **(10) - (13)** at a heating rate of 5°C/min

Table 2.5 shows the final percentages of the decomposition and compares them with the expected values if decomposition was to Cu_2S and CuS; it also includes the percentage if the initial step is decomposition of the xanthate, leaving $½Cu_2S(PPh_3)_4$. Figure 2.17 shows decomposition of **(10)** that begins at 201°C and ends at 278°C, resulting in 11.3% weight remaining, a value very close to the predicted value of 11.2% if decomposition was to $½Cu_2S$.

Decomposition of **(11)** begins at 158°C and ends at 245°C with 4.2% weight remaining, which does not match either decomposition to $½Cu_2S$ (10.9) or CuS (13.1) and so some sublimation must have taken place. As such it is hard to confirm the decomposition product.

Decomposition of **(12)** takes place in two distinct steps, starting at 118°C, leaving a 79.8% residue by 159°C, which is comparable to initial decomposition of the xanthate. If the final decomposition product was CuS the decomposition of the xanthate would leave a residue of $CuS(PPh_3)_2$ with a weight percentage of 84.1%, which is too high. However if decomposition was to Cu_2S, initial decomposition of

the xanthate would leave a residue of $½Cu_2S(PPh_3)_4$, with a percentage of 81.9%, this is fairly close to the value seen. Decomposition then continues until 258°C leaving 8.3% weight, this value does not match either decomposition to $½Cu_2S$ (10.8) or CuS (12.9) and so some sublimation must have taken place. Results from the first decomposition step suggest that final decomposition is to $½Cu_2S$.

Decomposition of **(13)** starts at 82°C, leaving an 80.1% residue by 146°C, comparable to initial decomposition of the xanthate, leaving a residue of $½Cu_2S(PPh_3)_4$, predicted to be 80.4%. Decomposition continues until 268°C leaving 6.6% weight, this value does not match either decomposition to $½Cu_2S$ (10.6) or CuS (12.6) and so some sublimation must have taken place. As with **(12)** the first step suggests that decomposition is to $½Cu_2S$. A powder diffraction pattern of the decomposition product of **(10)** was taken but this was not crystalline.

As the only step seen in the decomposition involves the loss of the phosphine, it is not possible to determine exactly which decomposition mechanism is seen. However, as the xanthate decomposition is much more facile in **(13)**>**(12)**>**(11)**>**(10)** this could indicate a step in the decomposition that involves stabilisation of a charge by the alkyl group, which would confirm the Chagaev decomposition mechanism. The decomposition would be more facile with larger and more branched organic substituents because they will stabilise the charge more readily.

Table 2.5 Comparison of decomposition profiles of **(10)** – **(13)**

	(10)	**(11)**	**(12)**	**(13)**
% 1st Step observed	-	-	79.8	80.1
% $½Cu_2S(PPh_3)_4$	-	-	81.9	80.4
% $CuS(PPh_3)_2$	-	-	84.1	82.5
% 2nd Step observed	11.3	4.2	8.3	6.6
% $½Cu_2S$	11.2	10.9	10.8	10.6
% CuS	13.3	13.1	12.9	12.6

The synthesis of copper xanthates with different substituents has not significantly affected the end temperature of the decomposition. With this in mind an attempt to change the phosphine donor was made. Phosphite, $P(OPh)_3$, is known to be a weaker sigma donor than triphenyl phosphine, PPh_3, so an attempt was made to

synthesise $(P(OPh)_3)_2Cu(S_2COEt)$ **(14)**. Due to the ease of availability of tributyl phosphine, $P(^nBu)_3$, this was also used to synthesise $(P^nBu_3)_2Cu(S_2COEt)$ **(15)** and $(P^nBu_3)_2Cu(S_2COBu)$ **(16)**. The synthesis used a one pot method that combined the two step synthesis of the previous copper xanthates. Copper chloride was added to a solution of sodium ethyl xanthate and the appropriate phosphine in $CHCl_3$, the filtrate was dried *in vacuo*. The structure of **(14)** was confirmed by X-Ray Crystallography and the empirical formula confirmed by microanalysis and NMR. **(15)** and **(16)** were oils, whose composition was confirmed by microanalysis and NMR.

Structural analysis

Crystals of **(14)** formed from the oily solid obtained in the synthesis of **(14)**. The structure is shown below (Figure 2.18). Selected bond distances and angles are shown in Table 2.6.

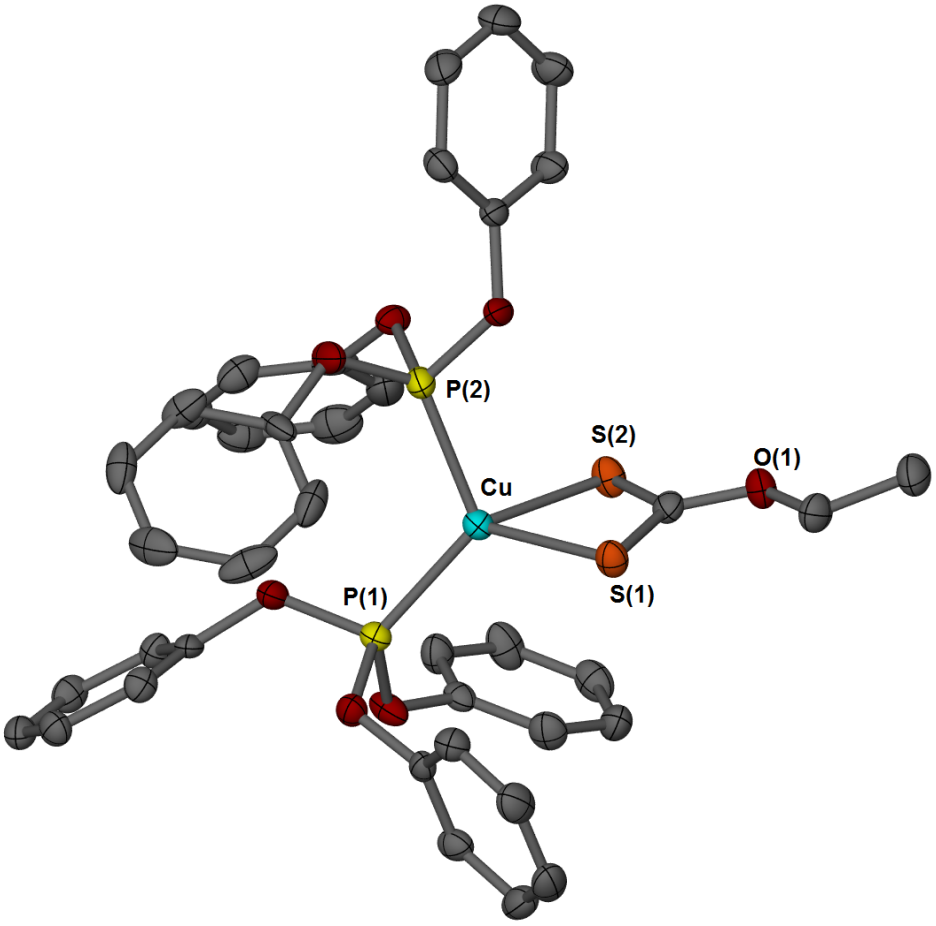

Figure 2.18 Structure **(14)**, thermal ellipsoids drawn at 50%

The structure of **(14)** shows two $P(OPh)_3$ groups coordinated to the central copper atoms in much the same way as the previous copper structures. The xanthate group is isobidentate. The bond lengths between Cu and P(1) and P(2) are 2.1846(10) and 2.2282(10) respectively, these are significantly shorter than the bond lengths seen in the other copper crystal structures. This contradicts our assumption that phosphite is a weaker sigma donor than phosphine, however there are also steric affects to be considered, the phosphite does not have rigid phenyl groups as opposed to a phopshine ligand which does. This enables the phenyl ligands to bend and allows a closer interaction between the P and Cu centres. The bond lengths between Cu and S(1) and S(2) are 2.3600(10) and 2.4020(10) respectively, these are also significantly shorter than the bond lengths seen in the other copper crystal structures. The differences in bond length between Cu-S(1) and Cu-S(2) are similar to that of **(10)** and **(13),** showing a larger degree of isobidenticity than **(11)** and **(12).** The S(1)-C(1) and S(2)-C(1) bond lengths are 1.684(3) and 1.691(3) respectively.

Table 2.6 Selected bond distances (Å) and angles (°) of **(14)**

	(14)
Cu-S(1)	2.3600(10)
Cu-S(2)	2.4020(10)
S(1)-C(1)	1.684(3)
S(2)-C(1)	1.691(3)
Cu-P(1)	2.1846(10)
Cu-P(2)	2.2282(10)
P(1)-Cu-P(2)	116.91(4)
S(1)-Cu-S(2)	75.96(3)

Materials analysis

TGAs of **(14)** - **(16)** are shown in Figure 2.19, and detailed in Table 2.7.

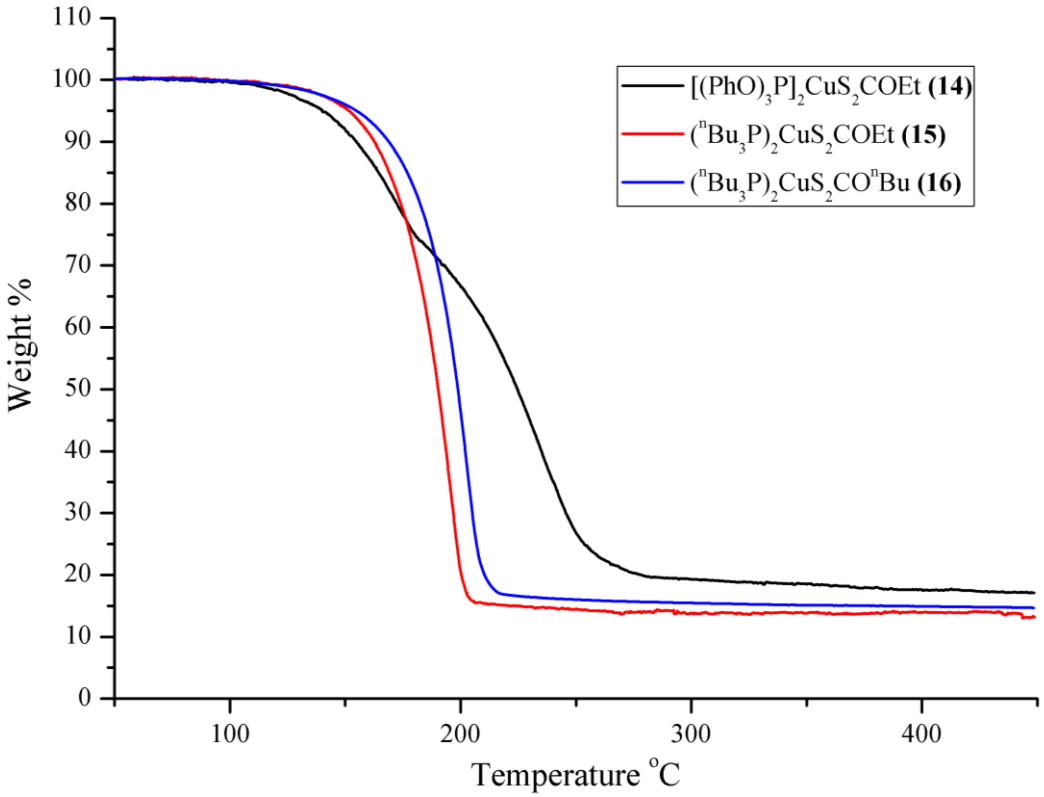

Figure 2.19 TGA of **(14)** - **(16)** at a heating rate of 5°C/min

Decomposition of **(14)** starts at 116°C, leaving a 73.8% residue by 182°C, this is not comparable to initial decomposition of the xanthate, leaving a residue of ½$Cu_2S(P(OPh)_3)_4$, if final decomposition is to Cu_2S, predicted to be 86.9%. It is also not comparable to initial decomposition to $CuS(P(OPh)_3)_2$, predicted to be 88.9% if decomposition if to CuS. This could indicate that some sublimation has already taken place by 182°C. Decomposition continues until 284°C leaving 19.1% weight, this value is higher than the predicted values of decomposition to ½Cu_2S (9.8%) or CuS (11.8%), suggesting incomplete decomposition or carbon contamination.

Decomposition of **(15)** starts at 110°C and ends at 208°C leaving 14.6% weight residue. This value is close to both the predicted value of decomposition to CuS (16.1%) and ½Cu_2S (13.5%). Similarly, decomposition of **(16)** starts at 115°C and ends at 219°C, leaving a residue of 15.9%. This value is slightly higher than the both predicted value for CuS (15.4%) and Cu_2S (12.8%). In both cases the decomposition product is ambiguous and PXRD of the residue showed an amorphous product.

However the TGA of **(10)** shows clean decomposition to Cu_2S and it would seem strange to have a different product for such closely related compounds. As a result it is more likely that decomposition is to Cu_2S in both cases with some contamination seen in the final products.

Table 2.7 Comparison of decomposition profiles of **(14)** – **(16)**

$(R_3P)_2CuS_2COR'$	% if Cu_2S	% if CuS	% recorded
R=OPh, R'=Et (14)	9.8	11.8	19.1
R= ^{n}Bu, R'=Et (15)	13.5	16.1	14.6
R= ^{n}Bu, R'= ^{n}Bu (16)	12.8	15.4	15.9

CVD Trials

Due to the low decomposition temperature obtained using $^nBu_3P$ as the donor and the higher stability over long periods of time **(16)** was chosen as the precursor for CVD trials for the deposition of Cu_2S or CuS. Due to the lack of volatility seen in the TGA analysis, AAVCD was chosen as the preferred deposition technique. **(16)** (0.82mmol) was dissolved in THF (50ml) and AAVCD was performed at 300°C on glass.

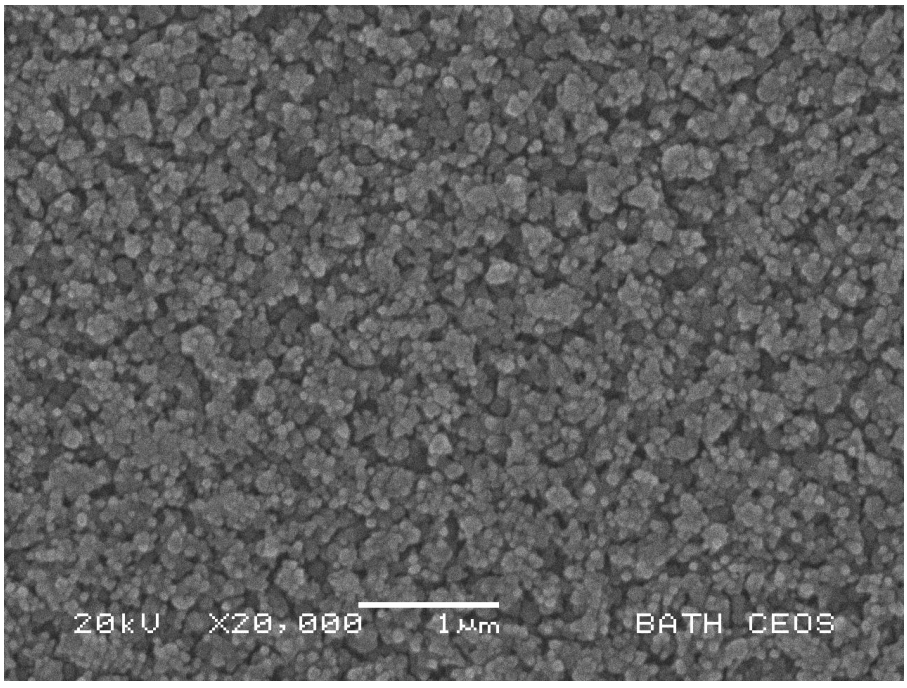

Figure 2.20 SEM image of Cu_2S on glass

Films are yellow/brown in colour. SEM imaging (Figure 2.20) shows a very textured film with larger spheres (200-250nm) composed of much smaller spheres (75nm) uniformly distributed across the film. Quantitative EDX analysis shows the presence of Cu and S in a 3.0 : 1.5 ratio, confirming deposition of Cu_2S films. PXRD confirms the crystallinity of the films, with three peaks seen (Figure 2.21). Which correspond to the (0, 0, 2), (0, 0, 4) and (0, 0, 6) reflections in hexagonal Cu_2S.[30]

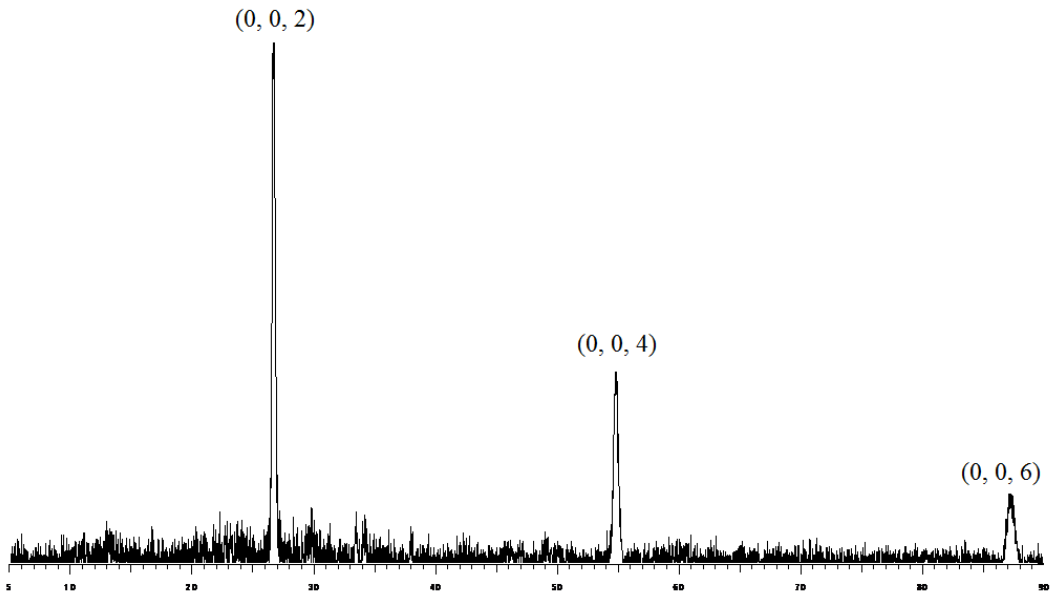

Figure 2.21 PXRD Pattern of Cu_2S on glass, indexing is to PDF 84-0209

2.2.5 Conclusions

A comparison of the onset and end point of decomposition and the products obtained is detailed in Table 2.7. In terms of the Zn xanthates, the onsets of decomposition vary across a wide range but the end points are all fairly similar. With the exception of **(5)**, all Zn xanthates show a similar decomposition profile, with very sharp initial decomposition then a slow final step. None show any appreciable volatility and so AACVD would have to be the deposition method used. For AACVD to be possible the precursors have to have some solubility, only **(4)**, **(5)** and **(6)** show any appreciable solubility. **(6)** did not decompose cleanly, with a end product that was higher in weight than expected for ZnS, so **(4)** or **(5)** are the most promising Zn precursors.

For the Sn precursors, **(8)** is much more thermally unstable and will decompose over a period of days after synthesis. **(7)** is more thermally stable and decomposes

cleanly to form SnS_2 with some volatility seen. For the Sb precursor synthesised, the onset of decomposition of **(9)** is relatively low, however due to the second step the end point of decomposition makes it comparable with the Cu xanthate synthesised.

For the Cu xanthates, in all cases the only clear decomposition product has been seen in the TGA of **(10)**, where decomposition to Cu_2S is observed. **(11)** – **(13)** show some volatility, with final values lower than the predicted values for CuS and Cu_2S, however as **(10)** has been shown to decompose cleanly to Cu_2S, it seems sensible to assume that the same can be said of **(11)** – **(13)**. The same can be said for **(14)** – **(16)** where the final products are higher in weight than either CuS or Cu_2S. The Cu xanthates see a definite lowering in decomposition temperature when the phopshine group is changed from Ph_3P to $^{n}Bu_3P$. **(15)** and **(16)** have much closer decomposition temperature to the main bulk of the decomposition of the Zn, Sn and Sb xanthates synthesised.

For the deposition of Cu_2ZnSnS_4 either **(4)** or **(5)** have the highest solubility and the cleanest decomposition to ZnS with no contamination seen in the final product percentages, however **(4)** has a cleaner decomposition profile. **(4)** is more closely matched to **(7)** in terms of thermal stability and the main bulk of the decomposition, when compared to **(8)**.

(15) and **(16)** show the lowest decomposition temperature of the Cu xanthates, these are most closely matched with the decomposition temperatures of **(4)** and **(7)**. **(16)** is much more stable over long periods of time so this precursor would provide a better match with **(4)** and **(7)**. It would also be interesting to try AACVD using **(5)** in place of **(4)** to see if the difference in decomposition profile affects the deposition product.

For the deposition of $CuSbS_2$ AACVD was also the deposition method of choice as **(9)** is not very volatile. The main bulk of the decomposition of **(9)** happens from 93°C - 144°C, as such **(15)** or **(16)** are the best match in terms of decomposition temperature. As mentioned above, **(15)** is not stable over long periods of time and so the best match for $CuSbS_2$ would be to use **(9)** and **(16)** as precursors.

Table 2.8 Comparison of decomposition temperatures and products of **(1)** – **(16)**

	Onset	End point	Product
$Zn(S_2COEt)_2$ (1)	128°C	370°C	ZnS
$Zn(S_2CO^iPr)_2$ (2)	200°C	325°C	ZnS
$Zn(S_2CO^nPr)_2$ (3)	50°C	341°C	ZnS
$Zn(S_2CO^nBu)_2$ (4)	110°C	343°C	ZnS
$Zn(S_2CO^nHex)_2$ (5)	127°C	341°C	ZnS
$Zn(S_2COEt)_2$.TMEDA (6)	125°C	328°C	ZnS
$Sn(S_2COEt)_2$ (7)	158°C	186°C	SnS_2
$Sn(S_2COEt)_4$ (8)	73°C	139°C	SnS_2
$Sb(S_2COEt)_3$ (9)	93°C	262°C	Sb_2S_3
$(Ph_3P)_2CuS_2COEt$ (10)	201°C	278°C	Cu_2S
$(Ph_3P)_2CuS_2CO^iPr$ (11)	158°C	245°C	Cu_2S
$(Ph_3P)_2CuS_2CO^tBu$ (12)	118°C	258°C	Cu_2S
$(Ph_3P)_2CuS_2CO^tAmyl$ (13)	82°C	268°C	Cu_2S
$[(OPh)_3P]_2CuS_2COEt$ (14)	116°C	284°C	Cu_2S
$(^nBu_3P)_2CuS_2COEt$ (15)	110°C	208°C	Cu_2S
$(^nBu_3P)_2CuS_2CO^nBu$(16)	115°C	219°C	Cu_2S

2.3 Experimental

Synthesis of $Zn(S_2COEt)_2$ ***(1):*** A solution of KS_2COEt (1.08g, 6.72mmol) in water (30ml) was added to a stirred solution of $Zn(NO_3).6H_2O$ (1g, 3.36mmol) in water (20ml). A white precipitate formed and stirring was continued for one hour. The solution was filtered and the precipitate dried *in vacuo* (0.84g, 82%, mp 130-134°C). Analysis found (calc for $C_6H_{10}O_2S_4Zn$): C 23.4 (23.4), H 3.27 (3.27). ^{1}H NMR (300MHz, $CDCl_3$) δ ppm: 4.59 (q, J=6.91 Hz, 4H, CH_2), 1.49 (t, *J*=7.16 Hz, 6H, CH_3), ^{13}C NMR (300MHz, $CDCl_3$) δ ppm: 230.2 (CS_2), 74.2 (CH_2), 14.0 (CH_3)

Also prepared by the same method were:

$Zn(S_2CO^iPr)_2$ ***(2):*** Using NaS_2CO^iPr (1.17g, 7.39mmol) and $Zn(NO_3).6H_2O$ (1g, 3.36mmol). Yield = 0.89g, 79%, mp 155-157°C. Analysis found (calc for

$C_8H_{14}O_2S_4Zn$): C 28.4 (28.6), H 4.14 (4.20). ^{1}H NMR (300 MHz, $CDCl_3$): 5.33 (sept, *J*=6.30 Hz, 2H, CH), 1.47 (d, *J*=6.03 Hz, 12H, CH_3), ^{13}C NMR (300 MHz, $CDCl_3$): 228.9 (CS_2), 83.5 (CH), 21.5 (CH_3)

Zn($S_2CO^nPr)_2$ ***(3)****:* Using NaS_2CO^nPr (1.06g, 6.72mmol) and $Zn(NO_3).6H_2O$ (1g, 3.36mmol). Yield = 0.94g, 84%, mp 161-163°C (d). Analysis found (calc for $C_8H_{14}O_2S_4Zn$): C 28.8 (28.8), H 4.17 (4.23). ^{1}H NMR (300MHz, $CDCl_3$) δ ppm: 4.47 (t, *J*=6.59 Hz, 4H, OCH_2), 1.88 (sxt, *J*=7.20 Hz, 4H, CH_2CH_3), 1.04 (t, *J*=7.50 Hz, 6H, CH_3), ^{13}C NMR (300MHz, $CDCl_3$) δ ppm: 230.2 (CS_2), 79.7 (OCH_2), 21.82 (CH_2CH_3), 10.3 (CH_3)

Zn($S_2CO^nBu)_2$ ***(4)****:* Using KS_2CO^nBu (1.27g, 6.72mmol) and $Zn(NO_3).6H_2O$ (1g, 3.36mmol). Yield = 1.04g, 85%, mp 108-110°C. Analysis found (calc for $C_{10}H_{18}O_2S_4Zn$): C 33.1 (33.0), H 4.97 (4.99). ^{1}H NMR (300MHz, $CDCl_3$) δ ppm: 4.50 (t, J=6.59 Hz, 4H, $OCCH_2$), 1.81 (quin, J=7.20 Hz, 4H, $CH_2CH_2CH_2$), 1.46 (sxt, J=7.50 Hz, 4H, CH_2CH_3), 0.96 (t, J=7.35 Hz, 6H, CH_3) ^{13}C NMR (300MHz, $CDCl_3$) δ ppm: 229.7 (CS_2), 77.7 ($OCCH_2$), 30.3 ($CH_2CH_2CH_2$), 19.0 (CH_2CH_3), 13.6 (CH_3)

Zn($S_2CO^nHex)_2$ ***(5)****:* Using KS_2CO^nHex (1.35g, 6.72mmol) and $Zn(NO_3).6H_2O$. Yield = 0.84g, 60%, mp 118-120°C. Analysis found (calc for $C_{14}H_{26}O_2S_4Zn$): C 40.0 (40.2), H 6.36 (6.27). ^{1}H NMR (500MHz, $CDCl_3$) δ ppm: 4.51 (t, J=6.60 Hz, 4H, $OCCH_2$), 1.85 (quin, J=7.90 Hz, 4H, CH_2), 1.44 (quin, J=7.33 Hz, 4H, CH_2), 1.28-1.39 (m, 8H, $2CH_2$), 0.92 (t, J=6.60 Hz, 6H, CH_3) ^{13}C NMR (300MHz, $CDCl_3$) δ ppm: 230.5 (CS_2), 78.7 ($OCCH_2$), 31.3 (CH_2), 28.3 (CH_2), 25.4 (CH_2), 22.5 (CH_2), 14.0 (CH_3)

Synthesis of Zn($S_2COEt)_2$TMEDA ***(6)****:* TMEDA (0.19g, 1.63mmol) in EtOH (20ml) was added to a stirred solution of $Zn(S_2COEt)_2$ (0.5g, 1.62mmol) in EtOH (150ml) and stirring was continued for one hour whereby a white precipitate formed. Solution was filtered and the precipitate dried *in vacuo*, recrystallisation from THF on cooling to -20 produced colourless crystals (0.61g, 90%, mp 128-129°C). Analysis found (calc for $C_{12}H_{26}N_2O_2S_4Zn$): C 34.2 (34.1), H 6.16 (6.21), N 6.76 (6.64). ^{1}H NMR (300MHz, $CDCl_3$) δ ppm: 4.48 (q, J=7.16 Hz, 4H, $OCCH_2$), 2.71 (s, 4H, NCH_2),

2.62 (s, 12H, NCH_3), 1.41 (t, J=7.16 Hz, 6H, CH_3) ^{13}C NMR (300MHz, $CDCl_3$) δ ppm: 225.9 (CS_2), 71.1 ($OCCH_2$), 59.5 (NCH_2), 46.8 (NCH_3), 14.1 (CH_3)

Synthesis of $Sn(S_2COEt)_2$ ***(7)****:* A solution of KS_2COEt (1.7g, 10.6mmol) in water (20ml) was added to a stirred suspension of $SnCl_2$ (1g, 5.27mmol) in water (50ml). A pale yellow precipitate formed and stirring was continued for one hour. The solution was filtered and the precipitate dried *in vacuo*. Recrystallisation was from methanol (1.20g, 63%, mp 46-52°C). Analysis found (calc for $C_6H_{10}O_2S_4Sn$): C 19.3 (19.9), H 2.73 (2.79). ^1H NMR (300 MHz, $CDCl_3$) δ ppm: 4.64 (q, *J*=7.03 Hz, 4H, CH_2), 1.49 (t, *J*=7.20 Hz, 6H, CH_3), ^{13}C NMR (300 MHz, $CDCl_3$) δ ppm: 225.9 (CS_2), 70.9 (CH_2), 13.9 (CH_3), ^{119}Sn NMR (300 MHz, $CDCl_3$) δ ppm: 195.2

Synthesis of $Sn(S_2COEt)_4$ ***(8)****:* KS_2COEt (2.8g, 17.5mmol) was added to a stirred solution of $SnCl_4$ (1g, 3.89mmol) in toluene (100ml). A bright orange solution formed and stirring was continued for one hour. The solution was filtered and the solvent removed from the filtrate *in vacuo,* leaving an orange oil. Hexane (50ml) was added and stirred for 1 hour, leaving a yellow precipitate which was filtered and dried *in vacuo* (1.52g, 65%, mp 61-64°C). Analysis found (calc for $C_{12}H_{20}O_4S_8Sn$): C 23.7 (23.8), H 3.26 (3.34). ^1H NMR (300 MHz, $CDCl_3$) δ ppm: 4.55 (q, *J*=7.16 Hz, 8H, CH_2), 1.49 (t, *J*=7.16 Hz, 12H, CH_3), ^{13}C NMR (300 MHz, $CDCl_3$) δ ppm: 220.7 (CS_2), 74.3 (CH_2), 14.0 (CH_3), ^{119}Sn NMR (300 MHz, $CDCl_3$) δ ppm: 63.1

Synthesis of $Sb(S_2COEt)_3$ ***(9)****:* A solution of $SbCl_3$ (1.00g, 4.38mmol) in CH_2Cl_2 (50ml) was added to a stirred suspension of KS_2COEt (2.11g, 13.0mmol) in CH_2Cl_2 (50ml). Stirring was continued overnight. A yellow solution remained with a white precipitate, this was filtered and the filtrate was dried with $MgSO_4$. Slow evaporation left pale yellow crystals. (1.40g, 66%, mp 68-70°C). Analysis found (calc for $C_9H_{15}O_3S_6Sb$): C 22.0 (22.3), H 3.13 (3.12). ^1H NMR ($CDCl_3$): 4.65 (q, J=7.16 Hz, 6H, CH_2), 1.47 (t, J=7.16 Hz, 9H, CH_3), ^{13}C NMR ($CDCl_3$): 222.4 (CS_2), 72.0 (CH_2), 13.9 (CH_3)

$(Ph_3P)_3CuCl$ was prepared following a literature method, a solution of Ph_3P (34.5g, 131.5mmol) in chloroform (150ml) was added to a stirred suspension of CuCl (3.27g, 33mmol) in chloroform (50ml). After stirring for 2 hours white crystals

began to form. Solution was reduced to 80ml and the resulting white slurry was filtered and dried *in vacuo* (29g, 99%).[28]

Synthesis of $(PPh_3)_2Cu(S_2COEt)$ ***(10)****:* A solution of $(Ph_3P)_3CuCl$ (3g, 3.39mmol) in chloroform (50ml) was added to a stirred suspension of KS_2COEt (0.6g, 3.76mmol) in chloroform (50ml). A yellow solution formed with a white precipitate (excess KS_2COEt and KCl). The solution was filtered and diethyl ether (100ml) added to aid crystallisation. Cooling to -20°C gave pale yellow crystals (1.62g, 68%, mp 180-185°C). Analysis found (calc for $C_{39}H_{35}OP_2S_2Cu$): C 65.7 (66.0), H 4.96 (4.97). ^{1}H NMR (300 MHz, CD_2Cl_2) δ ppm: 7.18-7.43 (m, 30H, Ph), 4.42 (q, *J*=7.03 Hz, 2H, CH_2), 1.36 (t, *J*=6.97 Hz, 3H, CH_3), ^{13}C NMR (300 MHz, CD_2Cl_2) δ ppm: 227.9 (CS2), 134.6 (Ph), 134.2 (Ph), 130.1 (Ph), 129.0 (Ph), 69.7 (CH_2), 14.6 (CH_3), ^{31}PNMR (300 MHz, CD_2Cl_2) δ ppm: 1.09.

Also prepared using the same method were:

$(PPh_3)_2Cu(S_2CO^iPr)$ ***(11)****:* Using $(Ph_3P)_3CuCl$ (3g, 3.39mmol) and KS_2CO^iPr (0.65g, 3.76mmol). Yield = 1.59g, 65%, mp 186-189°C. Analysis found (calc for $C_{40}H_{37}OP_2S_2Cu$): C 66.4 (66.5), H 5.20 (5.16). ^{1}H NMR (300 MHz, CD_2Cl_2) δ ppm: 7.19-7.41 (m, 30H, Ph), 5.41 (sept, J=6.10 Hz, 1H, CH), 1.34 (d, J=6.03 Hz, 6H, CH_3), ^{13}C NMR (300 MHz, CD_2Cl_2) δ ppm: 227.2 (CS_2), 134.5 (Ph), 134.2 (Ph), 130.1 (Ph), 129.0 (Ph), 77.2 (CH), 22.0 (CH_3), ^{31}P NMR (300 MHz, CD_2Cl_2) δ ppm: 0.92

Synthesis of $(PPh_3)_2Cu(S_2CO^tBu)$ ***(12)****:* Using $(Ph_3P)_3CuCl$ (3g, 3.39mmol) and NaS_2CO^tBu (0.64g, 3.76mmol). Yield = 1.42g, 57%, mp 134-136°C. Analysis found (calc for $C_{41}H_{39}OP_2S_2Cu$): C 66.2 (66.8), H 5.41 (5.33). ^{1}H NMR (300MHz, CD_2Cl_2) δ ppm: 7.13-7.44 (m, 30H, Ph), 1.67 (s, 9H, CH_3) ^{13}C NMR (300MHz, CD_2Cl_2) δ ppm: 227.5 (CS_2) 134.7 (Ph), 134.2 (Ph), 130.0 (Ph), 128.9 (Ph), 87.9 ($C(CH_3)_3$)24.48 (CH_3) ^{31}P NMR (300MHz, CD_2Cl_2) δ ppm: 0.84

Synthesis of $(PPh_3)_2Cu(S_2CO^tAmyl)$ ***(13)****:* Using $(Ph_3P)_3CuCl$ (3g, 3.39mmol) and NaS_2CO^tAmyl (0.69g, 3.76mmol). Yield = 1.32g, 52%, mp 126-129°C. Analysis found (calc for $C_{42}H_{41}OP_2S_2Cu$): C 66.9 (67.1), H 5.49 (5.50). ^{1}H NMR (300MHz,

CD_2Cl_2) δ ppm: 7.17-7.41 (m, 30H, Ph), 2.10 (q, J=7.54 Hz, 2H, CH_2), 1.61 (s, 6H, CCH_3), 0.96 (t, *J*=7.35 Hz, 3H, CH_2CH_3) ^{13}C NMR (300MHz, CD_2Cl_2) δ ppm: 227.5 (CS_2), 134.8 (Ph), 134.2 (Ph) 130.0 (Ph), 128.9 (Ph), 90.5 (OC), 33.3 (CH_2), 26.2 (CCH_3), 8.8 (CH_2CH_3), ^{31}P NMR (300MHz, CD_2Cl_2) δ ppm: 0.81

Synthesis of $(P(OPh)_3)_2Cu(S_2COEt)$ ***(14)****:* $P(OPh)_3$ (3.14g, 10.1mmol) was added to a stirred suspension of CuCl (0.5g, 5.05mmol) and KS_2COEt (0.89g, 5.55mmol) in 200ml $CHCl_3$. After stirring for 3 hours a yellow solution with a white precipitate remained, this solution was filtered. The solvent was removed *in vacuo* whereby a yellow oil remained. This was washed 3 times with hexane, leaving a wet yellow solid, on standing for a week pale yellow crystals formed (2.68g, 66%, mp 134-136°C). Analysis found (calc for $C_{39}H_{35}CuO_7P_2S_2$): C 58.2 (58.2), H 4.30 (4.39). ^1H NMR (300MHz, CD_2Cl_2): 7.12-7.40 (m, 30H, Ph), 4.10 (q, *J*=7.20 Hz, 2H, CH_2), 1.28 (t, *J*=6.97 Hz, 3H, CH_3) ^{13}C NMR (300MHz, CD_2Cl_2): 227.8, (CS_2), 151.5 (Ph), 130.2 (Ph), 125.2 (Ph), 121.5 (Ph), 69.8 (CH_2), 14.4 (CH_3), ^{31}P NMR (300MHz, CD_2Cl_2): 115.04

Also prepared using the same method were:

$(^nBu_3P)_2Cu(S_2COEt)$ ***(15)****:* Using $^nBu_3P$ (2.04g, 10.1mmol), CuCl (0.5g, 5.05mmol) and KS_2COEt (0.89g, 5.55mmol). Yielding an oil, 1.81g, 61%. Analysis found (calc for $C_{27}H_{59}OP_2S_2Cu$): C 55.2 (55.1), H 9.98 (10.11). ^1H NMR ($CDCl_3$): 4.47 (q, *J*=7.15 Hz, 2H, CH_2), 1.52-1.61 (m, 12H, $6CH_2$), 1.43-1.51 (m, 12H, $6CH_2$), 1.34-1.42 (m, 15H, $6CH_2$ and $COCH_2$), 0.91 (t, *J*=7.25 Hz, 18H, $COCH_2CH_3$) ^{13}C NMR ($CDCl_3$): 226.2 (CS_2), 68.7 (CH_2), 26.7 (CH_2), 25.2 (CH_2), 24.6 (CH_2), 14.1 (CH_3), 13.7 (CH_3), ^{31}P NMR ($CDCl_3$): -19.86

$(^nBu_3P)_2Cu(S_2CO^nBu)$ ***(16)****:* Using $^nBu_3P$ (2.04g, 10.1mmol), CuCl (0.5g, 5.05mmol) and NaS_2CO^nBu (0.88g, 5.55mmol). Yielding an oil, 2.12g, 68%. Analysis found (calc for $C_{29}H_{63}OP_2S_2Cu$): C 56.3 (56.5), H 10.26 (10.30). ^1H NMR (300MHz, $CDCl_3$): 4.41 (t, *J*=6.78 Hz, 2H, OCH_2), 1.73-1.81 (m, 2H, OCH_2CH_2), 1.63-1.72 (m, 2H, $OCH_2CH_2CH_2$), 1.51-1.61 (m, 12H, PCH_2), 1.43-1.50 (m, 12H, PCH_2CH_2), 1.33-1.43 (m, 12H, $PCH_2CH_2CH_2$), 0.88-0.99 (m, 21H, CH_3), ^{13}C NMR (300MHz, $CDCl_3$): 226.3 (CS_2), 72.3 (OCH_2), 30.5 (O CH_2CH_2), 26.6 (PCH_2 25.1 (PCH_2CH_2),

24.5 ($PCH_2CH_2\mathit{C}H_2$), 18.9 ($OCH_2CH_2\mathit{C}H_2$), 13.6 ($PCH_2CH_2CH_2\mathit{C}H_3$), 13.5 ($OCH_2CH_2CH_2\mathit{C}H_3$), ^{31}P NMR (300MHz, $CDCl_3$): -16.49

2.4 References

1. Mohamed, A. A.; Kani, I.; Ramirez, A. O.; Fackler, J. P., Jr., *Inorg. Chem.* **2004,** *43* (13), 3833.
2. Beattie, M. J. V.; Poling, G. W., *Trans. - Inst. Min. Metall., Sect. C* **1988,** *97*, C15.
3. Rao, R. S., *Xanthate and Related Compounds*. Dekker: New York, 1971.
4. Ren, T.-H.; Xue, Q.-J.; Wang, H.-Q., *Lubr. Eng.* **1995,** *51*, 847.
5. Garje, S. S.; Jain, V. K., *Coord. Chem. Rev.* **2003,** *236* (1–2), 35.
6. Twiss, D. F.; Thomas, F., *J. Soc. Chem. Ind., London* **1923,** *42*, 499.
7. Barreca, D.; Tondello, E.; Lydon, D.; Spalding, T. R.; Fabrizo, M., *Chem. Vapor Depos.* **2003,** *9*, 93.
8. Alam, N.; Hill, M. S.; Kociok-Kohn, G.; Zeller, M.; Mazhar, M.; Molloy, K. C., *Chem. Mater.* **2008,** *20* (19), 6157.
9. Afzaal, M.; Rosenberg, C. L.; Malik, M. A.; White, A. J. P.; O'Brien, P., *New Journal of Chemistry* **2011,** *35* (12), 2773.
10. Ikeda, T.; Hagihara, H., *Acta Crystallogr.* **1966,** *21*, 919.
11. Ito, T., *Acta Crystallogr.* **1972,** *B28*, 1697.
12. (a) Raston, C.; White, A.; Winter, G., *Aust. J. Chem.* **1976,** *29* (4), 731; (b) Cusack, J.; Drew, M. G. B.; Spalding, T. R., *Polyhedron* **2004,** *23* (14), 2315; (c) Glinskaya, L.; Klevtsova, R.; Leonova, T.; Larionov, S., *J. Struct. Chem.* **2000,** *41* (1), 161.
13. (a) Barreca, D.; Tondello, E.; Lydon, D.; Spalding, T. R.; Fabrizio, M., *Chem. Vapor Depos.* **2003,** *9* (2), 93; (b) Cheon, J.; Talaga, D. S.; Zink, J. I., *J. Am. Chem. Soc.* **1997,** *119* (1), 163.
14. Ewings, P. F. R.; Harrison, P. G.; King, T. J., *J. Chem. Soc., Dalton Trans.* **1976**, 1399.
15. Raston, C. L.; Tennant, P. R.; White, A. H.; Winter, G., *Aust. J. Chem.* **1978,** *31* (7), 1493.
16. Han, Q.; Wang, M.; Zhu, J.; Wu, X.; Lu, L.; Wang, X., *J. Alloys Compd.* **2011,** *509* (5), 2180.

17. (a) Snow, M.; Tiekink, E., *Aust. J. Chem.* **1987,** *40* (4), 743; (b) Cox, M. J.; Tiekink, E. R. T., *Z. Kristallogr.* **1998,** *213*, 487.
18. (a) Hoskins, B. F.; Tiekink, E. R. T.; Winter, G., *Inorg. Chim. Acta* **1985,** *97* (2), 217; (b) Hoskins, B. F.; Tiekink, E. R. T.; Winter, G., *Inorg. Chim. Acta* **1985,** *99* (2), 177.
19. Khwaja, M. A.; Cardwell, T. J.; Magee, R. J., *Anal. Chim. Acta* **1973,** *64* (1), 9.
20. Castro, J. R.; Molloy, K. C.; Liu, Y.; Lai, C. S.; Dong, Z.; White, T. J.; Tiekink, E. R. T., *J. Mater. Chem.* **2008,** *18*, 5399.
21. (a) Tang, K.; Jin, X.; Long, Y.; Cui, P.; Tang, Y., *J. Chem. Res., Synop.* **2000**, 452; (b) Wycliff, C.; Bharathi, D. S.; Samuelson, A. G.; Nethaji, M., *Polyhedron* **1999,** *18* (7), 949.
22. Bianchini, C.; Ghilardi, C. A.; Meli, A.; Midollini, S.; Orlandini, A., *Inorg. Chem.* **1985,** *24*, 932.
23. (a) Woods, R.; Hope, G. A., *Colloids Surf., A* **1998,** *137*, 319; (b) Yordanov, N. D.; Dimitrova, A., *Spectrochim. Acta, Part A* **2006,** *63A*, 826; (c) Yordanov, N. D.; Gancheva, V.; Mladenova, B.; Grampp, G., *Inorg. Chem. Commun.* **2003,** *6*, 54; (d) Murty, R. N.; Dash, R. N.; Rao, D. V. R., *J. Indian Chem. Soc.* **1984,** *61*, 943; (e) Zdravkova, M.; Yordanov, N. D.; Gochev, G., *Polyhedron* **1993,** *12*, 2645; (f) Ivanov, A. V.; Bredyuk, O. A.; Antzutkin, O. N.; Forsling, W., *Russ. J. Coord. Chem.* **2004,** *30*, 480.
24. Liu, Y. S.; Qin, D. H.; Wang, L.; Cao, Y., *Mater. Chem. Phys.* **2007,** *102* (2-3), 201.
25. Fawcett, J.; Hope, E. G.; Stuart, A. M.; Wood, D. R. W., *J. Fluorine Chem.* **2005,** *126*, 1117.
26. Ewings, P. F. R.; Harrison, P. G.; King, T. J., *J. Chem. Soc. Dalton Trans.* **1976**, 1399.
27. Parkin, I. P.; Price, L. S.; Hibbert, T. G.; Molloy, K. C., *J. Mater. Chem.* **2001,** *11* (5), 1486.
28. Reichle, W. T., *Inorg. Chim. Acta* **1971**, 325.
29. Cariati, F.; Ganadu, M. L., *Gazzetta Chimica Italiana* **1979,** *109*, 181.
30. Cava, R. J.; Reidinger, F.; Wuensch, B. J., *Solid State Ionics* **1981,** *5*, 501.

Chapter Three
Dithiocarbamates

3.1 Introduction

This chapter describes attempts to synthesise a range of asymmetric zinc, tin, antimony and copper dithiocarbamates and to test their decomposition properties. Due to the difficulties in the previous chapter to lower the decomposition temperature of the copper xanthates, it was decided to synthesise a range of dithiocarbamates, which generally have higher decomposition temperatures than xanthates. This approach would potentially raise the decomposition temperature of the tin, zinc and antimony precursors rather than lower the decomposition temperature of the copper precursors. The zinc and tin or antimony dithiocarbamates could then be mixed with the copper xanthates in CVD experiments. Copper dithiocarbamates have also been synthesised to investigate the best match in decomposition temperatures. The volatilities and solubilities have also been investigated to determine the most appropriate type of CVD to be used.

Dithiocarbamates are currently widely used as fungicides,[1] pesticides,[2] high pressure lubricants[3] and as accelerants in vulcanisation.[4] They have the ability to bond in either a monodentate or bidentate way (Figure 3.1). They are generally more thermally stable than xanthates and tend to decompose at higher temperatures than their corresponding xanthate, for example $Sn(S_2COEt)_2$ decomposes at 158-186°C and $Sn(S_2CNEt_2)_2$ decomposes at 210-360°C.[5] They do however have an advantage over xanthates as the two organic substituents can be changed independently of each other, so the properties of the dithiocarbamates are more tuneable, for example asymmetric dithiocarbamates can be more volatile and more soluble.

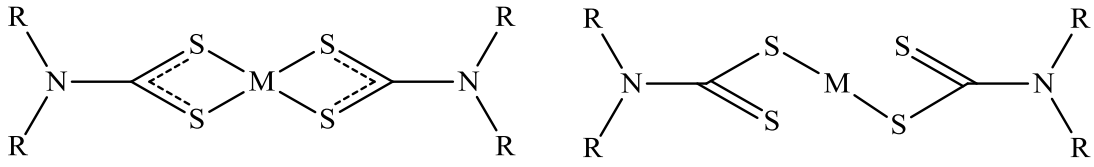

Figure 3.1 Bidentate and monodentate coordination of dithiocarbamate ligands

3.1.1 Zinc Dithiocarbamates

The structural chemistry of zinc dithiocarbamates has been well studied. Structurally, most zinc dithiocarbamates form dimers with one bridging ligand per zinc centre.[6] Examples of dimers include symmetrical dithiocarbamates

$Zn(S_2CNR_2)_2$ (R=Me,[7] Et[8]) and also asymmetric dithiocarbamates $Zn[S_2CN(Me)R]_2$ (R=Et, ^{n}Pr, ^{i}Pr, ^{n}Bu) (Figure 3.2.).[9] An increase in substituent size enables the formation of monomers in $Zn(S_2CNR_2)_2$, (R=Cy,[10] Bn[11]). $Zn(S_2CN^{i}Bu)_2$ is unusual in its structure with one monomeric molecule and one dimeric molecule in the unit cell.[12]

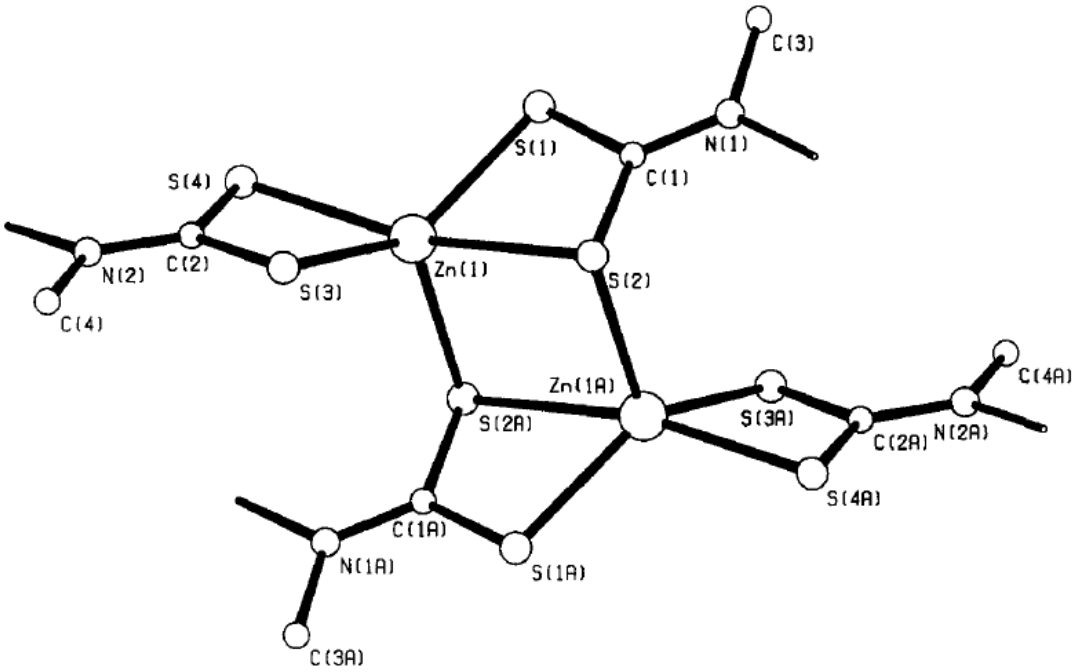

Figure 3.2 General structure of $Zn(S_2CNMeR)_2$, R=Et, ^{n}Pr, ^{i}Pr, ^{n}Bu[9]

Much work has been done on the deposition of ZnS from dithiocarbamate precursors. Initially, $Zn(S_2CNEt_2)_2$ was widely used as a single-source precursor, although the volatility is fairly low and LPCVD was used to deposit films of ZnS,[13] AACVD has also been used to deposit ZnS films from $Zn(S_2CNEt_2)_2$.[14] The use of asymmetric substituents increases the volatility[9] and crystalline films of ZnS have been deposited from $Zn(S_2CN(Me)Bu)_2$.. Nanoparticles of ZnS have been formed from thermolysis of $Zn(S_2CNHC_6H_{13})_2$ at 300°C.[15]

3.1.2 Tin Dithiocarbamates

One of the first reports of tin dithiocarbamates was in the preparation of $Sn(S_2CNR_2)_2$ (R=Me, Et) from ammonium dithiocarbamate salts.[16] Since then many tin dithiocarbamates have been prepared, with the majority being organotin(IV)

complexes. Despite this, there are still many reports of both Sn(II) and Sn(IV) binary dithiocarbamates. Structurally, they are very similar to xanthates, with bidentate coordination seen in $Sn(S_2CNEt_2)_2$,[17] as is seen in $Sn(S_2COEt)_2$. Also a distorted octahedral coordination, with two bidentate and two monodentate ligands is seen in $Sn(S_2CNMe_2)_4$,[18] much the same as in $Sn(S_2COEt)_4$.[19] $Sn(S_2CN(CH_2)_4)_4$ has an unusual structure where all sulphur atoms are bonded to the tin centre, with two dithiocarbamate groups isobidentate and two anisobidentate, giving a dodecahedral arrangement (Figure 3.3).[20]

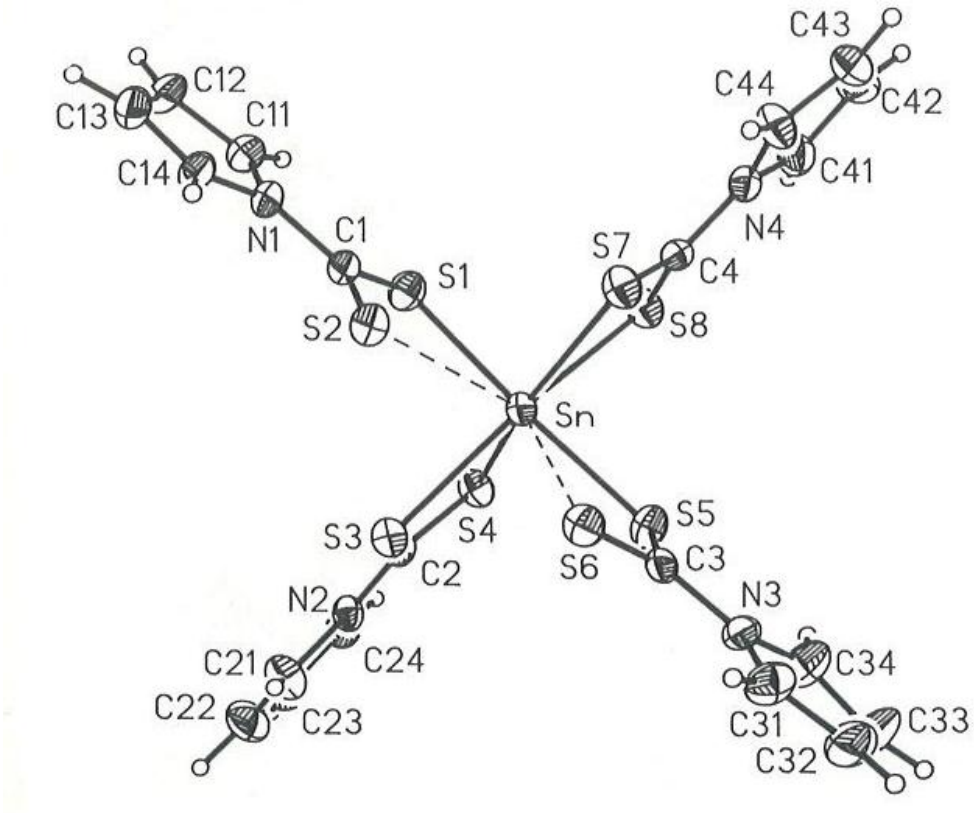

Figure 3.3 Structure of $Sn(S_2CN(CH_2)_4)_4$[20]

The deposition of tin sulphide films from dithiocarbamate precursors has not been widely studied, although the decomposition of tin dithiocarbamate species has been investigated since 1975 with the thermal decomposition study of $Sn(S_2CNEt_2)_2$.[16] Deposition of SnS has been achieved with the heteroleptic precurors $Me_3Sn(S_2CN(CH_3)C_4H_9)$ and $^nBuSn[S_2CN(CH_3)C_4H_9]_3$, although this required a small amount of H_2S as an additional sulphur source. Films of SnS have also been deposited using single source precursors $Sn(SR)_2(S_2CNEt_2)_2$ (R = Cy , CH_2CF_3). The growth of SnS nanoparticles has been reported from organotin(IV) precursors $Ph_2Sn(S_2CNEt_2)_2$, $Ph_3Sn(S_2CNEt_2)$, Ph $Sn(S_2CNEt_2)_3$ and $Bu_2Sn(S_2CNC_4H_8)_2$.[21]

3.1.3 Antimony (III) Dithiocarbamates

Structurally all the binary antimony dithiocarbamates are very similar, with three long Sb-S bonds and three shorter Sb-S bonds with a stereochemically active lone pair.[22] They can exist as a monomeric species in a distorted trigonal prismatic arrangement, as seen in $Sb[S_2CN(CH_2CH_2OH)_2]_3$[23] or one sulphur atom from a molecule can interact with the antimony atom in another molecule, creating a dimer, as seen in $Sb[S_2CN(Me)Bu]_3$ (Figure 3.4).[24]

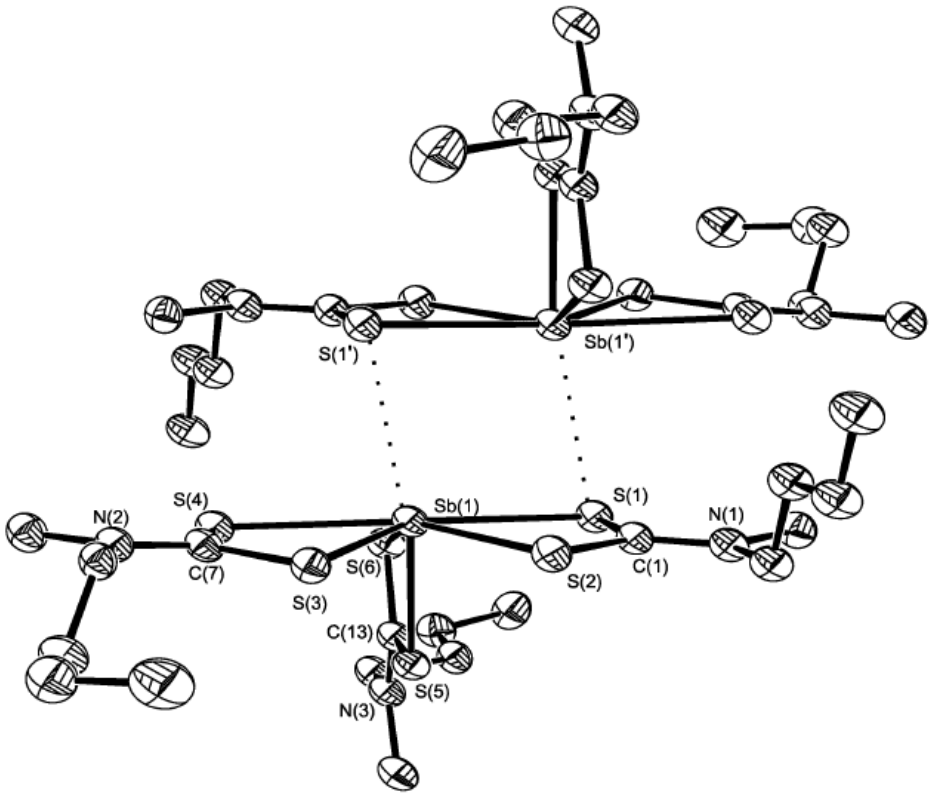

Figure 3.4 Structure of $Sb[S_2CN(Me)^nBu]_3$[24]

The deposition of Sb_2S_3 from antimony dithiocarbamates has only been studied very recently, with very few reports in literature. The first report of Sb_2S_3 films deposited from dithiocarbamate precursors is in use of $Sb[S_2CN(Me)R]_3$, R = Bu, Hex, Bz in AACVD experiments.[24] A later report with a comparison between xanthate, thiolate and dithiocarbamate precursors found that xanthates gave the best results due to their low decomposition temperatures.[25] The dithiocarbamate precursors also tended to incorporate oxygen into their films much more readily; this could be due to the higher temperatures needed to decompose the dithiocarbamate precursors and the ready oxidation of Sb_2S_3 to Sb_2O_3 at elevated temperatures.[26]

3.1.4 Copper Dithiocarbamates

Many Cu(II) dithiocarbamates have been synthesised and structurally characterised; all structures exhibit distorted square planar geometry about the Cu atom.[6] Structurally Cu(II) dithiocarbamates can be monomeric, as seen in $Cu[S_2CN(Me)Ph]_2$[27] although they are much more likely to form an interaction between the Cu centre and one S atom of another complex to form a dimer, as seen in $Cu(S_2CNEt_2)_2$.[28] Very little work has been done on binary Cu(I) dithiocarbamate complexes as they tend to be unstable,[6] however, the addition of a phopshine donor stabilises the complex, leading to monomeric structures, as seen in $(Ph_3P)_2CuS_2CN(Me)Bn$ (Figure 3.5).[29]

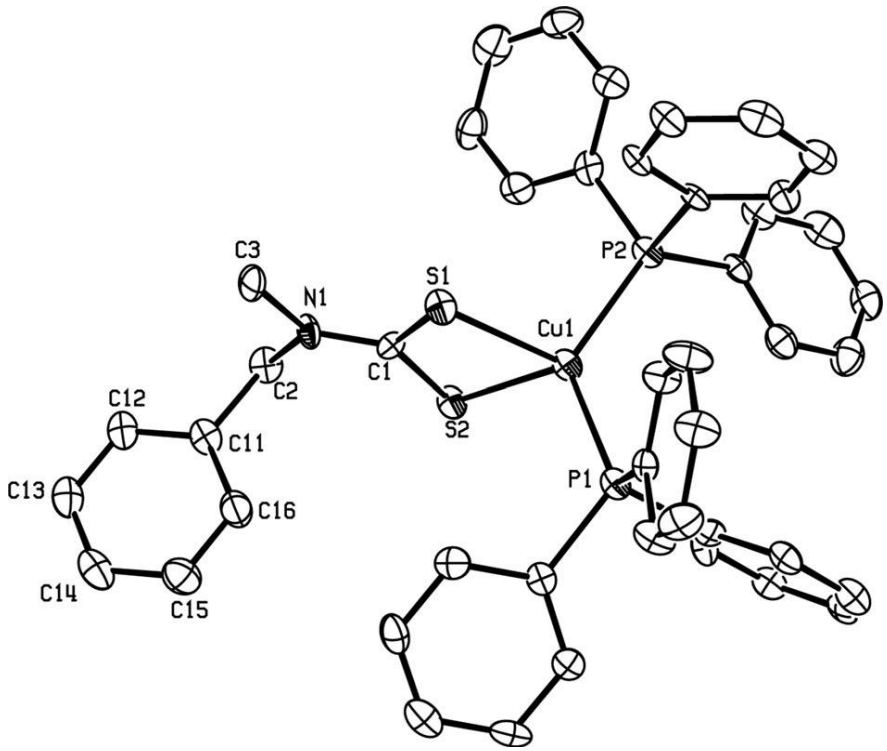

Figure 3.5 Structure of $(Ph_3P)_2CuS2CN(Me)Bn$[29]

Although there have been no reports of deposition using Cu(I) dithiocarbamates, films of CuS have been grown from $Cu(S_2CNEt_2)_2$ under LPCVD conditions.[30]

3.2 Results and Discussion

3.2.1 Zinc Dithiocarbamates

Lithium dithiocarbamates were made following a literature method, in which BuLi was added to a solution of HN(Me)Bu or HN(Me)Bn in hexane. This solution was stirred for one hour after which CS_2 was added and stirring continued for 12 hours. Precipitates were filtered and dried *in vacuo* and characterised by NMR. $Zn[S_2CN(Me)Bu]_2$ **(17)** and $Zn[S_2CN(Me)Bn]_2$ **(18)** were prepared following a literature method;[9] a solution of $LiS_2CN(Me)Bu$ or $LiS_2CN(Me)Bn$ in water was added to a stirred solution of $Zn(NO_3)_2$; the precipitate was filtered and dried *in vacuo*, and products were characterised by elemental analysis and NMR.

Materials Analysis

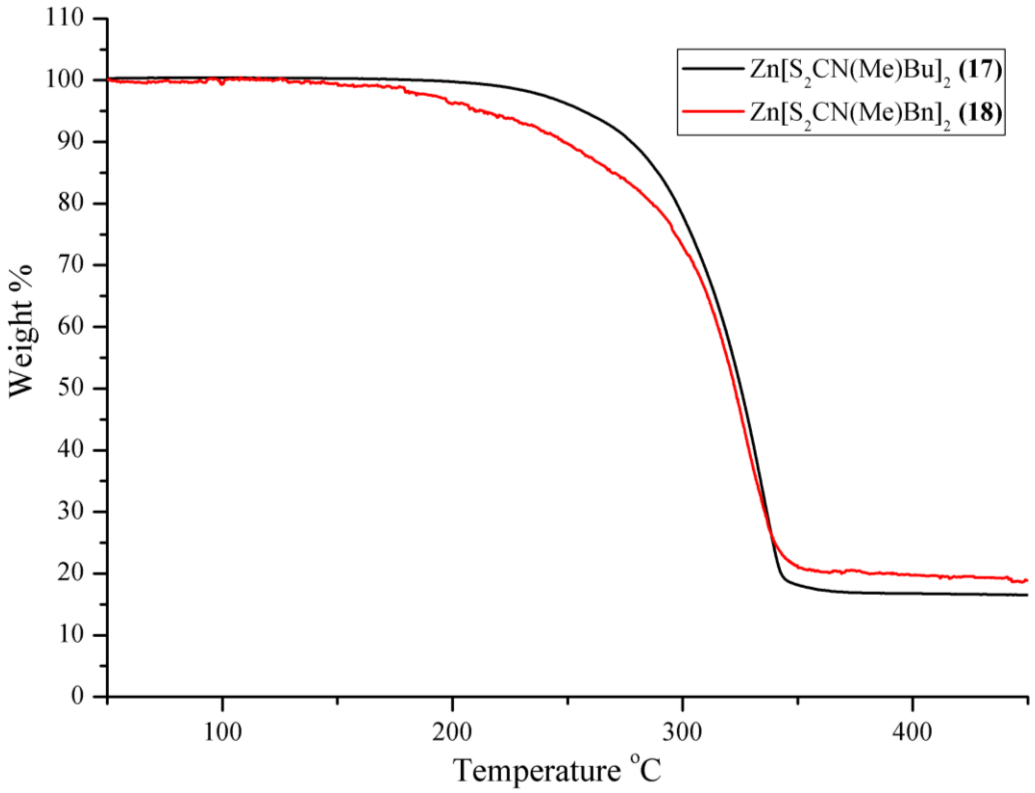

Figure 3.6 TGAs of **(17)** and **(18)** with a heating rate of 5°C/min

Both **(17)** and **(18)** decompose cleanly to ZnS with very similar decomposition profiles (Figure 3.6). **(17)** shows slow decomposition from 208°C to 358°C, with a

16.9% residual weight remaining. This is lower than that expected for ZnS (24.7%), indicating some volatility in the precursor. Similarly, **(18)** shows slow decomposition from 173°C to 362°C, with a final weight % of 20.2%, which is only slightly lower than that expected for ZnS (21.0%).

3.2.2 Tin Dithiocarbamates

$Sn[S_2CN(Me)Bu]_2$ **(19)** and $Sn[S_2CN(Me)Bn]_2$ **(20)** were prepared following a literature method,[31] in which a solution of $LiS_2CN(Me)Bu$ or $LiS_2CN(Me)Bn$ in water was added to a stirred slurry of $SnCl_2$ in water; the products were filtered and dried *in vacuo* and characterised by elemental analysis and NMR.

Structural Analysis

Crystals of $\{Sn[S_2CN(Me)Bn]S\}_2$ **(21)** were obtained when a solution of **(20)** in $CHCl_3$ was left to stand for a period of 3 months. **(21)** is a decomposition product of **(20)**, where **(20)** has partially decomposed and the residual sulphur containing products have oxidised **(20)** with the addition of sulphur to form an Sn(IV) dimer (Figure 3.7).

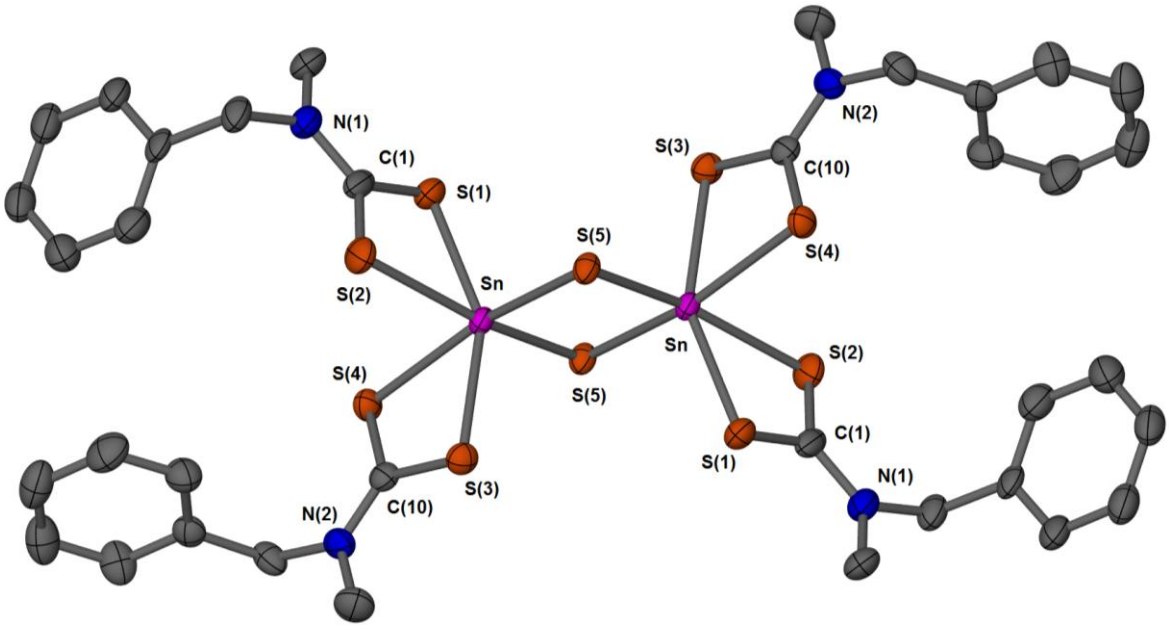

Figure 3.7 Structure of **(21)**, thermal ellipsoids drawn at 50% probability

There have been two similar structures reported in literature, $[Sn(S_2CNEt_2)_2S]_2$[32] and $[Sn(S_2CN4\text{-}Me\text{-}Pip)_2S]_2$[33] which were both formed from the decomposition of $Sn(S_2CNEt_2)_4$ or $Sn(S_2CN4\text{-}Me\text{-}Pip)_4$ in CH_2Cl_2 or $CHCl_3$; while

$Sn(S_2CNEt_2)_4$ was found to decompose at room temperature, $Sn(S_2CN4\text{-}Me\text{-}Pip)_4$ required refluxing in CH_2Cl_2 for a prolonged period of time. For comparison selected bond distances of **(21)** and $[Sn(S_2CNEt_2)_2S]_2$ are shown in Table 1.

The structure of **(21)** shows two dithiocarbamate ligands attached to each tin centre. The tin(II) dithiocarbamate appears to have oxidised to a tin(IV) species, picking up a sulphur atom, possibly from another, already decomposed tin(II) dithiocarbamate, this sulphur atom forms a bridge between two tin centres, forming a dimer. The Sn-S distances are all very similar, although one ligand shows more isobidentate coordination character than the other, with Sn-S(3) and Sn-S(4) being much closer to each other in value than Sn-S(1) and Sn-S(2) are. The same can be said of $[Sn(S_2CNEt_2)_2S]_2$, although this is seen to a lesser extent in this structure.

Table 3.1 Selected bond distances (Å) of **(21)** and $[Sn(S_2CNEt_2)S]_2$[32]

	$\{Sn[S_2CN(Me)Bn]_2S\}_2$ (21)	**$[Sn(S_2CNEt_2)_2S]_2$[32]**
Sn-S(1)	2.5415(11)	2.5276(5)
Sn-S(2)	2.6329(10)	2.5986(5)
Sn-S(3)	2.5742(11)	2.6075(5)
Sn-S(4)	2.5918(10)	2.5772(5)
Sn-S(5)	2.4573(10)	2.4454(5)
Sn-S(5)'	2.4376(10)	2.4550(5)
S(1)-C(1)	1.720(5)	1.732(2)
S(2)-C(1)	1.729(5)	1.730(2)
S(3)-C(10)	1.731(4)	1.7234(19)
S(4)-C(10)	1.723(4)	1.7365(19)

Materials Analysis

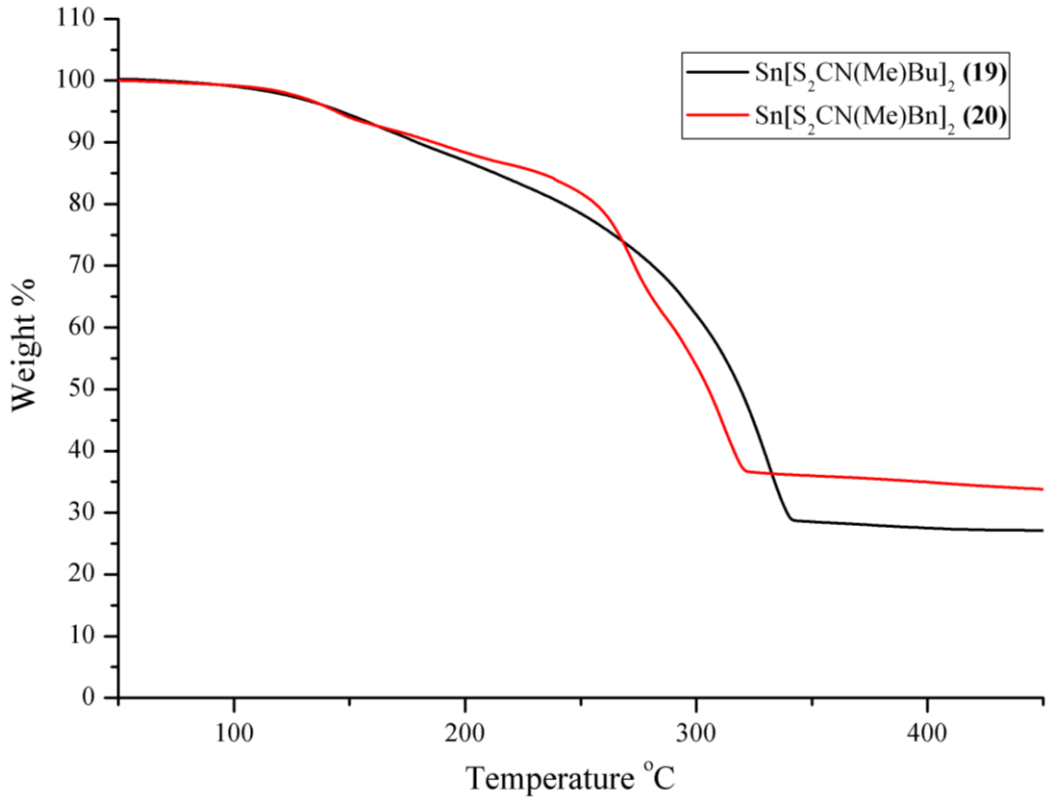

Figure 3.8 TGAs of **(19)** and **(20)** with a heating rate of 5°C/min

TGA of **(19)** shows some volatility while **(20)** shows decomposition to SnS_2 (Figure 3.8). **(19)** shows a gradual weight loss from 91°C, which becomes sharper at 284°C, leaving a residual weight of 71.9%. Decomposition ends at 343°C, leaving a final weight % of 28.7%, which is lower than the predicted values for both SnS (34.2%) and SnS_2 (41.3%), indicating some volatility in the precursor.

Decomposition of **(20)** is very complicated, with many steps seen. Initial decomposition starts at 105°C, with a slight change in rate at 152°C. The rate of decomposition increases at 244°C with a slight change in rate at 279°C. Decomposition finishes at 322°C, leaving a residual weight of 36.7%, comparable to the predicted value for SnS_2 (35.9%).

3.2.3 Antimony Dithiocarbamates

$Sb[S_2CN(Me)Bu]_3$ **(22)** and $Sb[S_2CN(Me)Bn]_3$ **(23)** were prepared following a literature method,[24] $LiS_2CN(Me)Bu$ or $LiS_2CN(Me)Bn$ in MeOH were added to a stirred solution of $SbCl_3$, the precipitate recrystalised from CH_2Cl_3 and characterised by microanalysis and NMR.

Materials Analysis

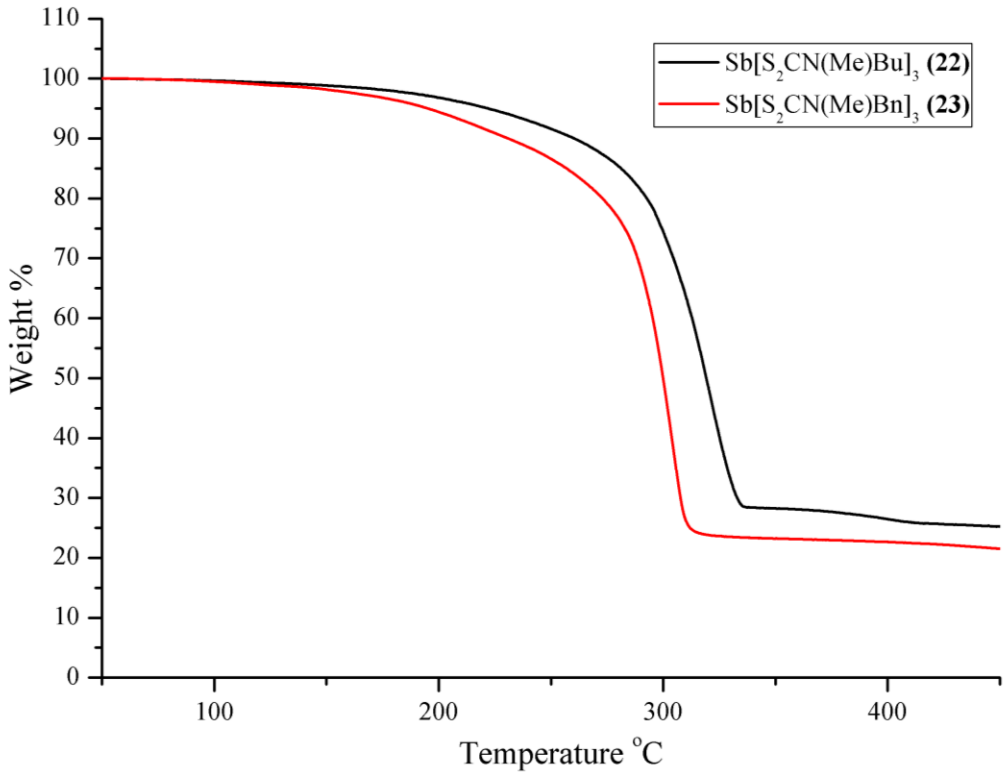

Figure 3.9 TGAs of **(22)** and **(23)** with a heating rate of 5°C/min

TGA of **(22)** and **(23)** shows the both have only one clear step in their decomposition pathways (Figure 3.9). TGA of **(22)** shows onset of decomposition at 165°C, ending at 338°C, leaving a residual weight of 28.4%, which is comparable to that expected for $½Sb_2S_3$ (27.9%). A very similar decomposition profile is seen with **(23)**, where decomposition starts at 150°C and ends at 319°C, leaving a 23.9% residue; this is slightly higher than that expected for $½Sb_2S_3$ (19.4%) indicating incomplete decomposition.

3.2.4 Copper Dithiocarbamates

$(Ph_3P)_2CuS_2CN(Me)Bu$ **(24)** and $(Ph_3P)_2CuS_2CN(Me)Bn$ **(25)** were prepared in a one pot reaction between CuCl, Ph_3P and $LiS_2CN(Me)Bu$ or $LiS_2CN(Me)Bn$ in $CHCl_3$. The products were crystallised with the addition of Et_2O and cooling to -20°C and were characterised by microanalysis and NMR.

Structural Analysis

Addition of Et_2O to a solution of **(24)** or **(25)** in $CHCl_3$ and cooling to -20°C gave crystals of **(24)** and **(25)** (Figure 3.10). The structure of **(25)** has already been reported.[29]

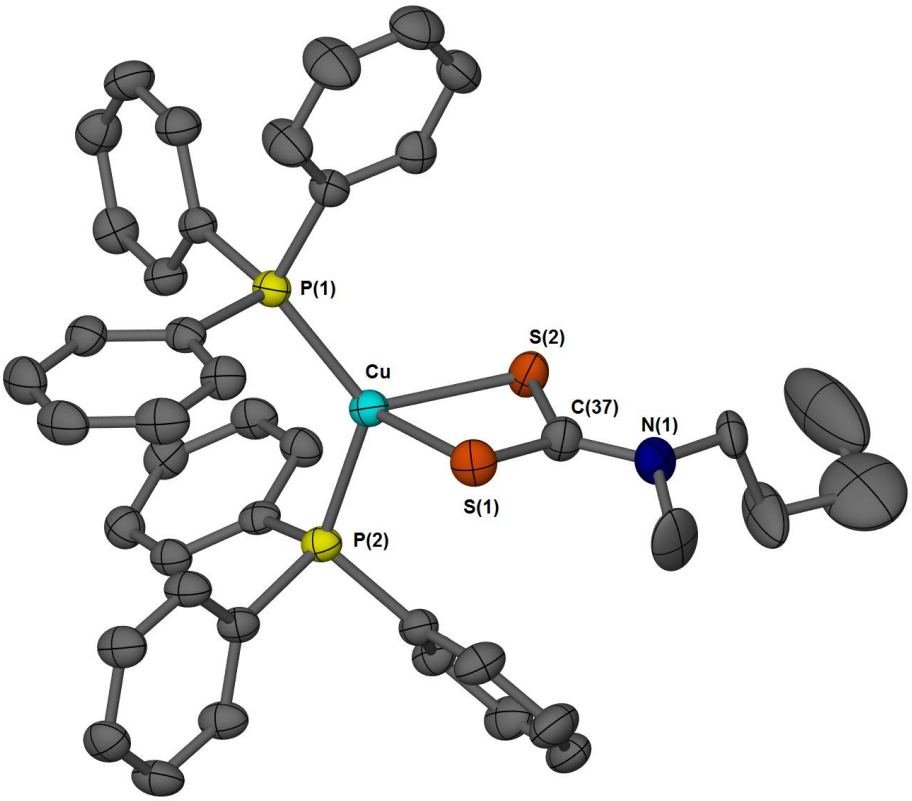

Figure 3.10 Structure of **(24)**, thermal ellipsoids drawn at 50% probability

Selected bond distances and angles of **(24)** and **(25)** are surmised in Table 3.2. In both cases there are two Ph_3P groups bonded to the central Cu atom. Due to the presence of these bulky donating ligands, both **(24)** and **(25)** are monomeric in structure. Both dithiocarbamate groups show isobidentate coordination, and in both cases the Cu-S(1) and Cu-S(2) bond lengths are essentially the same. The S-C bond lengths are also very similar.

Table 3.2 Selected bond distances (Å) and angles (°) of **(24)** and **(25)**[29]

	(24)	**(25)**[29]
Cu-S(1)	2.3922(8)	2.402(14)
Cu-S(2)	2.3926(8)	2.398(12)
S(1)-C(37)	1.716(3)	1.708(4)
S(2)-C(37)	1.716(3)	1.729(5)
Cu-P(1)	2.2361(8)	2.2378(14)
Cu-P(2)	2.2657(8)	2.2603(13)
P(1)-Cu-P(2)	125.91(3)	124.88(5)
S(1)-Cu-S(2)	75.66(3)	75.29(4)

Materials Analysis

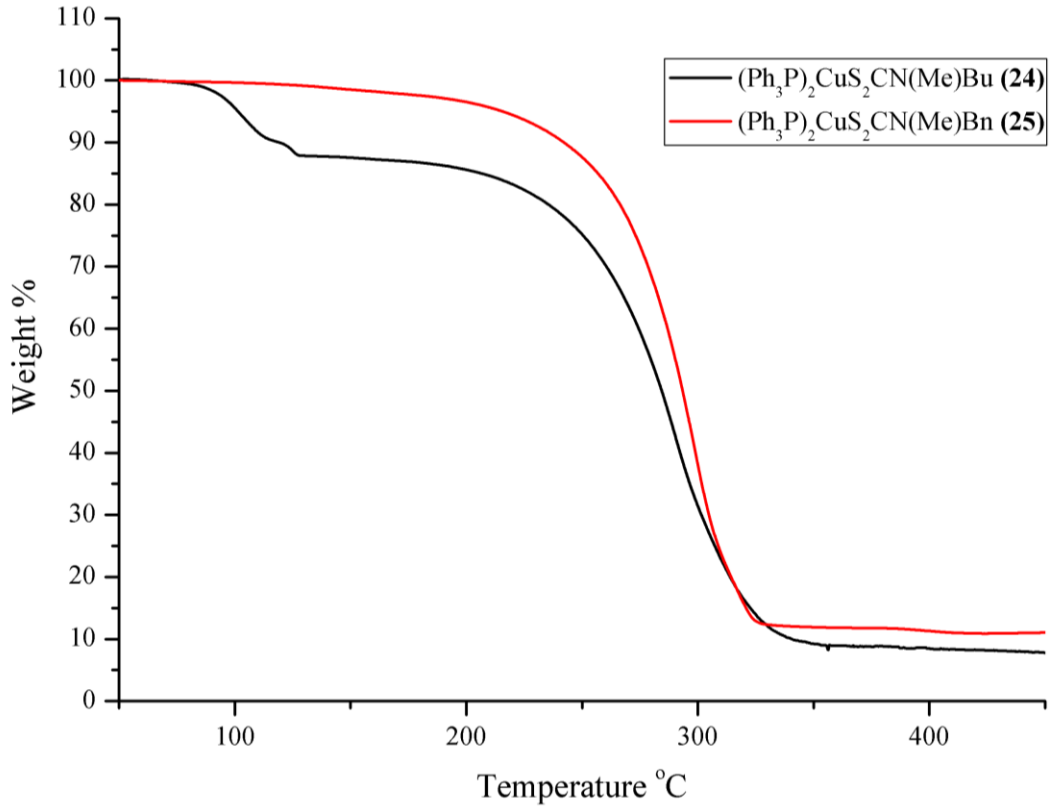

Figure 11. TGAs of **(24)** and **(25)** with a heating rate of 5°C/min

There are three steps seen in the decomposition of **(24)** (Figure 11). Decomposition starts at 79°C going down to 90.5% at 115°C, where a second, very small, step is seen, ending at 129°C (87.9%). Both of these percentages are higher than expected if initial decomposition of the dithiocarbamate has taken place leaving $(Ph_3P)_2CuS$ (82.6%) or ½$(Ph_3P)_4Cu_2S$ (80.5%), as is seen in the triphenylphosphine

adducts of copper xanthates. The third step is much larger, ending at 352°C with a residual weight remaining of 9.2%, which is comparable to that expected for ½Cu_2S (10.5%) and much lower than that expected for CuS (12.7%).

The decomposition profile of **(25)** is much simpler, with only one step seen from 197°C to 326°C, leaving a residual weight of 10.9% which is comparable to that expected for ½Cu_2S (10.1%) and slightly lower than that expected for CuS (12.5%).

3.2.5 Conclusions

Although the onset of decomposition in the dithiocarbamate precursors differs over a range of 79°C - 208°C, the TGAs of all precursors show similar end points in the decomposition profiles, over a much smaller range of 319°C - 362°C (Table 3.3).

A comparison of all TGAs from Chapter 2 and 3 shows that in general the decomposition temperatures of the xanthates are much lower than the dithiocarbamates (Table 3.3). However, although the zinc and antimony xanthates have much lower onsets of decomposition, they all show a second slower final decomposition, which is not seen in any dithiocarbamates tested. This second slower decomposition step means that although the main bulk of the decomposition is much lower in temperature in the xanthates tested, in the case of the zinc xanthates the second step brings the end point of decomposition to a similar temperature as is seen in the dithiocarbamates. The copper xanthates have end points of decomposition over a range of 208-284°C, *ca*. 80°C lower than any of the dithiocarbamates.

With respect to choosing a mixture of precursors for the deposition of Cu_2ZnSnS_4 there are various different considerations to be taken into account. The best matches would ideally have similar onsets of decomposition and similar end points. The precursors with the best match in both onset of decomposition and end point of decomposition are **(4)** or **(5)** for zinc, **(20)** for tin and **(14)** for copper (highlighted in red). However due to potentially different decomposition rates due to the difference between xanthates and dithiocarbamates it was decided that a mixture of only xanthates or only dithiocarbamates would be advantageous.

Some of the xanthates tested showed an initial sharp decomposition with a much slower final step. As the xanthates have almost fully decomposed after this initial step it was decided that this could be considered as the final step and any residual contamination could be removed by the addition of an annealing step in the

film production. Considering the initial decomposition and the onset of decomposition, the xanthate precursors that show the best match are **(1)** or **(4)** for zinc, **(7)** for tin and **(15)** or **(16)** for copper (highlighted in blue). Due to the lack of solubility of **(1)**, this precursor was discounted and it was decided to use **(4)**. **(16)** is much more stable over a long period of time than **(15)** so this was chosen as the copper precursor.

In terms of dithiocarbamate precursors all of the end points are fairly similar but the onset of decomposition varies a lot. Both **(17)** and **(18)** have very similar onset and end points of decomposition. However, the onset of decomposition is much higher in **(17)** and **(18)** than is seen in either of the tin dithiocarbamates synthesised. **(24)** has a similar onset and end point of decomposition to both **(19)** and **(20)**. Due to this is was decided to choose the closest match in onset and end points of decomposition of the tin and copper dithiocarbamates [**(19)** and **(24)**]. As both of the zinc precursors have very similar decomposition profiles it was decided to use the zinc precursor with the same ligand as **(19)** and **(24)** (highlighted in green). It was decided to also try and mixture of **(18), (20)** and **(25)** as a comparison.

With regards to deposition of $CuSbS_2$ a similar train of thought was employed. The decision was taken to use an all xanthate mixture and to match the initial decomposition value rather than the final end point in the antimony precursor. As **(9)** decomposed initially at a very low temperature the copper xanthates that were best matched were **(15)** and **(16)**. Due to the long term stability of **(16)**, this was the precursor chosen to mix with **(9)**.

The antimony dithiocarbamate precursors synthesised show very similar decomposition profiles. As a result of this it was decided to try a mixture of **(22)** and **(24)** and a mixture of **(23)** and **(25)** as a comparison.

Table 3.3 Comparison of decomposition temperatures and products of **(1)** – **(25)**

	Onset (°C)	Initial (°C)	End (°C)		Onset (°C)	End (°C)	
$Zn(S_2CO^nPr)_2$ **(3)**	50	170	341	$Zn[S_2CN(Me)Bn]_2$ **(18)**	173	362	ZnS
$Zn(S_2CO^nBu)_2$ **(4)**	110	177	343	$Zn[S_2CN(Me)Bu]_2$ **(17)**	208	358	ZnS
$Zn(S_2COEt)_2$.TMEDA **(6)**	125	153	328				
$Zn(S_2CO^nHex)_2$ **(5)**	127	170	341				
$Zn(S_2COEt)_2$ **(1)**	128	173	370				
$Zn(S_2CO^iPr)_2$ **(2)**	200	248	325				
$Sn(S_2COEt)_4$ **(8)**	73		139	$Sn[S_2CN(Me)Bu]_2$ **(19)**	91	343	SnS_2
$Sn(S_2COEt)_2$ **(7)**	158		186	$Sn[S_2CN(Me)Bn]_2$ **(20)**	105	322	SnS_2
$(Ph_3P)_2CuS_2CO^tAmyl$ **(13)**	82		268	$(Ph_3P)_2CuS_2CN(Me)Bu$ **(24)**	79	352	Cu_2S
$(^nBu_3P)_2CuS_2COEt$ **(15)**	110		208	$(Ph_3P)_2CuS_2CN(Me)Bn$ **(25)**	197	326	Cu_2S
$(^nBu_3P)_2CuS_2CO^nBu$ **(16)**	115		219				Cu_2S
$[(PhO)_3P]_2CuS_2COEt$ **(14)**	116		284				Cu_2S
$(Ph_3P)_2CuS_2CO^tBu$ **(12)**	118		258				Cu_2S
$(Ph_3P)_2CuS_2CO^iPr$ **(11)**	158		245				Cu_2S
$(Ph_3P)_2CuS_2COEt$ **(10)**	201		278				Cu_2S
$Sb(S_2COEt)_3$ **(9)**	93	144	262	$Sb[S_2CN(Me)Bn]_3$ **(23)**	150	319	Sb_2S_3
				$Sb[S_2CN(Me)Bu]_3$ **(22)**	165	338	Sb_2S_3

3.3 Experimental

Synthesis of $Zn[S_2CN(Me)Bu^n]_2$ ***(17)****:* A solution of $LiS_2CN(Me)Bu^n$ (1.14g, 6.74mmol) in water (30ml) was added to a stirred solution of $Zn(NO_3).6H_2O$ (1g, 3.36mmol) in water (20ml). A yellow precipitate formed and stirring was continued for one hour. The solution was filtered and washed with H_2O and the precipitate dried *in vacuo* (0.98g, 86%, mp 116-118°C). Analysis found (calc for $C_{12}H_{24}N_2S_4Zn$): C 36.8 (37.1), H 6.20 (6.23), N 7.24 (7.22). ^{1}H NMR (300MHz, $CDCl_3$) δ ppm: 3.82 (t, *J*=7.90 Hz, 4H, NCH_2), 3.39 (s, 6H, NCH_3), 1.70 (quin, *J*=7.63 Hz, 4H, NCH_2CH_2), 1.35 (sxt, *J*=7.35 Hz, 4H, CH_2CH_3), 0.93 (t, *J*=7.35 Hz, 6H, CH_2CH_3), ^{13}C NMR (300MHz, $CDCl_3$) δ ppm: 202.9 (CS_2), 60.0 (NCH_2), 42.2 (NCH_3), 28.8 (NCH_2CH_2), 19.7 (CH_2CH_3), 13.6 (CH_2CH_3)

Also prepared by the same method:

$Zn[S_2CN(Me)Bn]_2$ ***(18)****:* Using $LiS_2CN(Me)Bn$ (0.69g, 3.40mmol) and $Zn(NO_3).6H_2O$ (0.5g, 1.69mmol) Yielding a white precipitate (0.62g, 81%, mp 134-135°C). Analysis found (calc for $C_{18}H_{20}N_2S_4Zn$): C 47.3 (47.4), H 4.24 (4.42), N 5.97 (6.14). ^{1}H NMR (300MHz, $CDCl_3$) δ ppm: 7.29-7.46 (m, 10H, Ph), 5.14 (s, 4H, CH_2), 3.38 (s, 6H, CH_3), ^{13}C NMR (300MHz, $CDCl_3$) δ ppm: 205.0 (CS_2), 134.6 (Ph), 128.9 (Ph), 128.3 (Ph), 127.8 (Ph), 60.3 (CH_2), 41.6 (CH_3)

$Sn[S_2CN(Me)Bu^n]_2$ ***(19)****:* Using $LiS_2CN(Me)Bu^n$ (0.89g, 5.26mmol) and $SnCl_2$ (0.5g, 2.63mmol). Yielding a sticky dark orange solid (0.67g, 57%, mp 67-70°C). Analysis found (calc for $C_{12}H_{24}N_2S_4Sn$): C 32.4 (32.4), H 5.38 (5.43), N 6.19 (6.31). ^{1}H NMR (300 MHz, $CDCl_3$) δ ppm: 3.68 (t, *J*=8.10 Hz, 4H, NCH_2), 3.32 (s, 6H, NCH_3), 1.73 (quin, *J*=7.20 Hz, 4H, NCH_2CH_2), 1.37 (sxt, *J*=7.60 Hz, 4H, CH_2CH_3), 0.96 (t, *J*=7.30 Hz, 6H, CH_2CH_3), ^{13}C NMR (300 MHz, $CDCl_3$) δ ppm: 199.3 (CS_2), 59.7 (NCH_2), 42.2 (NCH_3), 29.3 (NCH_2CH_2), 20.5 (CH_2CH_3), 14.0 (CH_2CH_3) ^{119}Sn NMR (300 MHz, $CDCl_3$) δ ppm: 60.1

Sn[S₂CN(Me)Bn]2 ***(20)****:* Using LiS_2NMeBn (1.06g, 5.26mmol) and $SnCl_2$ (0.5g, 2.63mmol). Yielding a pale orange solid (0.71g, 53%, mp 136-138°C). Analysis

found (calc for $C_{18}H_{20}N_2S_4Sn$): C 42.1 (42.2), H 3.87 (3.94). ^{1}H NMR (300 MHz, $CDCl_3$) δ ppm: 7.29-7.52 (m, 10H, Ph), 5.11 (s, 4H, CH_2), 3.30 (s, 6H, CH_3), ^{13}C NMR (300 MHz, $CDCl_3$) δ ppm: 202.4 (CS_2), 134.8 (Ph), 128.7 (Ph), 128.1 (Ph), 127.8 (Ph), 57.72 (CH_2), 39.9 (CH_3), ^{119}Sn NMR (300 MHz, $CDCl_3$) δ ppm: 60.7

Synthesis of [Sn(S_2CN(Me)Bn)$_2$S]$_2$ ***(21):*** A solution of Sn(S_2NMeBn)$_2$ in $CHCl_3$ left for a period of 3 months formed a few crystals of [Sn(S_2NMeBn)$_2$S]$_2$. Analysis found (calc for $C_{18}H_{20}N_2S_5Sn$): C 39.9 (39.7), H 3.61 (3.71), N 4.90 (5.15). ^{1}H NMR (300 MHz, $CDCl_3$) δ ppm: 7.31-7.37 (m, 10H, Ph), 5.10 (s, 4H, CH_2), 3.32 (s, 6H, CH_3), ^{13}C NMR (300 MHz, $CDCl_3$) δ ppm: 218.2 (CS_2), 133.9 (Ph), 127.9 (Ph), 127.1 (Ph), 126.9 (Ph), 61.2 (CH_2), 41.8 (CH_3), ^{119}Sn NMR (300 MHz, $CDCl_3$) δ ppm: 246.0

Synthesis of Sb[S_2CN(Me)Bu^n]$_3$ ***(22):*** $SbCl_3$ (0.49g, 2.15mmol) was stirred in MeOH (5ml), LiS2CN(Me)Bu^n (1.08g, 6.4mmol) in MeOH (10ml) was added dropwise. The solution was and stirred overnight, forming a yellow precipitate. The solvent was removed *in vacuo* and 10ml CH_2Cl_2 was added. The soluble material was separated by canula filtration and the solvent removed in vacuo, leaving a yellow solid (0.85g, 65%, mp 99-101°C). Analysis found (calc for $C_{18}H_{36}N_3S_6Sb$): C 35.5 (35.6), H 5.89 (5.98), N 6.81 (6.92). ^{1}H NMR (300 MHz, $CDCl_3$) δ ppm: 3.85 (t, *J*=7.50 Hz, 6H, NCH_2), 3.40 (s, 9H, NCH_3), 1.70 (quin, *J*=8.00 Hz, 6H, NCH_2CH_2), 1.36 (sxt, *J*=7.50 Hz, 6H, CH_2CH_3), 0.95 (t, *J*=7.50 Hz, 9H, CH_2CH_3), ^{13}C NMR (300 MHz, $CDCl_3$) δ ppm: 200.0 (CS_2), 56.2 (NCH_2), 41.7 (NCH_3), 29.0 (NCH_2CH_2), 20.0 (CH_2CH_3), 13.8 (CH_2CH_3)

Also prepared by the same method:

Sb[S_2CN(Me)Bn]$_3$ ***(23):*** Using $SbCl_3$ (0.60g, 2.65mmol) and LiS_2CN(Me)Bn (1.6g, 7.9mmol). Yielding a yellow solid (1.68g, 89%, mp 58-60°C). Analysis found (calc for $C_{27}H_{30}N_3S_6Sb$): C 45.6 (45.7), H 4.15 (4.26), N 5.80 (5.93). ^{1}H NMR (300 MHz, $CDCl_3$) δ ppm: 7.30-7.42 (m, 15H, Ph), 5.13 (s, 6H, CH_2), 3.34 (s, 9H, CH_3) ^{13}C NMR (300 MHz, $CDCl_3$) δ ppm: 200.7 (CS_2), 134.5 (Ph), 128.9 (Ph), 128.2 (Ph), 127.9 (Ph), 59.3 (CH_2), 40.9 (CH_3)

Synthesis of $(PPh_3)_2CuS_2CN(Me)Bn$ ***(24)****:* A solution of $LiS_2CN(Me)Bu$ (0.57g, 3.37mmol) in chloroform (25ml) was added to a stirred suspension of CuCl (0.33g, 3.37mmol) and Ph_3P (1.77g, 6.75mmol) in chloroform (25ml). A brown solution formed with a white precipitate (KCl). The solution was filtered and diethyl ether (50ml) added to aid crystallisation. Cooling in the freezer to -20°C gave off white crystals (1.32g, 52%, mp 155-158°C). Analysis found (calc for $C_{42}H_{42}NP_2S_2Cu$): C 67.4 (67.3), H 5.53 (5.65), N 1.91 (1.87). ^{1}H NMR (300MHz, $CDCl_3$) δ ppm: 7.15-7.44 (m, 30H, Ph), 3.87 (t, *J*=7.54 Hz, 2H, NCH_2), 3.35 (s, 3H, NCH_3), 1.62 (quin, *J*=7.30 Hz, 2H, NCH_2CH_2), 1.33 (sxt, *J*=7.50 Hz, 2H, CH_2CH_3) 0.95 (t, *J*=7.20 Hz, 3H, CH_2CH_3) ^{13}C NMR (300MHz, $CDCl_3$) δ ppm: 207.9 (CS_2), 134.2 (d, *J*=25.4 Hz, Ph), 133.8 (d, *J*=14.9 Hz, Ph), 129.2 (s, Ph), 128.2 (d, *J*=8.1 Hz, Ph), 54.6 (NCH_2), 40.5 (NCH_3), 29.1 (NCH_2CH_2), 20.0 (CH_2CH_3), 14.0 (CH_2CH_3), ^{31}P NMR (300MHz, $CDCl_3$) δ ppm: -1.51

Also prepared by the same method:

Synthesis of $(PPh_3)_2CuS_2CN(Me)Bn$ ***(25)****:* Using $LiS_2CN(Me)Bn$ (0.69g, 3.40mmol), CuCl (0.33g, 3.37mmol) and Ph_3P (1.77g, 6.75mmol). Yielding pale brown crystals (1.65g, 63%, mp 154-156°C). Analysis found (calc for $C_{45}H_{40}NP_2S_2Cu$): C 69.1 (69.0), H 5.09 (5.15), N 1.85 (1.79). ^{1}H NMR (300MHz, $CDCl_3$) δ ppm: 7.17-7.46 (m, 30H, Ph), 5.23 (s, 2H, CH_2), 3.30 (br. s, 3H, CH_3), ^{13}C NMR (300MHz, $CDCl_3$) δ ppm: 224.5 (CS_2), 134.1 (d, *J*=26.1 Hz, Ph), 133.4 (d, *J*=14.3 Hz, Ph), 128.7 (Ph), 127.7 (d, *J*=8.1 Hz, Ph), 76.8 (NCH_2), 57.2 (NCH_3), ^{31}P NMR (300MHz, $CDCl_3$) δ ppm: -1.08

3.4 References

1. Verma, B. C.; Sood, S.; Pande, A.; Sharma, D. K., *Natl. Acad. Sci. Lett. (India)* **2000,** *23*, 104.
2. Kontou, S.; Tsipi, D.; Tzia, C., *Food Addit. Contam.* **2004,** *21*, 1083.
3. Shah, F. U.; Glavatskih, S.; Antzutkin, O. N., *Tribol. Lett.* **2012,** *45*, 67.
4. Rodgers, B.; Solis, S.; Tambe, N.; Sharma, B. B., *Rubber Chem. Technol.* **2008,** *81*, 600.
5. Bratspies, G. K.; Smith, J. F.; Hill, J. O.; Magee, R. J., *Thermochim. Acta* **1978,** *27* (1-3), 307.
6. Hogarth, G., Transition Metal Dithiocarbamates: 1978-2003. In *Progress in Inorganic Chemistry, Vol 53*, Karlin, K. D., Ed. John Wiley & Sons Inc: New York, 2005; Vol. 53, pp 71.
7. Klug, H., *Acta Crystallogr.* **1966,** *21* (4), 536.
8. Bonamico, M.; Mazzone, G.; Vaciago, A.; Zambonelli, L., *Acta Crystallogr.* **1965,** *19* (6), 898.
9. Motevalli, M.; O'Brien, P.; Walsh, J. R.; Watson, I. M., *Polyhedron* **1996,** *15* (16), 2801.
10. Cox, M. J.; Tiekink, E. R. T., *Z. Kristallogr.* **1999,** *214*, 184.
11. Decken, A.; Gossage, R. A.; Chan, M. Y.; Lai, C. S.; Tiekink, E. R. T., *Appl. Organomet. Chem.* **2004,** *18* (2), 101.
12. Ivanov, A. V.; Ivakhnenko, E. V.; Forsling, W.; Gerasimenko, A. V., *Dokl. Chem.* **2003,** *390* (4), 162.
13. Frigo, D. M.; Khan, O. F. Z.; O'Brien, P., *J. Cryst. Growth* **1989,** *96* (4), 989.
14. Pike, R. D.; Cui, H.; Kershaw, R.; Dwight, K.; Wold, A.; Blanton, T. N.; Wernberg, A. A.; Gysling, H. J., *Thin Solid Films* **1993,** *224* (2), 221.
15. Memon, A. A.; Afzaal, M.; Malik, M. A.; Nguyen, C. Q.; O'Brien, P.; Raftery, J., *Dalton Trans.* **2006,** (37), 4499.
16. Perry, D.; Geanangel, R. A., *Inorg. Chim. Acta* **1975,** *13* (2), 185.
17. Hoskins, B. F.; Martin, R. L.; Rohde, N. M., *Aust. J. Chem.* **1976,** *29*, 213.
18. Potenza, J.; Jolinson, R. J.; Mastropaolo, D., *Acta Crystallogr., Sect. B* **1976,** *32* (3), 941.
19. Raston, C. L.; Tennant, P. R.; White, A. H.; Winter, G., *Aust. J. Chem.* **1978,** *31* (7), 1493.

20. Seth, N.; Gupta, V. D.; Noth, H.; Thomann, M., *Chem. Ber.-Recl.* **1992,** *125* (7), 1523.
21. Menezes, D. C.; de-Lima, G. M.; Carvalho, F. A.; Coelho, M. G.; Porto, A. O., *Appl. Organomet. Chem.* **2010,** *24* (9), 650.
22. Heard, P. J., Main Group Dithiocarbamate Complexes. In *Progress in Inorganic Chemistry, Vol 53*, Karlin, K. D., Ed. 2005; Vol. 53, pp 1.
23. Venkatachalam, V.; Ramalingam, K.; Casellato, U.; Graziani, R., *Polyhedron* **1997,** *16* (7), 1211.
24. Rodriguez-Castro, J.; Mahon, M. F.; Molloy, K. C., *Chem. Vapor Depos.* **2006,** *12* (10), 601.
25. Castro, J. R.; Molloy, K. C.; Liu, Y.; Lai, C. S.; Dong, Z.; White, T. J.; Tiekink, E. R. T., *J. Mater. Chem.* **2008,** *18*, 5399.
26. Pitzer, E. W., *Appl. Spectrosc.* **1990,** *44* (9), 1498.
27. Martin, J. M.; Newman, P. W. G.; Robinson, B. W.; White, A. H., *J. Chem. Soc., Dalton Trans.* **1972,** (20).
28. Bonamico, M.; Dessy, G.; Mugnoli, A.; Vaciago, A.; Zambonelli, L., *Acta Crystallogr.* **1965,** *19* (6), 886.
29. Kumar, A.; Mayer-Figge, H.; Sheldrick, W. S.; Singh, N., *Eur. J. Inorg. Chem.* **2009**, 2720.
30. Nomura, R.; Miyawaki, K.; Toyosaki, T.; Matsuda, H., *Chem. Vapor Depos.* **1 996,** *2* (5), 174.
31. Fabretti, A. C.; Giusti, A.; Preti, C.; Tosi, G.; Zannini, P., *Polyhedron* **1986,** *5* (3), 871.
32. Barone, G.; Chaplin, T.; Hibbert, T. G.; Kana, A. T.; Mahon, M. F.; Molloy, K. C.; Worsley, I. D.; Parkin, I. P.; Price, L. S., *J. Chem. Soc., Dalton Trans.* **2002,** (6), 1085.
33. Fabretti, A. C.; Preti, C., *Journal of Crystallographic and Spectroscopic Research* **1989,** *19* (6), 957.

Chapter Four

Materials Work on Cu_2ZnSnS_4 and $CuSbS_2$

4.1 Introduction

This chapter describes attempts to deposit thin films of Cu_2ZnSnS_4 and $CuSbS_2$ using the precursors reported in Chapters Two and Three. AACVD was the chosen deposition method due to the lack of volatility in the precursors. The initial CVD trials were performed using xanthates as they have lower decomposition temperatures. Due to the difficulties of significantly lowering the decomposition temperature of the copper xanthate, CVD trials then focused on using a mixture of copper xanthate with tin and zinc dithiocarbamates or antimony dithiocarbamates and also using just dithiocarbamates. Doctor blading was investigated as an alternative deposition method and the synthesis of Cu_2ZnSnS_4 nanoparticles was explored using xanthate precursors.

4.1.1 Cu_2ZnSnS_4

Cu_2ZnSnS_4 has been widely investigated as a possible absorber layer in thin-film photovoltaic cells, with reports dating back to 1988 when Cu_2ZnSnS_4 was first recognised as a potential replacement to higher cost $CuInSe_2$ absorber layers.[1] With a band gap of 1.5eV and a high coefficient of absorption ($>10^4$ cm^{-1}),[2] studies have shown that the theoretical limit of efficiency for a solar cell with a Cu_2ZnSnS_4 absorber layer is 32.2%.[3]

Cu_2ZnSnS_4 thin films have been deposited from a variety of routes, namely spray pyrolysis,[4] sulphurisation of electrodeposited metal precursors,[5] non-vacuum electroplating,[6] spin coating,[7] pulsed laser deposition[8] and photochemical deposition,[9] sputtering,[1] co-evaporation,[10] multi-stage evaporation,[11] and sulphurisation of sol-gel deposited precursors.[12]. Currently the technique which has produced the highest efficiency cells was the deposition of Cu_2ZnSnS_4 by thermal evaporation of elemental Cu, Zn, Sn and S onto Mo coated glass and subsequent annealing under vacuum, this cell reach an efficiency of 8.4%.[13] This effieicny is the highest reported using solely sulphur, higher efficiencies can be produced by using a mixture of sulphur and selenium.[14]

Although at the time of study there had been no reports of thin films of Cu_2ZnSnS_4 deposited by CVD, O'Brien *et al.* have very recently reported the deposition of Cu_2ZnSnS_4 *via* AACVD using dithiocarbamate precursors.[15]

4.1.1 $CuSbS_2$

$CuSbS_2$ is another potential absorber layer which has been much less widely investigated. It is derived from replacing In or Ga in a CIS or CIGS layer with Sb. With a band gap reported to be between 1.38eV and 1.5eV and an absorption coefficient larger than $10^5 cm^{-1}$, $CuSbS_2$ is an appealing alternative due to the lower cost and higher abundance of Sb.[16]

Thin films of $CuSbS_2$ have been deposited using electrochemical deposition of metal precursors and subsequent annealing in a sulphur atmosphere,[17] chemical bath deposition,[18] sputtering,[19] thermal evaporation,[20] and spray pyrolysis.[21] Although cells have been made with $CuSbS_2$ absorber layers, no efficiencies appear to have been reported yet.[18, 22]

4.2 Results and discussion

4.2.1 AACVD Trials Using Only Xanthates

Cu_2ZnSnS_4

Initially, thermal decomposition of a stoichiometric mixture of $Zn(S_2COEt)_2$, **(1)**, $Sn(S_2COEt)_2$, **(7)** and $(Ph_3P)_2CuS_2COEt$, **(10)** was performed to prove that a mixture of xanthates could produce Cu_2ZnSnS_4. Decomposition was performed under argon and was taken to 400°C at 5 degrees per minute; this was left for 2 hours and then cooled at 1 degree per minute. The PXRD pattern showed peaks which matched those expected for Cu_2ZnSnS_4 (Figure 4.1), however it is known that the powder diffraction pattern of Cu_2ZnSnS_4 is very similar to that of ZnS, as a result of this only neutron diffraction or Raman spectroscopy can fully determine that Cu_2ZnSnS_4 has been produced. In this case, the absence of any peaks corresponding to SnS_x or Cu_xS strongly suggests the production of Cu_2ZnSnS_4 rather than ZnS.

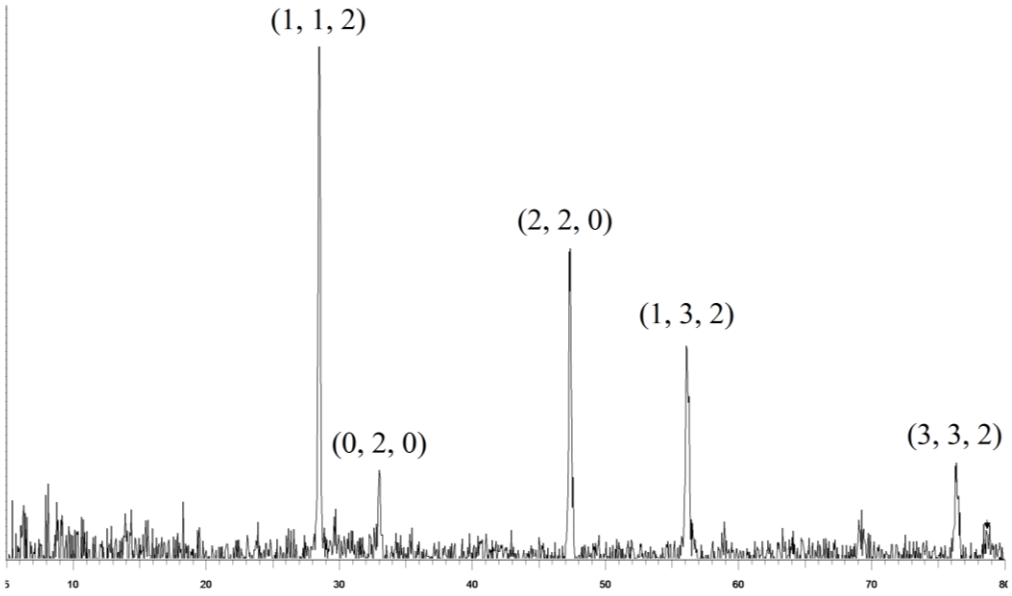

Figure 4.1 Powder diffraction pattern of thermal decomposition product, indexing is to PDF 34-1246

As the thermal decomposition results were promising, AACVD trials were performed using the mixture of xanthates deemed most suitable in Chapter 2, [$Zn(S_2CO^nBu)_2$, **(4)**, $Sn(S_2COEt)_2$, **(7)** and $(^nBu_3P)_2CuS_2CO^nBu$, **(16)**]. TGAs of all three xanthates show initial decomposition of **(7)** and **(16)** starts at a similar temperature, while **(4)** starts *ca* 50°C earlier; the main decomposition of all has finished by 225°C (Figure 4.2). Initial CVD trials at 250°C, 300°C and 350°C showed that best coverage and growth rates were seen in the sample grown at 250°C, so this was chosen as the reactor temperature. All three xanthates [0.41mmol of **(4)** and **(7)**, 0.82mmol of **(16)**] were dissolved in THF (50ml), AACVD was performed at 250°C for 2 hours onto Mo coated glass.

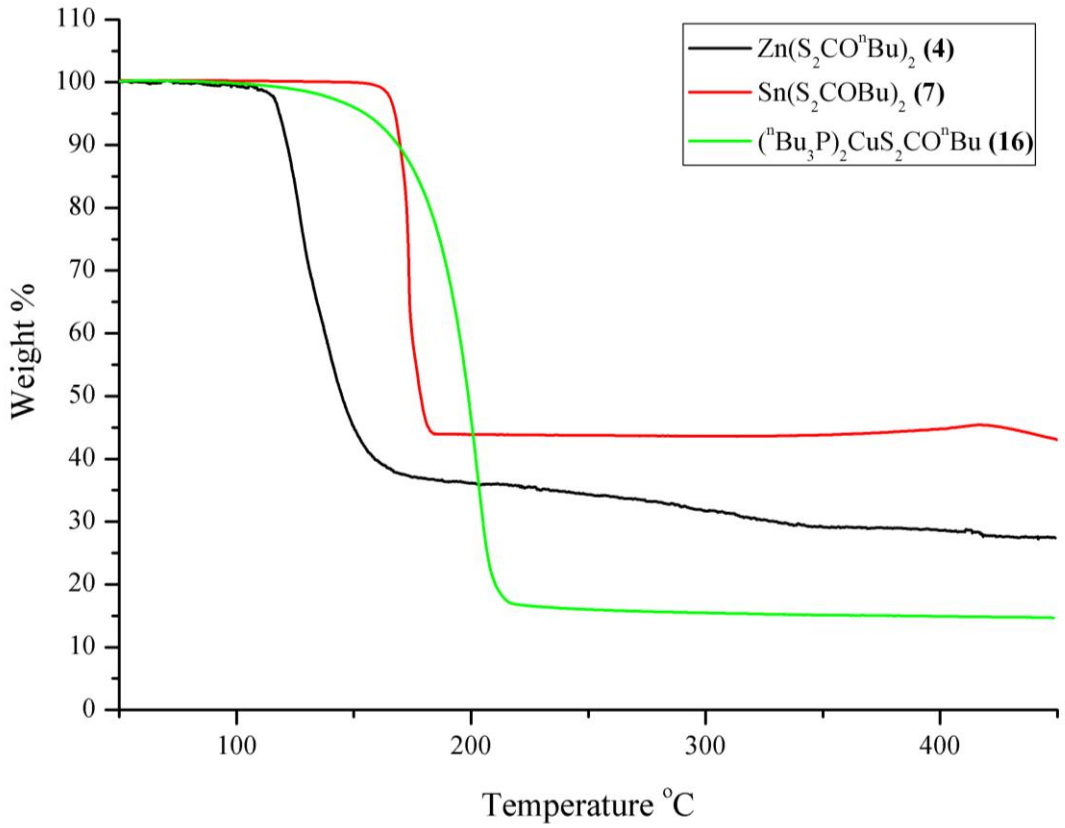

Figure 4.2 TGA of **(4)**, **(7)** and **(16)** with a heating rate of 5°C/min

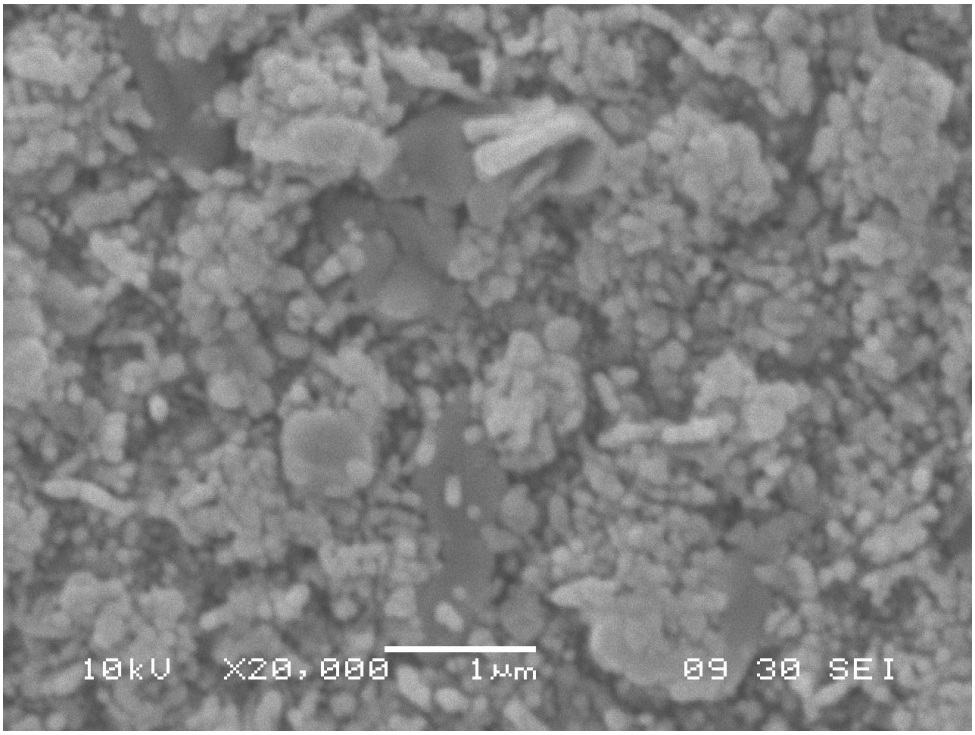

Figure 4.3 SEM image of film grown from **(4)**, **(7)** and **(16)**

Films were metallic and looked very smooth with many lines of refrigence seen. SEM imaging shows a textured films mainly composed of small spheres of 100nm, in some places these spheres have formed larger aggregates (Figure 4.3). There are also areas of larger, flattened particles ranging from 500nm - 1µm. Quantatative EDX shows a ratio of Cu : Zn : Sn of 2.0 : 7.2 : 5.9 when normalising the Cu content to 2 as the target films contain Cu : Zn : Sn in a 2 : 1 : 1 ratio, sulphur overlaps with Mo so the exact content could not be determined. PXRD showed peaks correcponding to SnS_2 and what could either be ZnS, CuS or Cu_2ZnSnS_4 (Figure 4.4). Flashing LED experiments showed some photoactivity which later band gap measurements confirmed to be mainly due to SnS_2 and possibly a much smaller smount of Cu_2ZnSnS_4. As the films were vastly Cu deficient the likelyhood is that the majority of the film is composed of ZnS and SnS_2 with a small amount of Cu_2ZnSnS_4.

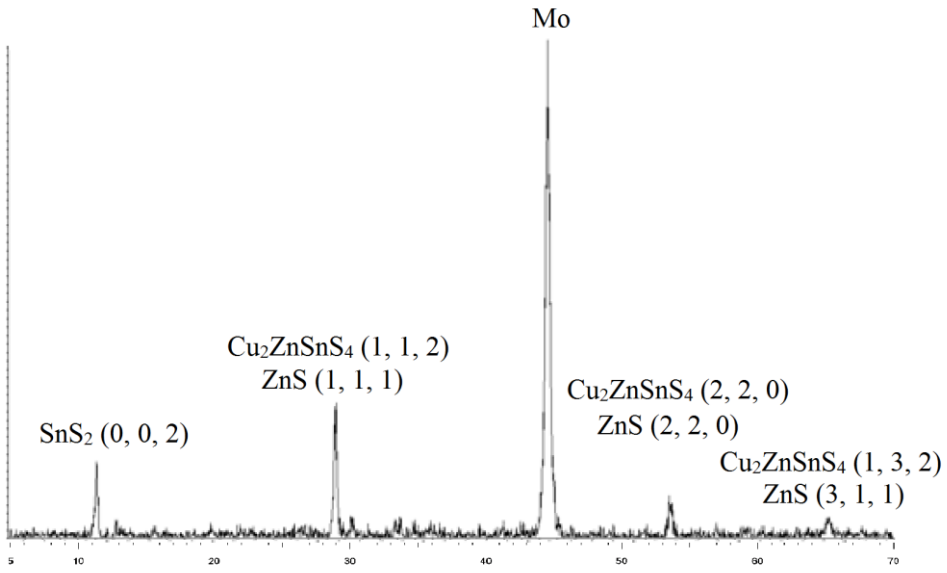

Figure 4.4 PXRD of film grown from **(4)**, **(7)** and **(16)**, indexing is to SnS_2 PDF 89-3198, ZnS PDF 65-1691, Cu_2ZnSnS_4 PDF 34-1246

Due to the difference in the decomposition profile of **(5)** (Figure 4.5), AACVD was attempted using a mixture of $Zn(S_2CO^nHex)_2$, **(5)**, $Sn(S_2COEt)_2$, **(7)** and $(^nBu_3P)_2CuS_2CO^nBu$, **(16)** at two different temperatures, 250°C and 400°C. 250°C is the temperature used with the previous mix of xanthates and so can be a direct comparison to the effects of changing the precursor. As **(5)** has an end point of decomposition much later than the other xanthate, 400°C was chosen as the second

temperature for a trial as all precursors are fully decomposed by then (Figure 4.5). **(5)** (0.41mmol), **(7)** (0.41mmol) and **(16)** (0.82mmol) were dissolved in THF (50ml), AACVD was performed for 2 hours onto Mo coated glass at 250°C and 400°C.

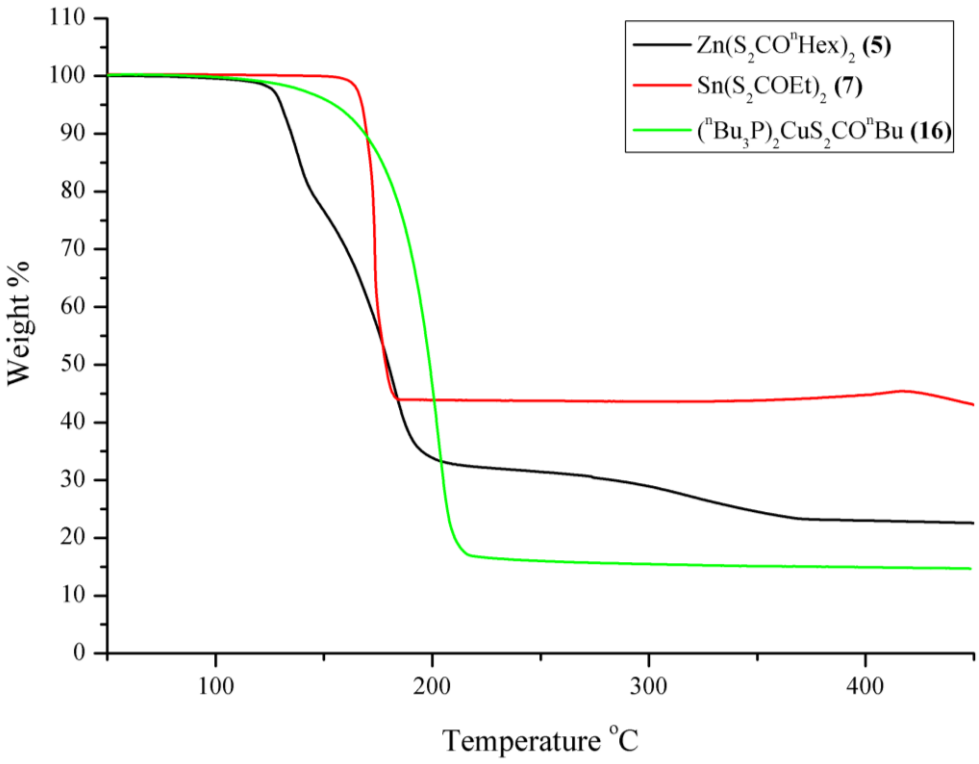

Figure 4.5 TGA of **(5)**, **(7)** and **(16)** with a heating rate of 5°C/min

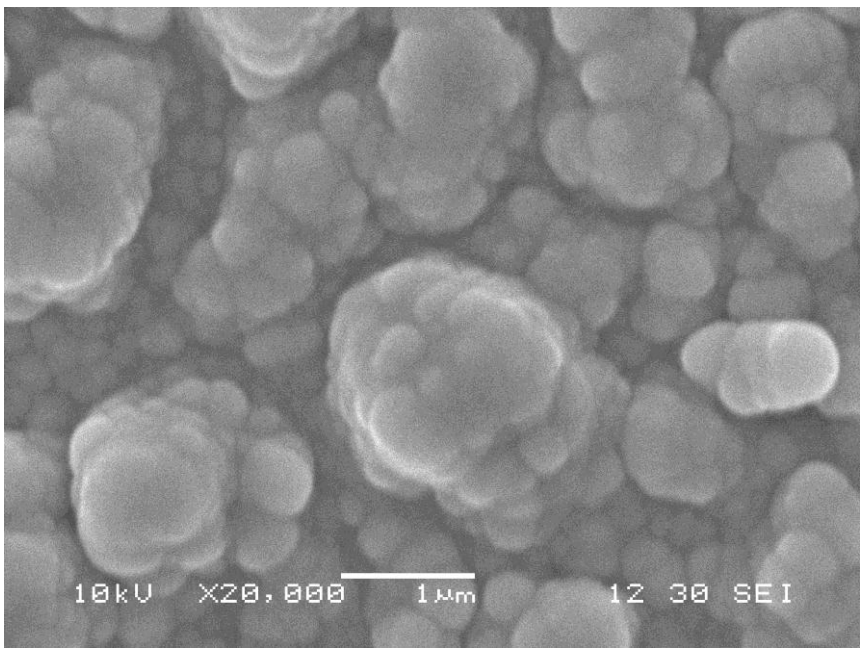

Figure 4.6 SEM image of film grown from **(5)**, **(7)** and **(16)** at 250°C

Films grown at 250°C were black in colour and looked powdery. SEM imaging revealed textured continuous films consisting of spherical particles of 200-500nm that appear to have grown horizontally, forming columns (Figure 4.6). EDX confirms the presence of Cu, Zn and Sn in a 2.0 : 7.3 : 3.1 ratio, indicating very Cu and Sn deficient films. PXRD revealed the presence of SnS_2 and Cu_2S phases but no ZnS or Cu_2ZnSnS_4 phases were seen (Figure 4.7). The most likely explanation for this is that the component Zn, Sn and Cu sulphides have been deposited rather than Cu_2ZnSnS_4 and in this case the ZnS is amorphous.

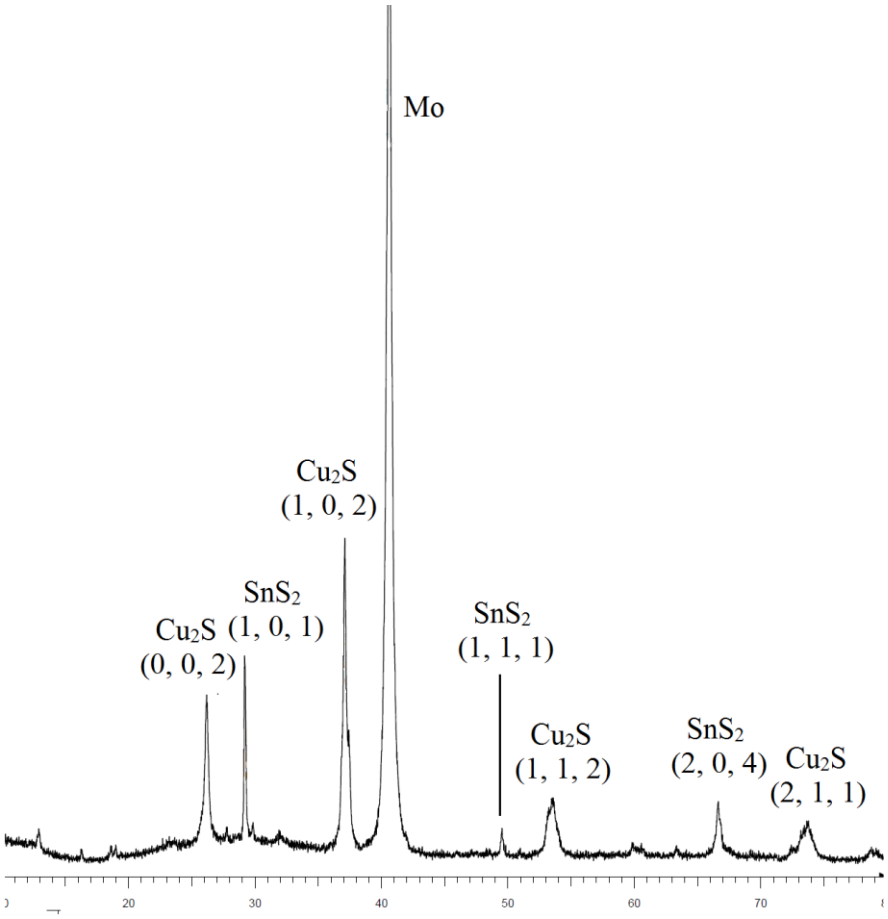

Figure 4.7 PXRD of film grown from **(5)**, **(7)** and **(16)** at 250°C, indexing is to Cu_2S PDF 84-0209, SnS_2 PDF 89-3198

Films grown at 400°C were also metallic in colour and looked smooth. SEM imaging shows a distinct change in morphology of the films (Figure 4.8). Here the films consist of circular plates that have grown mostly horizontally with some growing more angular to the surface. The plates range from 1 - 2µm in size and have very rough edges. EDX confirms the presence of Cu, Zn and Sn in a 2.0 : 9.2 : 6.0

ratio, indicating very Cu deficient films and the incorrect stoichiometry of Zn and Sn. PXRD showed that these films were amorphous.

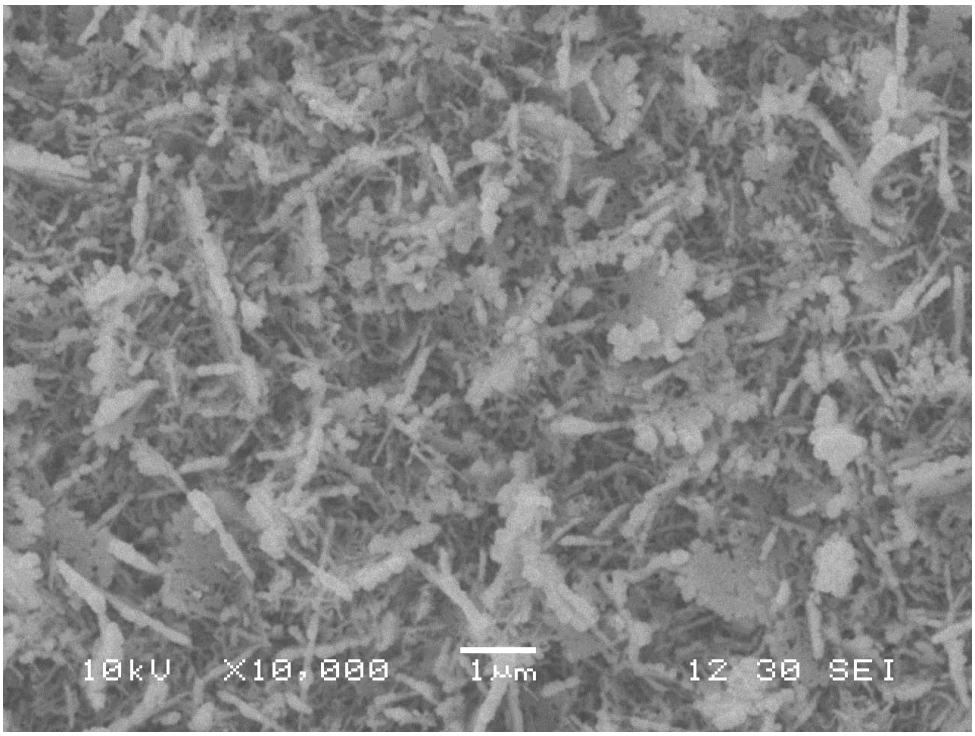

Figure 4.8 SEM image of film grown from **(5)**, **(7)** and **(16)** at 400°C

$CuSbS_2$

For the deposition of $CuSbS_2$, thermal decomposition of a 2:1 mixture of $Sb(S_2COEt)_3$, **(9)** and $(Ph_3P)_2CuS_2COEt$, **(10)** was attempted to verify the ability of xanthate precursors to form $CuSbS_2$. The powder diffraction pattern of the product (Figure 4.9) matched the powder diffraction pattern for $CuSbS_2$. Decomposition was performed under argon and was taken to 400°C at 5 degrees per minute; this was left for 2 hours and then cooled at 1 degree per minute.

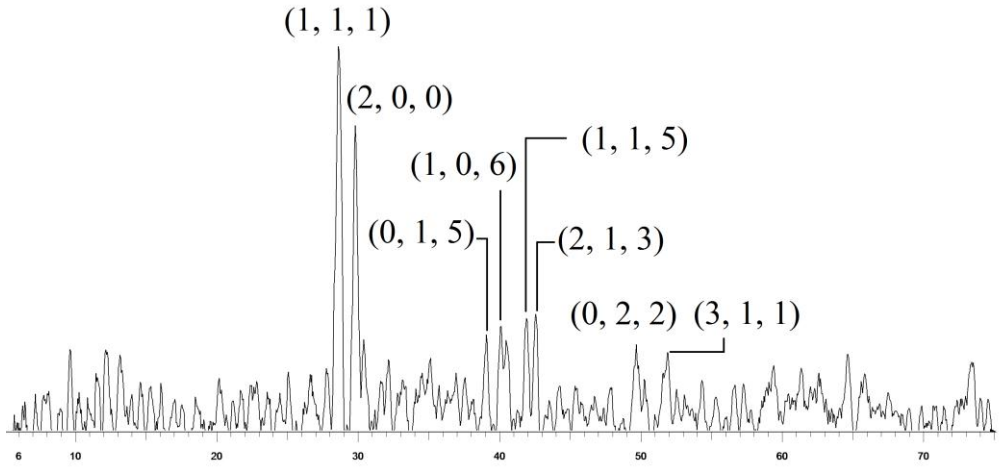

Figure 4.9 Powder diffraction pattern of $CuSbS_2$, indexing is to PFD 88-0822

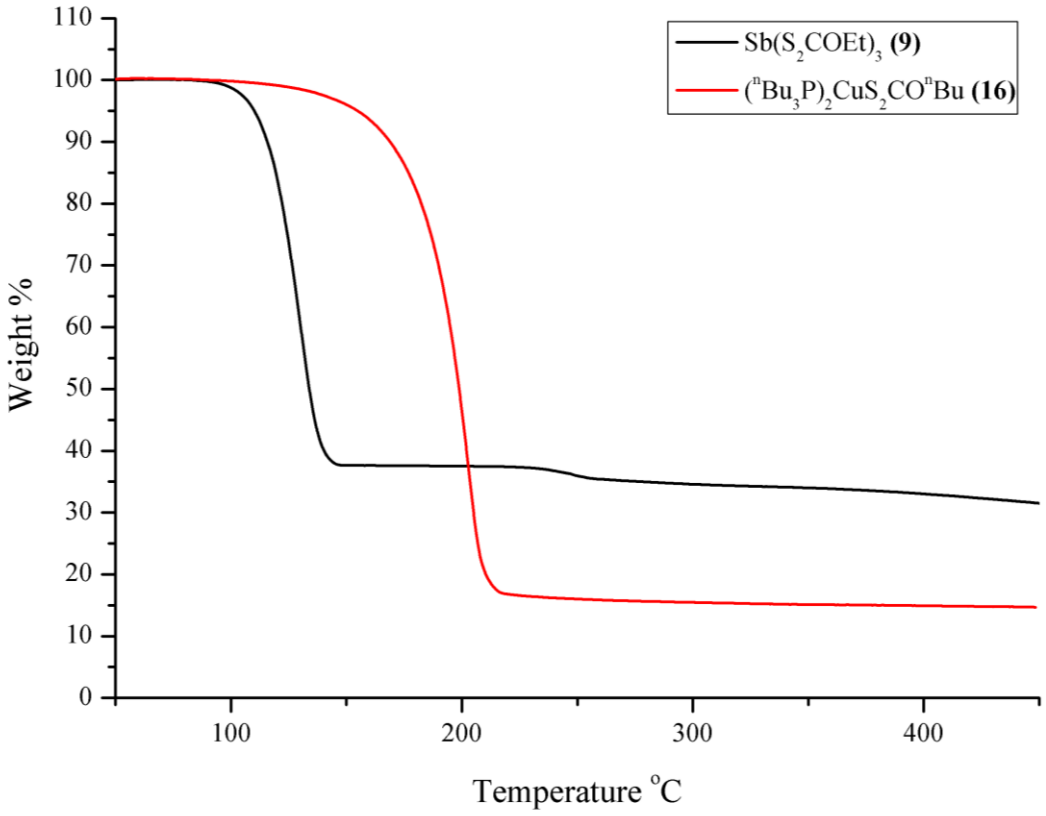

Figure 4.10 TGA of **(9)** and **(16)** with a heating rate of 5°C/min

$Sb(S_2COEt)_3$, **(9)** and $(^nBu_3P)_2CuS_2CO^nBu$, **(16)** were chosen as precursors for the deposition of $CuSbS_2$ by CVD as they were the closest match in decomposition temperature (Figure 4.10). Both precursors have fully decomposed by 250°C and

show little volatility, as a result AACVD was the chosen method used for the deposition. Initial CVD trials were performed using reactor temperatures of 250°C , 300°C and 350°C, the films grown at 250°C showed superior coverage and growth rates so this was the temperature chosen for CVD. **(9)** (0.82mmol) and **(16)** (0.82mmol) were dissolved in THF (50ml) and films were grown for 1 hour on Mo coated glass.

Films were dark brown and powdery in appearance. SEM imaging reveals a continuous film with some pinholing. The film appears to consist of block of around 400nm that have fused together (Figure 4.11). EDX confirms the presence of Cu and Sb in a 1.0 : 1.1 ratio, making films slightly Cu deficient. Films proved to be amorphous by PXRD.

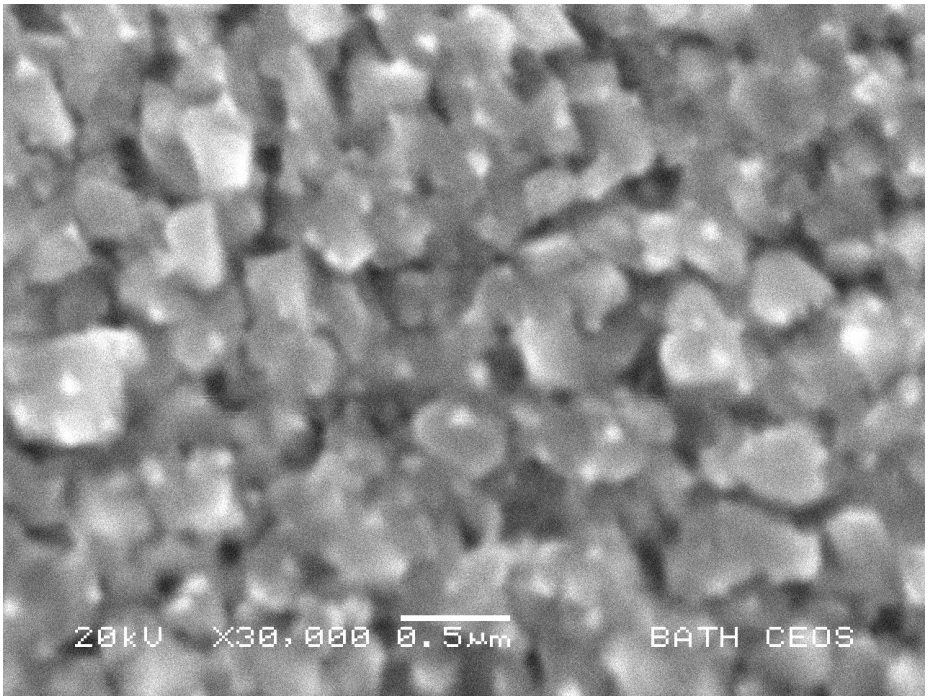

Figure 4.11 SEM image of film grown from **(9)** and **(16)**

4.2.2 AACVD Trials Using a Mixture of Xanthates and Dithiocarbamates

Cu_2ZnSnS_4

The copper deficiency in the films grown from using entirely xanthate precursors was possibly due to a slower rate of decomposition in the copper precursor due to the additional phopshine groups. Due to this a mixture of zinc and tin dithiocarbamates with **(16)** was chosen, which could force the faster decomposition of **(16)** due to the higher temperatures needed to decompose dithiocarbamates and therefore incorporate more copper into the films.

TGAs of $(^nBu_3P)_2CuS_2CO^nBu$, **(16)**, $Zn[S_2CN(Me)^nBu]_2$, **(17)** and $Sn[S_2CN(Me)^nBu]_2$, **(19)** shows the much lower (*ca* 150°C) end point of decomposition of **(16)** (Figure 4.12). Decomposition of all precursors has finished by 350°C and so AACVD was performed at 400°C. **(16)** (0.82mmol), **(17)** (0.41mmol) and **(19)** (0.41mmol) were dissolved in THF (50ml) and CVD was performed for 2 hours on Mo coated glass.

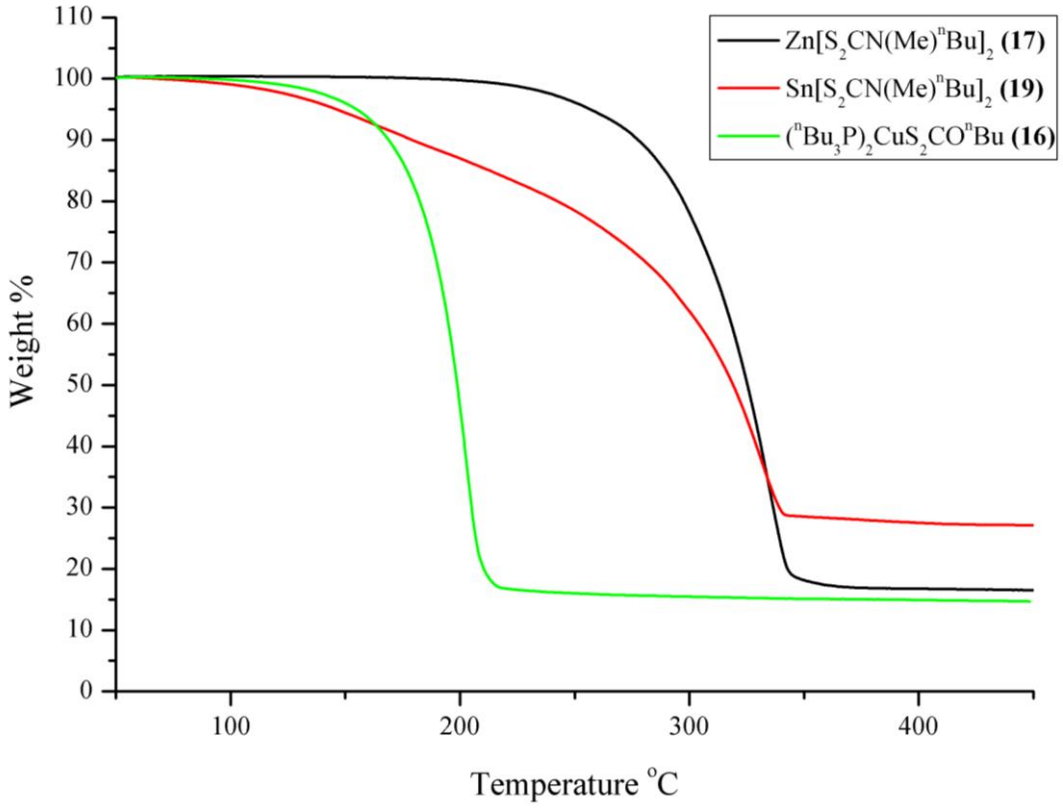

Figure 4.12 TGA of **(16)**, **(17)** and **(19)** with a heating rate of 5°C/min

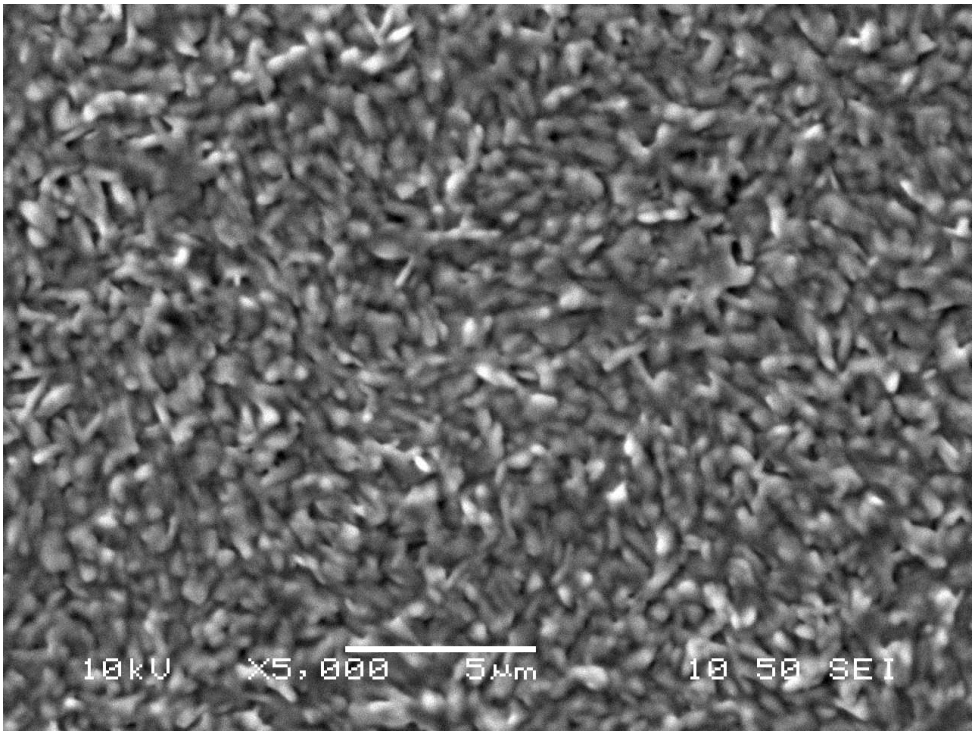

Figure 4.13 SEM image of film grown from **(16)**, **(17)** and **(19)**

Films were dark brown in colour and very powdery, and looked very thin. SEM imaging shows a continuous films with lots of pinholes (Figure 4.13). The film consists of many oval particles of *ca* 1µm fused together. EDX only confirmed Cu and Zn in the films in a 2.0 : 2.3 ratio, the lack of Sn found in the films is likely to be due to the films being too thin for a reliable result, as the quantities of Cu and Zn were also very low. The films were either too thin or amorphous so PXRD did not help characterisation.

A similar experiment was performed using $(^nBu_3P)_2CuS_2CO^nBu$, **(16)**, $Zn[S_2CN(Me)Bn]_2$, **(18)** and $Sn[S_2CN(Me)Bn]_2$, **(20)**. TGAs show very similar decomposition profiles, with all precursors fully decomposed by *ca* 350°C (Figure 4.14). AACVD was performed at 400°C using **(16)** (0.82mmol), **(18)** (0.41mmol) and **(20)** (0.41mmol) in THF (50ml) for 2 hours onto Mo coated glass.

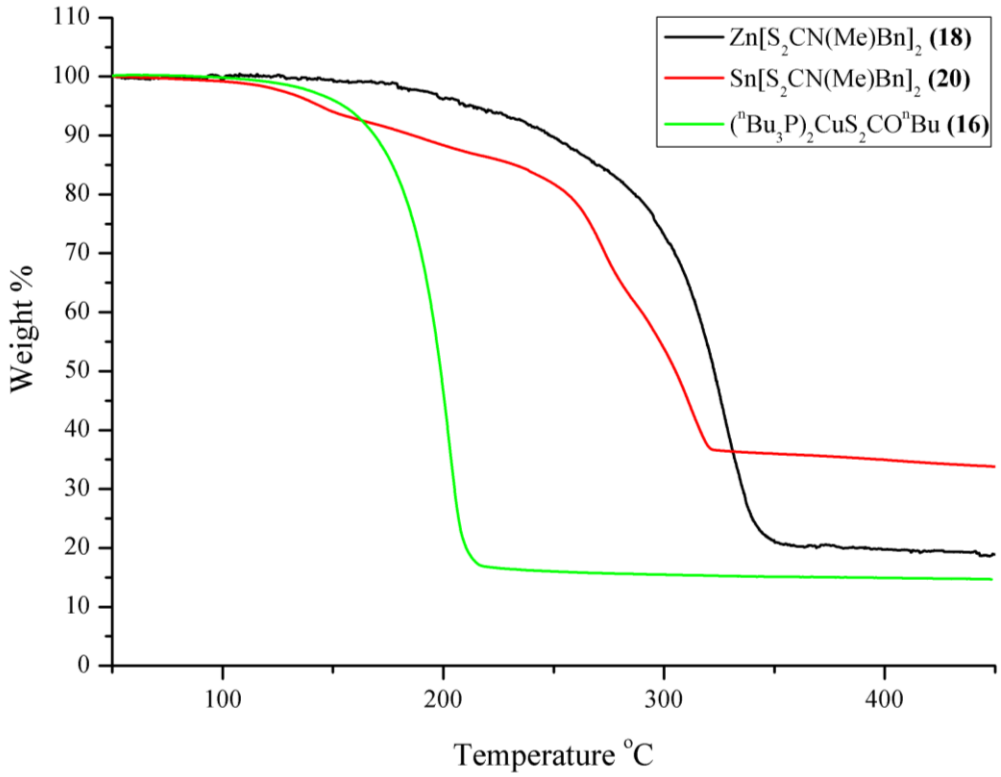

Figure 4.14 TGA of **(16)**, **(18)** and **(20)** with a heating rate of 5°C/min

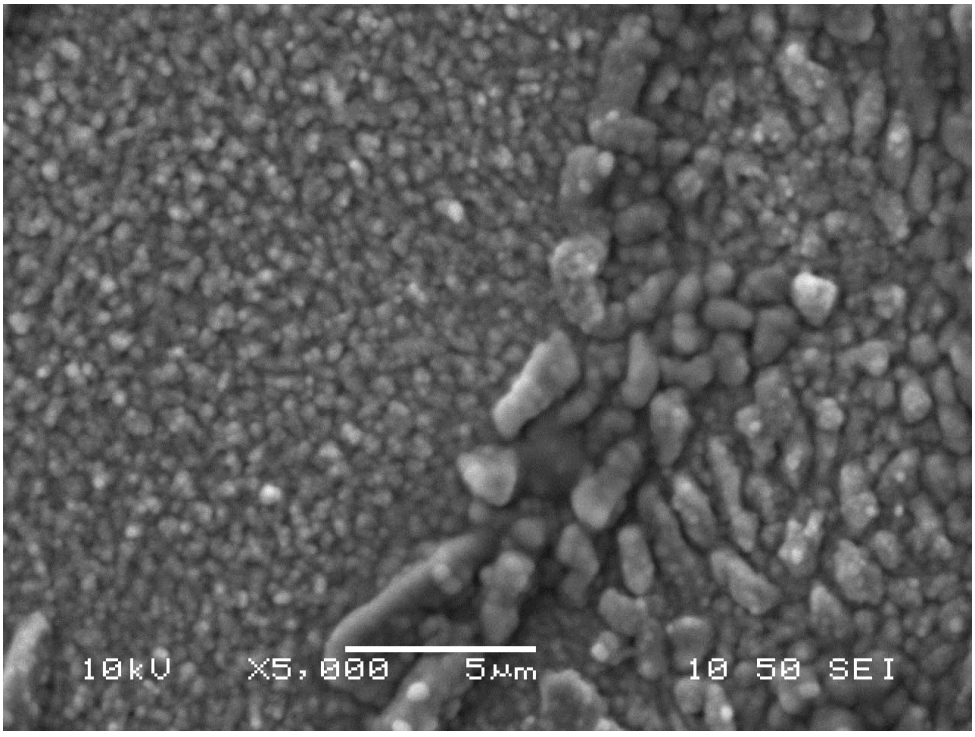

Figure 4.15 SEM image of film grown from **(16)**, **(18)** and **(20)**

Films were powdery and dark brown in colour. SEM imaging revealed a continuous film consisting of areas of smaller (500nm) particles and areas of much

larger (1µm-2.5µm) particles (Figure 4.15). EDX confirmed the presence of Cu and Zn in a 2.0 : 2.6 ratio but could find no Sn. This could be due once again to the film being very thin. PXRD showed that the films were either too thin for measurements or amorphous.

In both cases the films are very thin and no Sn was detetced in either sample. The films are also Cu deficient in relation to Zn, showing that the higher deposition temperature doesn not increase the Cu content to a degree suitable to make a high-quality abosrber layer.

$CuSbS_2$

A similar aproach was adopted with the attempted deposition of $CuSbS_2$ films from a mixture of $(^nBu_3P)_2CuS_2CO^nBu$, **(16)** and either $Sb[S_2CN(Me)^nBu]_3$, **(22)** or $Sb[S_2CN(Me)Bn]_3$, **(23)**. In both cases TGA shows that decomposition has finished by *ca* 350°C (Figure 4.16). AACVD was performed at 400°C using **(16)** (0.41mmol) with either **(22)** (0.41mmol) or **(23)** (0.41mmol) in THF (50ml) for 2 hours on Mo coated glass.

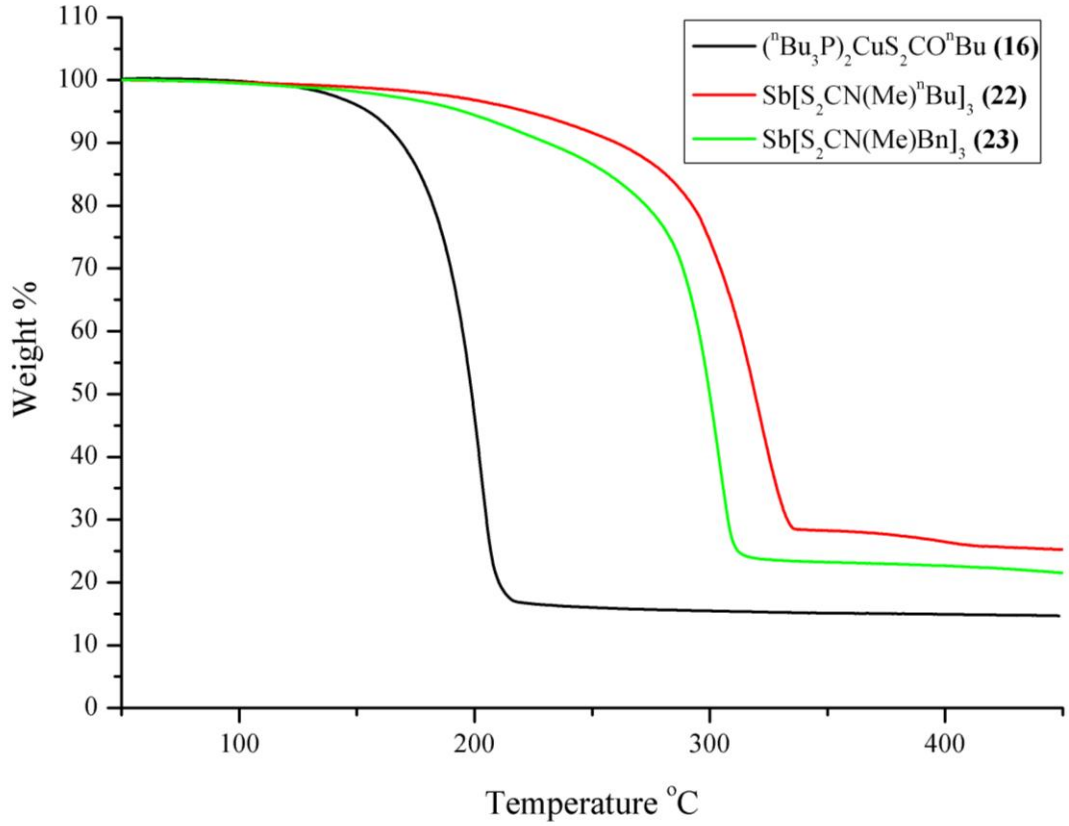

Figure 4.16 TGA of **(16)**, **(22)** and **(23)** with a heating rate of 5°C/min

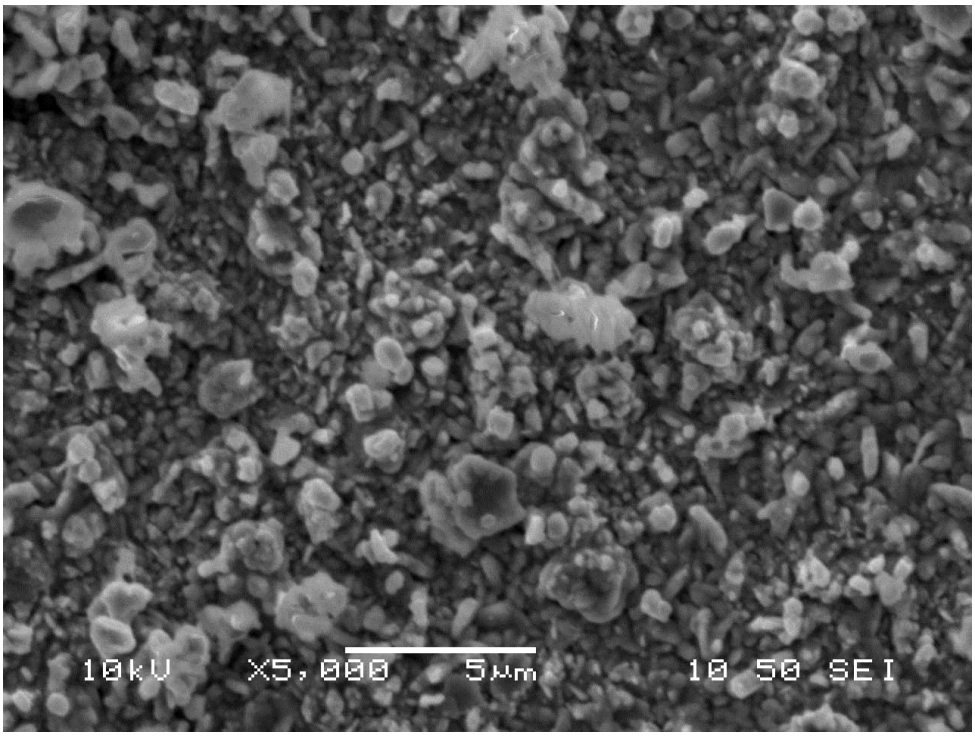

Figure 4.17 SEM image of film grown from **(16)** and **(22)**

Films produced from the deposition of **(16)** and **(22)** are powdery and brown in colour. SEM imaging reveals a textured continuous film consisting of angular particles of 500nm with deposits of particles of varying sizes ranging from 500nm – 2µm on the surface (Figure 4.17). EDX confirms that Cu and Sb are present in a 2.0 : 3.5 ratio, leaving the films copper deficient. PXRD only showed peaks for the Mo substrate, so the films were either amorphous or too thin.

Films grown from the precursors **(16)** and **(23)** were brown in colour and looked smoother than the previous run but still a little powdery. SEM imaging reveals a continuous film with some pinholing (Figure 4.18). The film is not uniform, some parts have cleary defined spherical particles ranging from 300 - 400nm, in some places these particle appear to have aglormorised to form larger globules ranging from 500nm - 2.5µm. In some places the film looks much flatter with the particles much less clearly defined. EDX confirms the presence of Cu and Sb in a 2.0 : 4.5 ratio, again showing copper deficincy in the films grown. PXRD shows peaks corresponding to SbO, showing that the film has somehow oxidised. It is possible that in the deposition only Cu_2S/CuS and Sb_2S_3 have been deposited rather than the

ternary $CuSbS_2$ and due to the high temperatures the Sb_2S_3 has oxidsed to Sb_2O_3, a phenomenom which has been seen previously in the AACVD of Sb_2S_3 using dithiocarbamate precursors.[23]

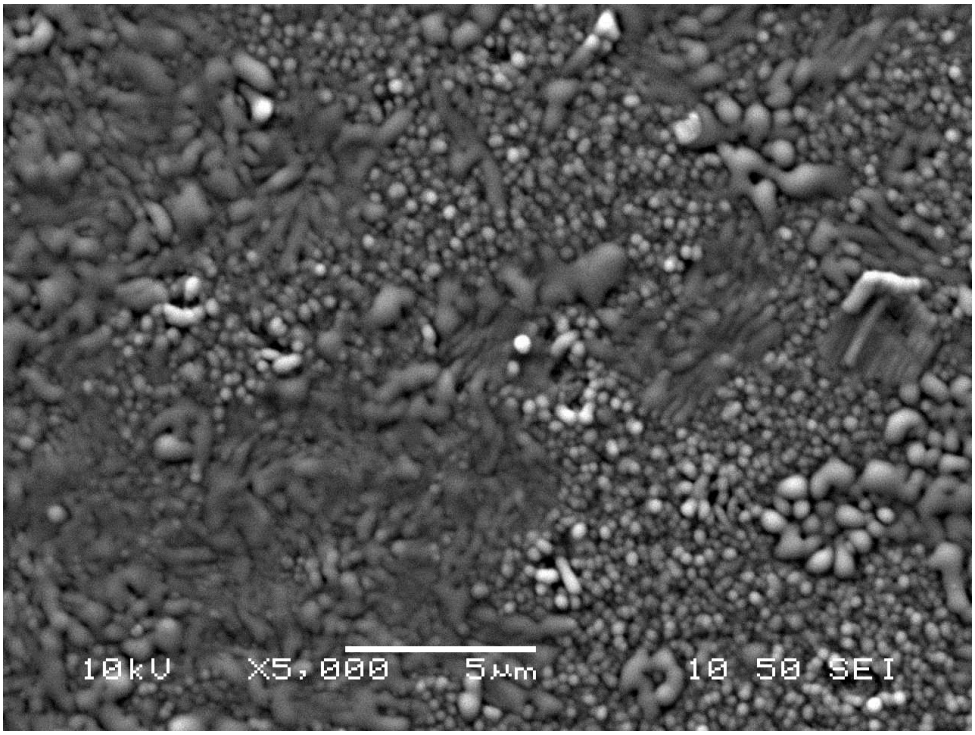

Figure 4.18 SEM image of film grown from **(16)** and **(23)**

4.2.3 AACVD Trials Using Only Dithiocarbamates

Cu_2ZnSnS_4

As the CVD trials using a mixture of Cu xanthate with Zn and Sn or Sb dithiocarbamates were unsuccessful in incorporating more Cu into the films, a mixture of Cu, Zn and Sn or Cu and Sb dithiocarbamates was attempted.

TGAs of $Zn[S_2CN(Me)^nBu]_2$, **(17)**, $Sn[S_2CN(Me)^nBu]_2$, **(19)** and $(Ph_3P)_2CuS_2CN(Me)^nBu$, **(24)** show that although the onset of decomposition is varied, all precursors have similar end points of decomposition, *ca* 350°C (Figure 4.19). AACVD was the chosen deposition method, due to both the lack of volatility and the poor thermal stability of **(24)**. **(17)** (0.41mmol), **(19)** (0.41mmol) and (24) (0.82mmol) were dissolved in THF (50ml) and CVD was performed for 2 hours at a reactor temperature of 400°C onto Mo coated glass.

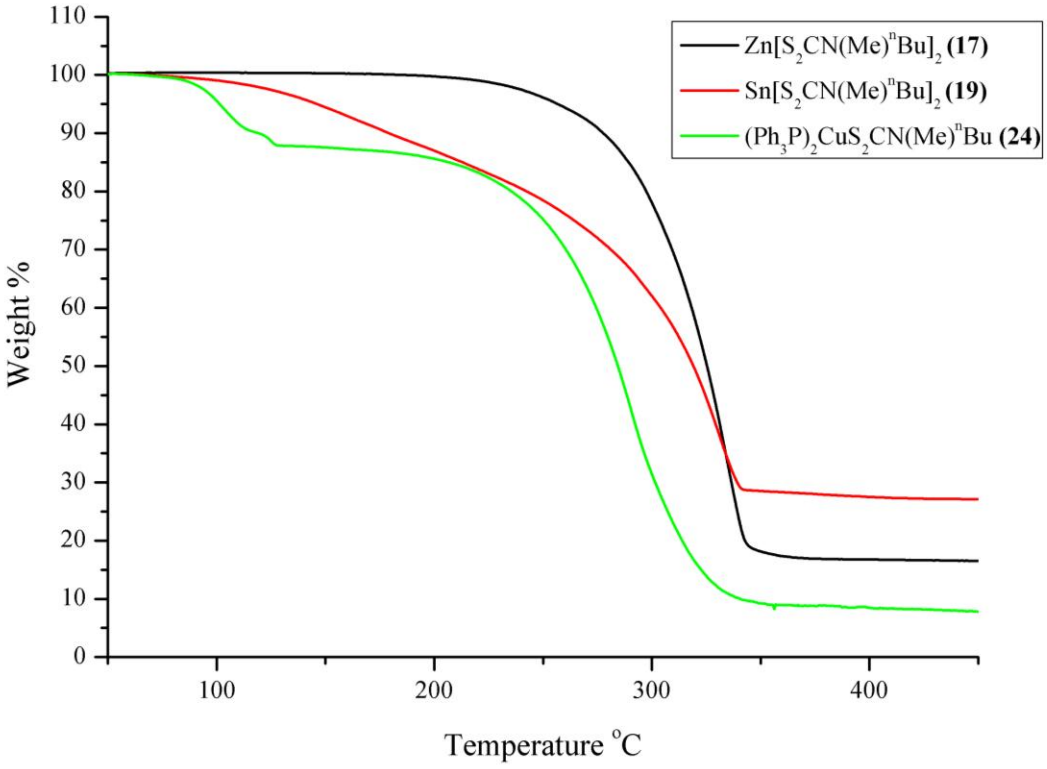

Figure 4.19 TGA of **(17)**, **(19)** and **(24)** with a heating rate of 5°C/min

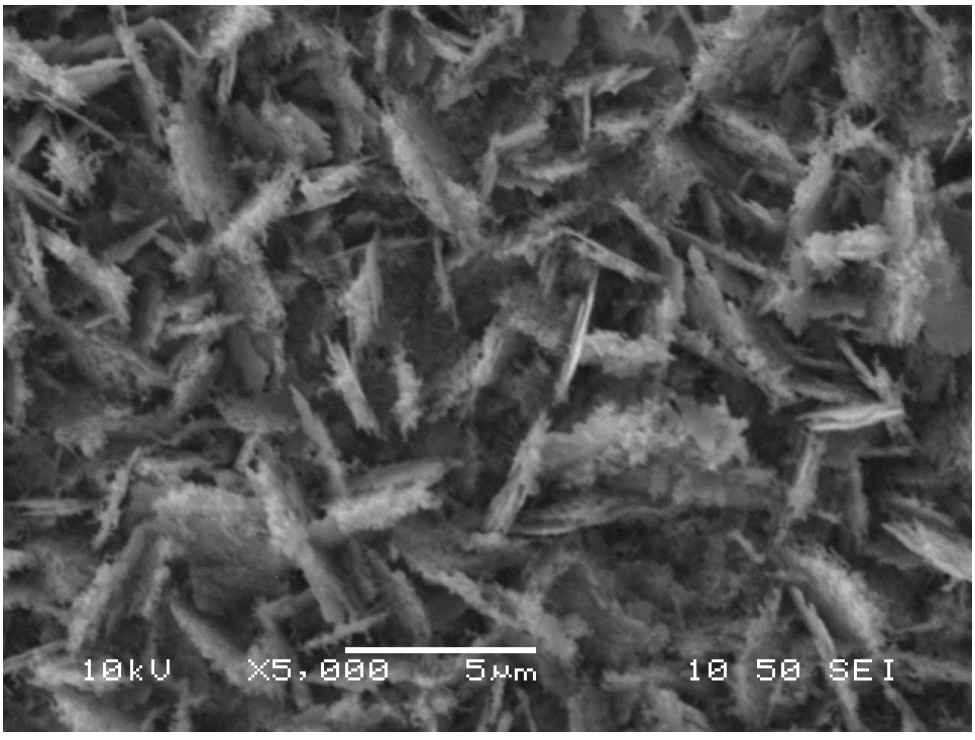

Figure 4.20 SEM image of film grown from **(17)**, **(19)** and **(24)**

Films are black and slightly powdery looking. SEM imaging reveals a uniform crystalline film with plates growing vertically from the surface of the substrate

(Figure 4.20). The places are circular and measure between 2µm and 5µm. EXD confirms the presence of Cu, Zn and Sn in a 2.0 : 1.2 : 0.7 ratio, showing that with this mix of precursors the copper deficiency in the films has been overcome, however the tin content is now roughly half of what is needed. PXRD was unsuccessful, possibly due to the films being too thin as they visually appear to be crystalline.

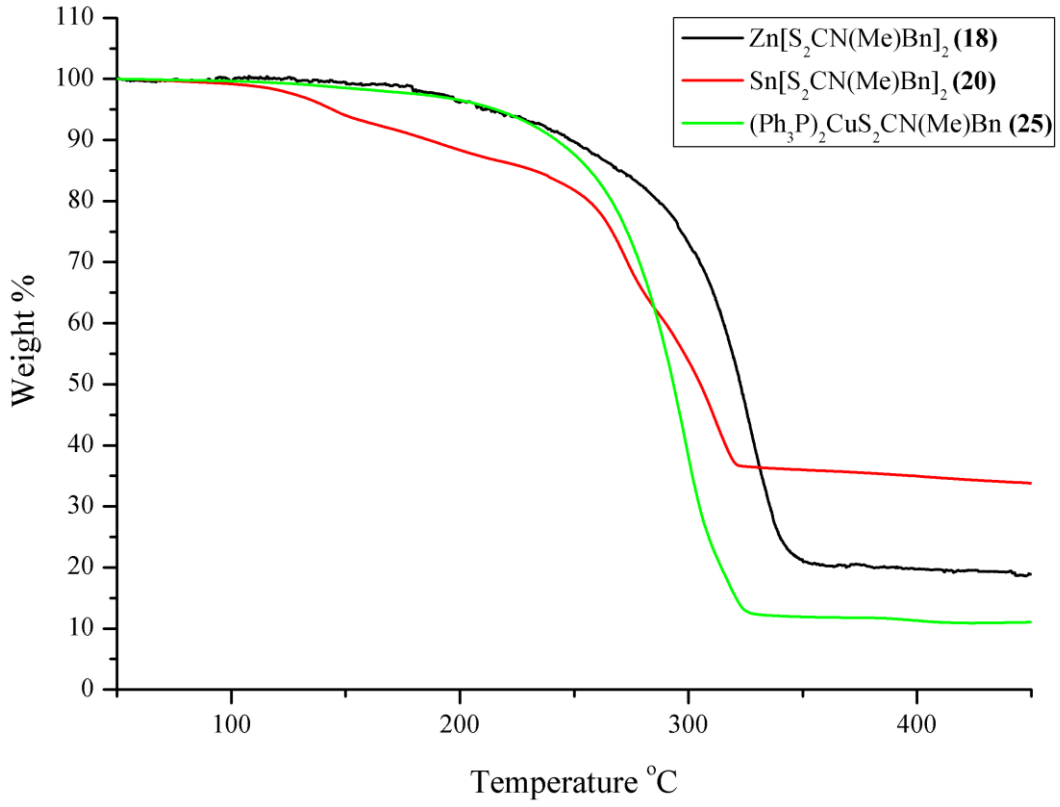

Figure 4.21 TGA of **(18)**, **(20)** and **(25)** with a heating rate of 5°C/min

As with the previous precursors, $Zn[S_2CN(Me)Bn]_2$, **(18)**, $Sn[S_2CN(Me)Bn]_2$, **(20)** and $(Ph_3P)_2CuS_2CN(Me)Bn$, **(25)** all have similar end points of decomposition although their onsets are very different (Figure 4.21). AACVD was also the chosen method due to the poor thermal stability of **(20)** and the lack of volatility seen in the precursors. Films were grown at 400°C from **(18)** (0.41mmol), **(20)** (0.41mmol) and **(25)** (0.82mmol) in THF (50ml) for 2 hours onto a substrate of Mo coated glass.

The appearance of the films was similar to previous runs, black in colour and powdery, however SEM imaging shows significant differences in the films (Figure 4.22). The films are much smoother and look completely continuous with no

pinholing. The surface of the film covered with oblong crystallites ranging from 1 - 2µm in length and 500nm - 1µm in width. EDX confirms the presence of Cu and Zn in a 1.0 : 1.0 ratio but could detect no Sn in the films; this could be an indication that the films are very thin as the amounts of Cu and Zn detected were very low. Attempts at PXRD was unsuccessful, possibly due to the lack of crystallinity in the films or the films could have been too thin.

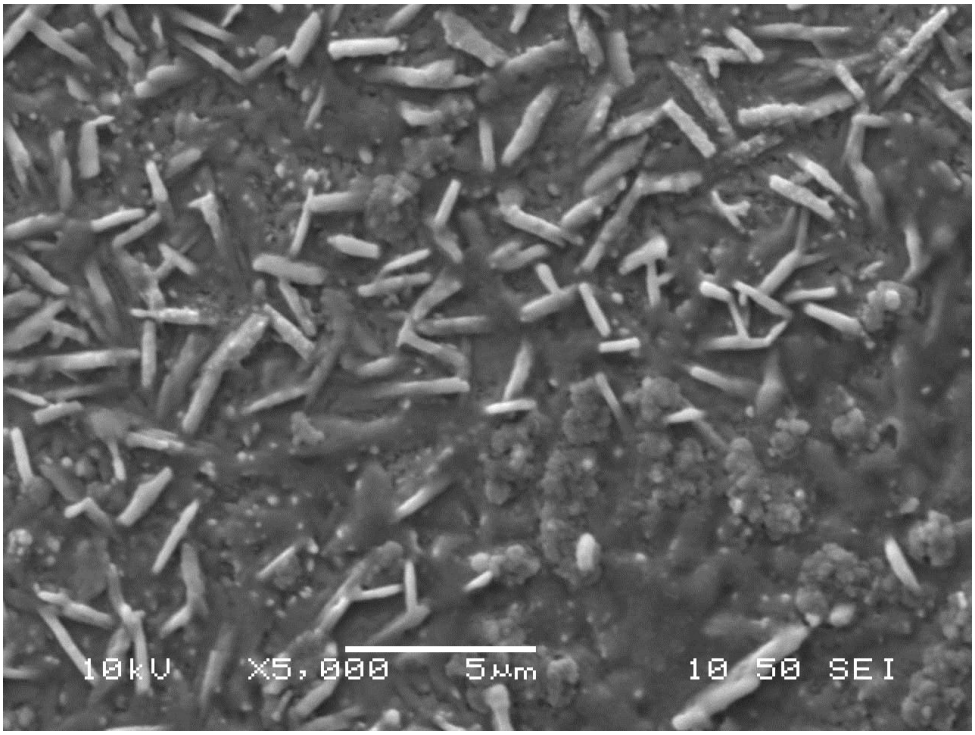

Figure 4.22 SEM image of film grown from **(18)**, **(20)** and **(25)**

$CuSbS_2$

A similar approach was employed for the deposition of $CuSbS_2$ from dithiocarbamate precursors. As with the previous precursors, decomposition onsets for $Sb[S_2CN(Me)^nBu]_3$, **(22)** and $(Ph_3P)_2CuS_2CN(Me)^nBu$, **(24)** are very different but the end point of decomposition for both is ca 350°C (Figure 4.23). As a result of this, CVD was performed at 400°C for a duration of 2 hours using **(22)** (0.33mmol) and **(24)** (0.33mmol) in THF (50ml) onto Mo coated glass.

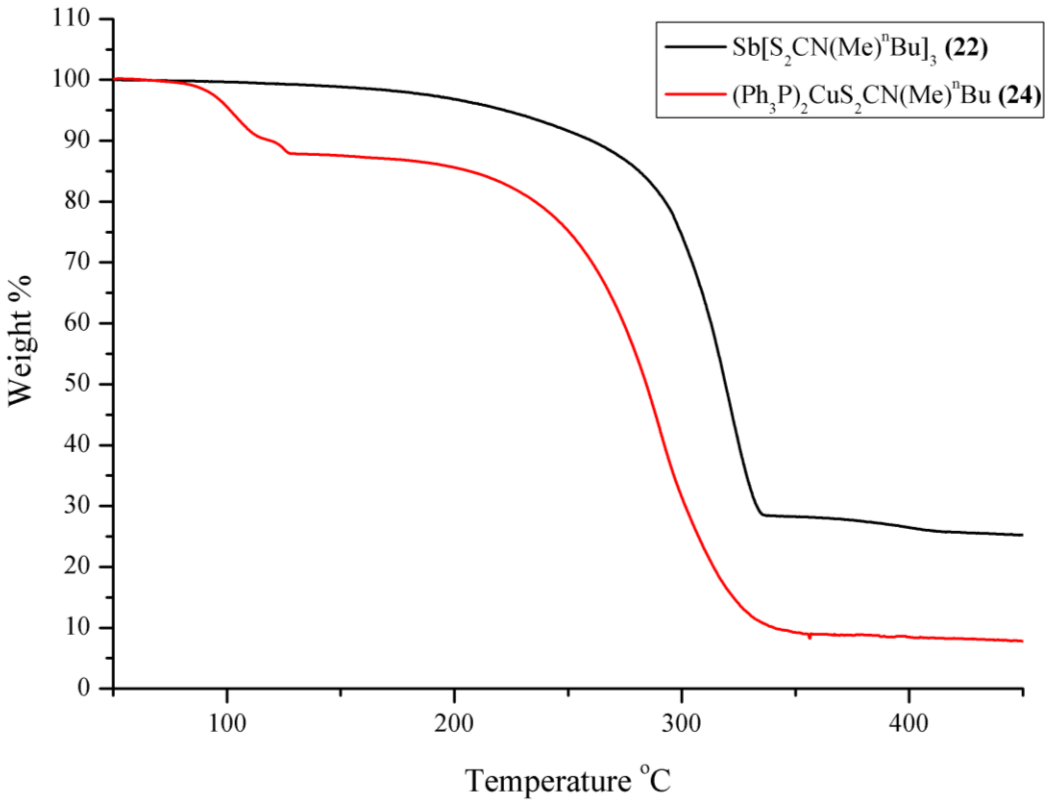

Figure 4.23 TGA of **(22)** and **(24)** with a heating rate of 5°C/min

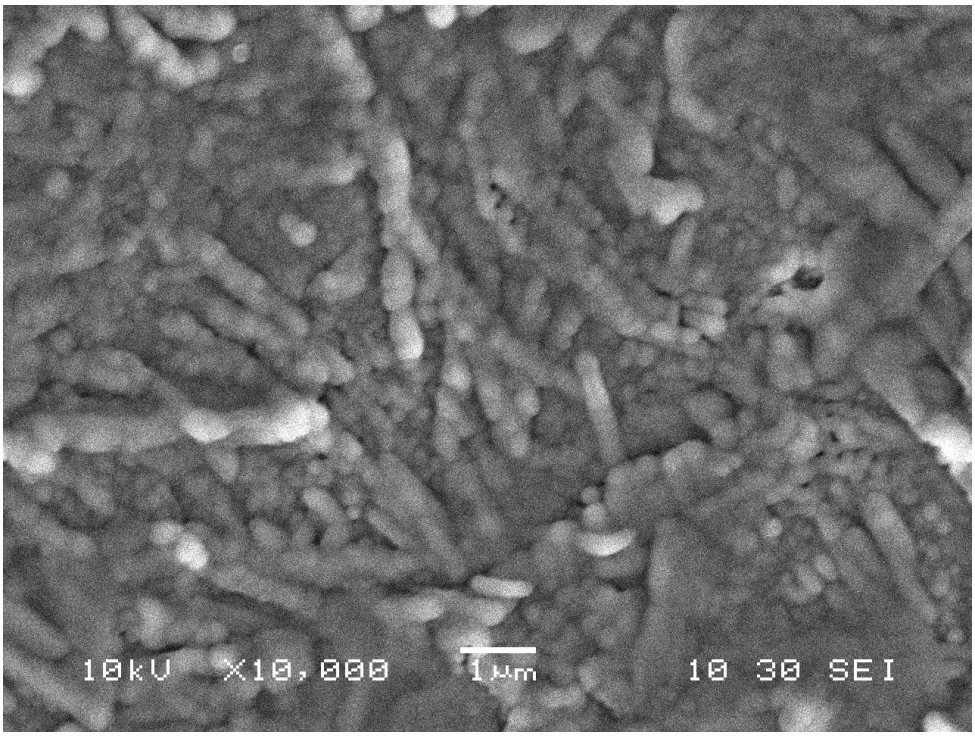

Figure 4.24 SEM image from film grown using **(22)** and **(24)**

Films produced look black and smooth. SEM imaging reveals a continuous films with long cylindrical features ranging from 1 - 5µm with some pinholes where the features meet (Figure 4.24). Some smaller spherical particles are visible in the films, all ca 200nm. EDX imaging reveals the presence of Cu and Sb in a 1.0 : 0.15 ratio. As opposed to other films grown, this film is Cu rich. PXRD shows peaks corresponding to $CuSbS_2$ (labeled 1), Sb_2S_3 (labeled 2) and Cu_2S (labeled 3) (Figure 4.25). D-spacings and identifications are shown in Table 4.1.

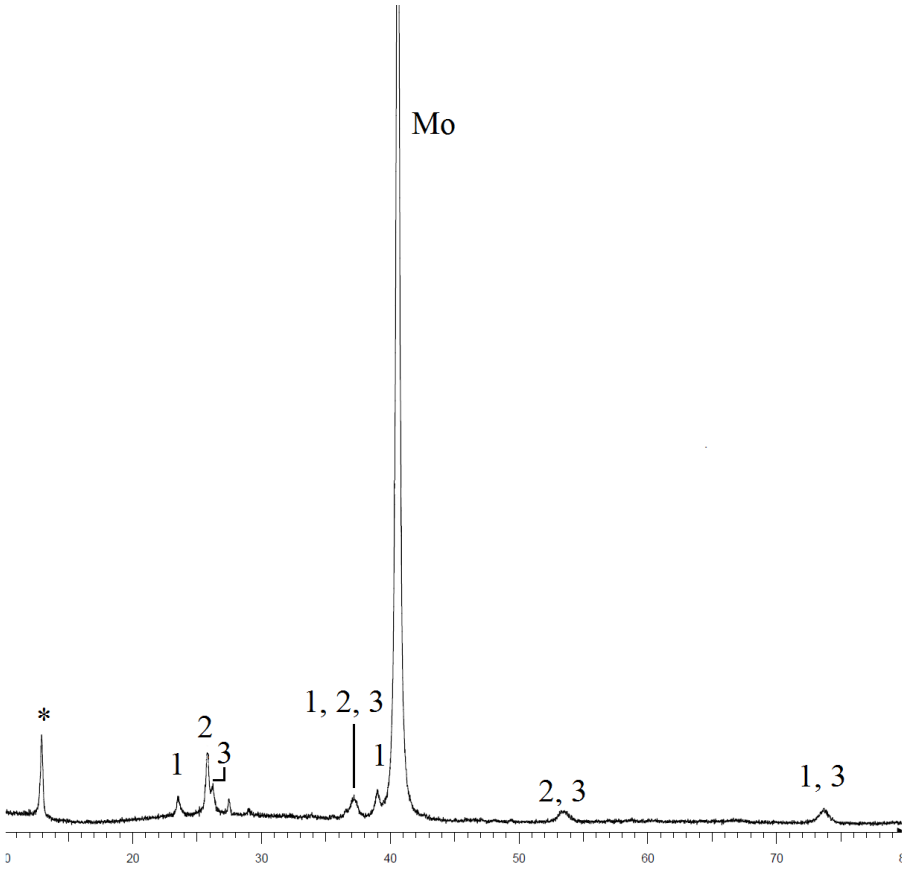

Figure 4.25 PXRD of film grown from **(22)** and **(24)**

Table 4.1 PXRD peaks and information

D-spacing	Identification	D-spacing	Identification
6.90	Unknown	2.41	$CuSbS_2$ (0, 0, 6), Sb_2S_3 (2, 1, 3), Cu_2S (1, 0, 2)
3.78	$CuSbS_2$ (1, 0, 3)	2.30	$CuSbS_2$ (0, 1, 5)
3.46	Sb_2S_3 (1, 1, 1)	1.72	Sb_2S_3 (2, 2, 2), Cu_2S (1, 1, 2)
3.40	Cu_2S (0, 0, 2)	1.28	$CuSbS_2$ (3, 2, 4), Cu_2S (2, 1, 1)

Indexing is to $CuSbS_2$ PDF 88-0822, Sb_2S_3 PDF 78-1347, Cu_2S PDF 84-0209

$Sb[S_2CN(Me)Bn]_3$, **(23)** and $(Ph_3P)_2CuS_2CN(Me)Bn$, **(25)** have very similar decomposition pathways, with gradual weight loss from *ca* 175°C and decomposition finishing by 330°C (Figure 4.26). Films were grown at 400°C using **(23)** (0.33mmol) and **(25)** (0.33mmol) in THF (50ml) for a duration of 2 hours onto Mo coated glass.

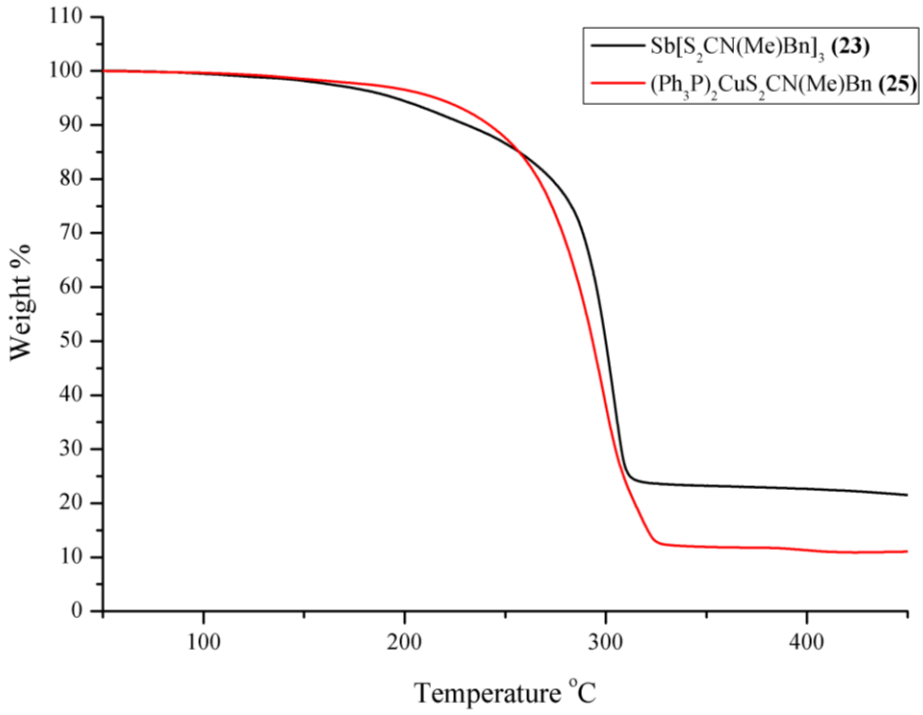

Figure 4.26 TGA of **(23)** and **(25)** with a heating rate of 5°C/min

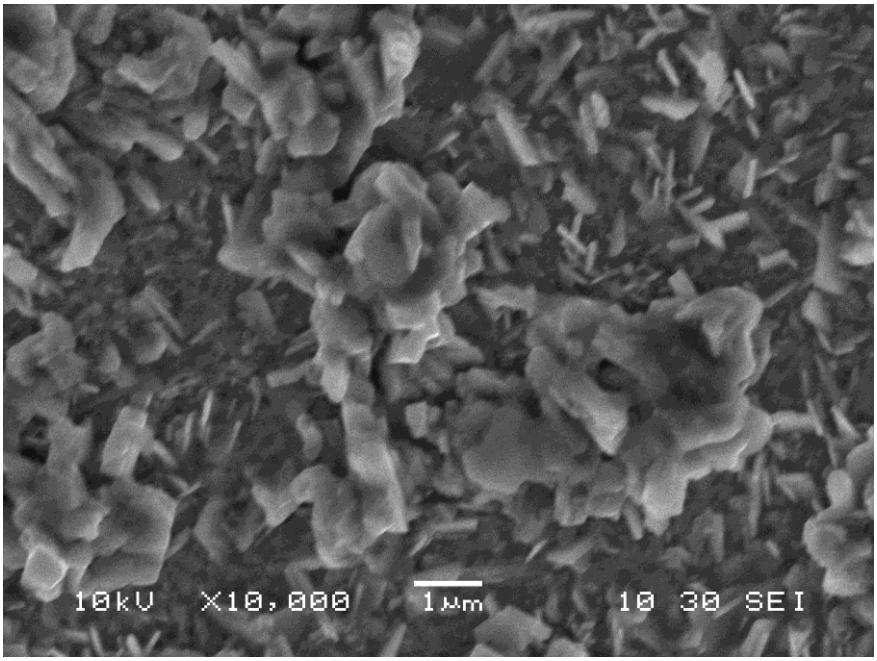

Figure 4.27 SEM Image of film grown from **(23)** and **(25)**

Films were black and looked powdery. SEM imaging reveals a textured film with smaller (0.5 - 1µm) rhomboidal crystallites visible on the surface of the film (Figure 4.27). Larger (2 - 5µm) structures have grown on the surface of the films, these are very angular but have no distinct geometry. EDX confirms the presence of Cu and Sb in a 1.0 : 1.1 ratio. This combination of precursors has given slightly Cu deficient films and a stoichiometry that is similar to the stoichiometry obtained using **(9)** and **(16)**. PXRD shows a mixture of phases, $CuSbS_2$ (labeled 1), Sb_2S_3 (labeled 2) and Cu_2S (labeled 3) (Figure 4.28). D-spacings and identifications are shown in Table 4.2.

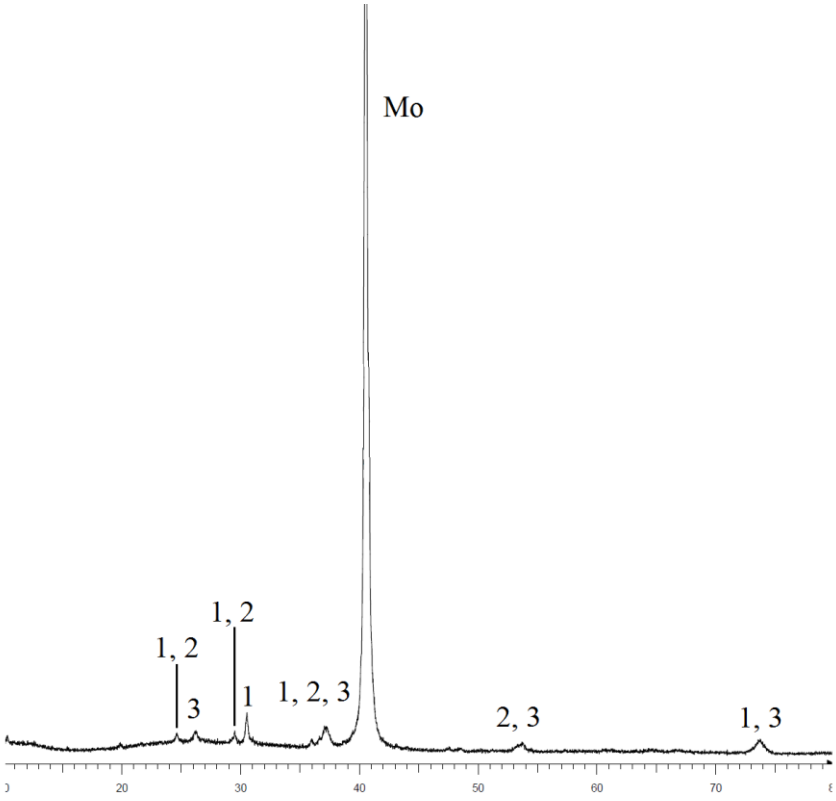

Figure 4.28 PXRD of film grown from **(23)** and **(25)**

Table 4.2 PXRD peaks and information

D-spacing	Identification	D-spacing	Identification
3.62	$CuSbS_2$ (0, 0, 4), Sb_2S_3 (1, 1, 0)	2.42	$CuSbS_2$ (0, 0, 6), Sb_2S_3 (2, 1, 3), Cu_2S (1, 0, 2)
3.40	Cu_2S (0, 0, 2)	1.71	Sb_2S_3 (2, 2, 2), Cu_2S (1, 1, 2)
3.03	$CuSbS_2$ (2, 0, 0), Sb_2S_3 (1, 1, 2)	1.28	$CuSbS_2$ (3, 2, 4), Cu_2S (2, 1, 1)
2.93	$CuSbS_2$ (1, 1, 2)		

Indexing is to $CuSbS_2$ PDF 88-0822, Sb_2S_3 PDF 78-1347, Cu_2S PDF 84-0209

4.2.4 AACVD of $CuSbS_2$ using salts and thiurea

Following work to deposit thin films of Cu_2ZnSnS_4 via spray pyrolysis of CuI, $Zn(O_2CMe)_2$, $SnCl_2$ and thioacetimide $[SC(NH_2)CH_3]$[24] it was decided to attempt a similar deposition of $CuSbS_2$ via AACVD of CuI (4.43mmol), $SbCl_3$ (4.43mmol) and thiurea $[SC(NH_2)_2]$ (44.34mmol) in EtOH (50ml). CVD was performed at a temperature of 250°C for 2 hours onto Mo coated glass.

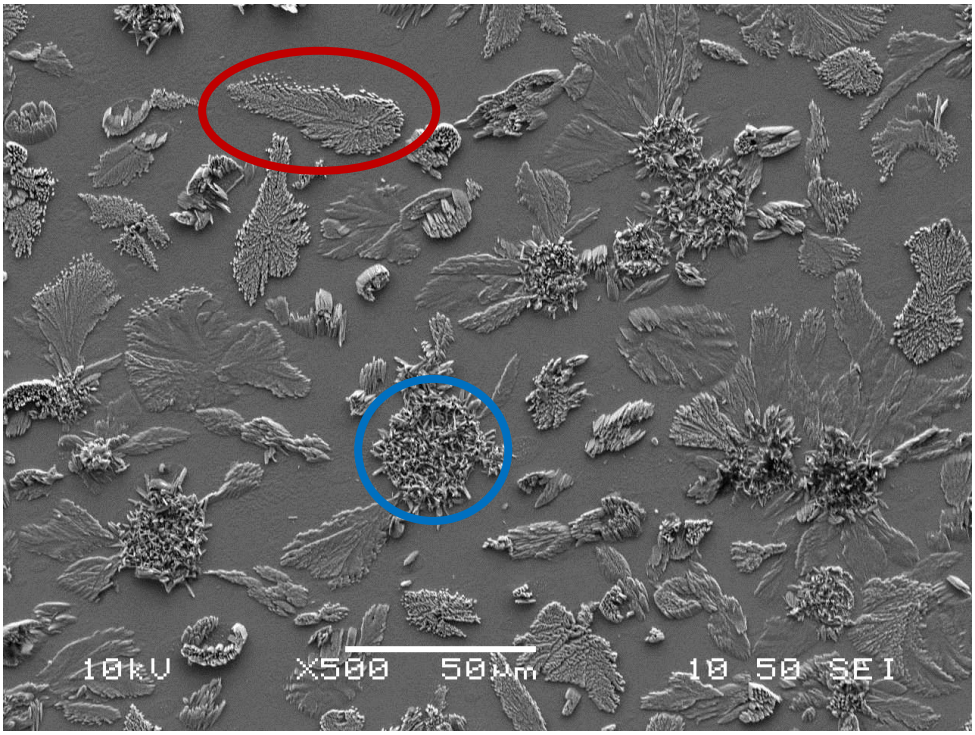

Figure 4.29 SEM image of film grown from CuI, $SbCl_3$ and thiurea

Films looked non-continuous and black, with crystallites visible to the eye on the surface of the glass. SEM imaging shows a non-continuous film with two distinct structures on the surface of the films; leaf shaped structures (highlighted in red) that range from 25 - 50µm in length and 10 - 25µm in width and spherical structures (highlighted in blue) which appear to have smaller crystallites growing horizontally from the surface of the glass and range from 20 - 40µm in diameter (Figure 4.29). EDX mapping shows that the leaf shaped structures contain Sb and S and the spherical structures contain Cu and S. PXRD of the films confirmed that the films consist of a mixture of Sb_2S_3 and CuS rather than the ternary phase $CuSbS_2$ (Figure 4.30.

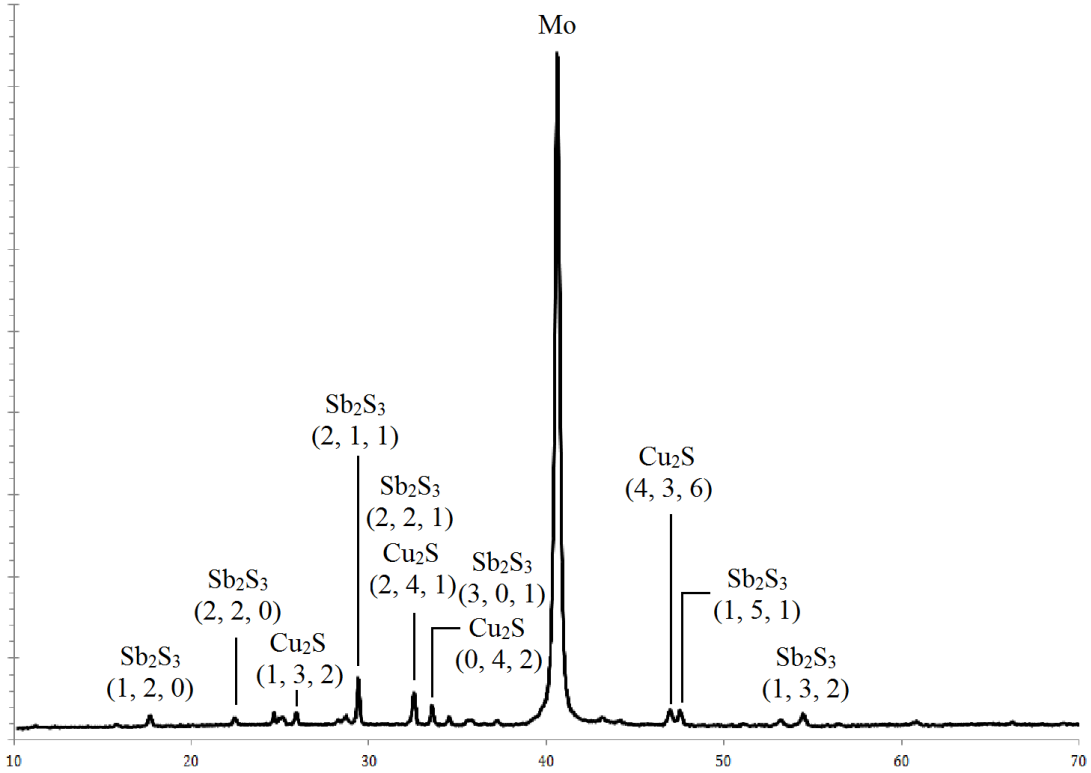

Figure 4.30 PXRD pattern from film grown using CuI, $SbCl_3$ and thiurea, indexing is to Cu_2S PDF 83-1462 and Sb_2S_3 PDF 06-0474

4.2.5 Doctor Blading of Cu_2ZnSnS_4

Doctor blading is a technique which involves the preparation of a precursor paste which is then applied to a glass slide with two pieces of tape on either side; the paste is then scraped away using a blade, leaving the precursor paste in a film which is approximately the same thickness as the tape. In this case the same xanthate precursors were used as had been previously using in CVD experiments. **(4)** (0.41mmol), **(7)** (0.41mmol) and **(16)** (0.82mmol) were dissolved in MeOH (30ml), PEG 6000 (0.04mmol) was added the solution stirred for 1 hour. MeOH was removed *in vacuo* and the resulting paste was applied to a glass microscope slide. The tape was removed and the sample annealed at 400°C for 30 minutes under N_2.

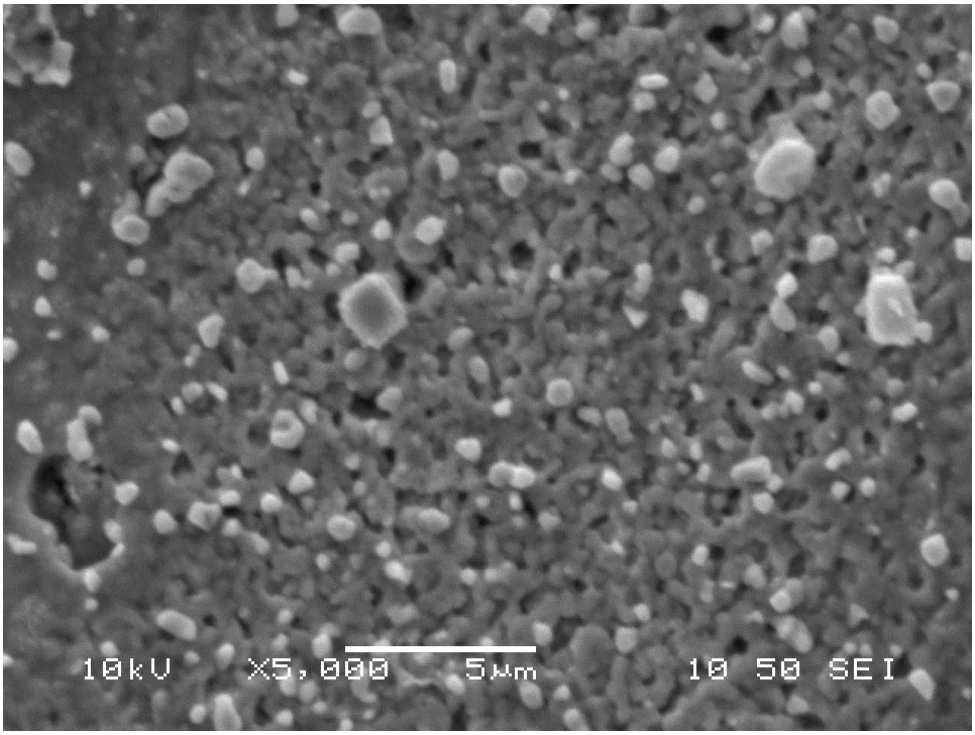

Figure 4.31 SEM image of doctor bladed film

Films were black in colour and looked very powdery with large cracks that were visible to the naked eye. SEM imaging shows the film in some parts was continuous with some pinholing (Figure 4.31). Crystallites ranging from 500nm - 2µm were sat on top of the surface of the film. The film itself has wide cracks running through it, up to 100 µm wide in places (Figure 4.32). These cracks had some material in them but not enough to make an overall continuous film. EDX confirmed the presence of Cu, Zn, Sn and S in a 2.0 : 1.1 : 1.0 : 3.6 ratio, giving a composition of $Cu_2Zn_{1.1}Sn_1S_{3.6}$. PXRD of the film showed a very complex powder pattern, corresponding to a mixture of ZnS or Cu_2ZnSnS_4 (labeled 1), Cu_2S (labeled 2) and SnS_2 (labeled 3) (Figure 4.33). Some peaks remain unidentified. D-spacings and peak identification are surmised in Table 4.3.

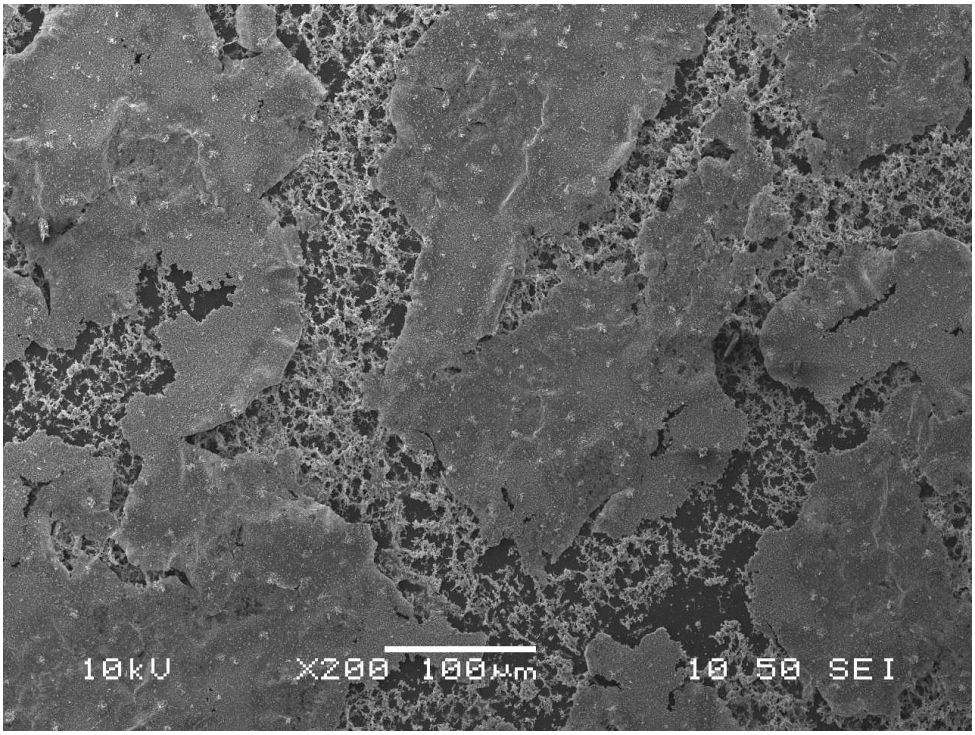

Figure 4.32 SEM image of doctor bladed film

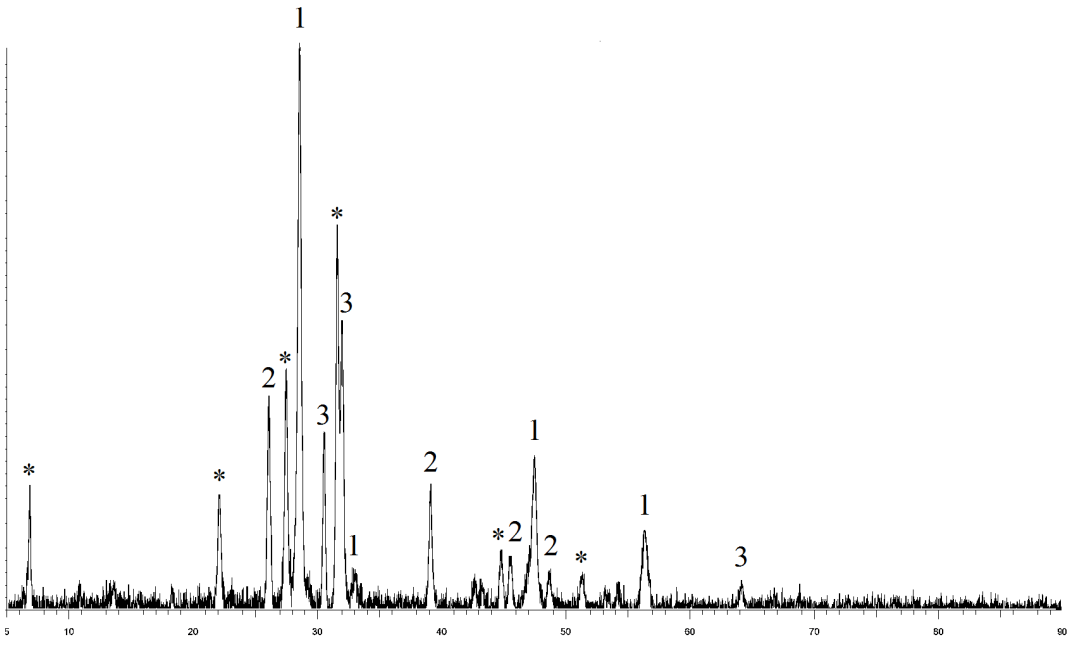

Figure 4.33 PXRD of film obtained from doctor blading

Table 4.3 PXRD peaks and identification

D-spacing	Identification	D-spacing	Identification
4.03	Unknown	2.31	Cu_2S (1, 0, 4)
3.42	Cu_2S (0, 0, 2)	2.02	Unknown
3.24	Unknown	2.00	Cu_2S (1, 1, 0)
3.13	ZnS (1, 1, 1) Cu_2ZnSnS_4 (1, 1, 2)	1.91	ZnS (2, 2, 0) Cu_2ZnSnS_4 (2, 2, 0)
2.93	SnS_2 (0, 0, 4)	1.88	Cu_2S (1, 0, 3)
2.84	Unknown	1.78	Unknown
2.79	SnS_2 (1, 0, 2)	1.63	ZnS (3, 1, 1) Cu_2ZnSnS_4 (1, 3, 2)
2.71	ZnS (2, 0, 0) Cu_2ZnSnS_4 (0, 2, 0)	1.45	SnS_2 (2, 0, 3)

Indexing is to SnS_2 PDF 89-3198, Cu_2S PDF84-0209, ZnS PDF 65-1691, Cu_2ZnSnS_4 PDF 34-1246

4.2.6 Synthesis of Cu_2ZnSnS_4 nanoparticles

The synthesis of nanoparticles from xanthate precursors followed a literature procedure for the formation of Cu_2ZnSnS_4 nanoparticles from dithiocarbamate precursors.[25] $Zn(S_2CO^nBu)_2$, **(4)**, (0.038mmol), $Sn(S_2COEt)_2$, **(7)**, (0.038mmol) and $(^nBu_3P)_2CuS_2CO^nBu$, **(16)**, (0.075mmol) were stirred together in 18ml octadecene and 2ml oleic acid and heated to 150°C; 3ml oleylamine was added to the solution and the temperature was maintained for 4 minutes after which solution was rapidly cooled in a water bath. When cool, 20ml EtOH was added to precipitate nanoparticles, the mixture centrifuged at 3500rpm for 10 minutes and the supernatant discarded. 20ml toluene was added for redisperse nanoparticles then 20 ml EtOH was added to reprecipitate the nanoparticles and the mixture was centrifuged again; this process was repeated 3 times. Nanoparticles were stored in toluene and analysed using TEM imaging and EDX measurements.

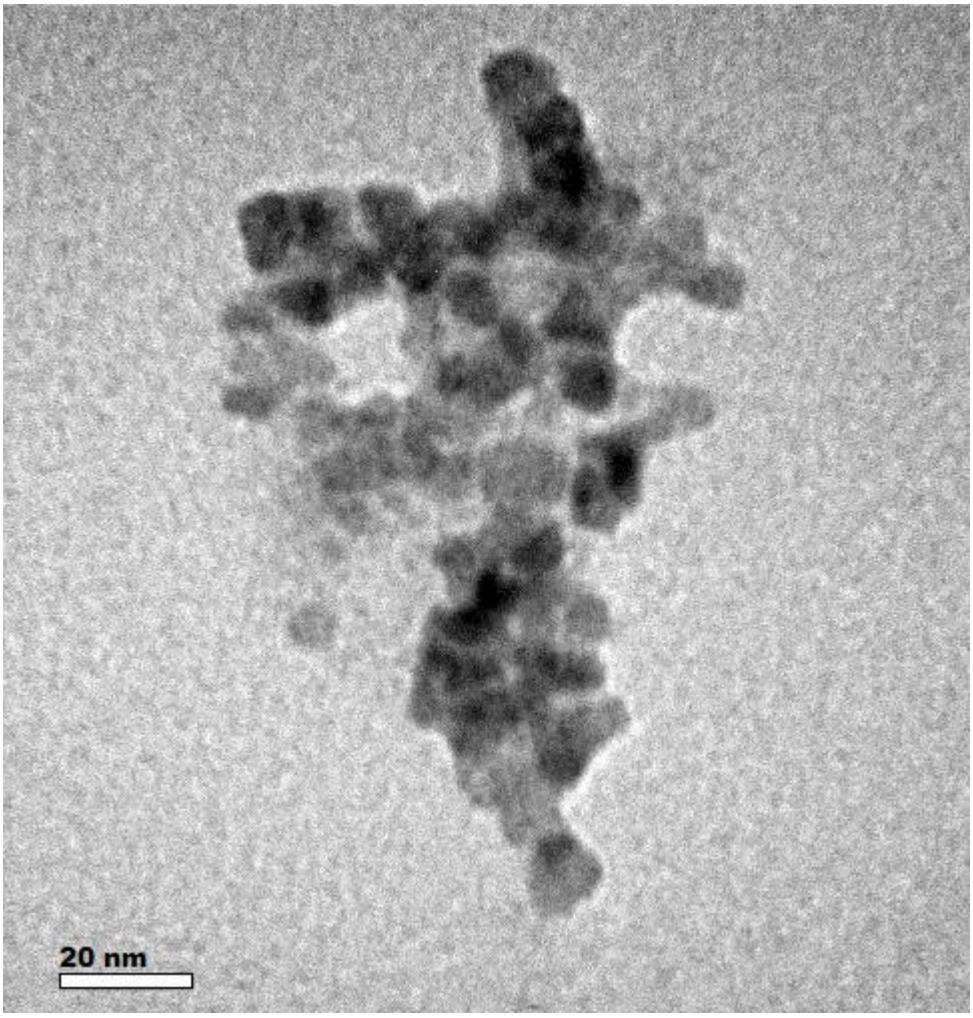

Figure 4.34 TEM image of nanoparticles

TEM imaging shows nanoparticle spheres ranging from 5 - 10nm (Figure 4.34). The nanoparticles don't have any distinct shape and electron diffraction showed them to be amorphous. EDX confirmed the presence of Cu, Zn, Sn and S in a ratio of 2.0 : 1.0 : 0.7 : 2.6. giving a formula of $Cu_2Zn_1Sn_{0.7}S_{2.6}$ for the nanoparticles; the stoichiometry of the metals is very close to the target stoichiometry, however the nanoparticles are sulphur deficient. The sulphur deficiency seen is not uncommon, generally when using a mixture of metal salts and elemental sulphur, a vast excess of sulphur is required to give the correct stoichiometry.[26]

4.2.6 Conclusions

As far as AACVD is concerned the best results came from using dithiocarbamate precursors. Using xanthates produced Cu deficient films in all cases. At first this was suspected to be due to a slower decomposition rate of the Cu xanthates due to the phopshine donors. However, raising the deposition temperature when using **(16)** with Sn and Zn or Sb dithiocarbamate precursors produced very thin films which were all Cu deficient with respect to Zn in the case of Cu_2ZnSnS_4 with no Sn detected in the films. In the case of $CuSbS_2$, thin films were also produced with roughly half the amount of Cu that there should have been in both cases.

For the deposition of thin films of Cu_2ZnSnS_4 using AACVD the combination of **(17)**, **(19)** and **(24)** produced films with the best stoichiometry, leaving a composition of $Cu_2Zn_{1.2}Sn_{0.7}S_x$ with the content of sulphur unknown due to the overlap of Mo and S in EDX measurements. Flashing LED experiments showed no photoactivity in the films so it is possible that either the films were too thin or the sulphur content was not correct.

For the deposition of $CuSbS_2$ by AACVD the combination of **(9)** and **(16)** or **(23)** and **(25)** produced films with the closest match in stoichiometry to the chosen material giving a composition of $Cu_1Sb_{1.1}S_x$ in both cases, once again with the content of sulphur unknown. No photoactivity was seen in either of these films so it is possible that either the sulphur stoichiometry was incorrect or these films were too thin.

In all cases AACVD deposition attempts were also made using glass substrates, therefore eliminating the overlap between S and Mo in EDX measurements but the films grown were far too thin for reliable measurements to be made.

Attempts to deposit $CuSbS_2$ using CuI, $SbCl_3$ and thiurea *via* AACVD only produced non continuous films of Sb_2S_3 and CuS. Doctor blading was also not successful with the films produced being non continuous and containing the individual sulphides rather than Cu_2ZnSnS_4.

Nanoparticle synthesis from **(4)**, **(7)** and **(16)** proved to be more successful, with 5 – 10nm particles produced with the composition $Cu_2Zn_1Sn_{0.7}S_{2.6}$. These particles could possibly be made into absorber layers by sintering onto conductive substrates as has been investigated previously with CdTe nanoparticles.[27] Subsequent annealing

in a sulphur environment could potentially eliminate the sulphur deficiency, this is a technique which has been used to introduce sulphur into films of the component metals deposited electrochemically to produce films of Cu_2ZnSnS_4 previously.[28]

4.3 Experimental

All AACVD experiments were performed on an Electro Gas CVD Rig using an ultrasonic bath to generate a nebular; further details of the apparatus are provided in the appendix. In a typical experiment the different precursors were dissolved in THF (50ml) in a stoichiometric mix (0.4 – 0.8mmol of each). Experiments were performed for a duration of 30 mins – 2 hours. The resulting films were analysed by SEM imaging, EXD measurements and PXRD with flashing LED experiments performed on the films with the most promising stoichiometry to determine whether they were photoactive. Details of the procedure for flashing LED experiments are provided in the appendix.

Synthesis of nanoparticles: **(4)** (0.038mmol), **(7)** (0.038mmol) and **(16)** (0.075mmol) were added to 18ml octadecene and 2ml oleic acid. The solution was degassed several times and heated to 150°C; all precursors dissolved leaving a brown solution. 3ml oleylamine was added to the solution and the temperature was maintained at 150°C for 4 minutes after which solution was rapidly cooled in a water bath. A dark brown suspension remained. When cool, 20ml EtOH was added to precipitate nanoparticles, the mixture centrifuged at 3500rpm for 10 minutes and the supernatant discarded. 20ml toluene was added for redisperse nanoparticles then 20 ml EtOH was added to reprecipitate the nanoparticles and the mixture was centrifuged again; this process was repeated 3 times. Nanoparticles were stored in toluene.

4.4 References

1. Ito, K.; Nakazawa, T., *Jpn. J. Appl. Phys.* **1988,** *27* (11), 2094.
2. Scragg, J. J.; Dale, P. J.; Peter, L. M., *Thin Solid Films* **2009,** *517* (7), 2481.
3. Guo, Q.; Hillhouse, H. W.; Agrawal, R., *J. Am. Chem. Soc.* **2009,** *131*, 11672.
4. Nakayama, N.; Ito, K., *Appl.Surf. Sci.* **1996,** *92*, 171.
5. Kurihara, M.; Berg, D.; Fischer, J.; Siebentritt, S.; Dale, P. J., *physica status solidi (c)* **2009,** *6* (5), 1241.
6. Ennaoui, A.; Lux-Steiner, M.; Weber, A.; Abou-Ras, D.; Kötschau, I.; Schock, H.-W.; R. Schurr; Hölzing, A.; Jost, S.; Hock, R.; Voß, T.; Schulze, J.; Kirbs, A., *Thin Solid Films* **2009,** *517* (7), 2511.
7. Yeh, M. Y.; Lee, C. C.; Wuu, D. S., *Journal of Sol-Gel Science and Technology* **2009,** *52* (1), 65.
8. Moriya, K.; Tanaka, K.; Uchiki, H., *Jpn. J. Appl. Phys. Part 1 - Regul. Pap. Brief Commun. Rev. Pap.* **2007,** *46* (9A), 5780.
9. Moriya, K.; Watabe, J.; Tanaka, K.; Uchiki, H., *physica status solidi (c)* **2006,** *3* (8), 2848.
10. Tanaka, T.; Kawasaki, D.; Nishio, M.; Guo, Q.; Ogawa, H., *Phys. Status Solidi* **2006,** *3* (8), 2844.
11. Weber, A.; Krauth, H.; Perlt, S.; Schubert, B.; Kötschau, I.; Schorr, S.; Schock, H. W., *Thin Solid Films* **2009,** *517*, 2524.
12. Tanaka, K.; Moritake, N.; Uchiki, H., *Sol. Energy Mater. Sol. Cells* **2007,** *91* (13), 1199.
13. Shin, B.; Gunawan, O.; Zhu, Y.; Bojarczuk, N. A.; Chey, S. J.; Guha, S., *Prog. Photovolt.* **2011**.
14. Ramasamy, K.; Malik, M. A.; O'Brien, P., *Chem. Commun.* **2012**.
15. Ramasamy, K.; Malik, M. A.; O'Brien, P., *Chemical Science* **2011,** *2* (6), 1170.
16. (a) Zhou, J.; Bian, G. Q.; Zhu, Q. Y.; Zhang, Y.; Li, C. Y.; Dai, J., *J. Solid State Chem.* **2009,** *182* (2), 259; (b) Rabhi, A.; Kanzari, M.; Rezig, B., *Thin Solid Films* **2009,** *517* (7), 2477.
17. Colombara, D.; Peter, L. M.; Rogers, K. D.; Painter, J. D.; Roncallo, S., *Thin Solid Films* **2011,** *519* (21), 7438.
18. Messina, S.; Nair, M. T. S.; Nair, P. K., *Thin Solid Films* **2007,** *515*, 5777.
19. Lazcano, Y. R.; Nair, M. T. S.; Nair, P. K., *J. Cryst. Growth* **2001,** *223*, 399.

20. Rabhi, A.; Kanzari, M.; Rezig, B., *Mater. Lett.* **2008,** *62*, 3576.
21. Rabhi, A.; Kanzari, M.; Rezig, B., *Thin Solid Films* **2009,** *517* (7), 2477.
22. Rodriguez-Lazcano, Y.; Nair, M. T. S.; Nair, P. K., *J. Electrochem. Soc.* **2005,** *152* (8), G635.
23. Rodriguez-Castro, J.; Mahon, M. F.; Molloy, K. C., *Chem. Vapor Depos.* **2006,** *12* (10), 601.
24. Fischereder, A.; Rath, T.; Haas, W.; Amenitsch, H.; Albering, J.; Meischler, D.; Larissegger, S.; Edler, M.; Saf, R.; Hofer, F.; Trimmel, G., *Chem. Mater.* **2010,** *22* (11), 3399.
25. Khare, A.; Wills, A. W.; Ammerman, L. M.; Norris, D. J.; Aydil, E. S., *Chem. Commun.* **2011,** *47* (42), 11721.
26. Steinhagen, C.; Panthani, M. G.; Akhavan, V.; Goodfellow, B.; Koo, B.; Korgel, B. A., *J. Am. Chem. Soc.* **2009,** *131* (35), 12554.
27. Jasieniak, J.; MacDonald, B. I.; Watkins, S. E.; Mulvaney, P., *Nano Lett.* **2011,** *11* (7), 2856.
28. Platzer-Björkman, C.; Scragg, J.; Flammersberger, H.; Kubart, T.; Edoff, M., *Sol. Energy Mater. Sol. Cells* **2012,** *98* (0), 110.

Chapter Five
Heterobimetallic Precursors

5.1 Introduction

This chapter describes attempts to make a series of heterobimetallic systems which contain two of the target metals for Cu_2ZnSnS_4 and $CuSbS_2$. The idea originates from reports of the synthesis of $(Ph_3P)_2CuInCl_4$ and the subsequent reaction to exchange the chlorine atoms with thiolate ligands (SR) as single-source precursors for $CuInS_2$.[1]

The possibility of a single-source precursor for the deposition of $CuInS_2$ was first investigated in 1993 with the synthesis of $(Ph_3P)_2CuIn(SEt)_4$ (Figure 5.1) and $(Ph_3P)_2CuIn(SBu^i)_4$. The structure contains copper and indium in a 1 : 1 ratio and sufficient sulphur to produce $CuInS_2$; TGA studies showed that on heating both compounds lost Ph_3P and RSR (R = Et, ^{i}Bu) to produce the desired compound at temperatures of 260°C and 396°C respectively.[2] This synthesis method was later adapted for the synthesis of a series of single-source precursors for the deposition of films of $CuInS_2$ and $CuInSe_2$ *via* AACVD.[3] These precursors have also been used to synthesise nanoparticles of $CuInS_2$ and $CuInSe_2$ via thermal decomposition in a non-coordinating solvent.[4]

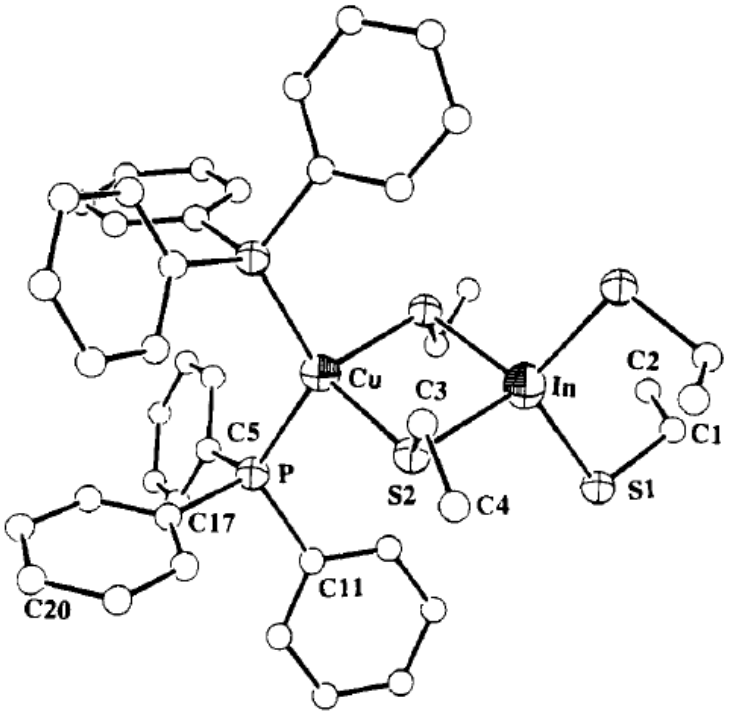

Figure 5.1 Structure of $(Ph_3P)_2CuIn(SEt)_4$[2]

The synthesis of $(Ph_3P)_2CuIn(SEt)_4$ was later refined to enable large quantities of the precursor to be made, which was previously problematic with the method developed initially. The initial method involved the addition of $InCl_3$ to KSR (R= Et, ^{i}Bu) to form $[InSR_4]K$ then the subsequent reaction with $[(Ph_3P)_2Cu(CH_3CN)_2]PF_6$.[2] In 2010 Margulieux *et al.* reported a new synthetic route which involved the synthesis and isolation of $(Ph_3P)_2CuInCl_4$ then the subsequent reaction with NaSEt to yield $(Ph_3P)_2CuIn(SEt)_4$. The advantages of this reaction are that large quantities of the product can be made and the Cl atoms can be replaced in a stepwise fashion by controlling the stoichiometry of the reaction to yield $(Ph_3P)_2CuInCl_3(SEt)$, $(Ph_3P)_2CuInCl_2(SEt)_2$ and$(Ph_3P)_2CuInCl(SEt)_4$ as well as $(Ph_3P)_2CuIn(SEt)_4$.[1] This method has also been used to yield heteroleptic complexes such as $(Ph_3P)_2CuIn(SePh)_2(SEt)_2$ which has potential application as a single-source precursors for the deposition of CuInSSe.[5]

The synthesis of precursors containing two of the target metals for Cu_2ZnSnS_4 and $CuSbS_2$ would alleviate some of the problems of matching precursor's decomposition temperatures, volatilities and solubilities as for Cu_2ZnSnS_4 only two precursors would be required and for $CuSbS_2$ the resulting precursor would be a single-source precursor.

5.1.1 Cu-S-Zn compounds

Compounds containing copper and zinc liked by a bridging sulphide group are uncommon in the literature. The synthesis of Cu[Zn(ecda)] (ecda = ethoxycarbonyl-1-cyanoethylene-2,2-dithiolate) was reported by Singh *et. al*; a study into the structure of the complex using IR, EPR and UV-Vis measurements led them to believe that the structure contains a bridging sulphide between the copper and zinc atoms.[6] A later study into the synthesis and characterisation of [ZnCu(cdc)] (cdc = cyanodithioimidocarbonate) revealed that the bonding is similar in this species too.[7]

5.1.2 Cu-S-Sn compounds

Similarly, reports of compounds containing Cu and Sn with a bridging sulphide are rare. In 2000 the first synthesis of such a compound was reported by Singh *et. al* with the synthesis of $[Bu_2Sn][Cu(ecda)_2]$; this compound was characterised using IR, EPR and UV-Vis measurements and was believed to contain a Cu-S-Sn centre.[8]

Another four similar complexes were also reported later in 2008, $[Me_2Sn][M(cdc)_2]$, $[^nBu_2Sn][M(cdc)_2]$, $[^nBu_3Sn]_2[M(cdc)_2]$ and $[Ph_3Sn]_2[M(cdc)_2]$.[9]

Only two other such compounds have been reported, $[(Ph_3P)_2Cu]_2SnS(edt)_2$ and $[(Ph_3P)Cu]_2Sn(SPh)_6$ (edt = 1,2-ethyldithiolate). These compounds have both been structurally characterised and contain thiolate groups that bridge between the copper and tin atoms.[10] The structure of $[(Ph_3P)Cu]_2Sn(SPh)_6$ is very close to the target structures that this chapter describes.

5.1.3 Cu-S-Sb compounds

There have only been a few reported compounds containing copper and antimony atoms that are linked by a bridging sulphide group. The first compound of this nature to be characterised is a copper(I) iodide complex which is stabilised by a triphenylstibine sulphide (Ph_3SbS) adduct.[11] The second class of compounds of this nature to be reported are a series of Cu(I)-Sb(III) coordination polymers that were synthesised using antimony(III) thiolates and CuSCN. Three compounds were synthesised and structurally characterised, namely $[Sb_2(edt)_2(\mu_3\text{-}S)CuCl(CuSCN)]_n$, $\{[Sb(edt)(pymt)]_2(CuSCN)_3\}_n$ and $[Sb(edt)(pymt)(CuCSN)_2]_n$ (edt = ethane-1,2-dithiolate, pymt = 2-pyrimidinethiol). All of these structures contain Cu(I) and Sb(III) atoms that are linked via a sulphide bridge (Figure 5.2).[12]

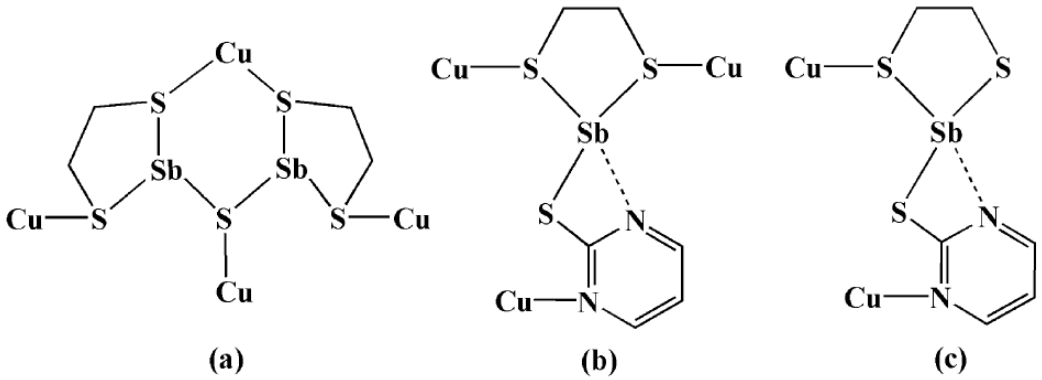

Figure 5.2 Coordination in (a) $[Sb_2(edt)_2(\mu3\text{-}S)CuCl(CuSCN)]_n$, (b) $\{[Sb(edt)(pymt)]_2(CuSCN)_3\}_n$ and (c) $[Sb(edt)(pymt)(CuCSN)_2]_n$[12]

5.2 Results and Discussion

5.2.1 Zn/Cu Heterobimetallic Species

$(Ph_3P)_4CuZnCl_4$ **(26)** was synthesised following a literature method for the synthesis of $(Ph_3P)_2CuInCl_4$.[1] $ZnCl_2$ and $(Ph_3P)_2CuCl$ were heated in toluene at 80°C for 4 hours. The resulting white crystals were characterised by microanalysis and NMR. $(Me_3P)_2Cu_2ZnCl_4$ **(27)** and $[(Me_3P)_4Cu]^+[ZnCl_4Cu(Me_3P)_2]^-$ **(28)** were synthesised using a modified version of the synthesis of **(26)** using $ZnCl_2$, CuCl and Me_3P and heating to 60°C in toluene for 1 hour**. (28)** was synthesised using an excess of Me_3P as there was less Me_3P in the structure obtained from **(27)** than was expected (Scheme 5.1). NMR could only confirm the presence of the phopshine groups as there are no other organic components in the molecule so the identification of **(26)** – **(28)** was reliant on crystallography and microanalysis.

$$ZnCl_2 + 2(Ph_3P)_2CuCl \xrightarrow[80^oC,\ N_2]{tol} (Ph_3P)_4Cu_2ZnCl_4\ \mathbf{(26)}$$

$$ZnCl_2 + 2CuCl + 4Me_3P \xrightarrow[60^oC,\ N_2]{tol} [(Me_3P)_2Cu_2Cl_4Zn]_n\ \mathbf{(27)}$$

$$ZnCl_2 + 2CuCl + 6Me_3P \xrightarrow[60^oC,\ N_2]{tol} [(Me_3P)_4Cu]^+[ZnCl_4Cu(PMe_3)_2]^-\ \mathbf{(28)}$$

Scheme 5.1 Synthesis of **(26)** – **(28)**

Crystals of **(26)** were obtained on slow cooling of the reaction to room temperature. The initial reaction was performed on a Zn : Cu, 1 : 1 basis, however the structure obtained always contained 2 molecules of Cu and 1 molecule of Zn (Figure 5.3); the procedure was later modified to a 1 : 2 basis to improve the yield.

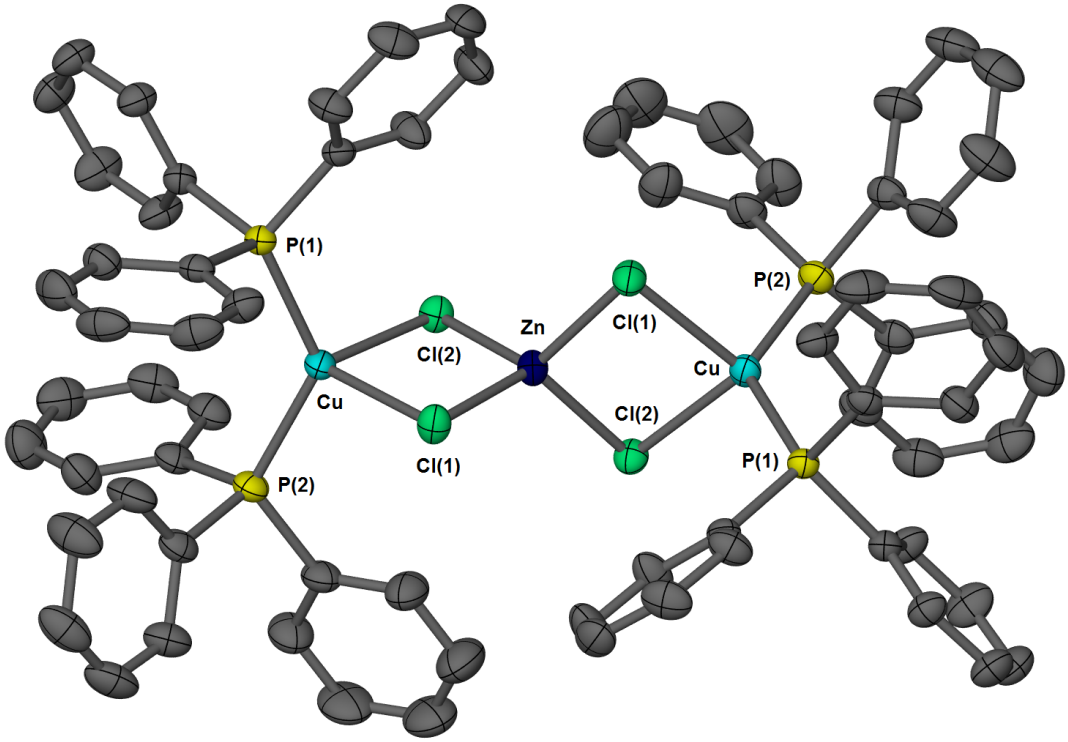

Figure 5.3 Structure of **(26)**, thermal ellipsoids drawn at 50% probability

The structure of **(26)** contains one Zn atom which grows to form a dimer containing two $Cu(Ph_3P)_2$ fragments which are joined to the Zn atom by bridging Cl atoms. The Zn atoms has a distorted tetrahedral geometry with bond angles ranging from 101.647(16)° – 123.294(17)°. The Cu atoms also demonstrate a distorted tetrahedral geometry with bond angles ranging from 92.154(16)° – 129.90(2)°. The increase in distortion seen in the Cu atom's geometry could be due to the steric crowding from the Ph_3P groups as the largest angle is seen between P(1) – Cu – P(2).

In both cases the Cl atoms are bridging over two metals with Zn-Cl bond lengths of 2.2709(5)Å and 2.2902(5)Å and longer Cu-Cl bond lengths of 2.4535(5)Å and 2.4555(5)Å. The Cu-P bond lengths are the same within experimental error, 2.2539(5)Å in Cu-P(1) and 2.2522(5)Å in Cu-P(2). Selected bond distances are described in Table 5.1. It appears that there are no other structures with a $CuCl_2Zn$ core in the literature.

Table 5.1 Selected bond distances (Å) in **(26)**

	(26)
Zn-Cl(1)	2.2709(5)
Zn-Cl(2)	2.2902(5)
Cu-Cl(1)	2.4555(5)
Cu-Cl(2)	2.2539(5)
Cu-P(1)	2.4535(5)
Cu-P(2)	2.2522(5)

Crystals of **(27)** were obtained on slow cooling of the reaction to room temperature. The structure is polymeric in the solid state with two Cu atoms and one Zn atom in the asymmetric unit (Figure 5.4). The two Cu atoms are three-coordinate, exhibiting a distorted trigonal planar geometry with bond angles ranging from 102.42(2)° – 139.36(2)° for Cu(1) and 100.85(2)° – 142.64(2)° for Cu(2); the Zn atom is four-coordinate and exhibits distorted tetrahedral geometry with bond angles ranging from 106.16(21)° – 112.64(3)°.

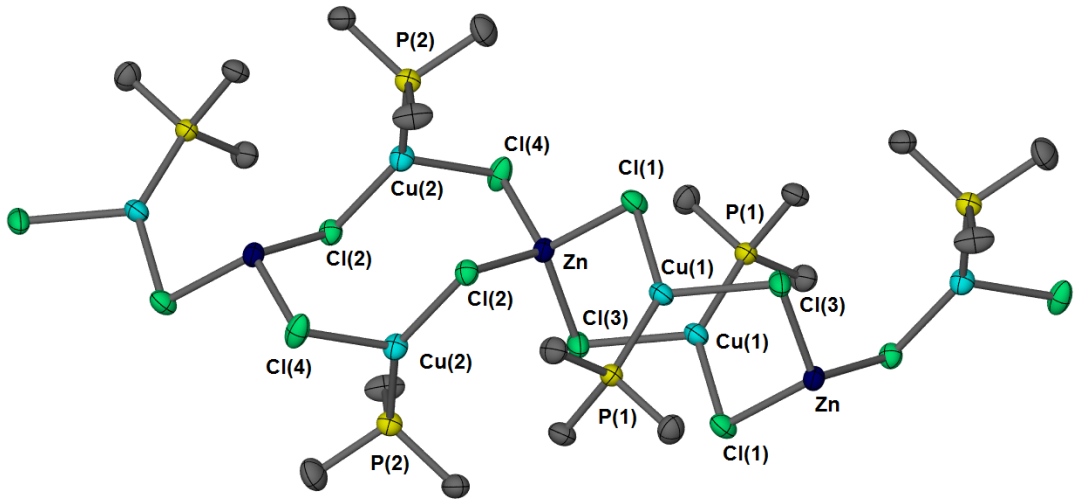

Figure 5.4 Structure of **(27)**, thermal ellipsoids drawn at 50% probability

All Cl bridge over one Zn centre and one Cu centre. There are two longer Zn-Cl bond lengths [Zn-Cl(1): 2.2927(6) and Zn-Cl(2): 2.2885(6)] and two shorter Zn-Cl bond lengths [Zn-Cl(3): 2.2563(6) and Zn-Cl(4): 2.2547(6)]. These are mirrored in the Cu-Cl bond lengths with two shorter bonds seen in Cu(1)-Cl(1) and Cu(2)-Cl(2) [2.2688(6), 2.2639(6); respectively] and two longer bonds seen in Cu(1)-Cl(3) and

Cu(2)-Cl(4) [2.3710(6) and 2.3849(6) respectively]. The Cu-P bond lengths are slightly different, 2.1913(6) in Cu(1)-P(1) and 2.1772(6) in Cu(2)-P(2). Selected bond lengths are shown in Table 5.2.

Table 5.2 Selected bond distances (Å) in **(27)**

	(27)
Zn-Cl(1)	2.2927(6)
Zn-Cl(2)	2.2885(6)
Zn-Cl(3)'	2.2563(6)
Zn-Cl(4)'	2.2547(6)
Cu(1)-Cl(1)	2.2688(6)
Cu(1)-Cl(3)	2.3710(6)
Cu(2)-Cl(2)	2.2639(6)
Cu(2)-Cl(4)	2.3849(6)
Cu(1)-P(1)	2.1913(6)
Cu(2)-P(2)	2.1772(6)

Crystals were obtained on cooling a solution of **(28)** in toluene to -20°C (Figure 5.5).

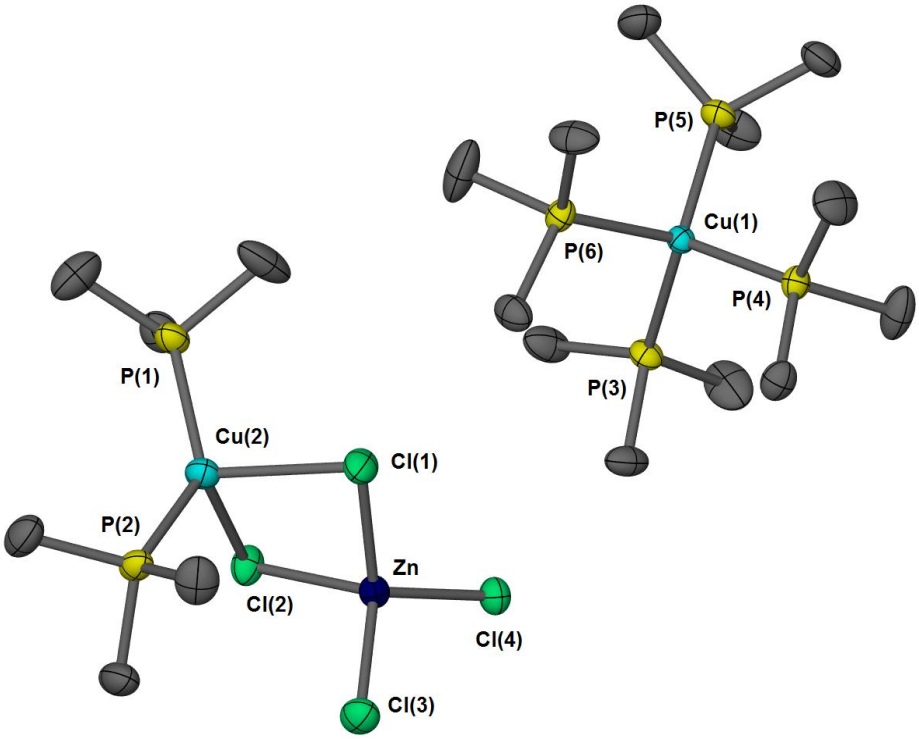

Figure 5.5 Structure of **(28)**, thermal ellipsoids drawn at 50% probability

Table 5.3 Selected bond distances (Å) in **(28)**

	(28)
Zn-Cl(1)	2.3266(6)
Zn-Cl(2)	2.3397(7)
Zn-Cl(3)	2.2458(7)
Zn-Cl(4)	2.2387(7)
Cu(2)-Cl(1)	2.5024(7)
Cu(2)-Cl(2)	2.4282(7)
Cu(2)-P(1)	2.2227(7)
Cu(2)-P(2)	2.2255(7)
Cu(1)-P(3)	2.2716(6)
Cu(1)-P(4)	2.2715(7)
Cu(1)-P(5)	2.2721(7)
Cu(1)-P(6)	2.2661(6)

The structure of **(28)** is a salt and contains an ion pair, $[Cu(Me_3P)_4]^+[ZnCl_4Cu(Me_3P)_2]^-$; in this case the addition of an excess of Me_3P changed the structure considerably. The $[Cu(Me_3P)_4]^+$ part of the structure contains an almost perfectly tetrahedral Cu atom, with bond angles ranging from 109.03(3)° – 111.69(5)°. The Cu-P bond distances are all very similar, ranging from 2.2661(6)Å – 2.2728(7)Å. $[Cu(Me_3P)_4]^+$ is a known cation and has been reported structurally with halide counter ions,[13] a copper alkyl counter ion,[14] a copper chloride counter ion,[15] as a counter ion to copper clusters[16] and to tantalum clusters.[17]

The $[ZnCl_4Cu(Me_3P)_2]^-$ part contains a $ZnCl_2Cu$ core which is very similar to that seen in **(26)**. It contains one distorted tetrahedral Zn atom and one distorted tetrahedral Cu atom with bond angles ranging from 90.00(2)° – 135.51(3)° and 96.70(2)° – 115.91(3)°; respectively. Of the four Cl atoms, two are bonded solely to the Zn atom and two bridge over the Zn and Cu atoms. The terminal Cl atoms exhibit shorter Zn-Cl bond lengths, 2.2458(7)Å and 2.2387(7)Å for Zn-Cl(3) and Zn-Cl(4), respectively. The μ_2-Cl atoms exhibit longer Zn-Cl bond lengths and longer still Cu-Cl bond lengths, 2.3266(6)Å and 2.3397(7)Å for Zn-Cl(1) and Zn-Cl(2), respectively and 2.5024(7)Å and 2.4282(7)Å for Cu(2)-Cl(1) and Cu(2)-Cl(2), respectively. The Cu-P bond lengths are very similar, 2.2227(7)Å and 2.2255(7)Å

for Cu(2)-P(1) and Cu(2)-P(2), respectively. Selected bond distances are shown in Table 5.3.

5.2.3 Sn/Cu heterobimetallic species

(29) and **(30)** were synthesised using the same reaction scheme as **(26)** and **(27)** (Scheme 5.2). $SnCl_2$ was heated to either 80°C with $(Ph_3P)_2CuCl$ [in the synthesis of **(29)**] or to 60°C with CuCl and Me_3P [in the synthesis of **(30)**]. Once again the determination of the products was reliant on crystallography and microanalysis and NMR could only confirm the presence of the phosphine donors.

$$SnCl_2 + (Ph_3P)_2CuCl \xrightarrow[80^oC,\ N_2]{tol} (Ph_3P)_2CuSnCl_3\ \mathbf{(29)}$$

$$SnCl_2 + CuCl + 2Me_3P \xrightarrow[60^oC,\ N_2]{tol} (Me_3P)_3CuSnCl_3\ \mathbf{(30)}$$

Scheme 5.2 Synthesis of **(29)** and **(30)**

Crystals of **(29)** were obtained on from the slow cooling of the reaction to room temperature (Figure 5.6).

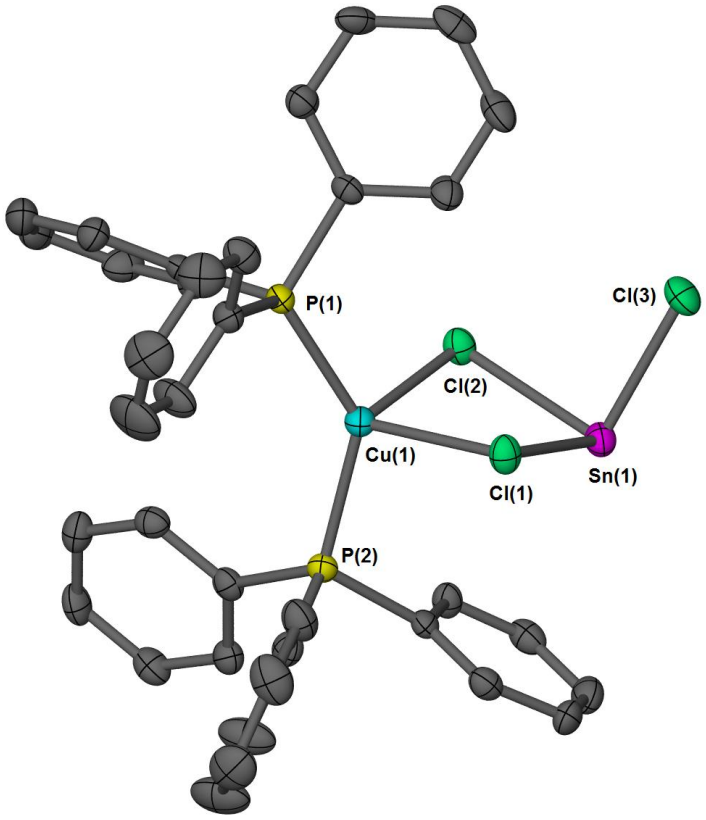

Figure 5.6 Structure of **(29)**, thermal ellipsoids drawn at 50% probability

The structure of **(29)** is monomeric with one three-coordinate Sn atom and one four-coordinate Cu atom. The Sn atom shows a very distorted trigonal pyramidal structure with bond angles ranging from 85.40(3)° – 92.89(4)° which indicated that the lone pair is stereochemically active, forcing the Cl atoms closer than expected. The Cu atoms adopts distorted tetrahedral geometry with bond angles ranging from 88.67(4)° – 135.81(4)°, a higher level of distortion than is seen in the structure of **(26)**. Again, the largest angle is between the two phosphine groups.

There are two μ_2-Cl atoms [Cl(1) and Cl(2)] and one terminal Cl atom [Cl(3)]; the μ_2-Cl atoms exhibit Sn-Cl bond lengths of 2.5402(10)Å and 2.5680(11)Å and shorter Cu-Cl bond lengths of 2.4516(11)Å and 2.5052(12)Å. The terminal Cl atom has an Sn-Cl bond length of 2.4562(12)Å, shorter than the Sn-Cl bond lengths displayed by the μ_2-Cl atoms but similar to the Cu-Cl bond lengths seen. Once again, the Cu-P bond lengths are very similar, 2.2448(11) and 2.2534(12) for Cu – P(1) and Cu – P(2) respectively. Selected bond distances are shown in Table 5.4. It appears that there are no other structures in the literature that have a $CuCl_2Sn$ core.

Table 5.4 Selected bond distances (Å) in **(29)**

	(29)
Sn-Cl(1)	2.5680(11)
Sn-Cl(2)	2.5402(10)
Sn-Cl(3)	2.4562(12)
Cu-Cl(1)	2.4516(11)
Cu-Cl(2)	2.5052(12)
Cu-P(1)	2.2448(11)
Cu-P(2)	2.2534(12)

Crystals of **(30)** were obtained by heating the white precipitate obtained on cooling the reaction mixture to room temperature to 100°C and then cooling slowly to room temperature in an oil bath. **(30)** was characterised by microanalysis and NMR as well as structural analysis.

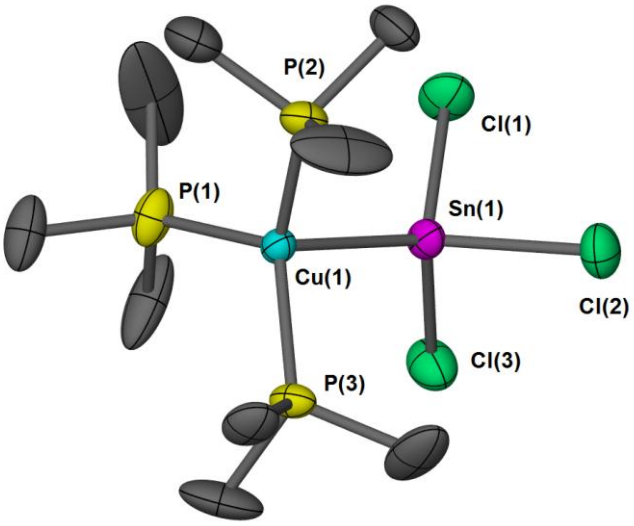

Figure 5.7 Structure of **(30)**, thermal ellipsoids drawn at 50% probability

The structure of **(30)** contains four inequivalent but essentially similar molecules of $(Me_3P)_3CuSnCl_3$ in the unit cell (Figure 5.7). This structure is very different from all the others reported in this chapter as it contains a direct Sn-Cu bond. In this case the Sn is acting as a 2 electron donor between $SnCl_3^-$ and $(Me_3P)_3Cu^+$. This kind of bonding interaction is unusual but not unheard of, both $Ar(SiMe_3)SnCu(SiMe_3)$ (Ar = $C_6H_3Mes_2$-2,6) and $MeB[3-(CF_3)Pz]_3CuSn(Cl)(Bn_2ATI)$ (Pz = pyrazolyl, Bn_2ATI = N-benzyl-2-(benzylamino)-troponiminate) have Sn(II)→Cu(I) bonds with bond lengths of 2.4992(5)Å and 2.4540(4)Å, respectively.[18] In **(30)**, the Sn-Cu bond distances do not differ much over the four molecules, ranging from 2.5662(14)Å – 2.6160(15)Å, slightly longer than the bond lengths seen in literature. There has also been a Sn(IV)-Cu(I) complex reported, $Ph_3SnCu(LPr)$ [LPr = 1,3-bis(2,6- diisopropylphenyl)imidazol-2-ylidene)], which has an Sn-Cu bond length of 2.469(5).[19]

A comparison of selected bond distances in the different molecules is detailed in Table 5.5 and the structure of a single molecule is shown in Figure 5.7. All Sn atoms are tetrahedral and exhibit a distorted structure with bond angles ranging from 95.75(13)° – 124.33(9)°, 95.26(14)° – 123.92(10)°, 96.53(13)° – 120.96(9)° and 94.69(12)° – 123.58(8)° for Sn(1), Sn(2), Sn(3) and Sn(4) respectively. In a similar fashion all Cu atoms exhibit a tetrahedral geometry which is distorted to a much lesser extent than is seen in the Sn atoms with bond angles ranging from 98.55(10)° -

117.41(15)°, 100.22(9)° - 117.67(19)°, 101.37(9)° – 118.94(12)° and 100.15(13)° - 118.24(13)° for Cu(1), Cu(2), Cu(3) and Cu(4) respectively.

The Sn-Cl bond distances are all very similar, ranging from 2.420(3)Å - 2.444(3)Å. Similarly the Cu-P bond distances are also very similar, ranging from 2.242(3)Å - 2.264(3)Å with not much variation seen both in the individual molecules and across all four molecules in the unit cell.

Table 5.5 Selected bond distances (Å) in **(30)**

Sn(1)-Cu(1)	2.5997(14)	**Sn(3)-Cu(3)**	2.5662(14)
Sn(2)-Cu(2)	2.6160(15)	**Sn(4)-Cu(4)**	2.6002(14)
Sn(1)-Cl(1)	2.435(3)	**Sn(3)-Cl(7)**	2.428(3)
Sn(1)-Cl(2)	2.426(3)	**Sn(3)-Cl(8)**	2.424(3)
Sn(1)-Cl(3)	2.444(3)	**Sn(3)-Cl(9)**	2.430(3)
Sn(2)-Cl(4)	2.420(3)	**Sn(4)-Cl(10)**	2.425(3)
Sn(2)-Cl(5)	2.441(4)	**Sn(4)-Cl(11)**	2.422(3)
Sn(2)-Cl(6)	2.443(4)	**Sn(4)-Cl(12)**	2.428(3)
Cu(1)-P(1)	2.264(3)	**Cu(3)-P(7)**	2.248(3)
Cu(1)-P(2)	2.242(3)	**Cu(3)-P(8)**	2.248(3)
Cu(1)-P(3)	2.250(3)	**Cu(3)-P(9)**	2.245(3)
Cu(2)-P(4)	2.247(4)	**Cu(4)-P(10)**	2.246(3)
Cu(2)-P(5)	2.258(3)	**Cu(4)-P(11)**	2.262(3)
Cu(2)-P(6)	2.253(3)	**Cu(4)-P(12)**	2.247(3)

5.2.3 Sb/Cu heterobimetallic species

(31) and **(32)** were synthesised using the same method as **(26)** and **(29)**. **(31)** was synthesised in the 1 : 1 reaction between $(Ph_3P)_2CuCl$ and $SbCl_3$ and **(32)** was synthesised in the 3 : 1 reaction between $(Ph_3P)_2CuCl$ and $SbCl_3$ in toluene at 80°C (Scheme 5.3). NMR confirmed the presence of the phosphine groups and microanalysis confirmed the empirical formula of both.

$$SbCl_3 + (Ph_3P)_2CuCl \xrightarrow[80^oC,\ N_2]{tol} [(Ph_3P)_2CuSbCl_4]_2 \textbf{ (31)}$$

$$SbCl_3 + 3(Ph_3P)_2CuCl \xrightarrow[80^oC,\ N_2]{tol} (Ph_3P)_3CuSbCl_4 \textbf{ (32)}$$

Scheme 5.3 Synthesis of **(31)** and **(32)**

Crystals were obtained from slow evaporation of a solution of **(31)** in THF. Crystals of **(32)** were obtained from cooling the reaction to -20°C. Interestingly, both have Cu and Sb in a 1 : 1 ratio but **(31)** forms a dimeric structure (Figure 5.8) whereas **(32)** is monomeric and has obtained an extra PPh_3 group (Figure 5.9), presumably from unreacted $(Ph_3P)_2CuCl$, that has decomposed in solution, leaving an additional Ph_3P group to bond to the copper. Table 5.6 surmises selected bond distances from the structure of **(31)** and **(32)**. A literature search revealed no other structures with Cu-Cl-Sb units.

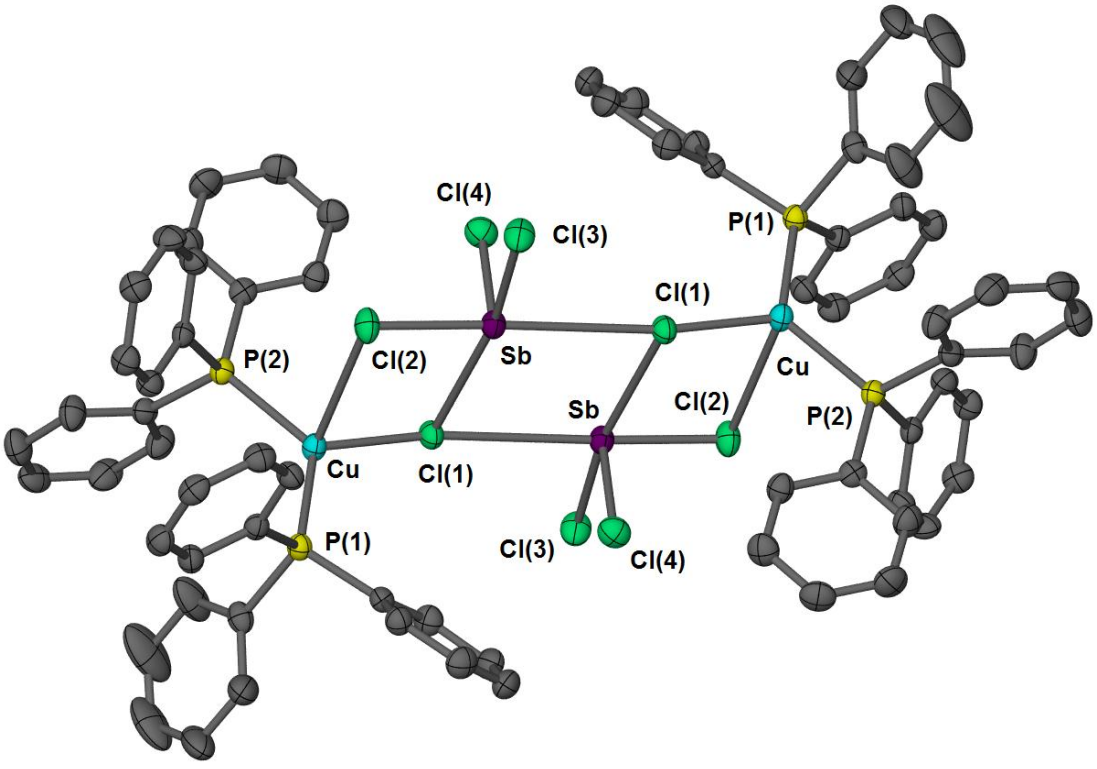

Figure 5.8 Structure of **(31)**, thermal ellipsoids drawn at 50% probability

The structure of **(31)** is a dimer with two Sb atoms and two Cu atoms, four Ph_3P groups, and eight Cl atoms. The Sb atom is five-coordinate and has a τ value of 0.13,

making the geometry slightly distorted square-based pyramid with Cl(4) axial and Cl(1), Cl(1)', Cl(2) and Cl(3) forming the base. τ values are a means to measure the degree of square-based pyramid geometry *vs.* trigonal bipyramidal geometry; Addison *et. al* devised a formula to measure this: $\tau = (\alpha - \beta)/60$ where α = largest angle and β = second largest angle. Where τ is 0, the geometry is square-based pyramidal and where τ is 1 the geometry is trigonal bipyramidal.[20] The Cu atom is four-coordinate and exhibits a distorted tetrahedral geometry with bond angles ranging from 81.91(2)° – 124.46(3)°.

Of the four Cl atoms, two are terminal, bonded solely to Sb, one is μ_2, bridging over one Sb and one Cu atom and one is μ_3, bridging over two Sb atoms and one Cu atom. Cl(3) and Cl(4) which are solely bonded to Sb have bond distances of 2.3474(8)Å and 2.3875(8)Å, respectively. Cl(2), which is bridging between Sb and Cu, has one shorter Sb-Cl contact [2.3899(7)Å] and one longer Cu-Cl contact [3.0070(9)Å]. The μ_3-Cl atom sits closer to the Cu atom with a Cu-Cl bond distance of 2.3129(7)Å and longer Sb-Cl contacts of 3.0736(7)Å and 3.211(6)Å. The Cu-P bond distances are the same within experimental error, 2.2668(8)Å and 2.2701(8)Å.

Table 5.6 Comparison of bond distances (Å) in **(31)** and **(32)**

	(31)		**(32)**
Sb-Cl(1)	3.0736(7)	**Sb-Cl(1)**	2.8005(9)
Sb-Cl(2)	2.3899(7)	**Sb-Cl(2)**	2.4473(10)
Sb-Cl(3)	2.3875(8)	**Sb-Cl(3)**	2.3549(11)
Sb-Cl(4)	2.3474(8)	**Sb-Cl(4)**	2.3474(10)
Cu-Cl(1)	2.3129(7)	**Cu-Cl(1)**	2.4240(9)
Cu-Cl(2)	3.0070(9)		
Cu-P(1)	2.2701(8)	**Cu-P(1)**	2.3402(10)
Cu-P(2)	2.2668(8)	**Cu-P(2)**	2.3532(9)
		Cu-P(3)	2.3244(10)

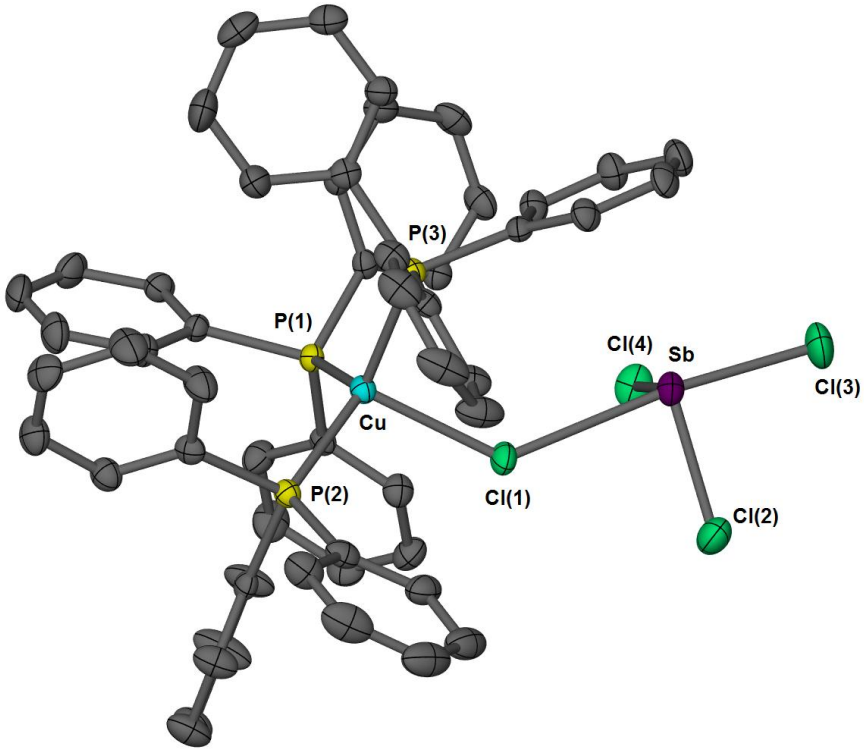

Figure 5.9 Structure of **(32)**, thermal ellipsoids drawn at 50% probability

The structure of **(32)** is monomeric which could be due to the steric crowding of the extra Ph_3P group, leaving no space for another molecule to coordinate with the Sb as is seen in the structure of **(31)**. There also appears to be an interaction between the lone pair of Sb and one phenyl ring which is bent directly over the Sb centre with a bond distance of 3.366Å between the Sb and the ring centroid (Figure 5.10). Interactions between aromatic rings and the Sb lone pair have been previously reported in literature in the structures of $SbCl_3$-Et_6C_6,[21] $SbBr_3$-9,10-dihydroanthracene,[22] $(MesSb)_4$-C_6H_6[23] and $SbCl_3$-1,4-bis(2-mercaptoethyl)benzene[24] with very different distances reported between the antimony and the ring centroid (2.96Å, 3.81Å, 3.27Å and 3.19Å, respectively). The distance seen in the structure of **(32)** is within the range of the previously reported values for Sb-Ph interactions.

The Sb is four-coordinate with a trigonal bipyramidal geometry with Cl(1) Cl(3) and Cl(4) in an almost planar arrangement and bond angles between Cl(2)-Sb-Cl(1), Cl(2)-Sb-Cl(3) and Cl(2)-Sb-Cl(4) being 83.73(3)°, 90.13(4)° and 96.45(4)°, respectively.

Of the four Cl atoms, only one is bridging over two different centres, the other three are bonded only to Sb. Of the terminal Cl atoms, there are two with very similar Sb-Cl bond distances, Cl(3) and Cl(4) [2.3549(11)Å and 2.3474(10)Å

respectively] and one, Cl(2), with a slightly longer Sb-Cl distance [2.4473(10)Å]. A similar, but not as marked, effect is seen in the structure of **(31)** with Cl(3) and Cl(4) differing in Sb-Cl bond lengths. Cl(1) bridges over the Cu and the Sb and has a shorter Cu-Cl bond distance [2.4240(9)] than the Sb-Cl bond distance [2.8005(9)], this is also seen in the structure of **(31)** but the asymmetry in bond lengths is larger in this structure.

The Cu-P bond lengths are longer than seen in the structure of **(31)**; this is probably due to the steric effect of an extra Ph_3P group which would force the Ph_3P groups further away from the Cu centre.

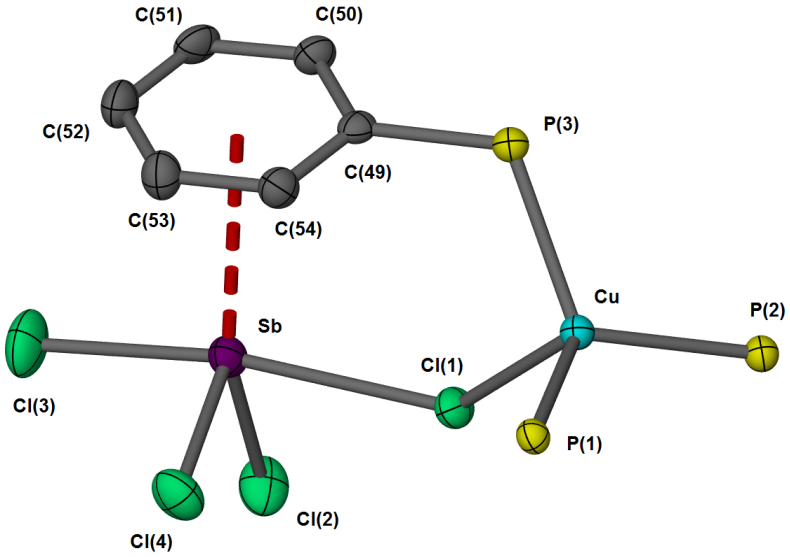

Figure 5.10 Structure of **(32)**, showing Ph-Sb interaction, thermal ellipsoids drawn at 50% probability

An attempt to synthesise a similar compound to **(31)** and **(32)** but with Me_3P donors rather than Ph_3P donors was attempted in a similar fashion to the synthesis of **(27)** and **(30)**; $SbCl_3$, CuCl and Me_3P were heated to 60°C in toluene and left to cool slowly. Initially, the reaction yielded yellow crystals which were discovered to be twinned, these were heated to 100°C and cooled slowly to try to improve their quality, however on cooling a yellow precipitate remained with some colourless crystals on the side of the Schlenk. These were structurally characterised and identified as **(33)**, $[Sb_2Cl_9]^{3-}[(Me_3P)_2Cu]^{+}[HPMe_3]_2^{+}$ which appears to be a minor hydrolysis product (Figure 5.11).

The reaction was repeated and appeared to yield a similar yellow product; once again the crystals were twinned and when heated to 100°C and cooled slowly

another minor product was obtained and structurally characterised from a few colourless crystals found within the yellow product, **(34)**, $[Sb_2Cl_7(Me_3P)_2]^-$ $[Cu(Me_3P)_4]^+$ (Figure 5.12).

Attempts to discover what the yellow precipitate were failed as NMR could only confirm the presence of Me_3P groups and microanalysis was inconclusive; structural analysis would be needed to confirm the identity of the yellow precipitate. As both **(33)** and **(34)** were only very minor products, only structural analysis could be carried out due to the small amount of product.

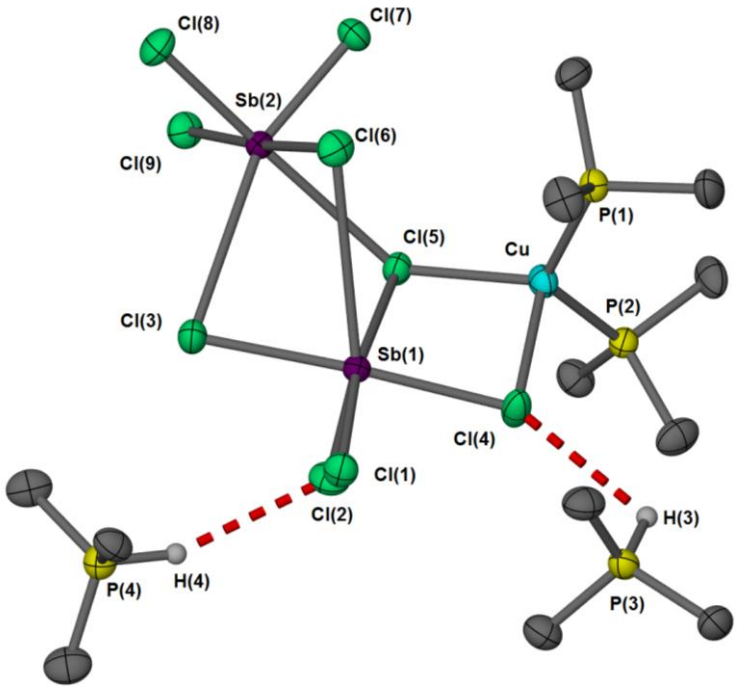

Figure 5.11 Structure of **(33)**, thermal ellipsoids drawn at 50% probability

The structure of **(33)** consists an $[Sb_2Cl_9]^{3-}$ anion which is coordinated to $[Cu(Me_3P)_2]^+$ via two Cl atoms; two $[HMe_3P]^+$ atoms are also hydrogen bonded to the $[Sb_2Cl_9]^{3-}$. Both Sb atoms exhibit a distorted octahedral geometry with adjacent bond angles ranging from 73.26 (3)°– 115.48(3)° and 77.56(3)° – 106.96(3)° and axial bond angles ranging from 148.65(3)° – 174.21(4)° and 158.91(3)° – 175.97(4)° for Sb(1) and Sb(2), respectively. It is unclear in this structure where the Sb lone pair is pointing. The Cu atom has a distorted tetrahedral geometry with bond angles ranging from 94.30(4)° - 122.80(4)°.

Of the nine Cl atoms in the structure, five are bonded solely to an Sb atom, two bridge over the two Sb centres, one bridges over one Sb atom and the Cu atom and

one bridges over both Sb centres and the Cu centre. The terminal Cl atoms have Sb-Cl bond lengths ranging from 2.3741(11)Å – 2.5890(11)Å, while the μ_2-Cl atoms have longer bond lengths, ranging from 2.4951(11)Å – 2.6163(11)Å with one very long Sb-Cl contact between Sb(2) and Cl(6) of 3.6159(12)Å. Cl(5). The only μ_3-Cl atom, has even longer Sb-Cl bond distances, 2.9692(10)Å and 3.0897(10)Å between Sb(1) and Sb(2), respectively. The Cu-Cl bond distances are odd in that the shorter bond distance comes from the interaction with Cl(5), the μ_3-Cl atom, at 2.3979(11)Å with the longer bond distance of 2.5931(12)Å arising from the interaction between Cu and Cl(4).

The Cu-P bond distances are the same, 2.2391(12)Å and 2.2337(12)Å for Cu-P(1) and Cu-P(2) respectively. There are two hydrogen bonds in the structure, between Cl(2) and H(4) and Cl(4) and H(3), measuring 2.72(5)Å and 2.80(4)Å, respectively.

Table 5.7 Selected bond distances (Å) in **(33)**

	(33)
Sb(1)-Cl(1)	2.4441(10)
Sb(1)-Cl(2)	2.3741(11)
Sb(1)-Cl(3)	2.6327(10)
Sb(1)-Cl(4)	2.5907(10)
Sb(1)-Cl(5)	2.9692(10)
Sb(1)-Cl(6)	3.6159(12)
Sb(2)-Cl(3)	3.4951(11)
Sb(2)-Cl(5)	3.0897(10)
Sb(2)-Cl(6)	2.6163(11)
Sb(2)-Cl(7)	2.3893(10)
Sb(2)-Cl(8)	2.4196(11)
Sb(2)-Cl(9)	2.5890(11)
Cu-Cl(4)	2.5931(12)
Cu-Cl(5)	2.3979(11)
Cu-P(1)	2.2391(12)
Cu-P(2)	2.2337(12)
Cl(2)-H(4)	2.72(5)
Cl(4)-H(3)	2.80(4)

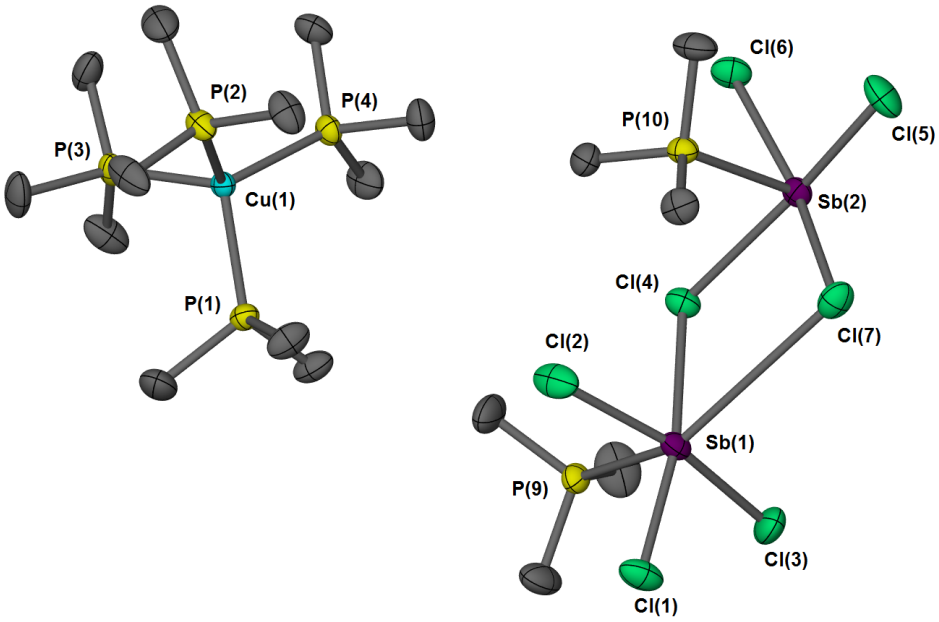

Figure 5.12 Structure of **(34)**, thermal ellipsoids drawn at 50% probability

Table 5.7 Selected bond distances (Å) in **(34)**

	(34)		**(34)**
Sb(1)-Cl(1)	2.4733(12)	**Sb(3)-Cl(8)**	2.5147(12)
Sb(1)-Cl(2)	2.5490(13)	**Sb(3)-Cl(9)**	2.6180(13)
Sb(1)-Cl(3)	2.6062(13)	**Sb(3)-Cl(10)**	2.5683(14)
Sb(1)-Cl(4)	2.8634(10)	**Sb(3)-Cl(11)**	2.5782(13)
Sb(1)-Cl(7)	3.7852(15)	**Sb(3)-Cl(13)**	3.5275(12)
Sb(2)-Cl(4)	2.8580(12)	**Sb(4)-Cl(11)**	3.0336(11)
Sb(2)-Cl(5)	2.4567(13)	**Sb(4)-Cl(12)**	2.4106(13)
Sb(2)-Cl(6)	2.6552(12)	**Sb(4)-Cl(13)**	2.5938(12)
Sb(2)-Cl(7)	2.5323(11)	**Sb(4)-Cl(14)**	2.5960(13)
Sb(1)-P(9)	2.5833(12)	**Sb(3)-P(11)**	2.5782(13)
Sb(2)-P(10)	2.5807(11)	**Sb(4)-P(12)**	2.5856(11)
Cu(1)-P(1)	2.2672(11)	**Cu(2)-P(5)**	2.2649(12)
Cu(1)-P(2)	2.2651(11)	**Cu(2)-P(6)**	2.2724(12)
Cu(1)-P(3)	2.2553(12)	**Cu(2)-P(7)**	2.2723(12)
Cu(1)-P(4)	2.2572(12)	**Cu(2)-P(8)**	2.2680(13)

The structure of **(34)** consists of two inequivalent but essentially the same molecules of $[Sb_2Cl_7(Me_3P)_2]^-[Cu(Me_3P)_4]^+$. The $[Sb_2Cl_7(Me_3P)_2]^-$ anion has two Sb atoms joined by a bridging Cl atom, each bonded to three other Cl atoms and a Me_3P group, with a $[Cu(Me_3P)_4]^+$ cation to balance the charge (Figure 5.12). Sb(1) is six-coordinate, exhibiting a very distorted octahedral geometry with opposite angles ranging from 144.97(3)° – 167.13(4)° and adjacent angles ranging from 66.74(3)° - 125.85(4)°. The high degree of distortion is probably due to the stereochemically active lone pair which would force the Cl atoms closer together than expected. Sb(2) is five-coordinate and exhibits a slightly distorted square-based pyramidal geometry with a τ value[20] of 0.07 and the four Cl atoms forming the base of the pyramid with the Me_3P group in the axial position. In the case of Sb(2) the lone pair is probably pointing away from the base of the pyramid. The Cu atom exhibits almost perfect tetrahedral geometry with bond angles ranging from 107.78(5)° – 111.77(4)° for Cu(1).

In each $[Sb_2Cl_7(Me_3P)_2]^+$ molecule there are five Cl atoms bonded solely to Sb atoms and two bridging Cl atoms. The terminal Cl atoms have Sb-Cl bond distances ranging from 2.4106(13)Å – 2.6552(12)Å over both molecules. The bridging Cl atoms display different degrees of symmetry, with one [Cl(4)] exhibiting Sb-Cl bond distances that are the same within experimental error [2.8580(12)Å and 2.8634(10)Å], and one [Cl(7)] with one much longer contact and one short contact [2.5323(11)Å and 3.7852(15)Å].

All Cu-P bond distances are also very similar, ranging from 2.2553(12)Å – 2.2724(12)Å. Selected bond distances are shown in Table 5.7. Similarly, the Sb-P bond distances are all very similar, ranging from 2.5782(13)Å – 2.5856(11)Å. Structures containing an Sb-P bond are uncommon in the literature. Most structures with monodentate phopshine ligands bonded to an antimony centre are cationic, such as $[(Me_3PSbPh_2)_4X]^+$ (X = Cl, Br),[25] $[(Ph_3P)_nSbPh_2]^+$ (n = 1, 2)[26] and $[(Me_3P)_2SbCl_2]^+$.[27] One neutral complex containing monodentate phopshine ligand has been reported, $[SbI_3(PMe_3)]_n$ although other structures with bidentate phosphine ligands such as 1,2- bis(dimethylphosphino)ethane have also been reported.[28] The only anionic structure containing monodentate phopshine ligands bonded to an antimony centre is the structure of $[Sb_2Br_7(PEt_3)_2]^-$ which is stabilised by a $[PEt_3H]^+$ cation. This structure is very similar to the structure of **(34)**, although in this structure three Br atoms bridge over the two Sb centres with two terminal Br atoms

on each Sb. In the structure of $[Sb_2Br_7(PEt_3)_2]^-$ $[PEt_3H]^+$ the Sb-P bond distances are exactly the same, both 2.637(5)Å; these are longer than the bond distances seen in the structure of **(34)**.[29]

5.2.4 Reactions with NaSEt and $(TMS)_2S$

Attempts to exchange the Cl atoms with NaSEt were undertaken following a literature method for the synthesis of $(Ph_3P)_2CuIn(SEt)_4$.[1] **(26)**, **(27), (29), (30)** or **(31)** were added to a slurry of NaSEt in toluene and heated to 80°C (Scheme 5.4). It was decided not to use **(32)** as this is more sterically hindered than **(31)** and so would be more difficult to replace the Cl atoms with SEt groups.

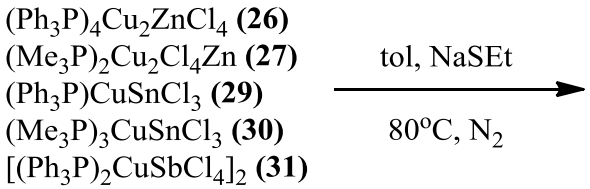

Scheme 5.4 Reactions with NaSEt

This synthesis method was later changed to first dissolving the NaSEt in EtOH and adding this to **(26)**, **(27), (29), (30)** or **(31)** in toluene; this was because NaSEt is not readily soluble in toluene but is readily soluble in EtOH and it was decided that having all the starting materials in solution is much more favourable (Scheme 5.5).

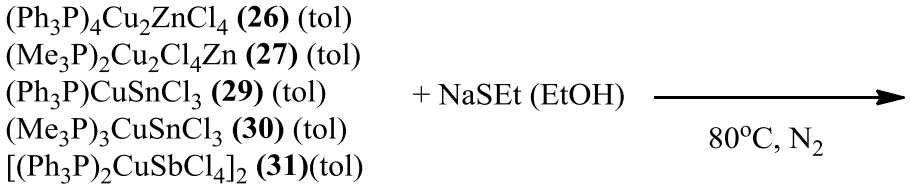

Scheme 5.5 Further reactions with NaSEt

In all cases crystals were obtained on slow cooling to room temperature, however all crystals were of either $(Ph_3P)_2CuCl$ [in the synthesis using **(26)**, **(29)** and **(31)**] or $(Me_3P{=}O)CuCl$ [in the synthesis using **(27)** and **(30)**] and not the desired products. Presumably, the reaction with NaSEt had not led to the replacement of Cl atoms but instead the $(Ph_3P)_2CuCl$ or $(Me_3P)_xCuCl$ appears to have dissociated from

the other metal chloride and in the case of $(Me_3P)_xCuCl$ this has oxidised to form $(Me_3P{=}O)CuCl$.

As attempts using NaSEt were unsuccessful it was decided to try using $(TMS)_2S$ (TMS = $SiMe_3$) to exchange two Cl atoms with one S atom, leaving TMSCl as a by-product. A similar method to the original method attempted was used; $(TMS)_2S$ was added to a suspension of **(26)**, **(29)** or **(30)** in toluene and heated to 80°C (Scheme 5.6). In all cases the starting material decomposed, leaving a copper coloured metallic residue at the bottom of the Schlenk and a black/brown powder. The reaction was also attempted a room temperature but the outcome was the same.

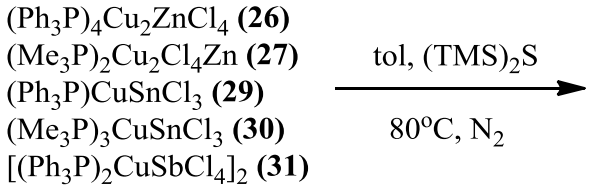

Scheme 5.6 Reactions with $(TMS)_2S$

Due to time constraints no further reactions to replace the Cl groups with sulphur containing ligands were attempted. However it seems likely that such systems could be made due to the success of the synthesis of both $(Ph_3P)_2CuIn(SEt)_4$ and $[(Ph_3P)Cu]_2Sn(SPh)_6$. Further work in this area is required to find a suitable synthesis method.

5.2.5 Conclusions

A range of heterobimetallic compounds have been made using $ZnCl_2$, $SnCl_2$ and $SbCl_3$ with Ph_3P and Me_3P adducts of CuCl. In the case of the Ph_3P adducts the structures were all similar with bridging Cl atoms; the structure of **(26)** was a surprise with a 2 : 1 stoichiometry of the Cu and Zn despite the synthesis using a 1 : 1 mixture of $ZnCl_2$ and $(Ph_3P)_2CuCl$. **(29)**, **(31)** and **(32)** all contain the two metals in a 1 : 1 stoichiometry. **(32)** was synthesised using a 3 : 1 ratio of $(Ph_3P)_2CuCl$ and $SbCl_3$ so the 1 : 1 ratio of Cu and Sb and the additional Ph_3P group was also a surprise, presumably the steric bulk of the Ph_3P groups hindered the formation of a 3 : 1 complex and the extra Ph_3P seen in the structure was from some unreacted, decomposed $(Ph_3P)_2CuCl$. In the reactions with Ph_3P adducts there are a mixture of monomers and dimers, **(29)** and **(30)** are monomeric whilst **(26)** and **(31)** are dimeric.

The use of Me_3P made the structures more unpredictable with a polymeric structure seen in **(27)** and a salt seen in **(28)**, which was essentially the same reaction but with an excess of Me_3P added. Both structures contain Cu and Zn in a 2 : 1 ratio which is expected as the reaction used CuCl and $ZnCl_2$ in a 2 : 1 ratio. **(30)** is a very interesting structure as the molecules contain a direct Sn-Cu bond which is very unusual. The ratio of Sn to Cu is 1 : 1 as expected but there is an excess of Me_3P which does not correlate with the amount added in the synthesis which would suggest that some $SnCl_2$ and CuCl remains unreacted. **(33)** and **(34)** are only minor products in the reaction between $SbCl_3$, CuCl and Me_3P show the unpredictability of using a more reactive donor such as Me_3P.

Any attempts to replace the Cl atoms with either $(SR)^-$ or S^{2-} groups were unsuccessful despite following the method used to replace Cl atoms with $(SEt)^-$ groups in the structure of $(Ph_3P)_2CuInCl_4$. As such, the precursors synthesised were not appropriate for attempts to deposit either Cu_2ZnSnS_2 or $CuSbS_2$ as they contain no sulphur in the structure and so materials studies were not performed.

5.3 Experimental

Synthesis of $(Ph_3P)_4Cu_2ZnCl_4$ ***(26)****:* $(Ph_3P)_2CuCl$ (1.00g, 1.61mmol) and $ZnCl_2$ (0.11g, 0.80mmol) were stirred together in toluene (50ml) at 80°C for 4 hours. After 4 hours all solid had dissolved. White crystals were obtained on slow cooling of the solution to room temperature (0.97g, 92%, mp 242-244°C). Analysis found (calc for $C_{72}H_{60}P_4Cl_4Cu_2Zn$): C 62.9 (62.7), H 4.44 (4.39). ^{1}H NMR (300 MHz, CD_2Cl_2) δ ppm: 7.04-7.86 (m, Ph), ^{13}C NMR (300 MHz, CD_2Cl_2) δ ppm: 134.5 (Ph), 133.0 (Ph), 130.4 (Ph), 129.18 (Ph), ^{31}P NMR (300 MHz, CD_2Cl_2) δ ppm: -3.48

Synthesis of $[(Me_3P)_2Cu_2Cl_4Zn]_n$ ***(27)****:* Me_3P (0.50g, 6.57mmol), CuCl (0.32g, 3.29mmol) and $ZnCl_2$ (0.22g, 1.64mmol) were stirred together in toluene (50ml) at 60°C for 1 hour. After 1 hour all solid had dissolved. White crystals were obtained on slow cooling of the solution to room temperature (0.42g, 53%, mp 120-124°C). Analysis found (calc for $C_6H_{18}P_2Cl_4Cu_2Zn$): C 14.9 (15.0), H 3.62 (3.77). ^{1}H NMR

(300 MHz, CD_2Cl_2) δ ppm: 1.27 (d, J=6.03 Hz, Me), ^{13}C NMR (300 MHz, CD_2Cl_2) δ ppm: 15.2 (d, J=19.9 Hz, Me), ^{31}P NMR (300 MHz, CD_2Cl_2) δ ppm: -45.14

Also prepared using the same method:

$[(Me_3P)_4Cu]^+[ZnCl_4Cu(PMe_3)_2]^-$ ***(28)****:* Using Me_3P (0.75g, 9.86mmol), CuCl (0.32g, 3.29mmol) and $ZnCl_2$ (0.22g, 1.64mmol). White crystals were obtained on cooling the solution to -20°C (0.73g, 56%, mp 74-75°C). Analysis found (calc for $C_{18}H_{54}P_6Cl_4Cu_2Zn$): C 26.5 (27.5), H 6.66 (6.92). ^1H NMR (300 MHz, CD_2Cl_2) δ ppm: 1.27 (d, *J*=4.14 Hz, Me), ^{13}C NMR (300 MHz, CD_2Cl_2) δ ppm: 15.4 (d, *J*=18.0 Hz, Me), ^{31}P NMR (300 MHz, CD_2Cl_2) δ ppm: -45.26

Synthesis of $(Ph_3P)_2CuCl_2SnCl$ ***(29)****:* $(Ph_3P)_2CuCl$ (0.50g, 0.80mmol) and $SnCl_2$ (0.15g, 0.80mmol) were heated in toluene at 80°C for 4 hours. Crystals were obtained on slow cooling of the solution to room temperature (0.52g, 79%, mp 163-165°C). Analysis found (calc for $C_{36}H_{30}P_2Cl_3CuSn$): C 53.3 (53.2), H 3.85 (3.72). ^1H NMR (300 MHz, CD_2Cl_2) δ ppm: 7.13-7.46 (m, Ph) ^{13}C NMR (300 MHz, CD_2Cl_2) δ ppm: 134.4 (d, *J*=15.0 Hz, Ph), 132.1 (d, *J*=31.0 Hz, Ph), 130.9 (s, Ph), 129.5 (d, *J*=9.3 Hz, Ph) ^{31}P NMR (300 MHz, CD_2Cl_2) δ ppm: -0.29 ^{119}Sn NMR (300 MHz, CD_2Cl_3) δ ppm: --67.55 (br)

Also prepared using the same method:

$(Me_3P)_3CuSnCl_3$ ***(30)****:* Using Me_3P (0.50g, 6.57mmol), CuCl (0.32g, 3.29mmol) and $SnCl_2$ (0.62g, 3.29mmol) at 60°C, yielding 0.75g, 66%, mp 205-207°C. Crystals suitable for diffraction were obtained by heating solution to 100°C and cooling slowly in oil bath. Analysis found (calc for $C_9H_{27}P_3Cl_3CuSn$): C 20.8 (20.9), H 5.34 (5.27). ^1H NMR (300 MHz, THF-d8) δ ppm: 1.36 (d, *J*=4.90 Hz) ^{13}C NMR (300 MHz, THF-d8) δ ppm: 17.2 (d, J=18.6 Hz), ^{31}P NMR (300 MHz, THF-d8) δ ppm: -40.90, ^{119}Sn NMR (400 MHz, 233K, THF-d8) δ ppm: -272.99 (br)

Synthesis of $(Ph_3P)_2CuCl_2SbCl_2$ ***(31)****:* $(Ph_3P)_2CuCl$ (0.50g, 0.80mmol) and $SbCl_3$ (0.18g, 0.80mmol) were stirred together in toluene (50ml) at 80°C for 4 hours. After 4 hours all solid had dissolved. After cooling to room temperature solvent was

removed *in vacuo* and remaining white solid was redissolved in THF. Slow evaporation gave colourless crystals (0.61g, 90%, mp 174-175°C). Analysis found (calc for $C_{36}H_{30}P_2Cl_4CuSb$): C 51.0 (51.0), H 3.68 (3.57). ^{1}H NMR (300 MHz, CD_2Cl_2) δ ppm: 7.24-7.50 (m, Ph) ^{13}C NMR (300 MHz, CD_2Cl_2) δ ppm: 134.4 (d, *J*=13.6 Hz, Ph), 132.1 (d, *J*=32.9 Hz, Ph), 131.0 (s, Ph), 129.5 (d, *J*=8.7 Hz, Ph) ^{31}P NMR (300 MHz, CD_2Cl_2) δ ppm: -0.66

Also prepared using the same method:

$(Ph_3P)_3CuCl_2SbCl_2$ ***(32)****:* $(Ph_3P)_2CuCl$ (1.50g, 2.40mmol) and $SbCl_3$ (0.18g, 0.80mmol) yielding 0.76g, 86%, mp 161-163°C on recystallisation from toluene at -20°C. Analysis found (calc for $C_{54}H_{45}P_3Cl_4CuSb$): C 58.3 (58.4), H 4.14 (4.09). ^{1}H NMR (300 MHz, CD_2Cl_2) δ ppm: 7.10-7.42 (m, Ph) ^{13}C NMR (300 MHz, CD_2Cl_2) δ ppm: 134.4 (d, *J*=14.9 Hz, Ph), 132.1 (d, *J*=27.3 Hz, Ph), 130.5 (d, *J*=1.2 Hz, Ph), 129.2 (d, *J*=9.3 Hz, Ph) ^{31}P NMR (300 MHz, CD_2Cl_2) δ ppm: -2.35

Synthesis of $[Sb_2Cl_9]^{3-}[(Me_3P)_2Cu]^+[HPMe_3]_2^+$ ***(33)****:* Me_3P (1g, 13.14mmol), CuCl (0.64g, 6.58mmol) and $SbCl_3$ (1.48g, 6.58mmol) were heated in toluene at 60°C for 1 hour. Redissolving the yellow precipitate formed by heating to 100C and leaving to cool slowly to room temperature produced a few colourless crystals.

Also prepared using the same method:

$[Sb_2Cl_7(Me_3P)_2]^-[Cu(Me_3P)_4]^+$ ***(34)****:* Using Me_3P (1g, 13.14mmol), CuCl (0.64g, 6.58mmol) and $SbCl_3$ (1.48g, 6.58mmol). A few crystals suitable for diffraction were obtained by heating solution to 100°C and cooling slowly in oil bath.

5.4 References

1. Margulieux, K. R.; Sun, C.; Zakharov, L. N.; Holland, A. W.; Pak, J. J., *Inorg. Chem.* **2010,** *49* (9), 3959.
2. Hirpo, W.; Dhingra, S.; Sutorik, A. C.; Kanatzidis, M. G., *J. Am. Chem. Soc.* **1993,** *115* (4), 1597.
3. Banger, K. K.; Jin, M. H. C.; Harris, J. D.; Fanwick, P. E.; Hepp, A. F., *Inorg. Chem.* **2003,** *42* (24), 7713.
4. Castro, S. L.; Bailey, S. G.; Raffaelle, R. P.; Banger, K. K.; Hepp, A. F., *Chem. Mater.* **2003,** *15* (16), 3142.
5. Sun, C.; Westover, R. D.; Margulieux, K. R.; Zakharov, L. N.; Holland, A. W.; Pak, J. J., *Inorg. Chem.* **2010,** *49* (11), 4756.
6. Singh, N.; Gupta, S., *Inorg. Chem. Commun.* **2000,** *3* (8), 446.
7. Singh, N.; Prasad, A.; Sinha, R. K., *Inorg. Chem. Commun.* **2006,** *9* (10), 1058.
8. Singh, N.; Kumar Rai, S., *Journal of Organometallic Chemistry* **2000,** *605* (1), 102.
9. Singh, N.; Kumar, A., *Synthetic Metals* **2008,** *158* (11), 442.
10. Wang, L.-S.; Sheng, T.-L.; Wang, X.; Chen, D.-B.; Hu, S.-M.; Fu, R.-B.; Xiang, S.-C.; Wu, X.-T., *Inorg. Chem.* **2008,** *47* (10), 4054.
11. King, M. G.; McQuillan, G. P., *Journal of the Chemical Society A: Inorganic, Physical, Theoretical* **1967**, 898.
12. Li, Z.-H.; Li, L.-H.; Wu, L.-M.; Du, S.-W., *European Journal of Inorganic Chemistry* **2009,** *2009* (6), 752.
13. Bowmaker, G. A.; Healy, P. C.; Engelhardt, L. M.; Kildea, J. D.; Skelton, B. W.; White, A. H., *Aust. J. Chem.* **1990,** *43* (10), 1697.
14. Dempsey, D. F.; Girolami, G. S., *Organometallics* **1988,** *7* (5), 1208.
15. Chi, K.-M.; Farkas, J.; Hampden-Smith, M. J.; Kodas, T. T.; Duesler, E. N., *J. Chem. Soc., Dalton Trans.* **1992,** (21), 3111.
16. (a) Schneider, S.; Dzudza, A.; Raudaschl-Sieber, G.; Marks, T. J., *Chem. Mater.* **2007,** *19* (11), 2768; (b) Eichhöfer, A.; Fenske, D.; Holstein, W., *Angew. Chem., Int. Ed.* **1993,** *32* (2), 242.
17. (a) Pätow, R.; Fenske, D., *Z. Anorg. Allg. Chem.* **2002,** *628* (12), 2790; (b) Pätow, R.; Fenske, D., *Z. Anorg. Allg. Chem.* **2002,** *628* (6), 1279.

18. (a) Klett, J.; Klinkhammer, K. W.; Niemeyer, M., *Chemistry – A European Journal* **1999,** *5* (9), 2531; (b) Dias, H. V. R.; Wang, X.; Diyabalanage, H. V. K., *Inorg. Chem.* **2005,** *44* (21), 7322.
19. Bhattacharyya, K. X.; Akana, J. A.; Laitar, D. S.; Berlin, J. M.; Sadighi, J. P., *Organometallics* **2008,** *27* (12), 2682.
20. Addison, A. W.; Rao, T. N.; Reedijk, J.; van Rijn, J.; Verschoor, G. C., *J. Chem. Soc., Dalton Trans.* **1984,** (7), 1349.
21. Schmidbaur, H.; Nowak, R.; Huber, B.; Mueller, G., *Organometallics* **1987,** *6* (10), 2266.
22. Schmidbaur, H.; Nowak, R.; Steigelmann, O.; Muller, G., *Chem. Berichte* **1990,** *123* (1), 19.
23. Ates, M.; Breunig, H. J.; Gulec, S.; Offermann, W.; Haberle, K.; Drager, M., *Chem. Berichte* **1989,** *122* (3), 473.
24. Corinne, A. A.; Virginia, M. C.; Lev, N. Z.; Darren, W. J., *Crystal Growth and Design* **2009,** *9* (7), 3011.
25. Wielandt, J. W.; Kilah, N. L.; Willis, A. C.; Wild, S. B., *Chem. Commun.* **2006,** (35), 3679.
26. Kilah, N. L.; Petrie, S.; Stranger, R.; Wielandt, J. W.; Willis, A. C.; Wild, S. B., *Organometallics* **2007,** *26* (25), 6106.
27. Chitnis, S. S.; Peters, B.; Conrad, E.; Burford, N.; McDonald, R.; Ferguson, M. J., *Chem. Commun.* **2011,** *47* (45), 12331.
28. Clegg, W.; Elsegood, M. R. J.; Graham, V.; Norman, N. C.; Pickett, N. L.; Tavakkoli, K., *J. Chem. Soc., Dalton Trans.* **1994,** (12), 1743.
29. Clegg, W.; Elsegood, M. R. J.; Norman, N. C.; Pickett, N. L., *J. Chem. Soc., Dalton Trans.* **1994,** (12), 1753.

Chapter Six
Precusors for ZnO:F

6.1 Introduction

This chapter describes attempts to make single-source precursors for the CVD of ZnO:F as a low cost, alternative TCO to the commonly used In_2O_3:Sn. Currently the only films of ZnO:F that have been deposited by CVD have used dual-source precursors.[1] Stanley *et. al* used a series of organotin fluorocarboxylates to deposit thin films of SnO_2:F;[2] following on from this work, a series of zinc and organozinc fluorocarboxylates have been synthesised and their decomposition properties studied in order to see if they could be used as CVD precursors.

Transparent conducting oxides (TCOs) are wide band gap semiconducting oxides which have been doped with an additional element to increase their conductivity. They have a wide range of applications, including flat screen displays,[3] electrochromic devices,[4] organic light emitting diodes,[5] thin film resistors[6] and energy efficient windows.[7] One use that is of much interest to this thesis is the application of TCOs in thin-film solar cells. The front contact in a solar cell is normally either a metal grid placed on top of the transparent n-type layer or a TCO deposited on top of the n-type layer (Figure 6.1)[7-8] traditionally either In_2O_3:Sn or SnO_2:F haven been used as a front contacts in thin-film solar cells.[9]

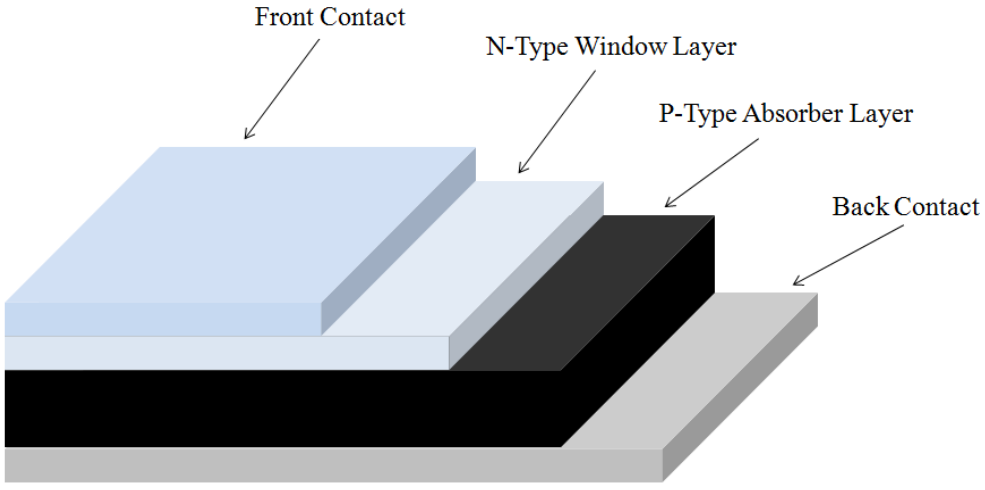

Figure 6.1 Simplified diagram of a thin-film solar cell

Currently the most widely used TCOs are SnO_2:F, ZnO:Al and In_2O_3:Sn, as these have been investigated for the longest.[10] However there are many new emerging TCOs that have been more widely investigated in the past 5-10 years, such

as ZnO:F,[11] In-Zn-O,[10], Cd_2SnO_4 [12] and ZnO:B.[13] ZnO:F is of particular interest as an alternative to SnO_2:F, ZnO:Al and In_2O_3:Sn and has been identified as having the highest transparency and being one of the least toxic TCOs, both very important considerations when choosing a TCO for use in solar cells; Zn is also cheaper than Sn and In.[9]

6.1.1 Fluorine-Doped Zinc Oxide

ZnO has a hexagonal wurtzite structure and is a wide bandgap semiconductor with a bandgap of 3.3eV;[1b] conductivity can be increased with the addition of dopants such as B,[14] Al,[15] Ga,[16] In[17] and F.[1a] In ZnO:F, fluorine atoms enter the ZnO lattice in substitutional form; Gordon *et. al* have theorised that due to this, fluorine doping gives the lowest resistivity to ZnO.[1a]

Thin films of ZnO:F have been deposited using spray pyrolysis[18], sol-gel spin coating[19] and sputtering.[20] Gordon *et. al* have studied the deposition of ZnO:F by CVD extensively and have deposited films initially using Et_2Zn, EtOH and C_3F_6 and later using Et_2Zn.TMEDA, EtOH and $C_6H_5C(O)F$. The earlier precursors grew films with a very low sheet resistance of 5Ω/square and a visible absorption of 3%.[1a, b]

6.1.1 Precursors for Zinc Oxide Thin Films

Dual-Source Precursors

Traditionally, ZnO has been deposited by APCVD with the use of Me_2Zn or Et_2Zn and an added oxidant such as H_2O or O_2.[21] However, the use of zinc alkyls with such strong oxidants is not ideal as this can lead to pre-reaction before the precursors arrive at the substrate. This can be remedied by using a less reactive source of oxygen such as CO_2,[22] N_2O[23] or an alcohol,[24] or by using an adduct such as R_2Zn.THF (R = Me, Et).[25] Currently, the most widely used method of depositing zinc oxide thin films is the use of an alkylzinc with an alcohol.[26]

Alkoxides

It has been suggested that the growth of films from alkylzinc precursors with the addition of alcohols results in a pre-reaction to form alkylzinc alkoxides before decomposition takes place.[27] As a result of this assumption films of ZnO have been grown from many zinc alkoxides. Zinc alkoxides tend to form tetramers when the

substituent is small, such as $(^{i}PrZn)_4(O^{i}Pr)_4$;[28] an increase in substituent size leads to dimers such as [EtZn(2,6-di-*tert*-butylphenoxide)]$_2$.[29] Despite their tetrameric structure, ZnO films have been grown from alkoxide precursors $MeZnO^{i}Pr$ and $MeZnO^{t}Bu$ using LPCVD without the need of an added oxidant.[30] The use of a bulky donor-functionalised alkoxide also yields a dimer (Figure 6.2), [MeZn(tdmap)]$_2$ (tdmap = 1,3-*bis*(dimethylamino)-2-(dimethylaminomethyl)-propan-2-oxide); films of ZnO have been deposited from this precursors using LPCVD. [31]

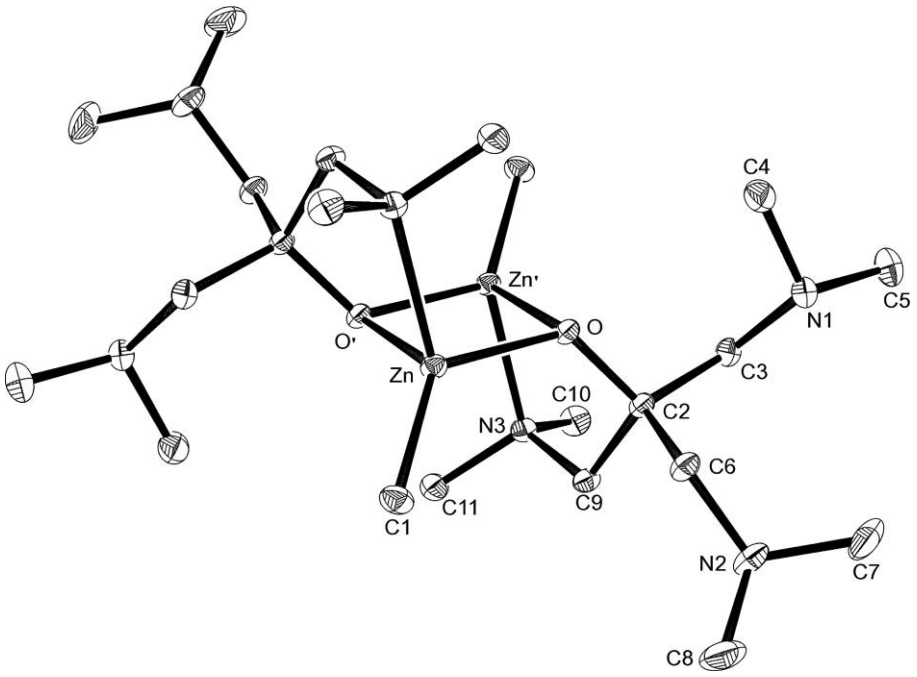

Figure 6.2 Structure of [MeZntdmap]$_2$[31]

β-Diketonates

β-diketonates exhibit keto – enol tautomerism whereby the tautomers exist in equilibrium in solution (Figure 6.3). With a metal cation present the enolic hydrogen can be lost and replaced by the metal cation, thereby forming a six membered metallocycle and shifting the equilibrium in favour of the enol form.[32]

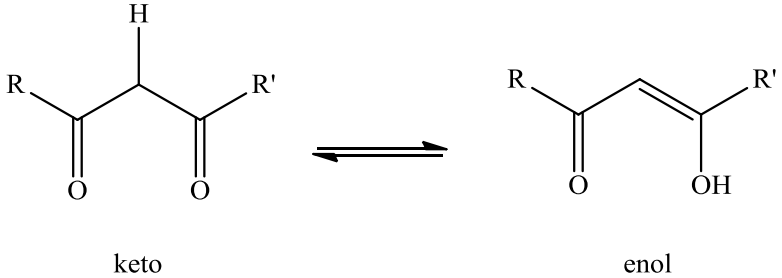

Figure 6.3 keto – enol tautomerism

β-diketonates have been widely used as precursors for the deposition of both main group and transition metal oxides.[27] However, they have been found to deposit films with a large amount of carbon contamination if no oxygen source if used in addition to the precursors.[33] ZnO has been deposited from zinc acetylacetonate, $Zn(O_2C_5H_7)_2$, by APCVD and LPCVD with the addition of oxygen gas into the reactor, no carbon contamination was reported to be seen in these films.[34]

Carboxylates

Metal carboxylates are a class of compounds with the general formula $M(O_2CR)_n$ and can exist in either a monodentate or bidentate form (Figure 6.4).

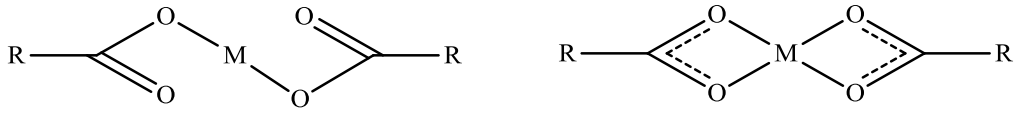

Figure 6.4 Monodentate and bidentate coordination of metal carboxylates

Zinc acetate, $Zn(O_2CMe)_2$, was first suggested as a precursor for the deposition of ZnO *via* atomic layer epitaxy,[35] and has since been employed to grow films of ZnO films by LPCVD[36] and APCVD.[37] Generally, an oxygen source is required in the deposition such as oxygen,[38] water[39] or hydrogen peroxide,[40] although high quality thin films of ZnO have been grown from $Zn(O_2CMe)_2$ alone *via* LPCVD.[41]

Stanley *et. al* tested a series of organotin fluorocarboxylates as precursors for the deposition of SnO_2:F *via* LPCVD, namely, $Bu_3SnO_2CCF_3$, $Bu_3SnO_2CC_2F_5$, $Bu_3SnO_2CC_3F_7$, $Et_3SnO_2CC_2F_5$ and $Me_2Sn(O_2CCF_3)_2$. They found that all precursors showed incorporation of fluorine into their films, and, with the exception of $Me_2Sn(O_2CCF_3)_2$, all precursors incorporated roughly the same amount of fluorine irrespective of the carboxylate group. Depositions from $Me_2Sn(O_2CCF_3)_2$ incorporated a higher amount of fluorine into the films; these films had a higher sheet resistance and resistivity than the other films grown. Although all other films displayed properties that were equivalent to films deposited from dual-source precursors, $Et_3SnO_2CC_2F_5$ proved to be the best precursor with rapid growth rates and uniform films.[2a]

6.2 Results and Discussion

6.2.1 Organozinc Fluorocarboxylates

Organozinc fluorocarboxylates were prepared following a literature method for the preparation of $EtZnO_2CPh$.[42] $C_2F_5CO_2H$ or $C_3F_7CO_2H$ was added to a stirred solution of Me_2Zn or Et_2Zn in hexane (Scheme 6.1). The resulting white precipitates were isolated and characterised by NMR and microanalysis. ^{13}C NMR confirms the ligand is intact, with coupling to fluorine seen in the carboxylate groups and peaks relating to the alkyl groups.

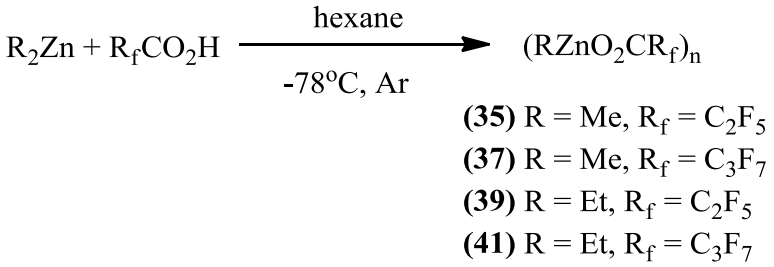

Scheme 6.1 Synthesis of **(35)**, **(37)**, **(39)** and **(41)**

.

Structural Analysis

Crystals suitable for diffraction were obtained on cooling a solution of **(39)** in hexane to -20°C (Figure 6.5). Crystals of **(41)** were obtained on heating a solution of **(41)** in hexane and leaving to cool slowly to room temperature (Figure 6.6). Crystals of **(35)** were also obtained using the same method as **(41)**, however these crystals were twinned so the data could not be fully refined, however the data was sufficient to show a similar structure to **(39)** and **(41)**.

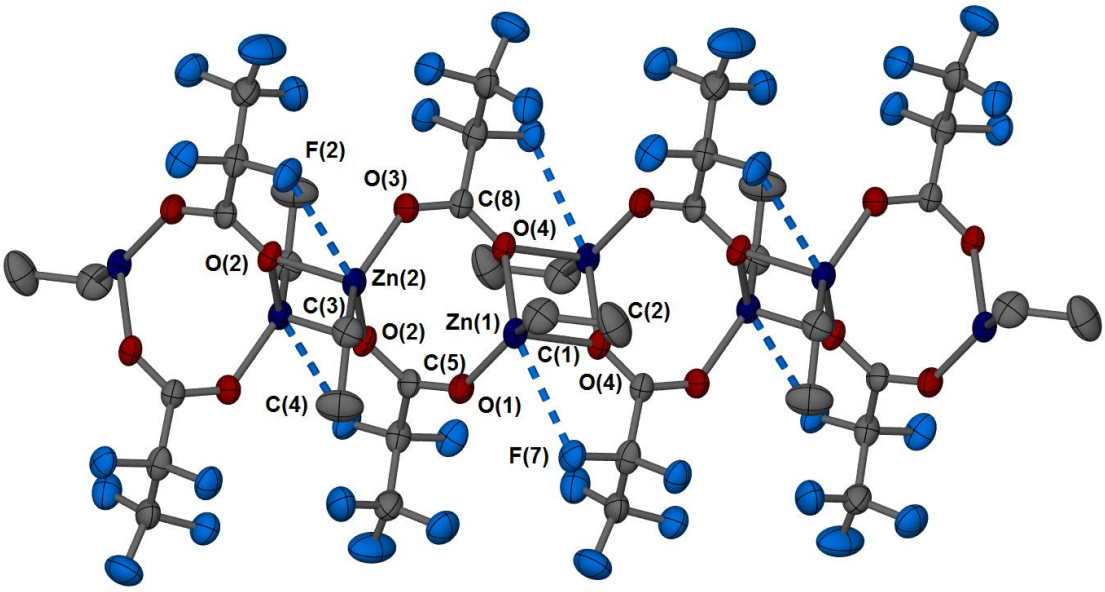

Figure 6.5 Structure of **(39)**, thermal ellipsoids drawn at 50% probability

Structurally, both **(39)** and **(41)** are very similar. Both exhibit a polymeric structure. However, **(39)** has two $EtZnO_2CR_f$ molecules in the asymmetric unit whereas **(41)** only has one. The Zn atoms all have a very distorted tetrahedral coordination with the carboxylate groups bridging over three zinc centres. Bond angles around the Zn centres in **(39)** range from 78.8(2)°-145.8(4)° around Zn(1) and 76.2(2)°-148.8(4)° around Zn(2); in **(41)** the range is from 77.40(7)°-140.15(10)°. The high degree of distortion could be due to the close contact between a fluorine atom on the carboxylate groups and the central zinc atoms [2.749(6)Å and 2.698(6)Å for Zn(1)-F(7) and Zn(2)-F(2) in **(39)** and 2.789(16)Å for Zn-F(2) in **(41)**]. All of the Zn-F bond distances are longer than the sum of the covalent radii (2.02Å) but shorter than the sum of the Van der Waals radii (2.86Å). This close contact effectively increases the coordination number of the Zn atoms to five; in which case all Zn atoms exhibit a distorted square-based pyramidal geometry with τ values of 0.12, 0.00 and 0.01 for Zn(1) and Zn(2) in **(39)** and Zn in **(41)**. τ values are a way to measure the degree of trigonality in a five-coordinate structure, as proposed by Addison *et. al* where $\tau = (\alpha - \beta)/ 60$ and α and β are the two largest angles. A value of 0 would indicate a square-based pyramidal arrangement whereas a value of 1 indicates an ideal trigonal bipyramidal arrangement.[43] In all cases the carboxylate groups are bidentate, with one longer Zn-O contact and one slightly shorter Zn-O contact, the shorter Zn-O contacts belong to the singly bridging-oxygen atoms [**(39)**: O(1), O(3), **(41)**: O(2)] with the longer Zn-O contacts belonging to the μ_2-oxygen

atoms; this is not uncommon and is seen in other similar structures.[42] In **(39)** the C-O bond distances seem unaffected by this, being the same within experimental error, however in **(41)** the C-O differ slightly. Selected bond distances and angles are shown in Table 6.1.

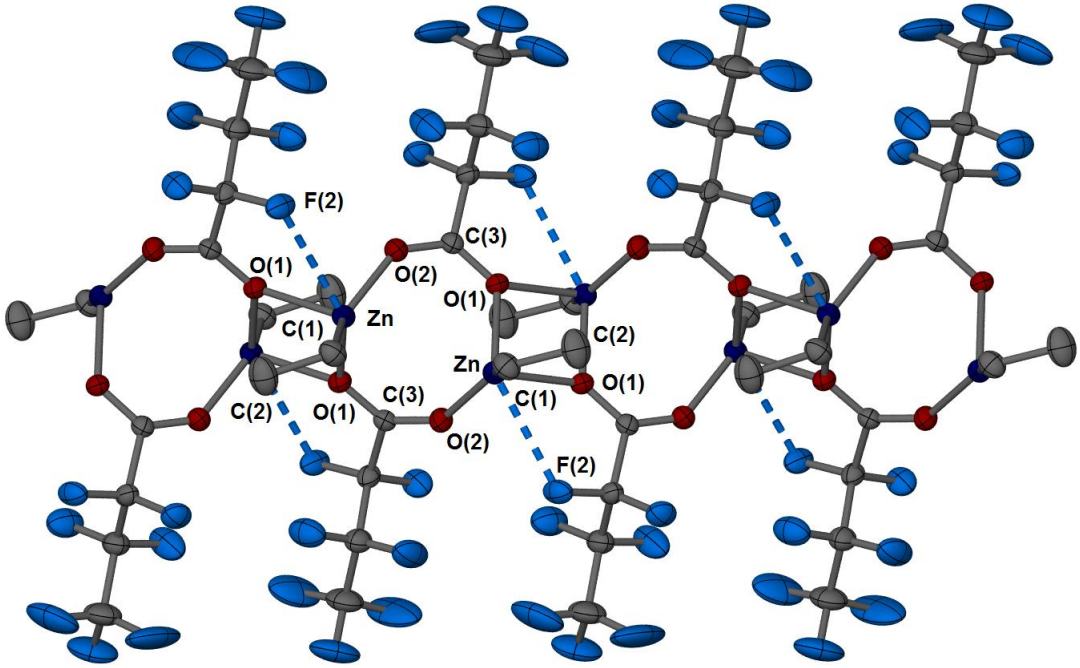

Figure 6.6 Structure of **(41)**, thermal ellipsoids drawn at 50% probability

Two other $RZnO_2CR'$ structures have been reported (R = Et, R' = Ph, m-terphenyl) which have much lower degrees of oligomerisation than the structures of **(39)** and **(41)**, with a hexameric structure when R' = Ph and a dimer when R' = m-terphenyl.[42, 44] A more direct comparison can be made between the structures of **(39)**, **(41)** and $EtZnO_2CCH_3$ which has a polymeric structure. Whereas **(39)** and **(41)** both form a polymer chain, $EtZnO_2CCH_3$ forms a sheet structure. $EtZnO_2CCH_3$ has $[EtZnO_2CCH_3]_2$ units in which each carboxylate ligand has one μ_2-oxygen atom bridging between the two zinc centres and one oxygen atom which is not involved in the bonding in the $[EtZnO_2CCH_3]_2$ units and is free to bond to other $[EtZnO_2CCH_3]_2$ units to form a sheet structure. The structure contains Zn_2O_2 rings which are seen in the structures of **(39)** and **(38)**, but they are linked by 16-membered $[Zn(O_2CCH_3)]_4$ rings rather than the $[Zn(O_2CR_f)]_2$ rings seen in **(39)** and **(41)**.[45]

Table 6.1 Selected bond distances (Å) and angles (°) in **(39)** and **(41)**

	(39)		**(41)**
Zn(1)-C(1)	1.952(10)	**Zn-C(1)**	1.939(3)
Zn(2)-C(3)	1.949(9)		
Zn(1)-O(1)	1.989(5)	**Zn-O(2)**	1.9853(17)
Zn(1)-O(4)	2.169(5)	**Zn-O(1)**	2.1528(17)
Zn(1)-O(4)'	2.188(6)	**Zn-O(1)'**	2.1634(16)
Zn(2)-O(3)	1.998(6)		
Zn(2)-O(2)	2.143(5)		
Zn(2)-O(2)'	2.185(5)		
Zn(1)-F(7)	2.749(6)	**Zn-F(2)**	2.789(16)
Zn(2)-F(2)	2.698(6)		
O(1)-C(5)	1.235(10)	**O(1)-C(3)**	1.262(3)
O(2)-C(5)	1.255(10)	**O(2)-C(3)**	1.237(3)
O(3)-C(8)	1.246(10)		
O(4)-C(8)	1.241(10)		
O(1)-Zn(1)-O(4)	90.1(2)	**O(1)-Zn-O(2)**	94.76(7)
O(1)-Zn(1)-O(4)'	91.8(2)	**O(2)-Zn-O(1)'**	93.26(7)
O(4)-Zn(1)-O(4)'	78.8(2)	**O(1)-Zn-O(1)'**	77.40(7)
C(1)-Zn(1)-O(1)	145.8(4)	**C(1)-Zn-O(2)**	140.15(10)
C(1)-Zn(1)-O(4)	113.0(4)	**C(1)-Zn-O(1)**	117.20(10)
C(1)-Zn(1)-O(4)'	116.4(4)	**C(1)-Zn-O(1)'**	115.45(9)
O(3)-Zn(2)-O(2)	91.7(2)		
O(3)-Zn(2)-O(2)'	92.5(2)		
O(2)-Zn(2)-O(2)'	76.2(2)		
C(3)-Zn(2)-O(3)	138.9(2)		
C(3)-Zn(2)-O(2)	122.3(3)		
C(3)-Zn(2)-O(2)'	116.1(3)		

Materials analysis

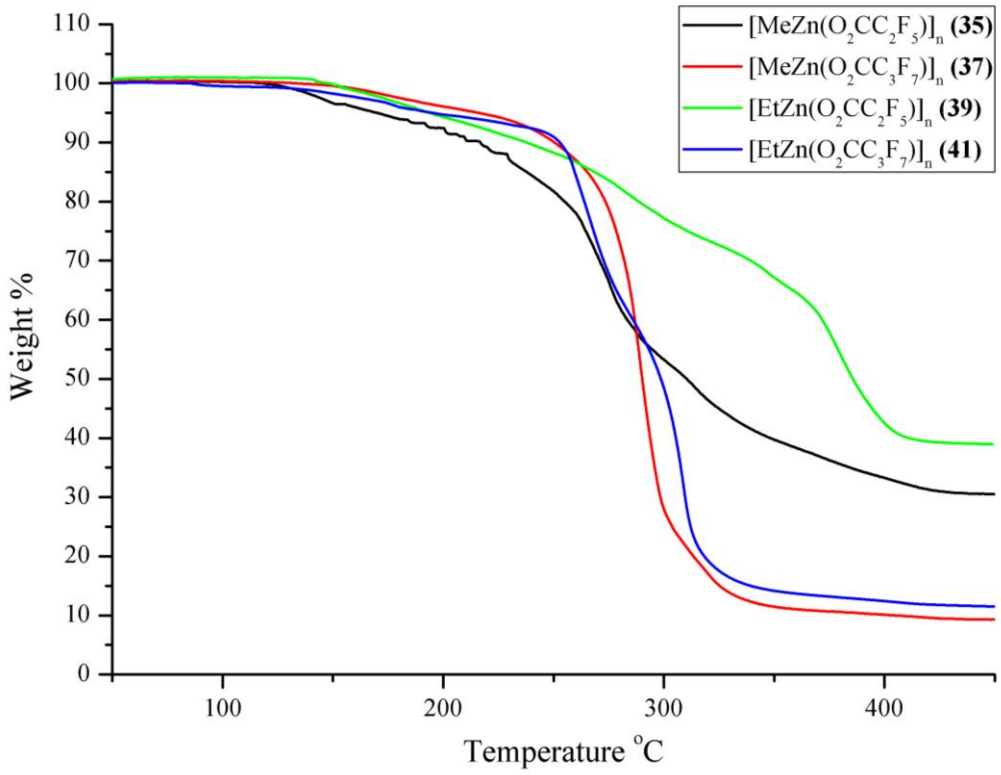

Figure 6.7 TGA of **(35)**, **(37)**, **(39)** and **(41)** with a heating rate of 5°C/min

The decomposition profiles of **(35)**, **(35)**, **(39)** and **(41)** appear to be very different (Figure 6.7). **(35)** and **(39)** decompose much more slowly than **(35)** and **(41)**. Decomposition of **(35)** starts at 126°C with a gradual loss in weight until 151°C, leaving a weight % of 96.5%, comparable to that expected from the loss of the Me, possibly as C_2H_6 (93.4%). Decomposition then continues with a complicated decomposition profile, with no clear steps but a gradual decrease in weight until 432°C, leaving a final residue of 30.5%, slightly lower than that expected for ZnO (33.0%) and much lower than that expected for ZnF_2 (42.1%).

Decomposition of **(37)** is much more defined, with three clear steps seen. The first step goes from 138°C to 238°C, leaving a 92.7% residue, comparable to the expected value for the loss of the Me group (94.9%). The decomposition is then much sharper with the second step ending at 303°C leaving a residual weight of 25.5%. The third step in the decomposition then takes place until 354°C, leaving a residual weight of 9.3%, much lower than that predicted for either ZnO (27.4%) or ZnF_2 (34.9%), suggesting some volatility in the precursor.

(39) has a similar decomposition profile to **(35)**, with gradual decomposition starting at 138°C and continuing till 258°C, leaving a residue of 86.9%, comparable to that expected for the loss of the Et group (88.3%). The decomposition is then slightly sharper until 265°C, and sharper still after that, finally ending at 414°C, leaving a residual weight of 38.9%. This is much higher than that expected for ZnO (31.2%), and is in fact much closer to that expected for ZnF_2 (39.9%). It is a possibility that decomposition is to ZnF_2, as there are very close contacts between the Zn and F atoms in the crystal structure**.** A thermal decomposition experiment was performed to try to identify the residue; **(39)** was heated to 400°C under N_2, the temperature was maintained for 1 hour and then cooled to room temperature at 1°C/min. The black residue left was shown to be amorphous by PXRD. This experiment was repeated with the black residue this time under an atmosphere of air. The white residue was crystalline but the peaks were unidentifiable.

(41) has a similar decomposition profile to **(35)** with a gradual weight loss starting at 140°C and ending at 245°C, leaving a 91.8% residue, comparable to that expected for the loss of the Et group (90.5%). A much sharper decomposition takes place from 245°C to 337°C, with s slight change in gradient seen at 282°C, corresponding to a 62.4% residual weight. The final weight % seen is 11.5%, which is once again much lower than that expected for ZnO (26.1%) or ZnF_2 (33.3%), indicating some volatility in the precursor.

With these precursors we see two very distinct decomposition profiles, seemingly dependant on the carboxylate ligand. While the two precursors with an $O_2CC_3F_7$ ligand [**(37)** and **(41)**] seem to decompose cleanly and show some volatility, the two with an $O_2CC_2F_5$ ligand (**(35)** and **(39)**) decompose much more gradually and show a much more complicated decomposition profile. In all cases there is no evidence for loss of CO_2 from the residual weights seen, which is odd as CO_2 loss is a common step in the decomposition of metal carboxylates and has been seen in the decomposition of $Zn(O_2CCH_3)_2$.[46]

CVD Trials

(37) was chosen as the precursor for CVD trials due to its superior volatility; LPCVD was the chosen technique as the precursor was not deemed volatile enough for APCVD. Films were grown at 450°C onto glass for 2 hours with the line and bubbler temperatures set to 150°C.

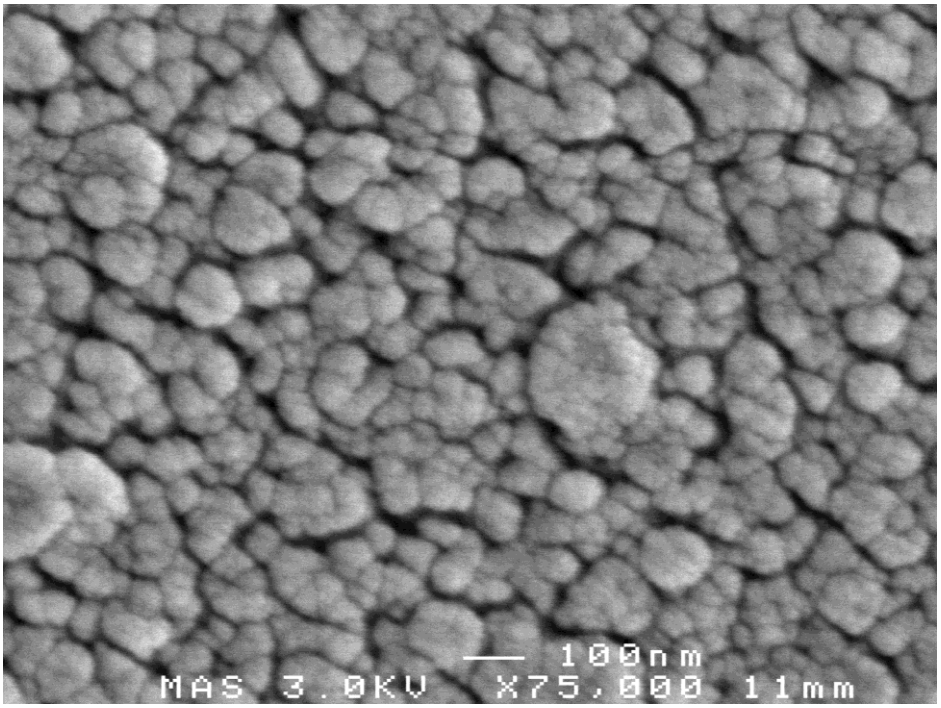

Figure 6.8 SEM image of film grown from **(35)**

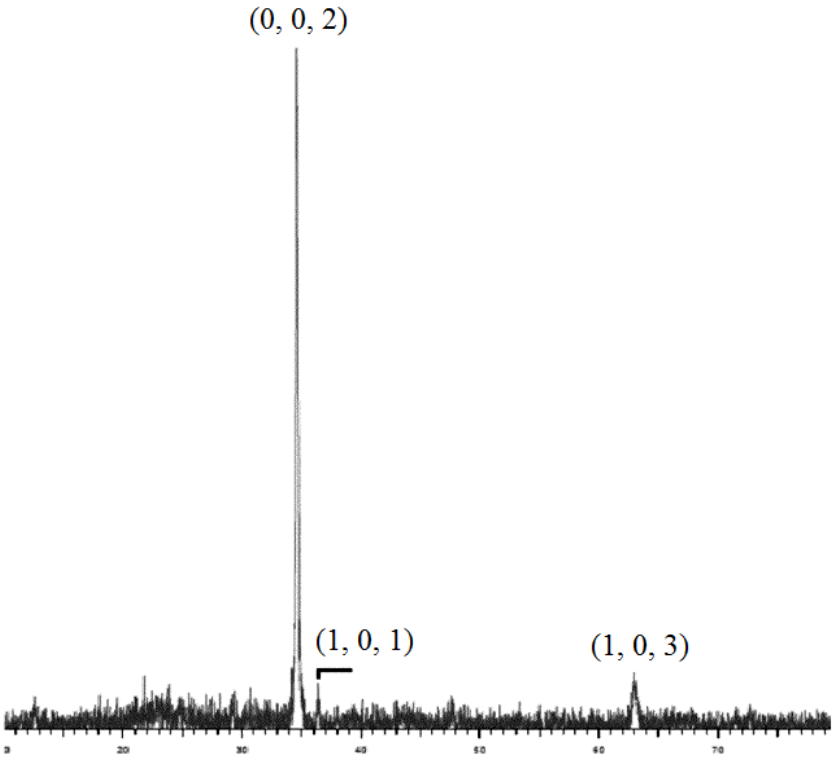

Figure 6.9 PXRD of film grown from **(35)**, indexing to PDF 89-1397

Films were transparent and did not conduct when tested with a voltammeter. SEM imaging reveals a uniform film consisting of crystallites of *ca.* 50 – 100nm

with cracks between clusters of these crystallites (Figure 6.8). EDX confirms the presence of Zn and O but could not detect any F in the film. PXRD confirms that ZnO has been produced. The film appears to be highly oriented with a very intense peak corresponding to the (0, 0, 2) index.

6.2.2 Related Organozinc Fluorocarboxylates

Initial attempts to recrystallise **(35)** and **(37)** by adding CH_2Cl_2 to the hexane solution and cooling to -20°C produced two oxidation products, $[Zn_5Me_2(OMe)_2(O_2CC_2F_5)_6]_2$, **(36)**, and $[Zn_5Me_2(OMe)_2(O_2CC_3F_7)_6]_2$, **(38)**. These are both oxidation products of **(35)** and **(37)**; it is possible that a small amount of oxygen in the CH_2Cl_2 caused this oxidation. The reaction between O_2 and dialkylzinc compounds is known to produce first zinc peroxides and then further reaction with O_2 gives alkoxides.[47] Both **(36)** and **(38)** were characterised by microanalysis and NMR; ^1H and ^{13}C NMR showed the different ZnOMe and MeZn peaks with ^1H shifts of -0.81ppm and 3.44ppm in **(36)** and -0.84ppm and 3.52ppm in **(38)** and an integration ratio of 1 : 1 which correspond to the MeZn and ZnOMe protons, repspectively.

Structural Analysis

Crystals suitable for diffraction were obtained on adding CH_2Cl_2 to a solution of **(35)** (Figure 6.12) or **(37)** in hexane and cooling to -20°C. Although the structure of **(38)** was too disordered to be fully resolved, the core of the structure was the same as that of **(36)**.

The structure of **(36)** consists of a cage of five zinc atoms, surrounded by six bridging carboxylate ligands, two OMe groups and two Me groups; one of the carboxylate ligands [based on C(18)] bridges to a symmetry-related second cage to yield a Zn_{10} aggregate. Of the five zinc atoms, Zn(1) is in the centre of the cage and is six-coordinated, exhibiting a slightly distorted octahedral structure with bond angles ranging from 80.7(3)° – 101.6(3)° between adjacent atoms and 168.1(3)° – 174.7(3)° between opposite atoms. Of the remaining four zinc centres, Zn(3) is five-coordinate and Zn(2), Zn(4) and Zn(5) are all four-coordinate.

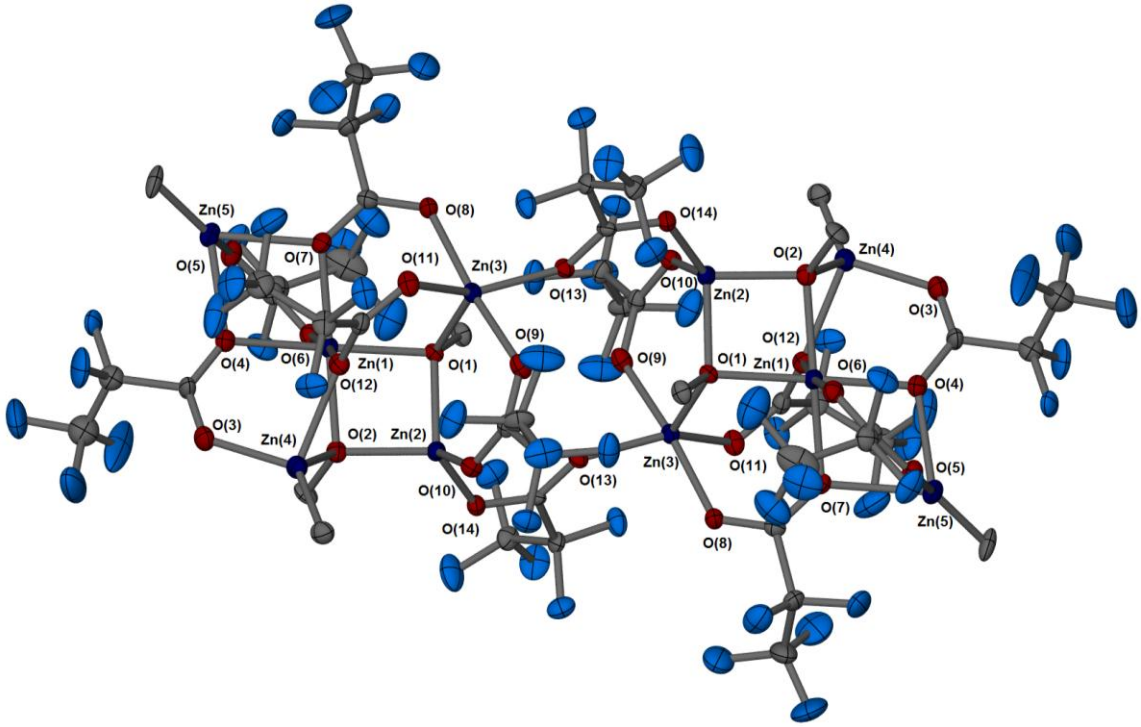

Figure 6.10 Structure of **(36)**, thermal ellipsoids drawn at 30% probability

Zn(3) exhibits very distorted geometry with a τ value of 0.42, which is roughly half way between square-based pyramid and trigonal bipyramidal geometry. Zn(2), Zn(4) and Zn(5) all exhibit distorted tetrahedral geometry, with a much higher degree of distortion seen in Zn(4) and Zn(5), with bond angles ranging from 88.6(3)° - 114.7(3)°, 76.2(3)° - 129.7(4)° and 75.9(3)° – 143.6(5)° respectively.

All the carboxylate groups bridge over at least two zinc centres; of the six carboxylate ligands three have both oxygen atoms bonded to one zinc atom each and the other three have one oxygen atom bridging over two zinc centres and the other bonded to just one zinc. The singly bridging oxygen atoms have bond distances that range from 1.923(8)Å – 2.071(9)Å while the μ_2-oxygen atoms have slightly longer bond distances, ranging from 2.103(7)Å – 2.258(7)Å. The oxygens of the OMe groups bridge over three zinc centres, Zn(1), Zn(2) and Zn(3) in the case of O(1) and Zn(1), Zn(2) and Zn(4) in the case of O(2). The bond distances range from 1.986(7)Å – 2.095(7)Å, within the same range as the singly bridging oxygen atoms of the carboxylate groups and slightly shorter than the μ_2-oxygen atoms. Both Me groups are bonded to only one zinc atom each [Zn(4) and Zn(5)] and sit on the outskirts of the cage. The core structure is shown in Figure 6.13 and selected bond lengths are shown in Table 6.2.

A similar structure has been reported by Orchard *et al.* $Zn_5Et_4(O_2CCH_3)_6$ has a similar formula to **(36)** and **(38)** but has four Et groups rather than two Et groups and two OEt groups. $Zn_5Et_4(O_2CCH_3)_6$ has a cage structure but does not have any acetate groups that bridge to a second Zn_5 cage as is seen in the structure of **(36)**.[45]

Table 6.2 Selected bond distances (Å) in **(36)**

	(36)
Zn(1)-O(1)	2.095(7)
Zn(1)-O(2)	2.081(8)
Zn(1)-O(4)	2.103(7)
Zn(1)-O(6)	2.010(8)
Zn(1)-O(7)	2.107(8)
Zn(1)-O(12)	2.180(8)
Zn(2)-O(1)	1.995(7)
Zn(2)-O(2)	1.986(7)
Zn(2)-O(10)	1.923(8)
Zn(2)-O(14)'	1.932(7)
Zn(3)-O(1)	2.023(7)
Zn(3)-O(8)	2.056(8)
Zn(3)-O(9)	2.071(9)
Zn(3)-O(11)	2.035(7)
Zn(3)-O(13)	2.014(7)
Zn(4)-O(2)	2.090(7)
Zn(4)-O(3)	2.026(8)
Zn(4)-O(12)	2.207(8)
Zn(4)-C(21)	1.931(13)
Zn(5)-O(4)	2.173(9)
Zn(5)-O(5)	1.955(8)
Zn(5)-O(7)	2.258(7)
Zn(5)-C(22)	1.908(11)

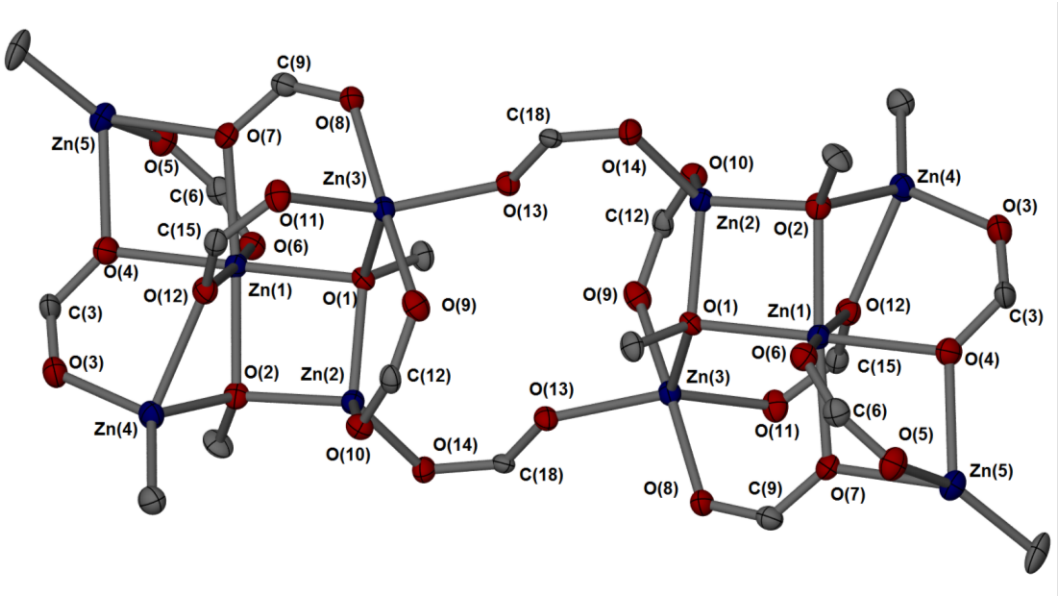

Figure 6.11 Structure of **(36)** with C_2F_5 groups omitted, thermal ellipsoids drawn at 30% probability

Crystals of $Zn_9(O_2CC_2F_5)_{12}(O)_2Et_2$, **(40)** were obtained from dissolving the hexane insoluble precipitate left from the synthesis of **(39)** in a hexane/CH_2Cl_2 mixture and cooling to -20°C. **(40)** was structurally characterised and the empirical formula confirmed by microanalysis. As this was a minor by-product in the synthesis of **(39)** there was not enough sample for characterisation by NMR.

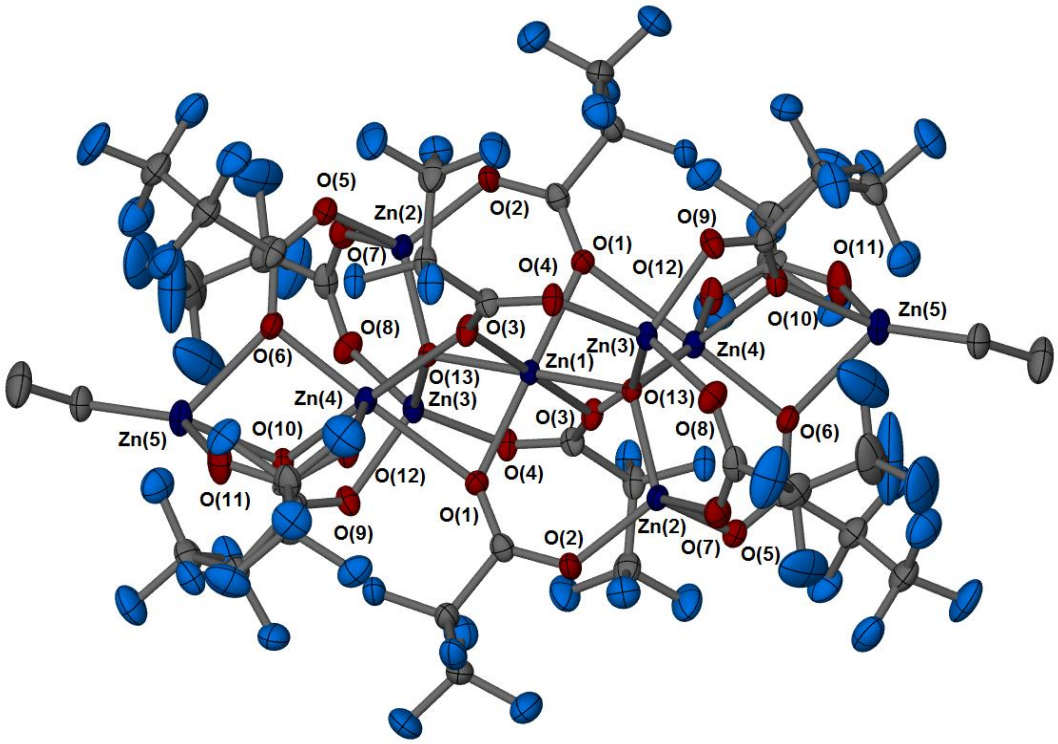

Figure 6.12 Structure of **(40)**, thermal ellipsoids drawn at 30% probability

The structure of **(40)** consists of five Zn atoms, one of which sits on a centre of inversion, six carboxylate groups, one central oxygen atom and one Et group; the central Zn atom grows to form a structure with the formula $Zn_9(O_2CC_2F_5)_{12}(O)_2Et_2$ (Figure 6.10). Selected bond lengths are shown in Table 6.3.

Of the five Zn atoms, two are six-coordinate with distorted octahedral coordination [Zn(1), Zn(4)] and three are four-coordinate with distorted tetrahedral coordination [Zn(2), Zn(3) and Zn(5)]. Of the two six-coordinate Zn atoms, Zn(1) exhibits a geometry which is much closer to a perfect octahedron with bond angles of 180.0° between opposite oxygen atoms and bond angles between 80.19(13)° and 99.81(13)° between adjacent oxygen atoms. Zn(4) shows a much more distorted geometry with bond angles ranging from 154.92(15)° - 178.03(15)° between opposite oxygen atoms and bond angles between 74.36(13)° and 103.57(14)° between adjacent oxygen atoms.

The four-coordinate zinc atoms also show differing degrees of distortion. Zn(2) and Zn(3) are less distorted with bond angles ranging from 98.20(18)° – 113.81(15)° and 99.31(18)° – 113.78(15)° respectively. Zn(5) shows much more distortion; bond angles range from 73.01(14)° – 135.2(2)°.

The six carboxylate groups all bridge over at least two zinc atoms. Four have one singly bridging oxygen and one μ_2 oxygen and two have two singly bridging oxygen atoms. The singly bridging oxygen atoms have Zn-O bond distances that range from 1.938(4)Å – 1.983(4)Å, while the μ_2 oxygen atoms have longer Zn-O bond distances, ranging from 2.101(4)Å – 2.454(4)Å. The oxygen atom in the centre, O(13), bridges over four Zn centres, Zn(1), Zn(2), Zn(3) and Zn(4) and has Zn-O bond distances that are within the same range as the singly bridging carboxylate oxygen atoms, 1.937(3)Å – 1.995(3)Å. The Et group is bonded to only one Zn centre, Zn(5) with a bond distance of 1.924(6)Å. Figure 6.11 shows the structure with C_2F_5 groups omitted for clarity. There do not appear to be any other structures that compare to the structure of **(40)**.

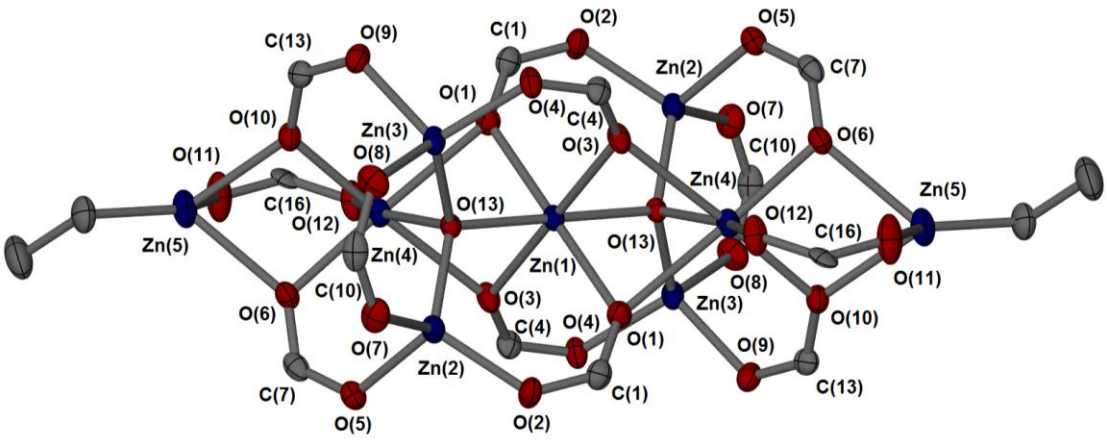

Figure 6.13 Structure of **(40)** with C_2F_5 groups omitted, thermal ellipsoids drawn at 30% probability

Table 6.3 Selected bond distances (Å) in **(40)**

	(40)
Zn(1)-O(1)	2.173(4)
Zn(1)-O(3)	2.172(4)
Zn(1)-O(13)	1.995(3)
Zn(2)-O(2)	1.942(4)
Zn(2)-O(3)	1.978(4)
Zn(2)-O(7)	1.955(4)
Zn(2)-O(13)	1.937(3)
Zn(3)-O(4)'	1.938(4)
Zn(3)-O(8)	1.957(4)
Zn(3)-O(9)	1.983(4)
Zn(3)-O(13)	1.939(3)
Zn(4)-O(1)'	2.423(4)
Zn(4)-O(3)	2.454(4)
Zn(4)-O(6)	2.108(4)
Zn(4)-O(10)	2.101(4)
Zn(4)-O(12)	1.938(4)
Zn(4)-O(13)	1.940(3)
Zn(5)-O(6)	2.270(4)
Zn(5)-O(10)	2.236(4)
Zn(5)-O(11)	1.950(5)
Zn(5)-C(19)	1.924(6)

The inclusion of oxygen atoms within the cage could be attributed to two different mechanisms. Lewinski *et al.* have synthesised a similar cage, $[Zn(O_2CPh)]_4O$, on addition of dry O_2 to $[EtZn(O_2CPh)]_n$. They theorised that the mechanism starts with attack of O_2 on the Zn-C bond to form a peroxide, $EtOOZn(O_2CPh)$. This peroxide could then form a cage with remaining $[EtZn(O_2CPh)]_n$ to form $[EtZn(O_2CPh)]_x[EtOOZn(O_2CPh)]_y$. Homolysis of the O-O bond then produces an alkoxyl radical and an oxyzinc radical which is stabilised by electron transfer from a remaining Zn-C bond. The alkyl radical is released and can combine either with another alkyl radical or an alkoxy radical, leaving a cage structure with a central oxygen atom (Scheme 6.2).[42]

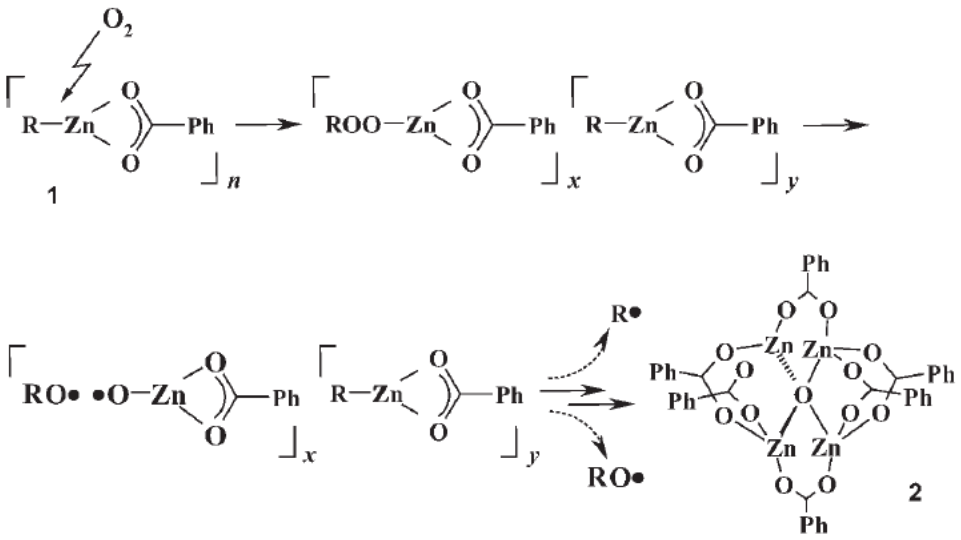

Scheme 6.2 Mechanism of O_2 attack on $[EtZn(O_2CPh)]_n$[42]

It is possible that the structure of **(40)** arises from a similar oxidation mechanism. A small amount of oxygen and a slight excess of $HO_2CC_2F_5$ could have been present in the synthesis of **(39)** which produced **(40)**.

Another possible mechanism is the hydrolysis of **(39)** to produce **(40)**. **(40)** can also be described as $(EtZnL)_2(ZnL_2)_5(ZnO)_2$ ($L = O_2CC_2F_5$) and it is possible that in solution **(39)** undergoes Schlenk equilibria to form a mixture of $EtZnO_2CC_2F_5$, Et_2Zn and $Zn(O_2CC_2F_5)_2$, and it is possible that a small amount of water in the solvent could hydrolyse the Et_2Zn to form ZnO (Scheme 6.3). The cage structure of **(40)** could be then be formed on cooling to -20°C. This Schlenk equilibrium has been seen previously in alkylzinc alkoxides.[48]

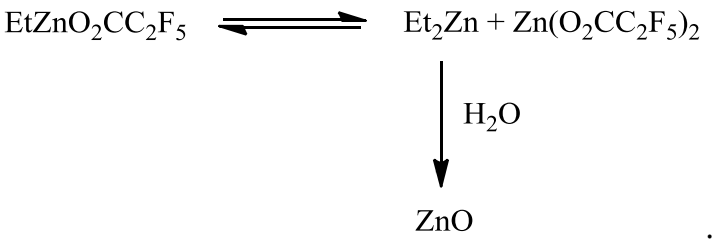

Scheme 6.3 Possible Schlenk Equilibria in **(39)**

Crystals of $Zn_8Et_4(OEt)_4(O_2CC_3F_7)_6(O)$, **(42)**, were obtained from initial attempts to recrystallise **(41)** from the addition of CH_2Cl_2 to the hexane solution and cooling to -20°C. Although the structure itself is very different to that of **(40)** it is likely that a similar mechanism is involved in the formation of **(42)** from **(41)** with either the hydrolysis or the oxidation of **(41)** from a small amount of either H_2O or O_2 in the solvent. **(42)** was characterised by microanalysis and NMR; ^1H and ^{13}C NMR showing the EtZn and ZnOEt groups [^1H δ of -0.01ppm (2H, $ZnCH_2$), 0.96ppm (3H, $ZnCH_2CH_3$), 1.07ppm (3H, OCH_2CH_3) and 3.74ppm (2H, OCH_2)] and ^{13}C NMR showing the coupling between ^{19}F and ^{13}C in the ligand.

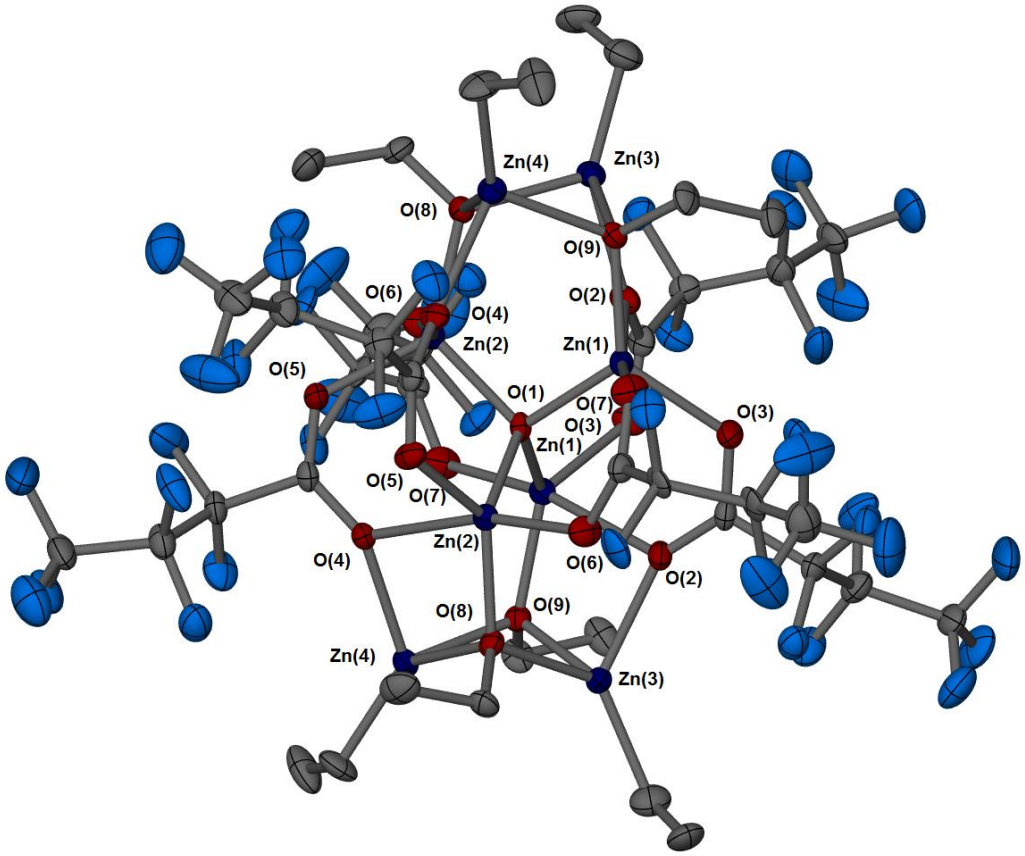

Figure 6.14 Structure of **(42)**, thermal ellipsoids drawn at 30% probability

The structure of **(42)** differs from that of **(36)** and **(38)**, with four zinc atoms in the asymmetric unit which double up to form a cage with the formula $Zn_8Et_4(OEt)_4(O_2CC_3F_7)_6(O)$. For clarity, the structure is shown in Figure 6.15 with C_3F_7 groups omitted. Selected bond lengths are shown in Table 6.4. Zn(1) and Zn(2) are both five-coordinate with distorted trigonal bipyramidal coordination and τ values of 0.66 and 0.61 respectively.[43] Zn(1) has two oxygens from the carboxylate groups in the axial positions [O(2) and O(7)] with one more carboxylate oxygen [O(3)], one oxygen from an OEt group [O(9)] and the central O(1) in the equatorial positions. Similarly, Zn(2) has O(4) and O(6) in axial position, both from carboxylate groups, and the central O(1) and O(8) from an OEt and O(5) from a carboxylate group in the equatorial positions.

Zn(3) and Zn(4) are both four-coordinate with a distorted tetrahedral structure and bond angles ranging from 78.9(2)° – 130.8 (5)° and 79.4(2)° – 130.8(4)° respectively. Both five-coordinate Zn atoms are located more centrally within the cage and are only bonded to oxygen atoms whereas the four-coordinate Zn atoms are on an edge of the cage and show coordination to both the oxygen atoms and the Et groups.

All carboxylate ligands bridge over a number of zinc centres; in two of the carboxylate ligands [based on C(1) and C(5)], one oxygen is bonded to only one zinc while the other oxygen bridges over two zinc centres, the other carboxylate ligand [based on C(9)] has both oxygen atoms bonded to only one zinc centre each. The singly bridging oxygens all have similar bond distances, ranging from 2.005(6)Å – 2.049(7)Å, the μ_2-oxygen atoms have longer bond distances ranging from 2.111(6)Å – 2.406(6)Å. The two Et groups are bonded to only one Zn atom each, Zn(3) and Zn(4), whereas the two OEt groups bridge over three Zn centres, Zn(1), Zn(3) and Zn(4) in the case of O(9) and Zn(2), Zn(3) and Zn(4) in the case of O(8). The Zn - O bond distances in the μ_3-OEt groups are within the same range as seen in the singly bridging-oxygen atoms of the O_2CR_f groups and are slightly shorter than the μ_2-oxygens, ranging from 1.975(6)Å – 2.122(5)Å. O(1) is in the centre of the cage, bridging over four zinc centres with only two unique bond distances of Zn(1)-O(1) 1.955(4)Å and Zn(2)-O(1) 1.950(4)Å. There appear to be no other similar cage structures in the literature.

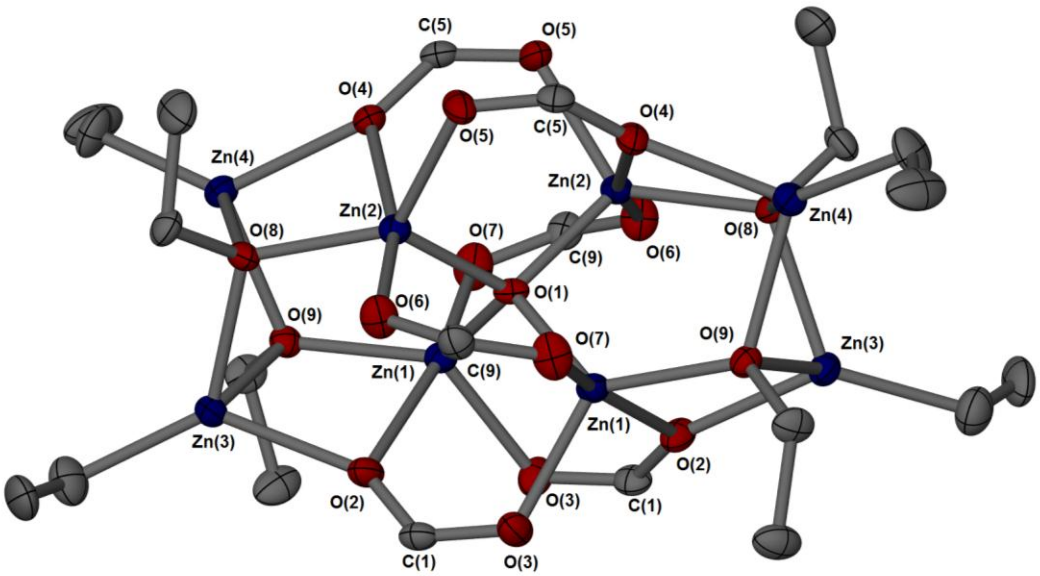

Figure 6.15 Structure of **(42)** with C_3F_7 groups omitted, thermal ellipsoids drawn at 30% probability

Table 6.4 Selected bond distances (Å) in **(42)**

	(42)
Zn(1)-O(1)	1.955(4)
Zn(1)-O(2)	2.406(6)
Zn(1)-O(3)'	2.017(6)
Zn(1)-O(7)'	2.049(7)
Zn(1)-O(9)	1.975(6)
Zn(2)-O(1)	1.950(4)
Zn(2)-O(4)	2.356(6)
Zn(2)-O(5)'	2.005(6)
Zn(2)-O(6)	2.042(6)
Zn(2)-O(8)	1.980(6)
Zn(3)-O(2)	2.113(6)
Zn(3)-O(8)	2.122(5)
Zn(3)-O(9)	2.066(6)
Zn(3)-C(17)	1.991(12)
Zn(4)-O(4)	2.111(6)
Zn(4)-O(8)	2.055(5)
Zn(4)-O(9)	2.111(6)
Zn(4)-C(19)	1.956(9)

6.2.3 TMEDA Adducts of Organozinc Fluorocarboxylates

(43) - (46) were synthesised in the reaction between Me_2Zn or Et_2Zn and $HOOCC_2F_5$ or $HOOCC_3F_7$ in the presence of TMEDA in hexane, using an excess of Me_2Zn to Et_2Zn to ensure all carboxylic acid reacted (Scheme 6.4). All volatiles were removed *in vacuo*, yielding oils in all cases which were characterised by microanalysis and NMR. ^1H NMR showed the correct stoichiometry of alkylzinc species to the TMEDA ligand.

$$1.5R_2Zn + R_fCO_2H + TMEDA \xrightarrow[-78^oC,\ Ar]{\text{hexane}} (RZnO_2CR_f).TMEDA$$

(43) R = Me, $R_f = C_2F_5$
(44) R = Me, $R_f = C_3F_7$
(45) R = Et, $R_f = C_2F_5$
(46) R = Et, $R_f = C_3F_7$

Scheme 6.4 Synthesis of **(43)** – **(46)**

Structural Analysis

Crystals of **(45)** were grown from the product oil when left to stand for a period of a few days (Figure 6.16).

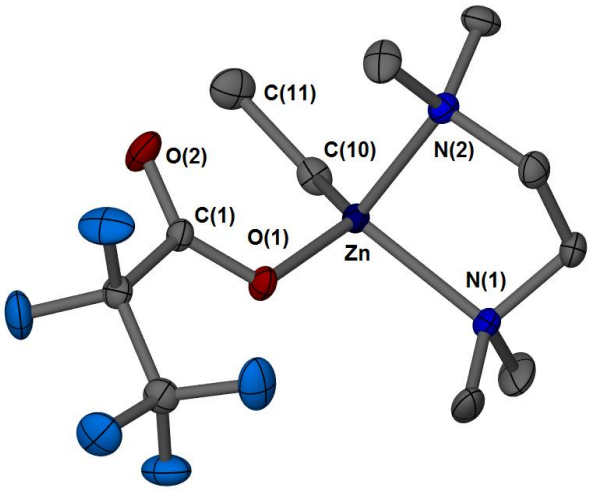

Figure 6.16 Structure of **(45)**, thermal ellipsoids drawn at 50% probability

The structure of **(45)** is monomeric in the solid state, with the carboxylate group showing monodentate coordination. The ligands are arranged about the central Zn atom in a distorted tetrahedral arrangement, with bond angles ranging from 84.86(6)° (N(1)-Zn-N(2)) to 126.98(8)° (C(10)-Zn-O(1)). The TMEDA group shows

isobidentate coordination, with bond lengths between the Zn and both N atoms the same. Interestingly, despite the monodentate coordination of the carboxylate group, the bond lengths between C(1) and both oxygen atoms are very similar, which can be explained by the presence of a hydrogen bond between O(2) and a hydrogen atom from an adjacent molecule (Figure 6.17). The C=O is still shorter than the C-O bond, which is probably due to the weak nature of the hydrogen bond between a non-polar CH from an adjacent TMEDA ligand and the C=O from the carboxylate ligand. Selected bond distances and angles are shown in Table 6.5. There appear to be no other similar $RZnO_2CR.TMEDA$ structures in the literature.

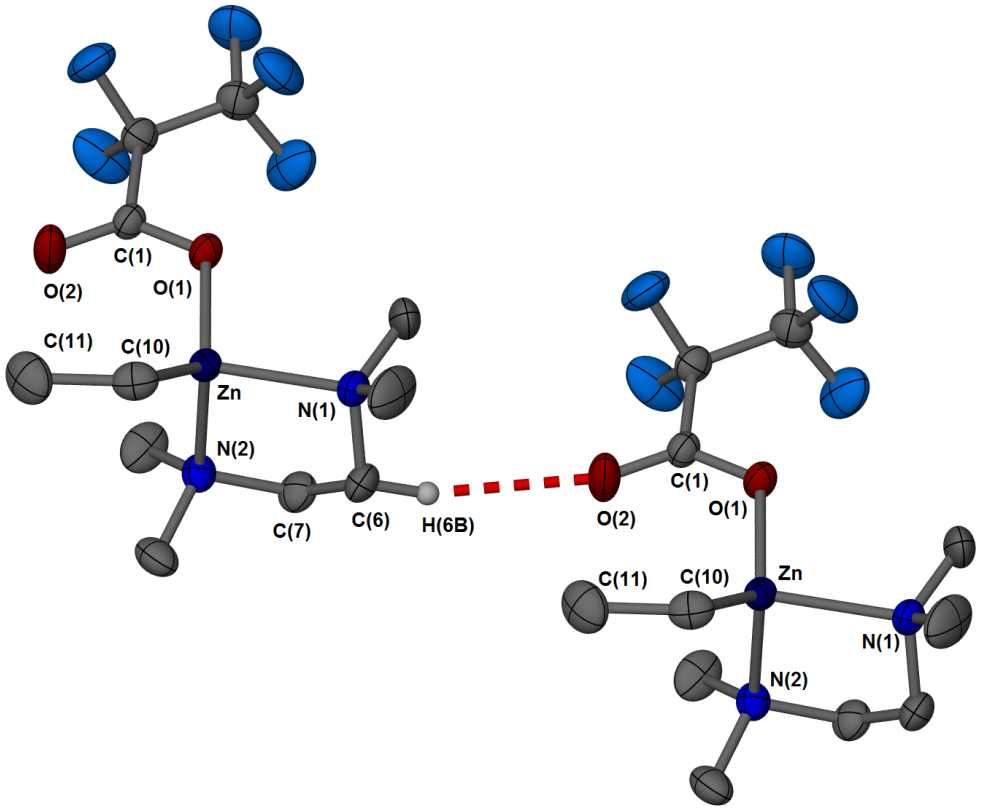

Figure 6.17 Structure of **(45)** showing hydrogen bond, thermal ellipsoids drawn at 50% probability

Table 6.5 Selected bond distances (Å) and angles (°) of **(45)**

	$EtZn(O_2CC_2F_5)$.TMEDA (45)
Zn-C(10)	1.977(2)
Zn-O(1)	2.0102(13)
Zn-N(2)	2.1388(17)
Zn-N(2)	2.1409(16)
O(1)-C(1)	1.262(2)
O2-C(1)	1.213(2)
O(2)-H(6B)	2.536
C(10)-Zn-O(1)	126.98(8)
C(10)-Zn-N(1)	120.15(9)
C(10)-Zn-N(2)	119.12(8)
O(1)-Zn-N(1)	96.22(6)
O(1)-Zn-N(2)	99.12(8)
N(1)-Zn-N(2)	84.86(6)

Materials analysis

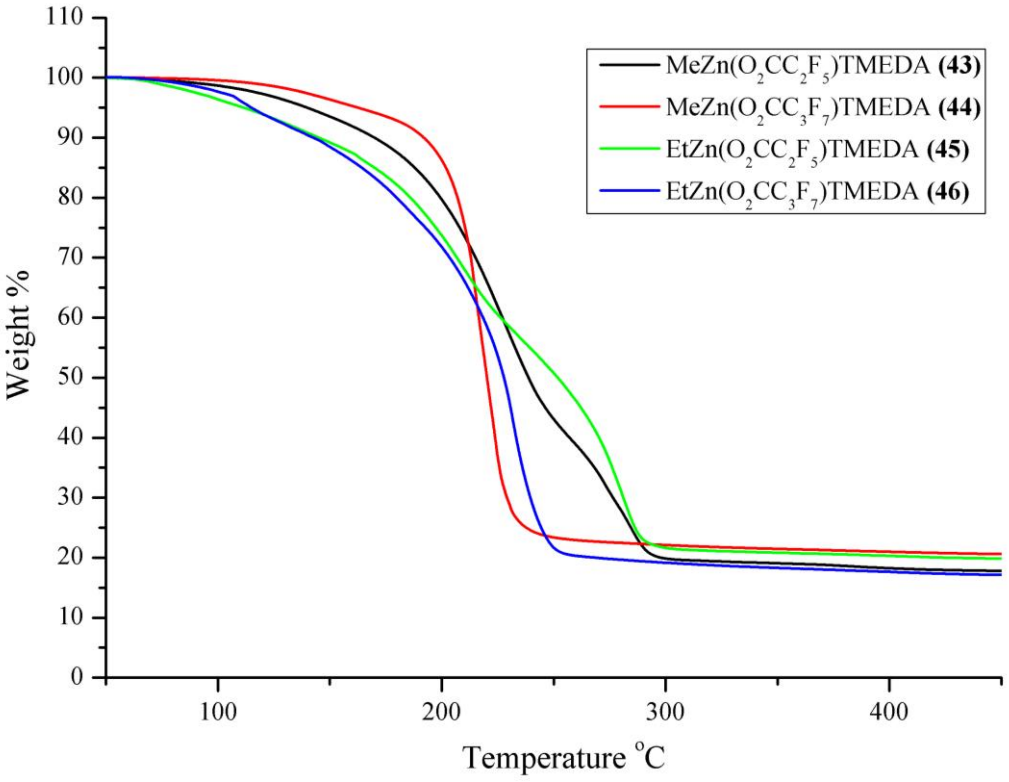

Figure 6.18 TGA of **(43) - (46)** with a heating rate of 5°C/min

TGA of **(43) - (46)** shows clean decomposition to ZnO (Figure 6.18). A gradual weight loss is seen in **(43)** from 91°C, with a change in gradient at around 140°C; the residual weight here is comparable to the loss of the Me group, 94.9% compared to the expected 95.8%, this second step continues until 245°C, where a third step is seen, which corresponds to a residual weight of 45.9%. This is lower than that expected for either dissociation of the TMEDA group (63.4%), or the decomposition of the carboxylate group (54.7%), however these steps are very close together so it is possible that the second process has started before the first has fully finished. Decomposition has finished by 307°C, leaving a final weight of 19.6% which is slightly lower than the 22.3% expected for ZnO, possibly indicating some volatility in the precursor.

Similarly decomposition of **(44)** starts with a gradual weight loss from 99°C to 177°C, leaving a 93.3% residue, slightly lower than that expected for loss of the Me group (96.3%). A much sharper decomposition then takes place, ending at 259°C, with a residual weight of 20.6%, very slightly higher than that expected for ZnO (19.6%).

Decomposition of **(45)** shows three steps, the first beginning with a gradual weight loss from 65°C to 161°C, leaving a residue of 87.4%, which is lower than the expected for the loss of the Et group (92.2%), the first two steps are quite difficult to differentiate between so it is possible that the fir two steps overlap slightly. The second step continues until 223°C, leaving a weight of 61.3%, which is comparable to the loss of the TMEDA ligand (61.0%). Decomposition continues until 304°C, leaving a final weight of 21.4%, very close to the expected value for decomposition to ZnO (21.5%).

Decomposition of **(46)** begins at 84°C with a gradual weight loss, this becomes a much sharper weight loss at 128°C, the residual weight of 94.2% is comparable to that expected for the loss of the Et group (93.1%). The much sharper decomposition has finished by 260°C, leaving a residual weight of 19.8%, slightly higher than that expected for ZnO (18.9%). All residual weights and expected weights are surmised in Table 6.6

Table 6.6 Steps seen in the TGAs of **(43)** – **(46)**

	(43)	**(44)**	**(45)**	**(46)**
1st Step % Observed	94.9	93.3	87.4	94.2
Expected for ZnO_2R_f.TMEDA	95.8	96.3	92.2	93.1
2nd Step % Observed	45.9	-	61.3	-
Expected for ZnO.TMEDA	54.7	-	52.7	-
Expected for ZnO_2R_f	63.4	-	61.0	-
Final Weight %	19.6	20.6	21.4	19.8
Expected for ZnO	22.3	19.6	21.5	18.9

From a comparison of all TGAs, a decomposition mechanism can be suggested. It seems very likely that the first step is the loss of the R group from the Zn. Then if we assume that all compounds decompose in a similar fashion the dissociation of TMEDA seems likely to be the next step in the decomposition profile, due to the closeness of the observed and expected values of **(45)**. The third and final step must then be the decomposition of the carboxylate group to afford ZnO. As this last step happens quickly there is no way to determine a decomposition mechanism for the final step, although it has previously been shown that the thermal decomposition of $Zn(O_2CCH_3)_2$ proceeds with the loss of CO_2 and CH_3COCH_3.[46]

CVD Trials

(44) was chosen as a precursor for LPCVD trials due to its clean decomposition profile and higher thermal stability. LPCVD was chosen although little volatility was seen in the precursors; it was hoped that under vacuum conditions volatility could be high enough to get some carry over. Films were grown on glass substrates at a reactor temperature of 400°C, with a line and bubbler temperature of 90°C and a pressure of 39.6 Torr for a duration of 90 mins.

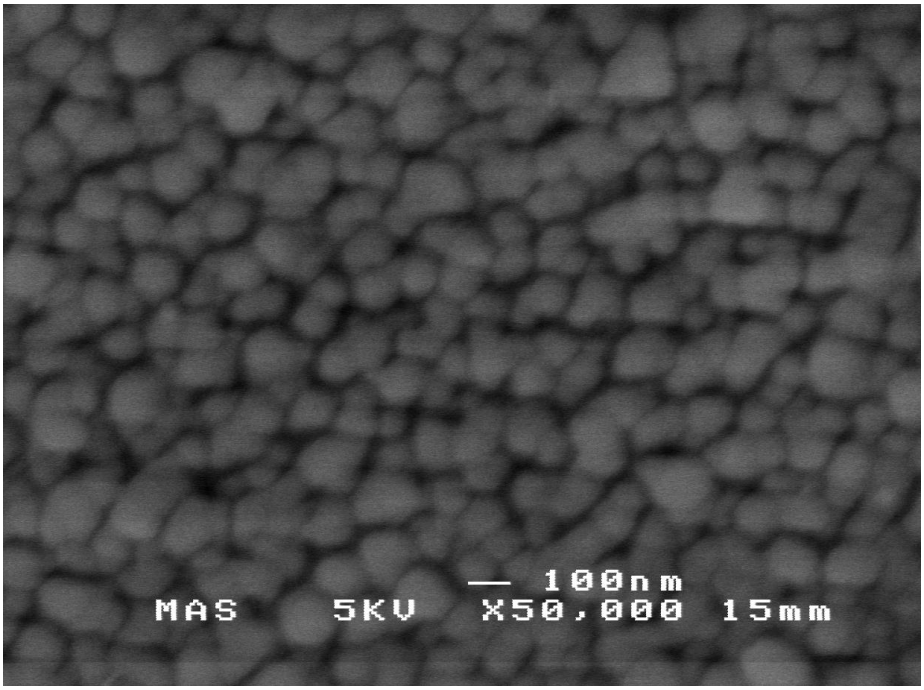

Figure 6.19 SEM image of film grown from **(44)**

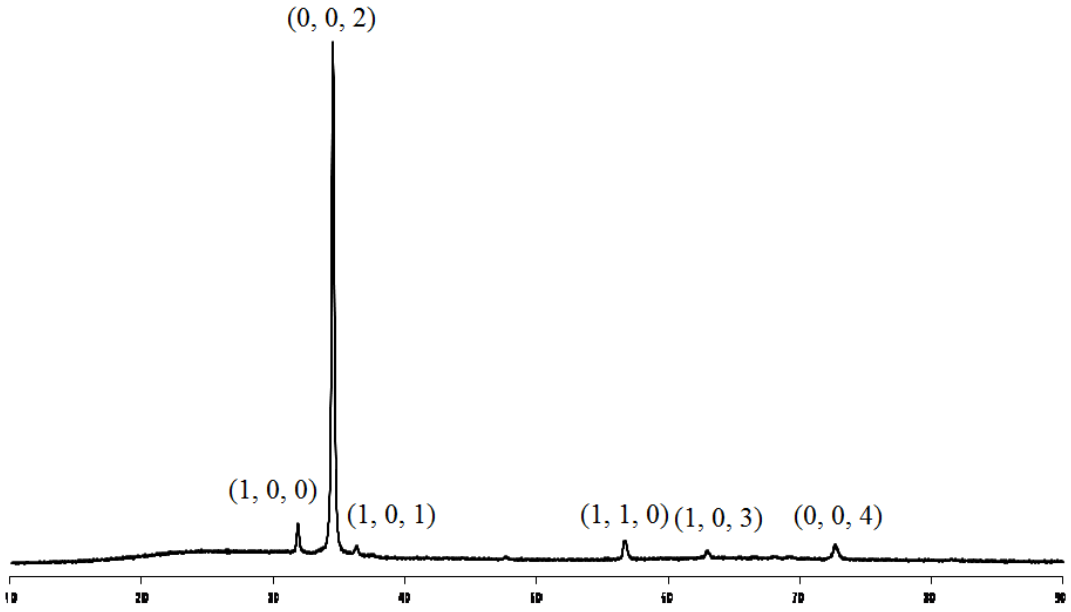

Figure 6.20 PXRD of film grown from **(47)**, indexing to PDF 89-139

Films were transparent and did not conduct when tested with a voltammeter. SEM imaging (Figure 6.19) shows a textured film with spheres ranging from 100-150nm in diameter. EDX confirms the presence of Zn and O but no F could be detected. The films were crystalline enough for PXRD measurements, which confirm the growth of ZnO (Figure 6.20). The PXRD suggests a highly oriented film, with a very intense peak corresponding to the (0, 0, 2) index and much smaller peaks

corresponding to the other indexes. The analysis on this film shows results that are very similar to the ZnO film grown from (35) which also had similar size crystallites, no fluorine incorporation and was highly (0, 0, 2) oriented.

6.2.4 TMEDA Adducts of Zinc Fluorocarboxylates

(47) and **(48)** were synthesised from the reaction between Et_2Zn and two equivalents of $HOOCC_2F_5$ or $HOOCC_3F_7$ in the presence of TMEDA in hexane (Scheme 6.5). All volatiles were removed *in vacuo* and products recrystalised in THF and characterised by microanalysis and NMR. ^1H NMR confirmed the presence of TMEDA and ^{13}C NMR confirmed the carboxylate ligand was intact.

$$Et_2Zn + 2R_fCO_2H + TMEDA \xrightarrow[-78^oC,\ Ar]{\text{hexane}} [Zn(O_2CR_f)_2.TMEDA]_2$$

(47) $R_f = C_2F_5$
(48) $R_f = C_3F_7$

Scheme 6.5 Synthesis of **(47)** and **(48)**

Structural Analysis

Crystals were obtained on cooling a solution of **(47)** in THF to -20°C (Figure 6.21). Significant bond distances are detailed in Table 6.7.

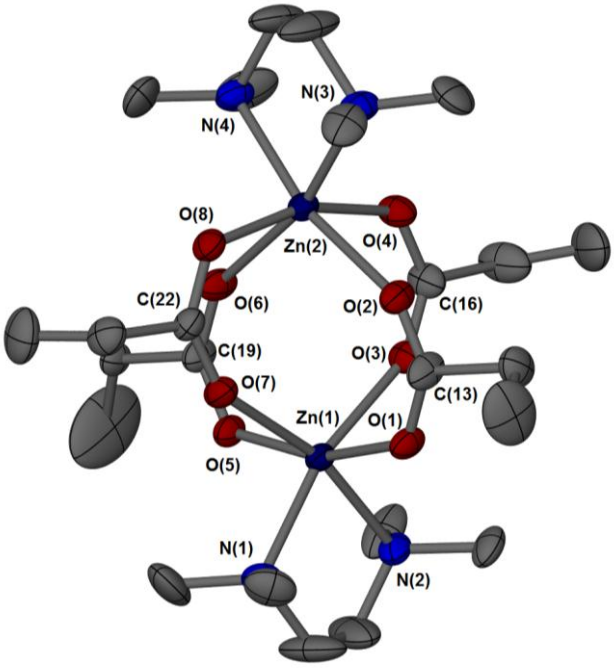

Figure 6.21 Structure of **(47)**, thermal ellipsoids drawn at 50% probability

Table 6.7 Selected bond distances (Å) of **(47)**

	(47)
Zn(1)-O(1)	1.978(2)
Zn(2)-O(2)	2.326(3)
Zn(1)-O(3)	2.134(3)
Zn(2)-O(4)	1.980(3)
Zn(1)-O(5)	1.972(2)
Zn(2)-O(6)	2.368(3)
Zn(1)-O(7)	2.350(3)
Zn(2)-O(8)	1.985(3)
O(1)-C(13)	1.241(5)
O(2)-C(13)	1.223(5)
O(3)-C(16)	1.220(5)
O(4)-C(16)	1.249(5)
O(5)-C(19)	1.263(4)
O(6)-C(19)	1.225(4)
O(7)-C(22)	1.235(4)
O(8)-C(22)	1.250(5)
Zn(1)-N(1)	2.185(3)
Zn(1)-N(2)	2.199(3)
Zn(2)-N(3)	2.168(3)
Zn(2)-N(4)	2.190(3)

(47) forms a dimer with four carboxylate ligands bridging between the two zinc centres and the two TMEDA ligands capping each zinc centre, which both have distorted octahedral coordination. All carboxylate groups show bidentate coordination with two carboxylates with shorter bonds to Zn(1) and longer bonds to Zn(2) and two with shorter bonds to Zn(2) and longer bonds to Zn(1). The O-C bond distances are affected by this, with one slightly shorter and one slightly longer bond in each of the carboxylate ligands. The TMEDA groups are isobidentate with bond distances that are the same in the group attached to Zn(1) and only slightly different in the TMEDA group attached to Zn(2).

Only one other $Zn(O_2CR)_2$.TMEDA structure appears to have been reported in literature, $Zn(O_2CCH_3)_2$.TMEDA. This structure is monomeric with two anisobidentate acetate ligands and an isobidentate TMEDA ligand.[49]

Crystals of $[Zn(O_2CC_3F_7)_2.TMEDA].H_2O$, **(49)** were obtained on cooling a solution of **(48)** in THF to -20°C for a period of 3 months (Figure 6.22). The structure is a hydrated version of **(48)**. The H_2O was probably present in the THF; other crystals that were not suitable for diffraction were the major product so it is possible that **(49)** is a minor by-product.

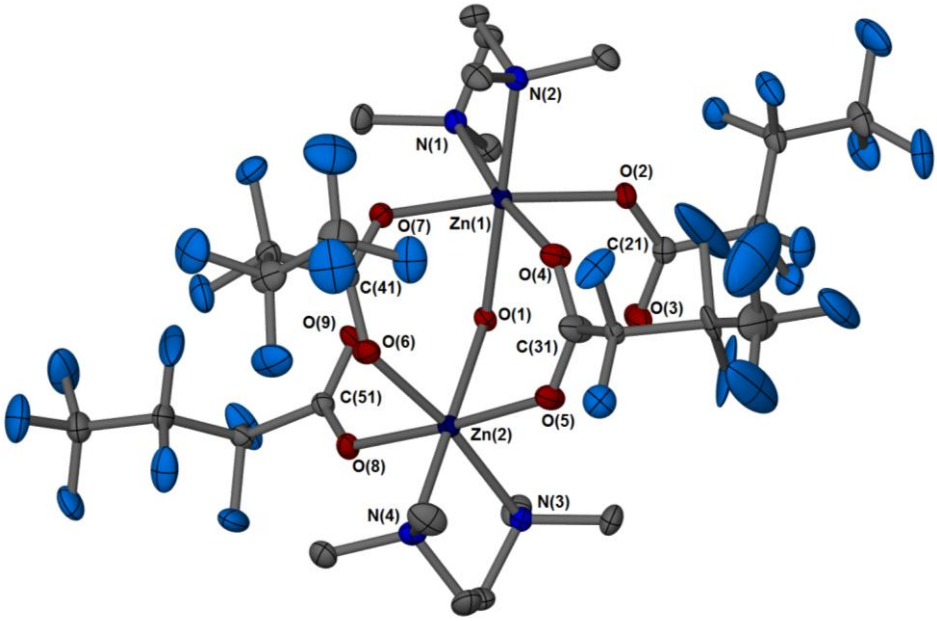

Figure 6.22 Structure of **(49)**, thermal ellipsoids drawn at 30% probability

The structure is a dimer, similar to that of **(48)** but the addition of a water molecule [O(1)] in the centre breaks up the symmetry and causes two bidentate carboxylate ligands, bridging over the two zinc centres, and two monodentate ligands. The two bidentate carboxylate groups have very similar bond distances between the oxygen and the zinc, ranging from 2.078(2)Å – 2.097(2)Å. The two monodentate carboxylate groups have slightly longer bonds, 2.143(2)Å for Zn(1) – O(2) and 2.127(2)Å for Zn(2) – O(8). The H_2O molecule which bridges between the two zinc centres has even longer bond lengths, 2.184(2)Å for Zn(1) – O(1) and 2.205(2)Å for Zn(2) – O(1).

The bond distances between the carbon and oxygen atoms in the carboxylate groups are all very similar, even in the groups that are monodentate. A monodentate

group would normally show a longer bond between the carbon and oxygen bonded to the zinc atom and a much shorter bond between the carbon and free oxygen. The similarity in the bond lengths can in this case be explained by hydrogen bonding between the free oxygen atoms and the central water molecule (Figure 6.23). The TMEDA ligands both show a degree of anisobidenticity with one longer Zn – N bond and one shorter Zn – N bond.

In both cases the Zn atoms are six-coordinated and exhibit a slightly distorted octahedral structure with opposite bond angles ranging from 171.98(9)° – 179.16(9)° and 171.42(9)° – 179.00(10)° for Zn(1) and Zn(2) respectively and adjacent bond angles ranging from 84.59(10)° – 96.02(9)° and 84.54(11)° – 94.80(10)° for Zn(1) and Zn(2) respectively. An almost identical structure is seen in $[Zn(O_2CCF_3)_2.TMEDA]_2.H_2O$. This structure also has octahedral Zn atoms which show very little deviation from the angles required for a perfect octahedron [opposite angles of 170.17(6)° - 176.61(6)° and 169.27(6)° - 178.81(6)° in Zn(1) and Zn(2) and adjacent angles of 84.09(6)° – 98.93(6)° and 83.69(6)° – 96.54(6)° in Zn(1) and Zn(2)]. The structure of $[Zn(O_2CCF_3)_2.TMEDA]_2.H_2O$ also has two monodentate and two bidentate carboxylates, with two TMEDA ligands capping the two Zn atoms.[50] A comparison between selected bond distances in **(49)** and $[Zn(O_2CCF_3)_2.TMEDA]_2.H_2O$ is given in Table 6.8.

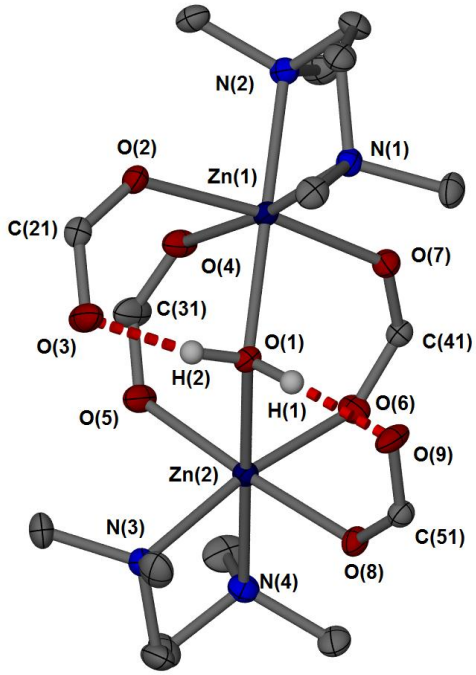

Figure 6.23 Structure of **(49)** with C_3F_7 groups omitted, thermal ellipsoids drawn at 30% probability

Table 6.8 Selected bond distances (Å) of **(49)**

	(49)	**$[Zn(O_2CCF_3)_2.TMEDA]_2.H_2O$**[50]
Zn(1)-O(1)	2.184(2)	2.2018(13)
Zn(2)-O(1)	2.205(2)	2.1863(13)
Zn(1)-O(2)	2.143(2)	2.1378(13)
Zn(1)-O(4)	2.089(2)	2.0839(13)
Zn(2)-O(5)	2.078(2)	2.0851(14)
Zn(1)-O(7)	2.097(2)	2.0869(13)
Zn(2)-O(6)	2.083(2)	2.0852(14)
Zn(2)-O(8)	2.127(2)	2.1467(14)
O(2)-C(21)	1.253(4)	1.237(2)
O(3)-C(21)	1.237(4)	1.231(2)
O(4)-C(31)	1.230(4)	1.230(2)
O(5)-C(31)	1.238(4)	1.238(2)
O(6)-C(41)	1.245(4)	1.235(2)
O(7)-C(41)	1.232(4)	1.225(2)
O(8)-C(51)	1.240(4)	1.236(2)
O(9)-C(51)	1.246(5)	1.223(2)
H(1)-O(9)	1.761(5)	1.761(5)
H(2)-O(3)	1.712(5)	1.712(5)
Zn(1)-N(1)	2.181(3)	2.1687(13)
Zn(1)-N(2)	2.159(3)	2.1885(16)
Zn(2)-N(3)	2.188(3)	2.1608(16)
Zn(2)-N(4)	2.169(2)	2.2100(16)

Materials analysis

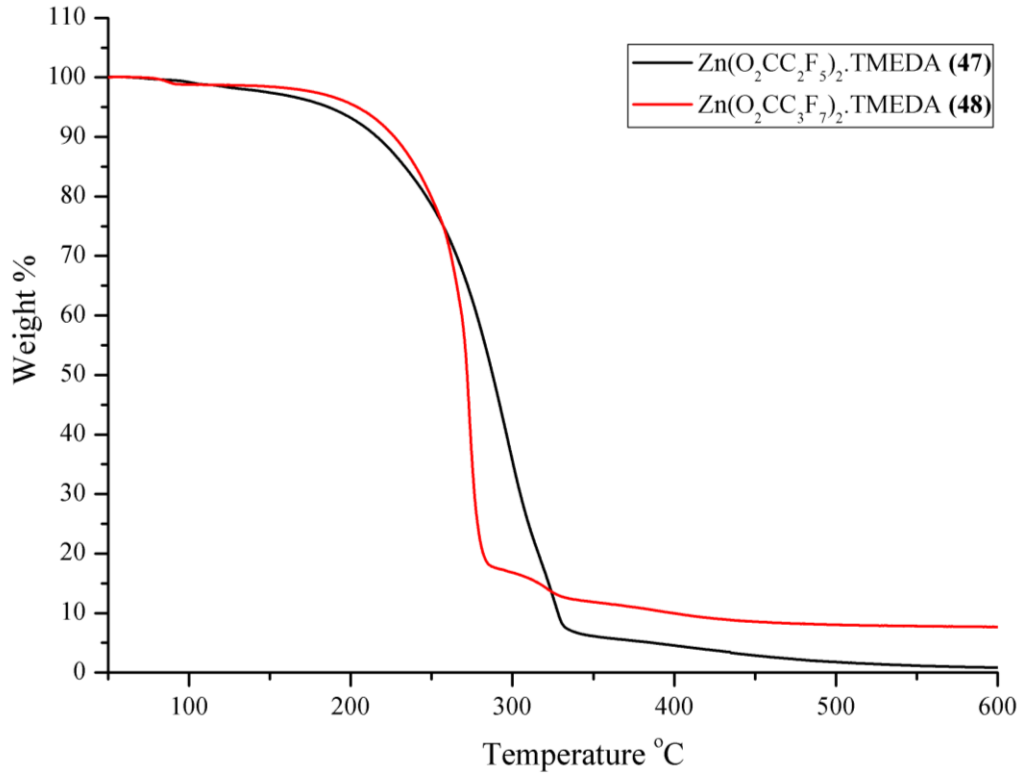

Figure 6.24 TGA of **(47)** and **(48)** with a heating rate of 5°C/min

TGAs of **(47)** and **(48)** show some volatility (Figure 6.24) **(47)** shows gradual weight loss from 97°C which becomes much sharper at 199°C, this ends at 347°C with a final weight of 6.25% which becomes gradually smaller until the measurement has stopped at 600°C, leaving a weight of 0.9%, much lower than that expected for ZnO (15.8%), indicating considerable volatility in the precursor.

(48) also shows gradual weight loss from 80°C which becomes much sharper at 172°C, ending at 288°C with a residue of 17.3%. A second smaller step is then seen, ending at 336°C leaving a residue of 12.3°C. Both steps have residues which are much lower than that expected for either the dissociation of the TMEDA ligand (80.8%) or the decomposition of the carboxylate groups (32.4%). A third and final step is seen from 336°C to 448°C, leaving a residue of 7.7%, also much lower than that expected for ZnO (13.2%).

CVD Trials

(47) was chosen as a precursor for LPCVD trials due to its superior volatility Films were grown on glass substrates at a reactor temperature of 450°C and a bubbler and line temperature of 150°C for 120 minutes at a pressure of 39.8 Torr.

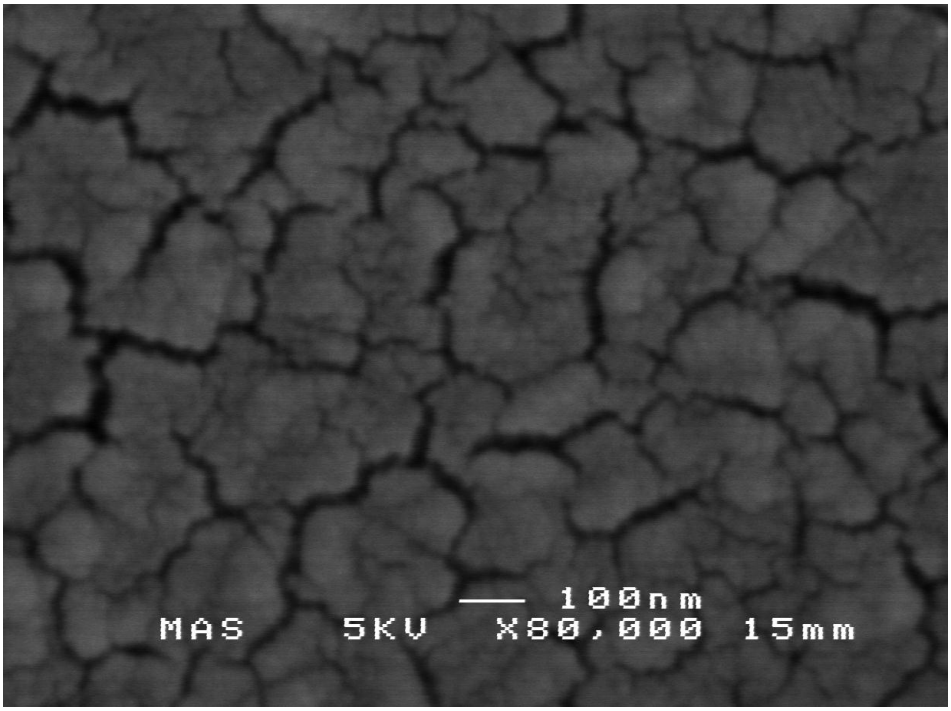

Figure 6.25 SEM image of films grown from **(47)**

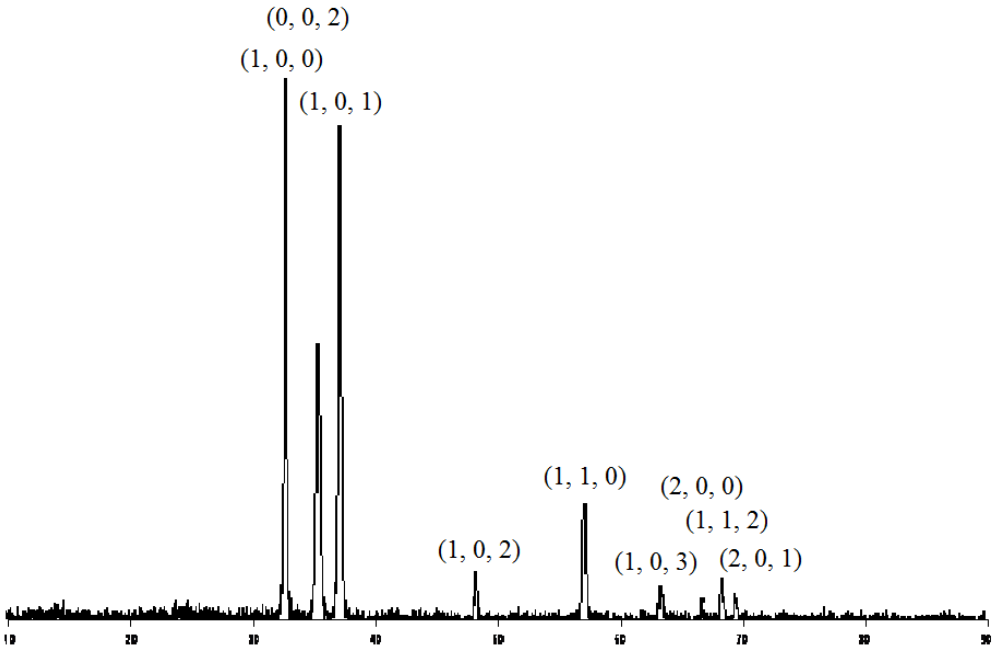

Figure 6.26 PXRD of film grown from **(47)**, indexing to PDF 89-1397

Films were transparent and did not conduct when tested with a voltammeter. SEM imaging (Figure 6.25) reveals a textured film with very small spheres, around 20nm in diameter. The film is cracked around clusters of varying size of these spheres. EDX measurements confirm the presence of Zn and O but show no F in the films. PXRD confirms the films are ZnO and shows much less orientation (Figure 6.26) than is seen in the films grown from **(35)** or **(44)**.

6.2.5 Conclusions

A number of potential precursors for the deposition of ZnO:F have been synthesised and their materials properties studied. For the series of organozinc fluorocarboxylates, the precursors with C_3F_7 groups showed a much cleaner decomposition mechanism and some volatility. As such, **(37)** was chosen as a precursor for LPCVD trials. Due to the close Zn-F interaction seen in the crystal structures of **(39)** and **(41)** it was hoped that this could lead to incorporation of fluorine in the films. However films did not conduct and no fluorine could be detected in the EDX measurements.

The insertion of oxygen into the Zn-R bond was observed when the precursors [**(35)** and **(37)**] came into contact was just a small amount of oxygen, forming $[Zn_5Me_2(OMe)_2(O_2CC_2F_5)_6]_2$ **(36)** and $[Zn_5Me_2(OMe)_2(O_2CC_3F_7)_6]_2$ **(38)**. This has been observed in methylzinc alkoxide precursors when an oxygen atmosphere converted the Me-Zn bond into first a peroxide, MeOOZnOR and subsequently an alkoxide, MeOZnOR.[48]

The inclusion of oxygen to afford a cage like structure in $Zn_9Et_2(O_2CC_2F_5)_{12}(O)_2$, **(40)** and $Zn_8Et_4(OEt)_4(O_2CC_3F_7)_6(O)$, **(42)** could arise from two different mechanisms. Either the oxygen inclusion was due to a small amount of oxygen in the solvent or it was due to a small amount of water in the solvent. Both mechanisms are plausible and have been observed in previously.[42, 48]

The use of TMEDA to form adducts brings the degree of oligomerisation down from polymer chains to monomeric species **(43)** – **(46)**. **(44)** was chosen as a precursor for LPCVD trials due to it's cleaner decomposition mechanism and volatility. EDX could not detect any fluorine in the films and PXRD confirmed that the films were ZnO.

6.3 Experimental

Synthesis of $[MeZn(O_2CC_2F_5)]_n$ ***(35)****:* C_2F_5COOH (0.65g, 4.0mmol) was added to a stirred solution of Me_2Zn (2ml of 2M solution in hexane, 4.0mmol) in hexane (10ml) at -78°C. Solution was stirred overnight while slowly warming up to room temperature, a white precipitate remained. Solution was warmed to 50°C, leaving a clear solution, crystals were obtained on slow cooling of the solution to room temperature (0.61g, 63%, mp 115-116°C). Analysis found (calc for $C_4H_3F_5O_2Zn$): C 19.8 (19.8), H 1.16 (1.25). ^{1}H NMR (300 MHz, THF-d8) δ ppm: -0.81 (s, 3H, CH_3), ^{13}C NMR (300 MHz, $CDCl_3$) δ ppm: 163.2 (br. s, CO_2), 119.8 (qt, *J*=286.6, 35.4 Hz, CF_3), 108.0 (tq, *J*=264.2, 37.2 Hz, CF_2), -18.2 (br. s, CH_3), ^{19}F NMR (400 MHz, THF-d8) δ ppm: -85.7 (br. s, CF_3), -123.0 (br. s, CF_2)

Synthesis of $[Zn_5Me_2(OMe)_2(O_2CC_2F_5)_6]_2$ ***(36)****:* Initial attempts to recrystalise **(35)** with the addition of CH_2Cl_2 (10ml) and cooling to 5°C produced **(36)** (0.38g, 41%, mp 81-83°C). Analysis found (calc for $C_{22}H_{12}F_{30}O_{14}Zn_5$): C 19.3 (19.0), H 1.03 (0.87). ^{1}H NMR (300 MHz, THF-d8) δ ppm: 3.44 (br. s, 3H, OCH_3), -0.81 (s, 3H, $ZnCH_3$), ^{13}C NMR (300 MHz, $CDCl_3$) δ ppm: 163.7 (br. s, CO_2), 119.8 (qt, *J*=285.9, 36.6 Hz, CF_3), 108.0 (tq, *J*=262.4, 37.8 Hz, CF_2), 53.8 (br. s, OCH_3), -18.2 (br. s, CH_3), ^{19}F NMR (400 MHz, THF-d8) δ ppm: -83.8 (s, CF_3), -121.2 (s, CF_2)

Synthesis of $[MeZn(O_2CC_3F_7)]_n$ ***(37)****:* Prepared using the same synthesis method as **(35)** using C_2F_5COOH (0.86g, 4.0mmol) and Me_2Zn (2ml of 2M solution in hexane, 4.0mmol). Yielding 0.72g, 62%, mp 81-83°C. Analysis found (calc for $C_5H_3F_7O_2Zn$): C 20.5 (20.6), H 1.17 (1.04). ^{1}H NMR (300 MHz, THF-d8) δ ppm: -0.80 (s, 3H, CH_3), ^{13}C NMR (300 MHz, $CDCl_3$) δ ppm: 165.5 (br. s, CO_2), 119.0 (qt, *J*=288.2, 34.3 Hz, CF_3), 109.8 (tsxt, *J*=266.3, 34.3, CF_2CF_3) ,109.6 (tt, *J*=265.3, 33.30Hz, O_2CCF_2), -18.4 (br. s, CH_3), ^{19}F NMR (500 MHz, $CDCl_3$) δ ppm: -82.4 (br. s, CF_3), -119.1 (br. s, CF_2), -128.3 (br. s, CF_2)

Synthesis of $[Zn_5Me_2(OMe)_2(O_2CC_3F_7)_6]_2$ ***(38)****:* Initial attempts to recrystalise **(37)** with the addition of CH_2Cl_2 (10ml) and cooling to 5°C produced **(38)**, yielding 0.41g, 36%, mp 141-142°C. Analysis found (calc for $C_{28}H_{12}F_{42}O_{14}Zn_5$): C 19.8 (19.9), H

0.77 (0.72). ^{1}H NMR (300 MHz, THF-d8) δ ppm: 3.52 (br. s, 3H, OCH_3), -0.84 (s, 3H, $ZnCH_3$) ^{13}C NMR (300 MHz, $CDCl_3$) δ ppm: 162.5 (br. s, CO_2), 117.5 (qt, *J*=286.6, 34.7 Hz, CF_3), 108.3 (tsxt, J=266.1, 39.1 Hz, *C*F_2CF_3), 108.2 (tt, J=267.3, 32.9 Hz, O_2CCF_2), 52.2 (br. s, OCH_3), -6.1 (s, $ZnCH_3$), ^{19}F NMR (400 MHz, THF-d8) δ ppm: -81.8 (s, CF_3), -118.5 (br. s, CF2), -127.9 (s, CF_2)

Synthesis of $[EtZn(O_2CC_2F_5)]_n$ ***(39)****:* Prepared using the same synthesis method as **(37)** using C_2F_5COOH (0.65g, 4.0mmol) and Et_2Zn (4ml of 1M solution in hexane, 4.0mmol), leaving a clear solution with a small amount of white precipitate. Crystals were obtained from was from filtering the solution and cooling to -20°C (0.71g, 70%, mp 89-91°C). Analysis found (calc for $C_5H_5F_5O_2Zn$): C 23.6 (23.4), H 1.91 (1.97). ^{1}H NMR (500 MHz, THF-d8) δ ppm: 1.17 (t, *J*=8.04 Hz, 3H, CH_3), 0.21 (q, *J*=8.20 Hz, 2H, CH_2), ^{13}C NMR (500 MHz, THF-d8) δ ppm: 164.1 (br. s, CO_2), 119.7 (qt, *J*=284.3, 34.5 Hz, CF_3), 108.0 (tq, *J*=264.3, 37.2 Hz, CF_2), 12.6 (s, CH_3), -2.7 (br. s, CH_2), ^{19}F NMR (500 MHz, THF-d8) δ ppm: -83.9 (br. s, CF_3), -121.2 (br. s, CF_2)

Synthesis of $Zn_9Et_2(O_2CC_2F_5)_{12}(O)_2$ ***(40)****:* From synthesis of **(39)**, the small amount of white precipitate was dissolved in CH_2Cl_2 (10ml) and hexane (10ml), solution was filtered and colourless crystals were obtained on cooling to 5°C (0.09g, 10%, mp 134-136°C). Analysis found (calc for $C_{40}H_{10}F_{60}O_{26}Zn_9$): C 18.2 (18.3), H 0.46 (0.38).

Synthesis of $[EtZn(O_2CC_3F_7)]_n$ ***(41)****:* Prepared using the same synthesis method as **(35)** using C_2F_5COOH (0.86g, 4.0mmol) and Et_2Zn (4ml of 1M solution in hexane, 4.0mmol). Yielding 0.79g, 65%, mp 96-99°C. Analysis found (calc for $C_6H_5F_7O_2Zn$): C 22.6 (23.5), H 1.56 (1.65). ^{1}H NMR (300 MHz, THF-d8) δ ppm: 1.17 (t, *J*=7.91 Hz, 3H, CH_3), 0.21 (q, *J*=8.10 Hz, 2H, CH_2), ^{13}C NMR (500 MHz, $CDCl_3$) δ ppm: 162.9 (br. s, CO_2), 119.1 (qt, *J*=288.0, 33.4 Hz, CF_3), 109.8 (tsxt, *J*=264.2, 35.3 Hz, *C*F_2CF_3), 109.6 (tt, *J*=264.2, 35.5 Hz, *C*$F_2CF_2CF_3$), 12.6 (s, CH_3), -2.8 (s, CH_2), ^{19}F NMR (500 MHz, $CDCl_3$) δ ppm: -81.8 (br. s, CF_3), -118.4 (br. s, CF_2), -127.8 (br. s, CF_2)

$Zn_8Et_4(OEt)_4(O_2CC_3F_7)_6(O)$ ***(42)****:* Initial attempts to recrystalise **(41)** with the addition of CH_2Cl_2 (10ml) and cooling to 5°C produced **(42)** (0.43g, 41%, mp 115-117°C). Analysis found (calc for $C_{40}H_{40}F_{42}O_{17}Zn_8$): C 22.7 (22.8), H 1.85 (1.92). ^{1}H

NMR (300 MHz, $CDCl_3$) δ ppm: 3.74 (q, *J*=7.03 Hz, 2H, OCH_2), 1.07 (t, *J*=7.20 Hz, 3H, OCH_2CH_3), 0.96 (t, *J*=7.90 Hz, 3H, $ZnCH_2CH_3$), -0.01 (q, *J*=7.91 Hz, 2 H, $ZnCH_2$), ^{13}C NMR (300 MHz, $CDCl_3$) δ ppm: 165.0 (br. s, CO_2), 119.1 (qt, *J*=286.1, 36.2 Hz, CF_3), 109.9 (tsxt, *J*=266.1, 36.2, Hz, CF_2CF_3), 109.8 (tt, *J*=267.0, 34.3 Hz, $CF_2CF_2CF_3$), 63.7 (br. s., OCH_2), 21.3 (br. s., OCH_2CH_3), 12.7 (s, $ZnCH_2CH_3$), -2.51 (br. s., $ZnCH_2$), ^{19}F NMR (400 MHz, THF-d8) δ ppm: -81.8 (s, CF_3), -118.5 (br. s, CF2), -127.8 (s, CF_2)

Synthesis of $MeZn(O_2CC_2F_5)TMEDA$ ***(43)****:* C_2F_5COOH (0.65g, 4.0mmol) was added to a stirred solution of Me_2Zn (3ml of 2M solution in hexane, 6.0mmol) and TMEDA (0.47g, 4.0mmol) in hexane (10ml) at -78°C. Solution was stirred overnight while slowly warming up to room temperature. Solvent and volatiles were removed *in vacuo*, a colourless oil remained (0.94g, 66%, mp 119-120°C). Analysis found (calc for $C_{10}H_{19}F_5N_2O_2Zn$): C 33.4 (33.5), H 5.33 (5.35), N 7.67 (7.82). ^1H NMR (300 MHz, THF-d8) δ ppm: 2.68 (s, 4H, NCH_2), 2.44 (s, 12H, NCH_3), -0.93 (s, 3H, $ZnCH_3$), ^{13}C NMR (300 MHz, THF-d8) δ ppm: 161.6 (t, J=24.8 Hz, CO_2), 120.2 (qt, J=285.9, 36.0 Hz, CF_3), 108.1 (tq, J=260.5, 36.6 Hz, CF_2), 57.7 (s, NCH_2), 46.9 (s, NCH_3), -18.7 (s, $ZnCH_3$), ^{19}F NMR (400MHz, THF-d8) δ ppm: -85.5 (CF_3), -122.7 (CF_2)

Also prepared by the same method:

$MeZn(O_2CC_3F_7)TMEDA$ ***(44)****:* Using C_3F_7COOH (0.86g, 4.0mmol), Me_2Zn (3ml of 2M solution in hexane, 6.0mmol) and TMEDA (0.47g, 4.0mmol). Yielding 1.42g, 87%, mp 97-99°C. Analysis found (calc for $C_{11}H_{19}F_7N_2O_2Zn$): C 32.2 (32.4), H 4.54 (4.69), N 6.94 (6.86). ^1H NMR (300 MHz, THF-d8) δ ppm: 2.69 (s, 4H, NCH_2), 2.45 (s, 12H, NCH_3), -0.93 (s, 3H, $ZnCH_3$), ^{13}C NMR (500 MHz, THF-d8) δ ppm: 161.7 (t, 25.1 Hz, CO_2), 119.3 (qt, J=286.6, 33.8 Hz, CF_3), 110.2 (tsxt, J=264.8, 36.0 Hz, CF_2CF_3), 109.8 (tt, J=263.8, 31.6 Hz, O_2CCF_2), 57.8 (s, NCH_2), 47.0 (s, NCH_3), -18.7 (s, $ZnCH_3$), 19F NMR (400MHz, THF-d8) δ ppm: -83.6 (CF_3), -119.9 (CF_2), -129.4 (CF_2)

$EtZn(O_2CC_2F_5)TMEDA$ ***(45)****:* Using C_2F_5COOH (0.65g, 4.0mmol), Et_2Zn (6ml of 1M solution in hexane, 6.0mmol) and TMEDA (0.47g, 4.0mmol). Yielding 1.36g,

91%. On standing, crystals formed in oil. Analysis found (calc for $C_{11}H_{21}F_5N_2O_2Zn$): C 35.3 (35.5), H 5.55 (5.69), N 7.47 (7.53). ^{1}H NMR (300 MHz, THF-d8) δ ppm: 2.68 (s, 4H, NCH_2), 2.45 (s, 12H, NCH_3), 1.18 (t, *J*=8.10 Hz, 3H, $ZnCH_2C\mathit{H}_3$), 0.10 (q, *J*=8.30 Hz, 2H, $ZnC\mathit{H}_2CH_3$), ^{13}C NMR (300 MHz, THF-d8) δ ppm: 162.2 (t, 26.1 Hz, CO_2), 120.2 (qt, J=284.7, 34.7 Hz, CF_3), 108.2 (tq, J=262.4, 37.2 Hz, CF_2), 57.8 (s, NCH_2), 47.1 (s, NCH_3), 13.4 (s, $ZnCH_2\mathit{C}H_3$), -3.3 (s, $Zn\mathit{C}H_2CH_3$), ^{19}F NMR (400MHz, THF-d8) δ ppm: -85.5 (CF_3), -122.6 (CF_2)

$EtZn(O_2CC_3F_7)$TMEDA ***(46)****:* Using C_3F_7COOH (0.86g, 4.0mmol), Et_2Zn (6ml of 1M solution in hexane, 6.0mmol) and TMEDA (0.47g, 4.0mmol). Yielding 1.51g, 89%. Analysis found (calc for $C_{12}H_{21}F_7N_2O_2Zn$): C 33.9 (34.1), H 4.86 (5.01), N 6.54 (6.64). ^{1}H NMR (300 MHz, THF-d8) δ ppm: 2.68 (s, 4H, NCH_2), 2.46 (s, 12H, NCH_3), 1.18 (t, *J*=8.10 Hz, 3H, $ZnCH_2C\mathit{H}_3$), 0.09 (q, *J*=8.30 Hz, 2H, $ZnC\mathit{H}_2CH_3$), ^{13}C NMR (500 MHz, THF-d8) δ ppm: 161.6 (t, *J*=24.5 Hz, CO_2), 119.3 (qt, *J*=287.0, 34.5 Hz, CF_3), 110.2 (tsxt, *J*=264.3, 36.1 Hz, $\mathit{C}F_2CF_3$), 108.2 (tt, *J*=264.3, 30.9 Hz, $O_2C\mathit{C}F_2$), 57.8 (s, NCH_2), 47.1 (s, NCH_3), 13.3 (s, $ZnCH_2\mathit{C}H_3$), -3.3 (s, $Zn\mathit{C}H_2CH_3$), 19F NMR (400MHz, THF-d8) δ ppm: -83.6 (CF_3), -119.8 (CF_2), -122.6 (CF_2)

Synthesis of $[Zn(O_2CC_2F_5)_2TMEDA]_2$ ***(47)****:* C_2F_5COOH (1.30g, 8.0mmol) was added to a stirred solution of Et_2Zn (4ml of 1M solution in hexane, 4.0mmol) and TMEDA (0.47g, 4.0mmol) in hexane (10ml) at -78°C. Solution was stirred overnight while slowly warming up to room temperature. Solvent and volatiles were removed *in vacuo*, a white solid remained. Solid was redissolved in THF (5ml) and colourless crystals were obtained on cooling to -20°C (1.74g, 86%, mp 97-99°C). Analysis found (calc for $C_{12}H_{16}F_{10}N_2O_4Zn$): C 28.3 (28.4), H 3.09 (3.19), N 5.52 (5.53). ^{1}H NMR (300 MHz, THF-d8) δ ppm: 2.73 (s, 4H, NCH_2), 2.50 (s, 12H, NCH_3), ^{13}C NMR (300 MHz, THF-d8) δ ppm: 162.7 (t, *J*=26.7 Hz, CO_2), 119.8 (qt, *J*=285.9, 34.7 Hz, CF_3), 108.1 (tq, *J*=263.0, 37.8 Hz, CF_2), 57.5 (s, NCH_2), 46.8 (s, NCH_3), ^{19}F NMR (400MHz, THF-d8) δ ppm: -85.7 (CF_3), -123.1 (CF_2)

Also prepared by the same method:

$[Zn(O_2CC_3F_7)_2TMEDA]_2$ ***(48)****:* Using C_3F_7COOH (1.71g, 8.0mmol), Et_2Zn (4ml of 1M solution in hexane, 4.0mmol) and TMEDA (0.47g, 4mmol). Yielding 2.05g,

85%, mp 119-120°C. Analysis found (calc for $C_{14}H_{16}F_{14}N_2O_4Zn$): C 27.8 (27.7), H 2.54 (2.66), N 4.73 (4.62). ^{1}H NMR (500 MHz, THF-d8) δ ppm: 2.72 (s, 4H, NCH_2), 2.49 (s, 12H, NCH_3) ^{13}C NMR (500 MHz, THF-d8) δ ppm: 162.8 (br. s, CO_2), 119.1 (qt, J=287.0, 34.5 Hz, CF_3), 110.0 (tsxt, J=266.1, 36.1 Hz, CF_2CF_3), 109.8 (tt, J=265.2, 37.1 Hz, O_2CCF_2), 57.7 (s, NCH_2), 47.0 (s, NCH_3), ^{19}F NMR (500MHz, THF-d8) δ ppm: -83.8 (t, *J*=8.67 Hz, CF_3), -120.6 (br. s, CF_2), -129.6 (s, CF_2)

*Synthesis of [Zn(O$_2$CC$_3$F$_7$)$_2$TMEDA]$_2$.H$_2$O **(49)**:* Recrystalisation of **(48)** from THF produced a few crystals of a hydrated molecule of **(48)**.

6.5 References

1. (a) Hu, J. H.; Gordon, R. G., *Solar Cells* **1991,** *30* (1-4), 437; (b) Liang, H. F.; Gordon, R. G., *J. Mater. Sci.* **2007,** *42* (15), 6388; (c) Guillen-Santiago, A.; Olvera, M. D. L.; Maldonado, A.; Reyes, A.; Asomoza, R., *Phys. Status Solidi A* **2002,** *191* (2), 499.
2. (a) Mahon, M. F.; Molloy, K. C.; Stanley, J. E.; Rankin, D. W. H.; Robertson, H. E.; Johnston, B. F., *Appl. Organomet. Chem.* **2005,** *19* (5), 658; (b) Molloy, K. C.; Stanley, J. E., *Appl. Organomet. Chem.* **2009,** *23* (2), 62.
3. Minami, T., *Semicond. Sci. Technol.* **2005,** *20* (4), S35.
4. Granqvist, C. G.; Green, S.; Niklasson, G. A.; Mlyuka, N. R.; von Kræmer, S.; Georén, P., *Thin Solid Films* **2010,** *518* (11), 3046.
5. Cui, J.; Wang, A.; Edleman, N. L.; Ni, J.; Lee, P.; Armstrong, N. R.; Marks, T. J., *Adv. Mater.* **2001,** *13* (19), 1476.
6. Nomura, K.; Ohta, H.; Takagi, A.; Kamiya, T.; Hirano, M.; Hosono, H., *Nature* **2004,** *432* (7016), 488.
7. Granqvist, C. G., *Sol. Energy Mater. Sol. Cells* **2007,** *91* (17), 1529.
8. Ginley, D. S., *Handbook of Transparent Conductors*. Springer: New York, 2010.
9. Gordon, R. G., *MRS Bull.* **2000,** *25* (8), 52.
10. Taylor, M. P.; Readey, D. W.; van Hest, M.; Teplin, C. W.; Alleman, J. L.; Dabney, M. S.; Gedvilas, L. M.; Keyes, B. M.; To, B.; Perkins, J. D.; Ginley, D. S., *Adv. Funct. Mater.* **2008,** *18* (20), 3169.
11. Ku, D. Y.; Kim, Y. H.; Lee, K. S.; Lee, T. S.; Cheong, B.; Seong, T. Y.; Kim, W. M., *Journal of Electroceramics* **2009,** *23* (2-4), 415.

12. Krishnakumar, V.; Ramamurthi, K.; Kumaravel, R.; Santhakumar, K., *Curr. Appl. Phys.* **2009,** *9* (2), 467.
13. Chen, X. L.; Xu, B. H.; Xue, J. M.; Zhao, Y.; Wei, C. C.; Sun, J.; Wang, Y.; Zhang, X. D.; Geng, X. H., *Thin Solid Films* **2007,** *515* (7-8), 3753.
14. Hu, J.; Gordon, R. G., *J. Electrochem. Soc.* **1992,** *139* (7), 2014.
15. Hu, J.; Gordon, R. G., *J. Appl. Phys.* **1992,** *71* (2), 880.
16. Hirata, G. A.; Siqueiros, J. M.; Diaz, J. A.; Contreras, O.; McKittrick, J.; Cheeks, T.; Lopez, O. A., *Thin Solid Films* **1996,** *288* (1-2), 29.
17. de la L. Olvera, M.; Maldonado, A.; Asomoza, R.; Konagai, M.; Asomoza, M., *Thin Solid Films* **1993,** *229* (2), 196.
18. Olvera, M. D. L.; Maldonado, A.; Asomoza, R.; Solorza, O.; Acosta, D. R., *Thin Solid Films* **2001,** *394* (1-2), 242.
19. Nam, G. M.; Kwon, M. S., *Electron. Mater. Lett.* **2011,** *7* (2), 127.
20. Yoon, H. S.; Lee, K. S.; Lee, T. S.; Cheong, B.; Choi, D. K.; Kim, D. H.; Kim, W. M., *Sol. Energy Mater. Sol. Cells* **2008,** *92* (11), 1366.
21. (a) Roth, A. P.; Williams, D. F., *J. Appl. Phys.* **1981,** *52* (11), 6685; (b) Smith, F. T. J., *Appl. Phys. Lett.* **1983,** *43* (12), 1108.
22. Lau, C. K.; Tiku, S. K.; Lakin, K. M., *J. Electrochem. Soc.* **1980,** *127* (8), 1843.
23. Solanki, R.; Collins, G. J., *Appl. Phys. Lett.* **1983,** *42* (8), 662.
24. Oda, S.; Tokunaga, H.; Kitajima, N.; Hanna, J.-i.; Shimizu, I.; Kokado, H., *Jpn. J. Appl. Phys.* **1985,** *24* (Part 1, No. 12), 1607.
25. Kaufmann, T.; Fuchs, G.; Webert, M.; Frieske, S.; Gäckle, M., *Crystal Research and Technology* **1989,** *24* (3), 269.
26. Triboulet, R.; Perriere, J., *Prog. Cryst. Growth Charact. Mater.* **2003,** *47* (2-3), 65.
27. Jones, A. C.; Hitchman, M. L., *Chemical Vapour Deposition Precursors, Processes and Applications*. The Royal Society of Chemistry,: Cambridge, 2009.
28. Jana, S.; Berger, R. J. F.; Frohlich, R.; Pape, T.; Mitzel, N. W., *Inorg. Chem.* **2007,** *46* (10), 4293.
29. Boyle, T. J.; Bunge, S. D.; Andrews, N. L.; Matzen, L. E.; Sieg, K.; Rodriguez, M. A.; Headley, T. J., *Chem. Mater.* **2004,** *16* (17), 3279.
30. Auld, J.; Houlton, D. J.; Jones, A. C.; Rushworth, S. A.; Malik, M. A.; O'Brien, P.; Critchlow, G. W., *J. Mater. Chem.* **1994,** *4* (8), 1249.

31. Johnson, A. L.; Hollingsworth, N.; Kociok-Kohn, G.; Molloy, K. C., *Inorg. Chem.* **2008,** *47* (24), 12040.
32. Otway, D. J.; Rees, W. S., *Coord. Chem. Rev.* **2000,** *210* (1), 279.
33. Turgambaeva, A. E.; Krisyuk, V. V.; Bykov, A. F.; Igumenov, I. K., *J. Phys. IV* **1999,** *9*, 65.
34. (a) Kashiwaba, Y.; Katahira, F.; Haga, K.; Sekiguchi, T.; Watanabe, H., *J. Cryst. Growth* **2000,** *221* (1-4), 431; (b) Haga, K.; Suzuki, T.; Kashiwaba, Y.; Watanabe, H.; Zhang, B. P.; Segawa, Y., *Thin Solid Films* **2003,** *433* (1-2), 131; (c) Purica, M.; Budianu, E.; Rusu, E.; Danila, M.; Gavrila, R., *Thin Solid Films* **2002,** *403-404*, 485.
35. Tammenmaa, M.; Koskinen, T.; Hiltunen, L.; Niinisto, L.; Leskela, M., *Thin Solid Films* **1985,** *124* (2), 125.
36. Mar, G. L.; Timbrell, P. Y.; Lamb, R. N., *Chem. Mater.* **1995,** *7* (10), 1890.
37. Jain, S.; Kodas, T. T.; Hampden-Smith, M., *Chem. Vapor Depos.* **1998,** *04* (02), 51.
38. Lu, J.; Ye, Z.; Huang, J.; Wang, L.; Zhao, B., *Appl. Surf. Sci.* **2003,** *207* (1-4), 295.
39. Kobayasm, K.; Matsubara, T.; Matsushima, S.; Shirakata, S.; Isomura, S.; Okada, G., *Journal of Materials Science Letters* **1996,** *15* (5), 457.
40. Sato, H.; Minami, T.; Miyata, T.; Takata, S.; Ishii, M., *Thin Solid Films* **1994,** *246* (1–2), 65.
41. Khan, O. F. Z.; O'Brien, P., *Thin Solid Films* **1989,** *173* (1), 95.
42. Lewinski, J.; Bury, W.; Dutkiewicz, M.; Maurin, M.; Justyniak, I.; Lipkowski, J., *Angewandte Chemie International Edition* **2008,** *47* (3), 573.
43. Addison, A. W.; Rao, T. N.; Reedijk, J.; van Rijn, J.; Verschoor, G. C., *J. Chem. Soc., Dalton Trans.* **1984,** (7), 1349.
44. Dickie, D. A.; Jennings, M. C.; Jenkins, H. A.; Clyburne, J. A. C., *Inorg. Chem.* **2005,** *44* (4), 828.
45. Orchard, K. L.; Harris, J. E.; White, A. J. P.; Shaffer, M. S. P.; Williams, C. K., *Organometallics* **2011,** *30* (8), 2223.
46. Duan, Y.; Li, J.; Yang, X.; Hu, L.; Wang, Z.; Liu, Y.; Wang, C., *Journal of Analytical and Applied Pyrolysis* **2008,** *83* (1), 1.
47. Lewinski, J.; Marciniak, W.; Lipkowski, J.; Justyniak, I., *J. Am. Chem. Soc.* **2003,** *125* (42), 12698.

48. Hollingsworth, N.; Johnson, A. L.; Kingsley, A.; Kockiok-Kohn, G.; Molloy, K. C., *Organometallics* **2011,** *30* (16), 4470.
49. Brown, D. A.; Errington, W.; Fitzpatrick, N. J.; Glass, W. K.; Kemp, T. J.; Nimir, H.; Ryan, A. T., *Chem. Commun.* **2002,** (11), 1210.
50. Brown, D. A.; Fitzpatrick, N. J.; Muller-Bunz, H.; Ryan, A. T., *Inorg. Chem.* **2006,** *45* (11), 4497.

Chapter Seven
Conclusions and Future Work

7.1 Deposition of Cu_2ZnSnS_4

With regards to the deposition of Cu_2ZnSnS_4, a range of zinc, tin and copper xanthates and dithiocarbamates have been synthesised and the materials properties investigated. The best matches in decomposition temperature and solubility were chosen and deposition attempts using AACVD were undertaken using firstly a mixture of only xanthates, then a mixture of copper xanthates with zinc and tin dithiocarbamates and finally using a mixture of all dithiocarbamates. The films which gave the best stoichiometry were deposited from a mixture of only dithiocarbamates, $Zn[S_2CN(Me)^nBu]_2$ **(17)**, $Sn[S_2CN(Me)^nBu]_2$ **(19)** and $(Ph_3P)_2CuS_2CN(Me)^nBu$ **(24)**. These precursors gave films with a composition of $Cu_2Zn_{1.2}Sn_{0.7}S_x$ where the sulphur content could not be confirmed by EDX due to an overlap in sulphur and molybdenum signals. The films were tested using a flashing LED experiment but showed no photoresponse. This could be due to the films still having too little tin in them, they could also be too thin or have incorrect sulphur content.

Attempts to synthesise nanoparticles from $Zn(S_2CO^nBu)_2$ **(4)**, $Sn(S_2COEt)_2$ **(7)** and $(^nBu_3P)_2CuS_2CO^nBu$ **(16)** proved to be more successful. The nanoparticles synthesised were between 5-10nm in size and had a composition of $Cu_2Zn_1Sn_{0.7}S_{2.6}$. Future work to improve the nanoparticles stoichiometry is required. This could be achieved by changing the reaction conditions such as temperature and time and also by introducing an additional sulphur source, such as elemental sulphur or thiurea.

7.2 Deposition of $CuSbS_2$

With regards to the deposition of $CuSbS_2$, antimony ethyl xanthate and two antimony dithiocarbamates were synthesised and their materials properties tested and compared with the copper xanthates and dithiocarbamates previously tested for the deposition of Cu_2ZnSnS_4. The precursors with the most promising matches in decomposition temperature and solubility were tested using AACVD. There were two mixtures that gave a stoichiometry of metals that was very close to the target films. Mixtures of $Sb(S_2COEt)_3$ **(9)** and $(^nBu_3P)_2CuS_2CO^nBu$ **(16)** or $Sb[S_2CN(Me)Bn]_3$ **(23)** and $(Ph_3P)_2CuS_2CN(Me)Bn$ **(25)** both gave film

compositions of $Cu_1Sb_{1.1}S_x$, once again with the sulphur content unknown. These films were both tested using a flashing LED experiment but once again gave no photoresponse. This could indicate that the films were either too thin or had the incorrect stoichiometry of sulphur.

AACVD experiments using a mixture CuI, $SbCl_3$ and thiurea produced films that contained Sb_2S_3 and Cu_2S phases rather than $CuSbS_2$. These films were also non continuous.

7.3 Heterobimetallic Precursors

A range of Zn/Cu, Sn/Cu and Sb/Cu heterobimetallic compounds were synthesised. With the exception of $(Me_3P)_3CuSnCl_3$ **(30)**, which has a direct Sn-Cu bond, all of the compounds had bridging chlorine atoms between the two different metal centres. Attempts to exchange the chlorine atoms with a sulphur containing ligand using both NaSEt and $(TMS)_2S$ were unsuccessful, resulting in the dissociation of the two metals from each other.

Further work is required to find a suitable synthesis method in order to synthesise structures that contain bridging sulphur atoms between the two different metal centres.

7.4 Deposition of ZnO:F

A range of organozinc fluorocarboxylates were synthesised and their materials properties studied. Structurally these proved to be polymers in the solid state, this is not normally favourable as polymers tend to be relatively involatile but materials analysis showed that two of the four precursors synthesised showed some volatility. LPCVD trials using $[MeZn(O_2CC_3F_7)]_n$ **(37)** deposited films of ZnO with no fluorine incorporation seen in the EDX measurements.

The insertion of oxygen was observed when the organozinc precursors came into contact with a small amount of oxygen or water. Two different kind of structures were observed, $[Zn_5Me_2(OMe)_2(O_2CC_2F_5)_6]_2$ **(36)** and $[Zn_5Me_2(OMe)_2(O_2CC_3F_7)_6]_2$ **(38)**, where the oxygen has been inserted into the Me-Zn bond and $Zn_9Et_2(O_2CC_2F_5)_{12}(O)_2$, **(40)** and $Zn_8Et_4(OEt)_4(O_2CC_3F_7)_6(O)$, **(42)** which are cage like structures with the oxygen in the centre of the cage.

The use of TMEDA to form adducts brings the degree of oligomerisation down from polymer chains to monomers. The materials properties of these monomers were

studies and $MeZn(O_2CC_3F_7)TMEDA$ **(44)** was chosen as a precursor for LPCVD trials due to it's cleaner decomposition mechanism and volatility however, EDX measurements could not detect any fluorine in the films and PXRD confirmed that the films were ZnO.

The synthesis of dimers containing two fluorocarboxylates ligands and capping TMEDA groups was achieved. LPCVD was attempted using $[Zn(O_2CC_2F_5)_2TMEDA]_2$ **(47)** but the films obtained did not contain any fluorine and were proved to be ZnO by PXRD.

All CVD trials produced films of ZnO with no detectable fluorine incorporation. This could be due to the absence of close Zn-F contacts in **(44)** and **(47)**. In the case of **(37)**, there was a close Zn-F contact in the solid state but this may be lost in the gas phase. The synthesis of compounds with a direct Zn-F bond could help with the incorporation of fluorine into the films.

A1.1 Laboratory Techniques

Reactions were carried out under an inert atmosphere using Schlenk techniques when required. Solvents were dried and degassed under an argon atmosphere over activated alumina columns using an Innovative Technology solvent purification system (SPS).

A1.2 Instrumentation

Microanalysis

Elemental analyses were performed using a Carlo Erba Flash 2000 Organic Elemental Analyser, operating at 900°C, with the oven at 70°C and a helium flow of 140ml / min.

Nuclear Magnetic Resonance Spectroscopy (NMR)

^{1}H, ^{13}C, ^{19}F and ^{119}Sn spectra were recorded on either a Bruker Avance 300 MHz, 400 MHz or 500 MHz FT-NMR Spectrometer (as detailed in experimental). Values are quoted in ppm, coupling constants are quoted in Hz. ^{1}H, ^{13}C spectra were recorded using $SiMe_4$ as an internal reference, ^{19}F spectra were recorded using $CFCl_3$ as an internal reference and ^{119}Sn spectra were recorded using the ^{1}H resonance of $SiMe_4$ as an internal reference.

X-Ray Crystallography

X-ray crystallography data was collected on a Nonius Kappa CCD diffractometer at 150K. Structure Determination and refinement were achieved using a SHELX suite of programs. Drawings were created using POV-Ray.

Thermogravimetric Analysis (TGA)

TGA spectra were recorded using a Perkin Elmer TGA 4000 Thermogravimetric Analyzer. The TGA furnace operates at temperatures ranging from 30 - 1000°C under an atmosphere of N_2. Pyris software was used to record and

interpret the data. A typical TGA experiment would heat from 50°C to 600°C at a heating rate of 5°C/min.

Powder X-Ray Diffraction (PXRD)

X-Ray diffraction analysis was carried out using a PANalytical X'Pert PRO Multi-Purpose Diffractometer with Cu Kα radiation. A PIXcel detector was used to collect data over an angular range of 10 - 90 °/2θ with a step size of 0.131 °/2θ.

Scanning Electron Microscopy (SEM)

SEM images were taken on a JEOL JSM 6480LV Scanning Electron Microscope using an accelerating voltage of 10 - 20kV. For higher magnification pictures (over 40,000 zoom) images were taken on a JEOL JSM 6301F Scanning Electron Microscope which has a field emission gun at an accelerating voltage of 3 - 10kV. When necessary films were sputtered with either gold or carbon in order to avoid charging and to improve secondary electron image quality.

Electron Dispersive X-Ray Analysis (EDX)

EDX measurements were taken on a JEOL JSM 6480LV Scanning Electron Microscope using an accelerating voltage of 10 - 20kV and using a cobalt standard.

Transmission Electron Microscopy (TEM)

TEM images were taken using a JEOL JEM 1200EXII Transmission Electron Microscope using an accelerating voltage of 20kV.
CVD experiments.

A1.3 CVD Reactors

The apparatus described was bought from ElecroGas Ststems and was designed for a variety of uses, namely APCVD, LPCVD and AACVD. The system consists of a cold wall reactor with associated gas lines and electronic heater controls. Only AACVD and LPCVD have been used in this study, so these will be discussed in detail.

AACVD Experiments

The nebuliser system used for AACVD is an ultrasonic humidifier from Pifco Health (model number 1077). A nebular is created via a piezoelectric transducer which is situated in the reservoir containing water. The piezoelectric transducer transmits ultrasound through the water and into the glass flask containing the precursor solution. The flask containing the precursor solution has a horizontal inlet and outlet through which the carrier gas flows. The nebular is carried on the gas stream to a substrate which is heated using an infrared light (Figure A1.1).

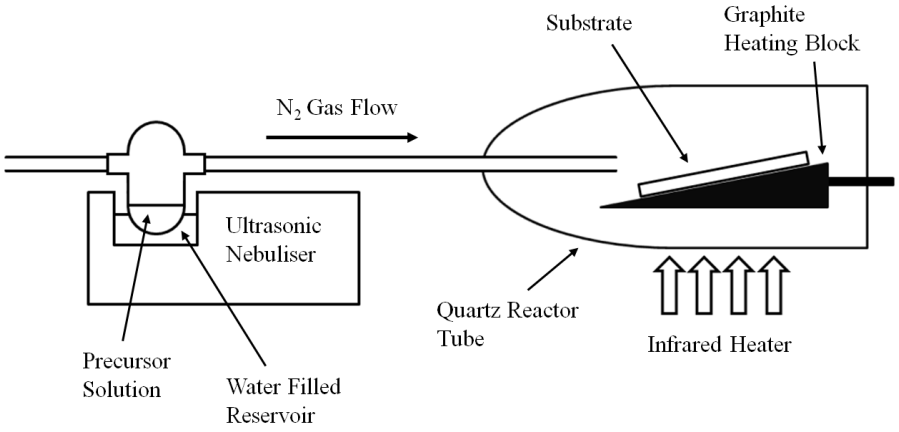

Figure A1.1 AACVD apparatus

LPCVD Experiments

For the LPCVD experiments the same cold wall reactor was used but rather than use the glass flask and nebuliser, a bubbler with a heated jacket was attached to the main gas line and a vacuum was employed (Figure A1.2). The bubbler and precursor lines can be heated to approximately 150°C to ensure that the precursor remains in the gas phase. A flow of N_2 carries the volatilised precursor to the heated substrate.

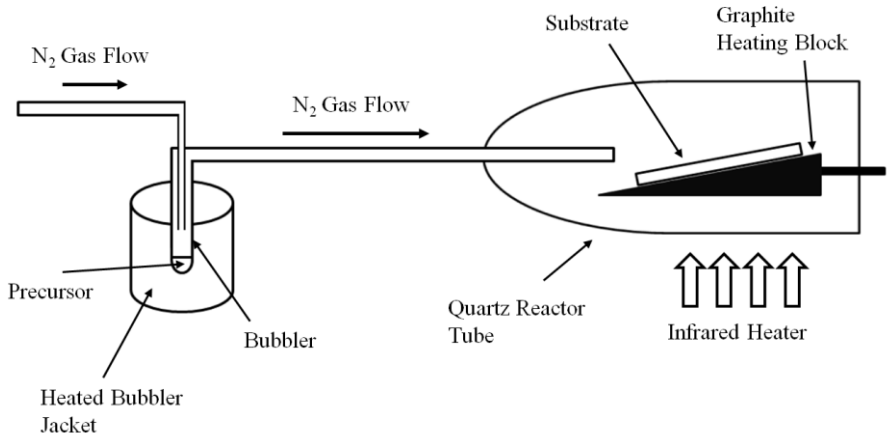

Figure A1.2 LPCVD apparatus

A1.4 Flashing LED Experiments

Flashing LED experiments were performed on films with promising stoichiometry. The films were placed into a glass container with an approximate volume of $2cm^3$ which was filled with a 2.0M aqueous solution of $Eu(NO_3)_3.6H_2O$ as an electron-scavenging redox electrolyte. Pulsed illumination from a high intensity light emitting diode was used to try to generate transient photocurrents. The photochemical response was measured using an Autolab 20 potentiostat at a potential of -0.4V vs Ag|AgCl using Pt wire as a counter electrode (Figure A1.3). In all experiments no significant response was recorded.

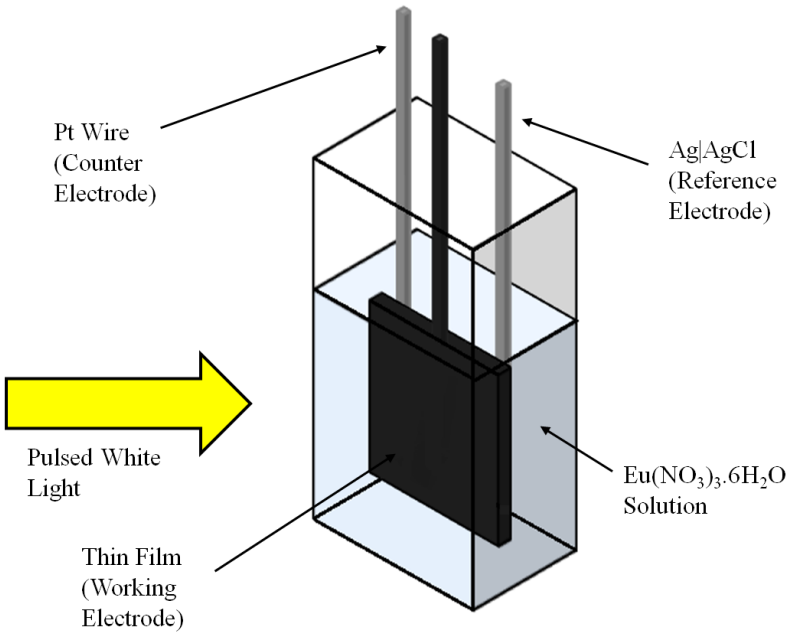

Figure A1.3 Flashing LED experiment apparatus

A2.1 X-Ray Crystallographic Information

All single crystal data relating to the structures reported in this thesis are provided on a CD.